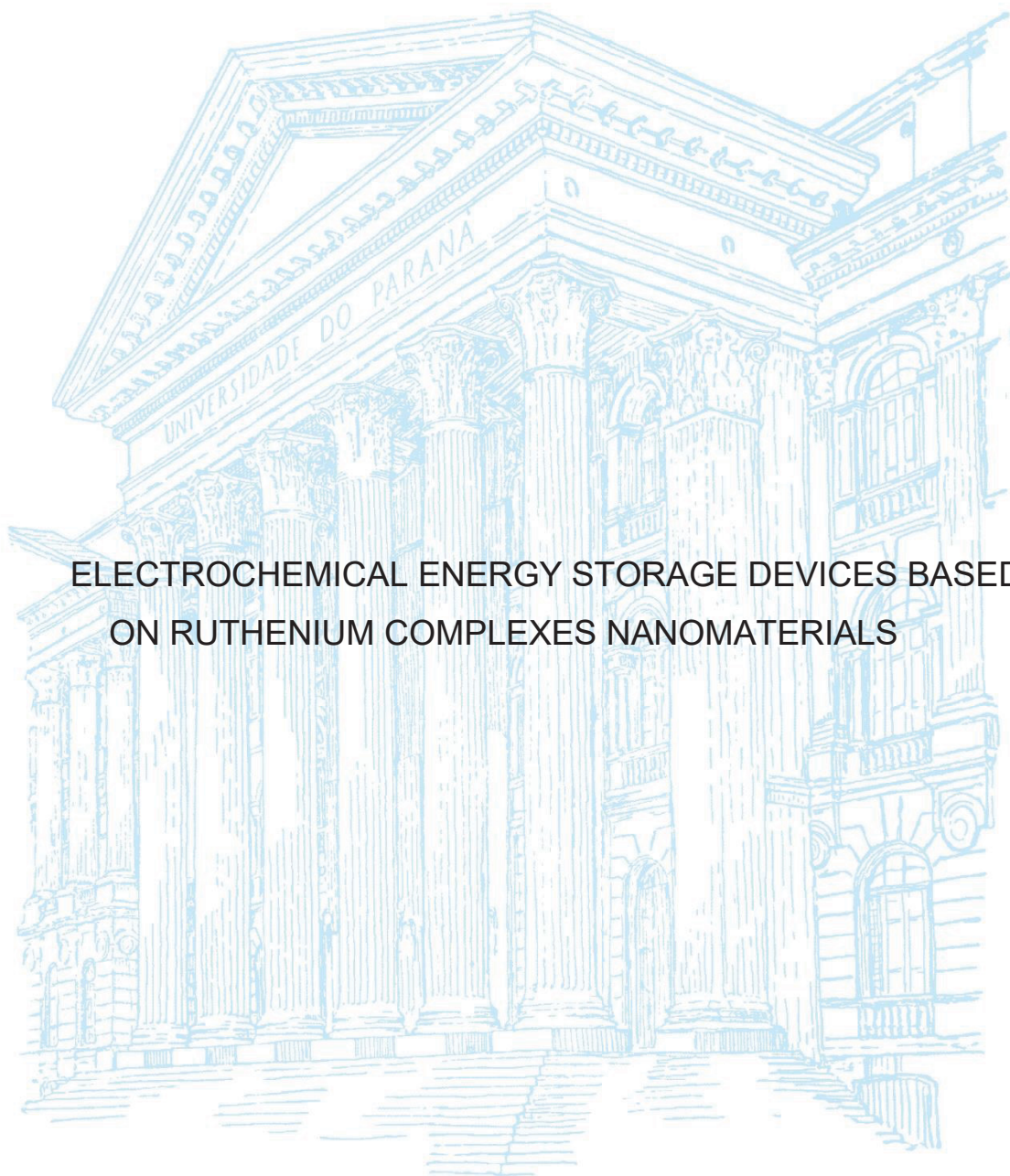


UNIVERSIDADE FEDERAL DO PARANÁ

ALEJANDRO ESTEBAN PEREZ MENDOZA



ELECTROCHEMICAL ENERGY STORAGE DEVICES BASED
ON RUTHENIUM COMPLEXES NANOMATERIALS

CURITIBA

2022

ALEJANDRO ESTEBAN PEREZ MENDOZA

ELECTROCHEMICAL ENERGY STORAGE DEVICES BASED
ON RUTHENIUM COMPLEXES NANOMATERIALS

Tese apresentada ao curso de Pós-Graduação em Química, Setor de Ciências Exatas, Universidade Federal do Paraná, como requisito parcial à obtenção do título de Doutor em Química.

Orientador: Prof. Dr. Herbert Winnischofer

Área de concentração: Química Inorgânica

CURITIBA

2022

Catálogo na Fonte: Sistema de Bibliotecas, UFPR
Biblioteca de Ciência e Tecnologia

P438e

Pérez Mendoza, Alejandro Esteban

Electrochemical Energy Storage Devices Based on Ruthenium
Complexes Nanomaterials [recurso eletrônico] / Alejandro Esteban Pérez
Mendoza - Curitiba, 2022.

Tese (Doutorado) - Programa de Pós-Graduação em Química, Setor de
Exatas, Universidade Federal do Paraná.

Orientador: Prof. Dr. Herbert Winnischofer

1. Eletroquímica. 2. Langmuir-Blodgett films. 3. Armazenamento. I.
Universidade Federal do Paraná. II. Winnischofer, Herbert. III. Título.

CDD 547.1226

Bibliotecário: Nilson Carlos Vieira Junior CRB9/1797

TERMO DE APROVAÇÃO

Os membros da Banca Examinadora designada pelo Colegiado do Programa de Pós-Graduação QUÍMICA da Universidade Federal do Paraná foram convocados para realizar a arguição da tese de Doutorado de **ALEJANDRO ESTEBAN PEREZ MENDOZA** intitulada: **Electrochemical Energy Storage Devices Based on Ruthenium Complexes Nanomaterials**, sob orientação do Prof. Dr. HERBERT WINNISCHOFER, que após terem inquirido o aluno e realizada a avaliação do trabalho, são de parecer pela sua aprovação no rito de defesa.

A outorga do título de doutor está sujeita à homologação pelo colegiado, ao atendimento de todas as indicações e correções solicitadas pela banca e ao pleno atendimento das demandas regimentais do Programa de Pós-Graduação.

CURITIBA, 16 de Março de 2022.



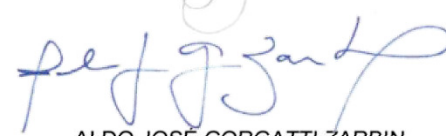
HERBERT WINNISCHOFER
Presidente da Banca Examinadora




JULIANO ALVES BONACIN
Avaliador Externo (UNIVERSIDADE ESTADUAL DE CAMPINAS)



KOITI ARAKI
Avaliador Externo (UNIVERSIDADE DE SÃO PAULO)



ALDO JOSÉ GORGATTI ZARBIN
Avaliador Interno (UNIVERSIDADE FEDERAL DO PARANÁ)



JOSÉ PEDRO MANSUETO SERBENA
Avaliador Externo (UNIVERSIDADE FEDERAL DO PARANÁ)

Dedicado a mis padres, Viviana y Efraín, por su amor que me ha sostenido en todo este viaje.

En memoria de mi abuela Nury Gutiérrez, quien también está presente en este paso.

ACKNOWLEDGMENTS

I thank my parents, Viviana and Efrain, for their unconditional support and encouragement to work for my goals, for being my great teachers of life inspiring my way, and for their great love what sustained me this far. I kindly thank my supervisor Prof. Herbert Winnischofer who gave me the opportunity for working with very interesting materials and techniques new to me in the Laboratório de Nanomateriais Inorgânicos at UFPR. I appreciate his great dedication to guiding my scientific work.

I thank Prof. Aldo Zarbin for accepting review this thesis and the previous revisions of my work, in the qualification exam and annual report, his suggestions improved my thesis. Also, I thank him for his willingness to help and the collaborative works carried out. I thank Professors João Batista, Flávio Matsumoto and Juliano Alves Bonacin for the discussions and their contributions to this work. Likewise, I thank Prof. José Serbena and Prof. Koiti Araki for accepting review this thesis and be always willing to help with my work providing materials and facilitating their equipment. Also, I am grateful to Prof. Elisa Souza Orth for the collaborative work in the development of hybrid material with graphene and ruthenium.

Further I thank Dr. Naiane Naidek from Grupo de Catálise e Cinética at UFPR for the collaboration in the synthesis of functionalized graphene, and Arianne Schmidt from Grupo de Química de Materiais at UFPR for the collaboration in the electronic microscopy characterization of the electrodes. Also, I am grateful to Prof. Julio Sagás for the XPS measurements, to CME - Centro de Microscopia Eletrônica at UFPR for Raman spectroscopy and to Tiago José dos Santos for ESI-MS measurements. I thank LCPAD - Laboratório Central de Processamento de Alto Desempenho at UFPR for the computational resources.

Special thanks to Dr. Elizangela Cavazzini Cesca for her help in the initial steps of my doctoral studies and for being my mentor in the laboratory. I thank Luis Ramirez for the support with the webpage showing the theoretical assignation of infrared spectra. I am grateful to my colleges of Laboratório de Química Inorgânica Aplicada Silvane, Elthon, Ketlyn, Rayssa for the time spent together and collaboration in the dairy activities. I thank my friends for the support and encouragement, Luis Ramirez and Laura Gaviria from the distance always took care of me. Hugo, Diego, Angela, and Maria who were like my close family during the last two years of pandemic. I was fortunate to find good friends from many places who support me during my stay in Brazil. I thank all of them for their care, support and all the good memories.

I thank all Professors who influenced in my personal, professional, and scientific formation, in particular Carlos, Rafael and Herbert. I thank CAPES that through OAS - Organization of American States program provided the financial support that made my formation as doctor possible.

*“Somewhere, something
incredible is waiting to be known“*

Carl Sagan

*“Never give up hope, no matter
how dark things seem”*

Clone Wars-the wrong jedi, 2013

RESUMO

O desenvolvimento de eletrodos que permitam atingir altas densidades de potência e energia em dispositivos eletroquímicos de armazenamento de energia é um dos principais desafios para garantir a demanda dos diversos equipamentos e aplicações que precisam fontes de energia. A melhoria da densidade de energia e potência requer eletrodos com composição química que apresentam processos faradaicos rápidos, e estruturas que ofereçam alto uso efetivo do material e alta velocidade de transporte de carga. Os clusters trinucleares de acetato de rutênio ($\text{Ru}_3\text{O}(\text{CH}_3\text{CO}_2)_6\text{L}_3$) exibem reações redox rápidas que podem ser exploradas em eletrodos para dispositivos eletroquímicos de armazenamento de energia. Por outro lado, a técnica de Langmuir Blodgett é um método interessante para obtenção de filmes finos com estruturas organizadas, que poderiam ser explorados como eletrodos que favoreçam a exposição do material e aumentem a velocidade de transporte de carga. O presente estudo propõe a fabricação e caracterização de eletrodos para dispositivos de armazenamento de energia baseados em clusters de acetato de trirutênio. Nanomateriais híbridos combinando clusters de acetato de trirutênio com grafeno foram sintetizados para fabricar filmes finos com o método drop-casting e Langmuir Blodgett (LB). A estrutura e composição dos eletrodos foram caracterizadas por microscopia eletrônica de varredura, espectroscopia Raman, infravermelho e UV-vis. Enquanto seu comportamento eletroquímico foi estudado por voltametria cíclica, curvas de carga e descarga e espectroscopia de impedância eletroquímica.

Os resultados demonstraram que os eletrodos com materiais híbridos foram fabricados com sucesso. Além disso, eles revelaram o efeito sinérgico do cluster de trirutênio e do grafeno, dado que o armazenamento de energia tem a contribuição tanto das reações redox do cluster de trirutênio quanto do processo capacitivo no grafeno. Mas a capacidade pode ser limitada pelo transporte de carga em altas densidades de corrente e velocidades de varredura. Esta limitação pode ser superada melhorando a estrutura do eletrodo como demonstrado por este trabalho. Os eletrodos LB mostraram maior eficiência no uso do material ativo (maior capacitância por unidade de massa) e melhor desempenho em altas taxas de descarga. O eletrodo LB do cluster de trirutênio armazenou uma carga próxima à teoricamente esperada se todo o material depositado sofrer uma reação redox, então eles exibiram capacitâncias tão altas quanto 204 F g^{-1} para o eletrodo de 18 monocamadas. Enquanto os eletrodos híbridos LB de até 8 monocamadas exibiram queda de capacitância significativamente menor em altas taxas de descarga. Por exemplo, o eletrodo híbrido LB com 8 monocamadas reteve 65% de sua capacitância enquanto o eletrodo "drop-casted" reteve apenas 26% de sua capacitância quando a corrente de descarga foi aumentada 14 vezes. Além disso o desempenho dos eletrodos LB foi demonstrado por meio de um microcapacitor de célula única construído como prova de conceito que exibiu uma capacitância máxima de $68 \mu\text{F cm}^{-2}$ em baixas correntes de descarga.

Palavras-chave: Armazenamento de energia, Supercapacitor, Cluster de trirutênio, Grafeno, Material híbrido, filmes de Langmuir-Blodgett.

ABSTRACT

The development of electrodes allowing to attain high power and energy densities in electrochemical energy storage devices is a main challenge in this research area. The improving of the energy and power density requires electrodes made up of materials with chemical composition able to undergo fast faradaic processes, and structures offering high effective use of the material and high rate of charge transport. Triruthenium acetate clusters ($\text{Ru}_3\text{O}(\text{CH}_3\text{CO}_2)_6\text{L}_3$) are materials exhibiting fast redox reactions, which could be exploited in electrodes for electrochemical energy storage devices. Whereas the Langmuir Blodgett (LB) technique is an interesting method to obtain thin films with organized structures, which could be exploited in the fabrication of electrodes with structures exhibiting faster charge transport and higher material exposition. So, herein is proposed the fabrication and characterization of electrodes for energy storage devices based on triruthenium acetate clusters. Hybrid nanomaterials combining triruthenium acetate clusters with graphene were synthesized to fabricate thin film electrodes with drop casting and Langmuir Blodgett (LB) technique. The structure and chemical composition of the electrode materials were characterized using infrared, Raman and UV-vis spectroscopy, Scanning Electron Microscopy, whereas their electrochemical behavior was studied using cyclic voltammetry, galvanostatic charge discharge curves and electrochemical impedance spectroscopy.

Results demonstrated that the hybrid electrodes were successfully manufactured. Also, they revealed the synergistic effect of the triruthenium cluster and graphene since energy storage have the contribution of both redox reactions of triruthenium cluster and the capacitance of graphene. But the capacity was limited by charge transport at high current densities and scan rates. This limitation could be overcome improving the electrode structure as demonstrated in this work. The LB electrodes exhibited higher effective use of the active material (higher capacitance by mass unit) and better performance at high discharge rates. The triruthenium cluster LB electrode stored a charge close to the theoretically expected if all material deposited undergoes a redox reaction, so they exhibited capacitances so high as 204 F g^{-1} for the 18 monolayers electrode. The hybrid LB electrodes up to 8 monolayers exhibited capacitance decay significantly lower at high discharge rates. For example, the hybrid LB electrode with 8 monolayers retained 65% of its capacitance, whereas the drop-casted only retained 26% of its capacitance when discharge current was increased 14 times. The performance of LB electrodes was demonstrated through a single cell micro capacitor constructed as proof of concept, which exhibited a maximum capacitance of $68 \mu\text{F cm}^{-2}$ at low discharge currents.

Keywords: Energy storage, Supercapacitors, Triruthenium clusters, Graphene, Hybrid material, Langmuir-Blodgett films.

LIST OF FIGURES

Figure 1-1- World electricity generation by source and World Electricity consumption between 1990 and 2018.	24
Figure 1-2- Requirements of different energy storage applications.	26
Figure 1-3- Scheme of Electrochemical Energy Storage Device and The Different Charge Storage Mechanisms occurring At Electrolyte/Electrode.....	27
Figure 1-4. Ragone plot showing the energy and power density of current electrochemical energy storage systems.	29
Figure 1-5. General classification of electrochemical energy storage devices and comparison of the main characteristic of these technologies.....	30
Figure 1-6. Scheme summarizing the key factors to improve the energy and power density of electrochemical energy storage systems.	32
Figure 1-7 - Strategies for Construction of High-Performance Energy Storage electrode Materials.	33
Figure 1-8- Illustration of hierarchical porosity: Scanning electron microscopy images of the cross section of calcined 3D hierarchical porous c/SnO _x composite derived from medulla of Suaeda glauca stems.	34
Figure 2-1- Typical Behavior in the Electrochemical Characterization of a, d) Capacitive, b, e) pseudocapacitive and c, f) battery-like Electrodes.	39
Figure 2-2- Schematic of RuO ₂ ·H ₂ O Hydrus structure and its Influence on Material Capacitance.....	42
Figure 2-3- 2D Co - Hexaminebenzene - MOF Structure.	44
Figure 2-4- Schematic representation of the hybridization between capacitor and battery – Like Materials.....	45
Figure 2-5- Schematic illustration of Langmuir-Blodgett technique.....	49
Figure 2-6- Schematic representation of triruthenium Acetate clusters.	51
Figure 2-7- Axis System (x, y, z) used to Construct the Qualitative Molecular Orbital Diagram of the Ru ₃ O unit and the local axis (x', y', z') of each ruthenium atom.....	52
Figure 2-8- Qualitative molecular orbital for the [Ru ₃ O[(CH ₃ CO ₂) ₆]L ₃] in D _{3h} symmetry....	53
Figure 3-1- Flow Diagram for Experimental Activities Carried Out During The Project.	55
Figure 3-2- Scheme of triruthenium cluster synthesis steps	56
Figure 3-3- Diagram of the Bubbling Process	58
Figure 3-4- Scheme illustrating the hybrid material structure and synthesis route.....	60
Figure 3-5- Scheme illustrating the Fabrication of Thin Film Electrodes Based on Graphene and Triruthenium Cluster.....	62
Figure 3-6- Photographies of electrolyte and Supercapacitor Devices.	63
Figure 4-1 - IR spectra of Synthesized Triruthenium Clusters	72

Figure 4-2 – UV-vis Spectra of Triruthenium Clusters Dispersed in Dichloromethane	74
Figure 4-3 – Cyclic Voltammogram of triruthenium Clusters in Acetonitrile	75
Figure 4-4- Frontier Molecular Orbital Diagram of the Different Triruthenium Clusters as Calculated from DFT	78
Figure 5-1- Scheme illustrating the hybrid material structure of Graphene and Triruthenium cluster.	79
Figure 5-2- IR spectra of Triruthenium Cluster, Graphene and Graphene-Triruthenium Cluster Hybrid Material.	80
Figure 5-3- Raman Spectra of Triruthenium Cluster, Graphene and Graphene-Triruthenium Cluster Hybrid Material.....	81
Figure 5-4- High Resolution XPS spectra of N1s Band of Graphene and Graphene-Triruthenium Cluster Hybrid Material.....	82
Figure 5-5- XPS survey spectra of Graphene and Graphene-Triruthenium Cluster Hybrid Material.....	83
Figure 5-6- SEM Images of Graphene and Graphene-Triruthenium Cluster Hybrid Material	84
Figure 5-7- X-ray Diffractogram of Graphene and Graphene Functionalized with Triruthenium Cluster.	85
Figure 5-8- Electrochemical Behavior of Triruthenium Cluster, Graphene and Graphene-Triruthenium Cluster Electrodes.....	86
Figure 5-9- Analysis of Current Variation with the scan rate in cyclic voltammeteries of Graphene and Graphene-Triruthenium Cluster.....	88
Figure 5-10- Estimated Inner and Outer Capacitance of Triruthenium Cluster, Graphene and Graphene-Triruthenium Cluster Electrodes.....	89
Figure 5-11- Nyquist plot of Triruthenium Cluster, Graphene and Graphene-Triruthenium Cluster obtained at 0.24 V (vs. SHE).	90
Figure 6-1- $\Pi - A$ isotherm for Amphiphilic Triruthenium Cluster at different barrier speeds.....	93
Figure 6-2- Infrared reflection absorption and Raman Spectra of Amphiphilic Triruthenium Cluster LB film.	94
Figure 6-3- UV-vis Spectra of Amphiphilic Triruthenium Cluster LB film.....	95
Figure 6-4- Scheme Of exciton Model Shown The Different geometrical arrangements of transition dipoles And Their Energies.....	96
Figure 6-5- Cyclic voltammogram of Langmuir Blodgett Electrodes and Some Voltammogram Parameters.	98
Figure 6-6- Capacitance of the electrodes with different number of deposited monolayers and their Variation with the scan rates.	99

Figure 6-7- Comparison of Molecule Loading with the Electrochemically Active Molecules and Analysis of Current peak variation with scan rate.	100
Figure 6-8- Capacitive Current Contribution to Cyclic Voltammogram.....	101
Figure 6-9- EIS results of Film with 8 ML at 0.06 V, 0.22 V, 0.31 V and 0.54 V.....	102
Figure 6-10- EIS Measured at 0.31 V of Films with different number of layers	104
Figure 7-1- Scheme of film electrode model with eight layers.	106
Figure 7-2- Scheme Showing Parameters Considered in Kinetic Model and in Charge Transport Description.....	109
Figure 7-3- Simulated Cyclic Voltammogram and Coverage in one monolayer Varying Adsorption Energy, interaction between molecules and the Charge diffusion parameters.	112
Figure 7-4- Experimental and Theoretical Cyclic voltammogram of LB Films of amphiphilic Triruthenium Cluster.....	114
Figure 8-1- Isotherm for Graphene Oxide films	118
Figure 8-2- SEM images of Graphene Oxide LB Films with 4 Monolayers Deposited on a silicon substrate at different surface pressure	120
Figure 8-3- UV-vis Spectra of Graphene and Graphene Triruthenium Cluster Langmuir-Blodgett Films.....	121
Figure 8-4 - Infrared reflection absorption and Raman Spectra of Graphene and Heterostructured Graphene-Triruthenium Cluster LB film.	122
Figure 8-5- SEM Images and EDS Map of the Hybrid Heterostructured Film and Graphene Films.....	123
Figure 8-6- Electrochemical Behavior of Graphene and Hybrid Graphene- Triruthenium Cluster Langmuir Blodgett Electrodes.....	125
Figure 8-7- Analysis of Current Variation with the scan rate in cyclic voltammeteries of Graphene and Hybrid Langmuir-Blodgett Films.	128
Figure 8-8- EIS results of Graphene and Hybrid Langmuir Blodgett Films.	130
Figure 8-9- Electrochemical Characterization of Asymmetrical Devices.....	133
Figure 8-10- Energy Storage Performance of Asymmetrical Devices.....	134
Figure A-1- Mass Spectrum of $[\text{Ru}_3\text{O}(\text{CH}_3\text{CO}_2)_6\text{Py}_2\text{AzoPy}]^+$	165
Figure A-2 - Mass Spectrum of $[\text{Ru}_3\text{O}(\text{CH}_3\text{CO}_2)_6\text{Py}_2\text{NH}_2\text{Py}]^+$	165
Figure A-3 - Mass Spectrum of Fragments Derived from $[\text{Ru}_3\text{O}(\text{CH}_3\text{CO}_2)_6\text{Py}_2\text{NH}_2\text{Py}]^+$..	166
Figure A-4- Mass Spectrum of $[\text{Ru}_3\text{O}(\text{CH}_3\text{CO}_2)_6\text{Py}_2\text{SHPy}]^+$	167
Figure A-5 – $^1\text{H-NMR}$ Spectrum of $[\text{Ru}_3\text{O}(\text{CH}_3\text{CO}_2)_6\text{Py}_2\text{AzoPy}]^+$	167
Figure A-6 – $^1\text{H-NMR}$ Spectrum of $[\text{Ru}_3\text{O}(\text{CH}_3\text{CO}_2)_6\text{Py}_2\text{NH}_2\text{Py}]$	168
Figure A-7 – $^1\text{H-NMR}$ Spectrum of $[\text{Ru}_3\text{O}(\text{CH}_3\text{CO}_2)_6\text{Py}_2\text{SHPy}]$	168

LIST OF TABLES

Table 4-1 b-Values from Current Peak Variation with Scan Rate for the Triruthenium Clusters.	76
Table 4-2 Half-wave potential of Triruthenium Clusters.....	77
Table 4-3 Energy and Location of Frontier Molecular Orbitals According to DFT Calculations	77
Table 5-1- Chemical Composition of Graphene-Triruthenium Cluster Hybrid Material From EDS and XPS.	83
Table 5-2- Estimated parameters of circuit model for Triruthenium Cluster Graphene and Graphene-Triruthenium Cluster Electrodes.....	91
Table 6-1- Estimated parameters values of circuit model elements and their Respective Estimation errors.	105
Table 7-1- Parameter values for simulation of voltammograms shown in Figure 7-4.....	113
Table 7-2- Reduction peak potential, Hal-Wave Potential and Peak Separation Obtained experimentally and from simulations.	115
Table 8-1- Capacitance of Hybrid graphene-triruthenium Cluster Electrodes Compared with other Works.	126
Table 8-2- Estimated parameters values of circuit model elements and their Respective Estimation errors.....	131

LIST OF DE ABBREVIATIONS AND ACRONYMS

AzoPy	- 4-(4-dodecyloxyphenylazo) pyridine
AzoPyRu	- $[\text{Ru}_3\text{O}(\text{CH}_3\text{CO}_2)_6\text{Py}_2\text{AzoPy}]^+\text{PF}_6^-$
CD	- Charge-Discharge
CV	- Cyclic voltammetry
DCM	- Dichloromethane
DFT	- Density Functional Theory
EDC	- 1-ethyl-3-(3-dimethylaminopropyl) carbodiimide
EDL	- Electrical Double Layer
EDLC	- Electrical Double Layer Capacitor
EDS	- Energy Dispersive Spectroscopy
EES	- Electrochemical Energy Storage
EIS	- Electrochemical Impedance Spectroscopy
GO	- Graphene Oxide
HOMO	- Highest Occupied Molecular Orbital
ICT	- Intracluster transition
IL	- Intraligand
IR	- Infrared
ITO	- Indium Tin Oxide
LUMO	- Lowest Occupied Molecular Orbital
LB	- Langmuir Blodgett
MeOH	- Methanol
MeOHRu	- $[\text{Ru}_3\text{O}(\text{CH}_3\text{CO}_2)_6\text{Py}_2\text{CH}_3\text{OH}]^+\text{PF}_6^-$
MLCT	- Metal Ligand Charge Transfer
MOF	- Metal Organic Framework
MO	- Molecular Orbital
NH ₂ Py	- 4-aminopyridine
NH ₂ Ru	- $[\text{Ru}_3\text{O}(\text{CH}_3\text{CO}_2)_6\text{Py}_2\text{NH}_2\text{Py}]^+\text{PF}_6^-$
NHS	- N-hydroxy-succinimide
rGO	- reduced graphene oxide
rGO-NH	- reduced graphene oxide functionalized with aminopyridine
rGO-NHRu	- reduced graphene oxide functionalized with triruthenium cluster
SEM	- Scanning Electronic Microscopy
SHE	- Standard Hydrogen Electrode
SHPy	- 4- Mercaptopyridine
SHRu	- $\text{Ru}_3\text{O}[(\text{CH}_3\text{CO}_2)_6\text{Py}_2\text{SHPy}]^+\text{PF}_6^-$

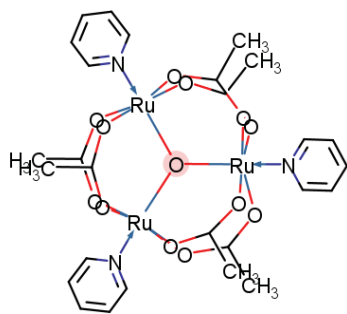
XPS	- X-ray Photoelectron Spectroscopy
XRD	- X-ray Diffraction
2D	- Two-dimensional
3D	- Three-dimensional

LIST OF SYMBOLS

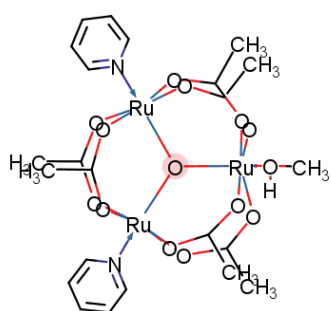
A	Area
A_e	Experimental electrode area
α	Charge transfer coefficient
b	Parameter representing the exponent of scan rate in law potential equation
C'	Real capacitance
C''	Imaginary capacitance
C_s	Specific capacitance
C_ϕ	Pseudocapacitive capacitance
C_A	Concentration of A
C_R	Concentration of R
D_e	Charge diffusion parameter
E	Electrode potential
E'	Equilibrium electrode potential
E^0	Standard electrode potential
ΔE_p	Peak potential difference
E_{pa}	Anodic peak potential
E_{pc}	Cathodic peak potential
$E_{1/2}$	Half-wave potential
η	overpotential respect to standard potential
ΔE_{ads}	Difference between adsorption Gibbs energy of reduced and oxidized species
F	Faraday constant
f	Frequency
G	Energy
ΔG	Gibbs energy difference
γ	lateral interaction parameter
Γ	Surface concentration of electroactive specie
θ	Surface coverage
I	Current
i	Specific current
i_D	Specific diffusive current
i_C	Specific capacitive current
i_p	Peak current
i_{pc}	cathodic peak current
i_{pa}	Anodic peak current

J_x	molar flux in x direction
Kn	Adimensional parameter relating charge displacement and dimensions of the film
k_f	rate parameter for reduction reaction
k_b	rate parameter for oxidation reaction
k^0	reaction rate at equilibrium
l_e^2	mean squared displacement traveled by the charge
L	Film thickness
ω	Angular frequency
P	Power
Π	Surface pressure
Q	Charge
q_T	Specific total charge
q_o	Specific outer charge
q_i	Specific inner charge
Q_C	"Capacitance" of constant phase element representing electrical double layer
Q_R	"Capacitance" of constant phase element representing redox charge storage
R	Ideal Gas constant
R_{el}	Electrical resistance
R_S	Solution resistance
R_{CT}	Charge transfer resistance
r_R	reaction rate in moles per unit of area
T	Temperature
τ	Time constant
V	Applied potential electrode
v	Scan rate
Z	Impedance
Z'	Real impedance
Z''	Imaginary impedance

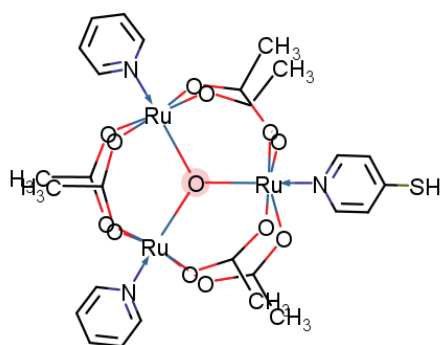
LIST OF COMPOUNDS STRUCTURES



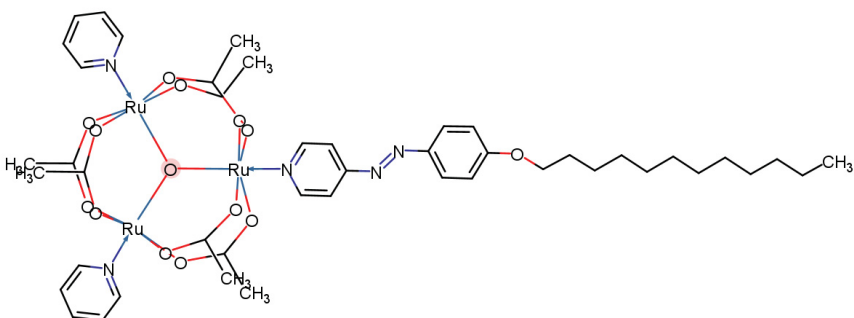
Py3Ru: [Ru₃O(CH₃CO₂)₆Py₃]



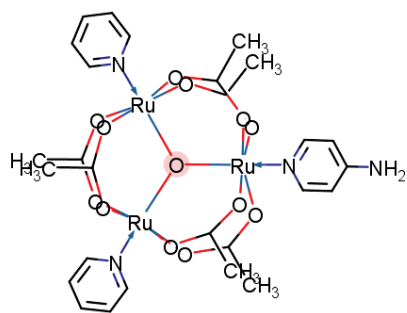
MeOHRu: [Ru₃O(CH₃CO₂)₆Py₂CH₃OH]



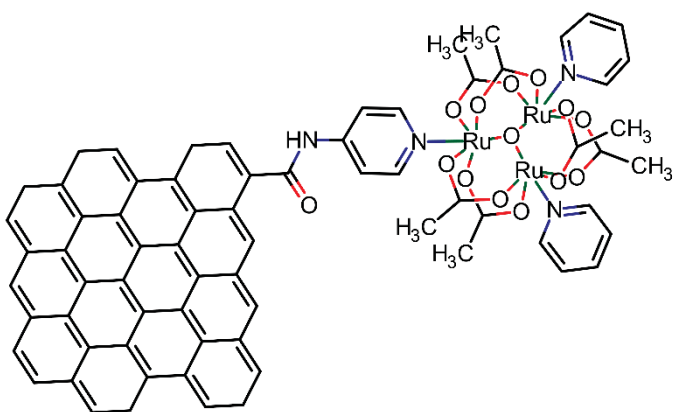
SHRu: [Ru₃O(CH₃CO₂)₆Py₂SHPy]



AzoRu: [Ru₃O(CH₃CO₂)₆Py₂AzoPy]



NH₂Ru: [Ru₃O(CH₃CO₂)₆Py₂NH₂Ru]



rGO-NHRu

TABLE OF CONTENTS

MOTIVATION	22
1 ELECTROCHEMICAL ENERGY STORAGE: FROM FUNDAMENTALS TO ELECTRODE DESIGN	24
1.1 REQUIREMENTS FOR ELECTROCHEMICAL ENERGY STORAGE	25
1.2 FUNDAMENTALS OF ENERGY STORAGE	26
1.2.1 Working Principle of Electrochemical Energy Storage	27
1.2.2 Classification of Electrochemical Energy Storage Devices	28
1.3 STRATEGIES TO IMPROVE THE ELECTROCHEMICAL ENERGY DEVICES	31
1.4 OBJECTIVES	37
1.4.1 Aim	37
1.4.2 Objectives	37
2 DESIGN OF ENERGY STORAGE ELECTRODES	38
2.1 PSEUDOCAPACITANCE	38
2.2 DEVELOPMENT OF MATERIALS FOR ELECTRODES	41
2.2.1 Pseudocapacitive Materials	41
2.2.2 Hybrid Materials	44
2.3 ELECTRODE STRUCTURES	46
2.4 OXO-CENTERED TRIRUTHENIUM ACETATE CLUSTERS	50
3 MATERIALS AND METHODS	55
3.1 MATERIALS SYNTHESIS	55
3.1.1 Synthesis of Triruthenium Clusters	55
3.1.2 Synthesis of Graphene-Triruthenium Cluster Nanocomposite	59
3.2 ELECTRODES AND SINGLE CELLS FABRICATION	60
3.2.1 Drop casted films	61
3.2.2 Langmuir Blodgett films	61
3.2.3 Single cell fabrication	62
3.3 MATERIALS AND ELECTRODES CHARACTERIZATION	63
3.3.1 Structural characterization	63
3.3.2 Electrochemical characterization	65
3.4 ESTIMATION OF ENERGY STORAGE PROPERTIES	65
3.4.1 Cyclic Voltammetry	65
3.4.2 Charge-discharge measurements	67
3.4.3 Electrochemical Impedance Spectroscopy (EIS)	68
3.5 SOFTWARE	69
4 TRIRUTHENIUM CLUSTERS PROPERTIES	70
4.1 STRUCTURE AND CHEMISTRY OF TRIRUTHENIUM CLUSTERS	70

4.2	ELECTRONIC PROPERTIES OF RUTHENIUM CLUSTERS	73
4.3	ELECTROCHEMICAL PROPERTIES OF RUTHENIUM CLUSTERS	74
5	HYBRID MATERIALS: GRAPHENE MODIFIED WITH TRIRUTHENIUM CLUSTER.....	79
5.1	STRUCTURE OF GRAPHENE MODIFIED WITH TRIRUTHENIUM CLUSTER.	80
5.2	ENERGY STORAGE IN DROP-CASTED ELECTRODES BASED ON GRAPHENE MODIFIED WITH TRIRUTHENIUM CLUSTER	85
5.2.1	Electrochemical Behavior of Graphene-Triruthenium cluster Electrodes	85
5.2.2	Analysis of Charge Storage on Graphene-Triruthenium cluster Electrodes	87
5.2.3	EIS of Graphene-Triruthenium cluster Electrodes	89
6	ELECTRODE STRUCTURES: LANGMUIR BLODGETT ELECTRODES OF AMPHIPHILIC RUTHENIUM COMPLEXES	92
6.1	STRUCTURE OF RUTHENIUM COMPLEXES LANGMUIR-BLODGETT FILMS	92
6.2	ENERGY STORAGE IN LANGMUIR-BLODGETT FILMS OF AMPHIPHILIC TRIRUTHENIUM CLUSTERS.....	97
6.2.1	Electrochemical Behavior of Amphiphilic Triruthenium Cluster Electrodes.	97
6.2.2	Analysis of Charge Storage on Amphiphilic Triruthenium Cluster Electrodes.	99
6.2.3	EIS of Amphiphilic Triruthenium Cluster Electrodes.	101
7	UNDERSTANDING ELECTROCHEMICAL BEHAVIOUR OF THIN FILMS BASED ON IMOBILIZED REDOX MOLECULES.....	106
7.1	MODEL DEVELOPMENT	106
7.1.1	Mass Balance	107
7.1.2	Constituent Equations and Additional Considerations	108
7.2	RESULTS FROM MODEL AND ANALYSIS.....	111
7.2.1	Effects of Main Parameters on Electrochemical Behavior	111
7.2.2	Interpretation of Experimental Results According to the Model.....	113
7.3	CLUES FROM MODEL TO IMPROVE REDOX FILM ELECTRODES	115
8	ELECTRODE STRUCTURES: ELECTRODES BASED ON RUTHENIUM COMPLEXES HYBRID LANGMUIR-BLODGETT HETEROSTRUCTURES	117
8.1	STRUCTURE OF HETEROSTRUCTURED GRAPHENE MODIFIED WITH TRIRUTHENIUM CLUSTER.....	118
8.2	ENERGY STORAGE IN HYBRID HETEROSTRUCTURED LANGMUIR-BLODGETT FILMS.....	124
8.2.1	Electrochemical Behavior of Hybrid Langmuir-Blodgett Electrodes	124
8.2.2	Analysis of Charge Storage on Hybrid Langmuir Blodgett Electrodes	127
8.2.3	EIS Hybrid Langmuir Blodgett Electrodes.....	129

8.3	ENERGY STORAGE DEVICES BASED ON HYBRID HETEROSTRUCTURED LANGMUIR-BLODGETT ELECTRODES.....	132
9	FINAL REMARKS	136
9.1	FUTURE WORK	138
	REFERENCES	140
APPENDIX A	SUPPLEMENTARY INFORMATION.....	165
APPENDIX B	ACADEMIC INFORMATIONS.....	171
APPENDIX C	PUBLICATIONS AND EVENTS.....	172

MOTIVATION

“Scientific truth is beyond loyalty and disloyalty.”
Isaac Asimov, *Foundation*, 1942

Investigate, from Latin *investigare* (in- "in, into" + *vestigare* "to track, trace"), means to trace out and their objective is to discover the truth. The science generate knowledge about how nature works acquiring sufficient evidence from experiences and guided by well-established scientific knowledge and reasoning. Also, the knowledge allows to make predictions about phenomena occurring in the world and offers a deep and intuitive appreciation of how nature works. So, the scientific truths are reliable, however they are not absolute, no matter how much evidence support it, they are refutable or susceptible to modifications that produce new scientific knowledge with a greater scope or accuracy.

Then, the ultimate motivation of the scientist should be, to my mind, the searching of deeper understanding of the nature which should allow to generate solutions for increasing the quality of life of all people. The scientists may be somewhat skeptical to question and judge the received information, honest and humble to objectively accept the facts, their mistakes, and to work closely with other colleagues. They may have great imagination to be able to completely change their point of view on reality, and perseverance to work constantly. Herein, it is presented the research results obtained during the walk that trained me as a scientist. The properties of novel materials and electrode architectures for energy storage devices were investigated expecting to contribute to the development of those key technologies, and in general to achieve a more sustainable world, this last was one of my motivations.

Sustainable development of the society is to propitiate conditions and better ways to promote the wellness and meet the needs of all people preserving the ability of future generations to meet their own needs. [1,2] Energy generation has a great environmental impact, since it relies on the use of fossil fuels [3]. So, it is required to develop a sustainable energy generation system for the world, which reduces contaminant emissions, preserves the environment and meets the energy requirements [1,4,5]. This task requires to diversify the energy sources by turning to renewable energy, which needs energy storage devices due to its intermittent nature, in this way, energy excesses can be stored to release it when is required [6,7]. Then, the development of electrochemical energy storage (EES) devices could be crucial for a reliable renewable energy generation [8]. Energy storage systems offering both high power and energy capacity are desirable, but the actual EES devices do not satisfy individually both requirements. [9–11].

The performances of many technologies can be improved by designing materials with appropriated chemistry and structures. The chemists understand how material world functions and how to manipulate it. They play a significant role in creating the material basis of our

society and economy, so they have an important responsibility in the advancing toward more sustainable world. Since they can design materials and processes that contribute to the development of technologies with low negative impact on human health and the environment. [12] Of course, appropriated material design also could increase the capacity and power density of EES devices. These materials may have chemistry and structures which allow fast redox reactions, high effective use of the material and fast charge transport [10,11,13–15]. triruthenium acetate clusters ($[\text{Ru}_3\text{O}[(\text{CH}_3\text{CO}_2)_6]\text{L}_3]$) could be promising materials for EES electrodes. [16–20] Since they exhibit electrochemically reversible and monoelectronic redox pairs in a potential range between 2.5 and -1.5 V respect to standard hydrogen electrode (SHE). [19,21–23]

So, here it is presented the advancements achieved respect to the development of electrodes for energy storage devices based on triruthenium acetate clusters with pyridine as ligand ($[\text{Ru}_3\text{O}[(\text{CH}_3\text{CO}_2)_6]\text{Py}_3]$) and a perspective of future material enhancements. The first chapter contains a general vision of the requirements and functioning principles of electrochemical energy storage devices to define fundamental concepts in this area and propose some strategies to improve the performance of these devices. In the second chapter is reviewed some concepts and previous works relevant for the proposed strategies to obtain efficient electrodes. So, some electrode material compositions and structures previously proposed on the literature, methods to control electrode architectures and the properties of $\text{Ru}_3\text{O}(\text{CH}_3\text{CO}_2)_6\text{L}_3$ found in previous work are presented.

The third chapter is devoted to the description of experimental and theoretical methods used in this work, the description of some methods such as the electrochemical characterization of energy storage electrodes and devices are extended to present some background of these methods. The fourth chapter present the characterization of the $[\text{Ru}_3\text{O}[(\text{CH}_3\text{CO}_2)_6]\text{L}_3]$ synthesized during this research and the discussion of theoretical and experimental results. The discussion of the structure and electrochemical performance of triruthenium cluster hybrid material with graphene (rGO-NHRu) is presented in the fifth chapter. The physical and electrochemical characterization of triruthenium cluster LB film is presented in the sixth chapter. The electrochemical behavior of triruthenium cluster LB films is further discussed in the seventh chapter with the aid of a mathematical model. Finally, the eight chapter present the discussion of the characterization of hybrid and heterostructured LB films, this electrode merges the idea of hybrid materials with structured electrodes. Perspectives for the future of this project are mentioned in the last chapter.

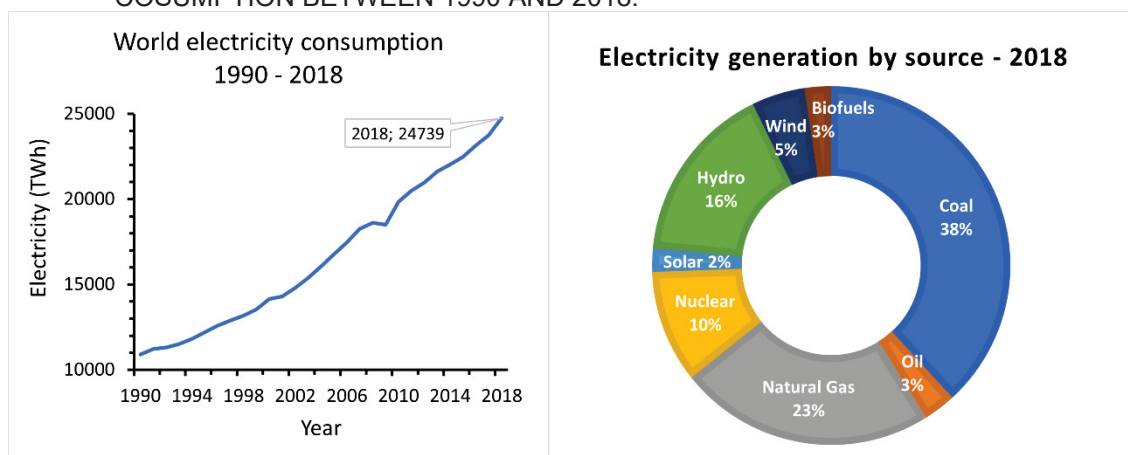
1 ELECTROCHEMICAL ENERGY STORAGE: FROM FUNDAMENTALS TO ELECTRODE DESIGN

“However,” resumed Gideon Spilett, “you do not deny that someday the coal will be entirely consumed?” [...] “That is reassuring for us, but a bad look-out for our great grandchildren!” observed Pencroft. “They will discover something else,” said Herbert.

Jules Verne, *The Mysterious Island*, 1874.

Electrical energy demand grows continuously (see Figure 1-1), 24739 TWh were consumed in 2018, which means an increment of 32% respect to 2008. [24] This is explained by the population growth and the actual society model whose comfort and economic activities relies on the use of electrical energy. Currently, electrical energy generation requires the intensive use of limited natural resources, particularly fossil fuels (67% of electrical energy comes from combustible fuels [24]) resulting in a great environmental impact. [3,25] 33.2 gigatons of CO₂ were emitted due to the combustible fuels used for energy generation, [24] contributing to the increment of CO₂ level in the atmosphere up to 411 ppm which is estimated to be significantly higher than any CO₂ level in the earth history. The higher CO₂ and methane levels in the atmosphere are the main factors leading to the global warming. [3,25]

FIGURE 1-1- WORLD ELECTRICITY GENERATION BY SOURCE AND WORLD ELECTRICITY CONSUMPTION BETWEEN 1990 AND 2018.



SOURCE: Adapted from International Energy Agency (IEA). [24]

So, it is required to work for a sustainable development using the energy in a more aware and efficient way. Great part of energy use is attributable to the economic system, in fact the pandemic situation experienced during 2020 due to the COVID-19 showed that the decreasing of manufacturing activities leads to decreased electrical energy consumption. [25] Furthermore, the development of technologies to attain sustainable energy generation systems would help to get closer to a sustainable development situation. It should reduce contaminant emissions and meets the energy requirements. [1,4,5] Hence, the sustainable energy generation system requires to diversify the energy sources by turning to renewable ones.

Electrochemical devices for energy generation and storage will play an important role in this task since they would allow the interconversion between chemical and electrical energy with high efficiency. Furthermore renewable sources (sun, wind and others) have intermittent nature requiring energy storage devices. [6,7] Then, the development of electrochemical energy storage devices could be crucial for a reliable renewable energy generation. [8] Moreover, EES have other different applications important in the actual society, some of them are described in the next section along with their power and energy requirements.

1.1 REQUIREMENTS FOR ELECTROCHEMICAL ENERGY STORAGE

The development of electrochemical energy storage systems is crucial for different applications [26,27]. For example, a reliable energy supply requires devices that store energy when an excess is produced to release it when energy is required, and respond quickly to abrupt voltage drops or increases to stabilize the power supply. [8,26,28] Particularly, a sustainable energy supply based on renewable energies, such as wind, biomass and solar energy, requires energy storage since renewable sources are intermittent, the sun is just available a few of hours per year and the wind streams are variable. [6,28–31]

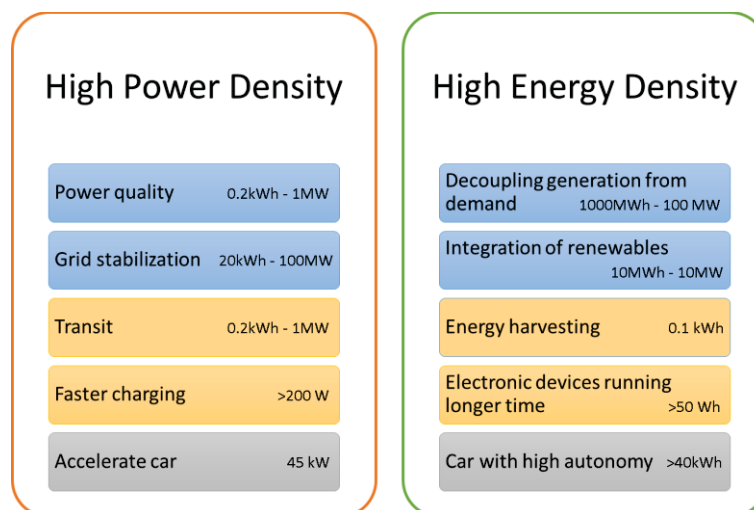
Consequently, around the world, different institutions are leading in efforts to address the requirement of electricity grids which integrate the variable renewable energy in a reliable way, including the development of energy storage systems. [32–35] As is shown in Figure 1-2, in the boxes at the top of the figure, they require high power (up to 100 MW [35]) to stabilize the grid, and to guarantee the quality of power supply absorbing abrupt voltage drops. They also require high energy capacity (up to 1000 MWh [35]) to store the energy generated in high production moments, which allows the decoupling of generation from demand and the renewable energy integration.

EES also can be used in micro-energy harvesting [36–38] and portable applications such as laptop computers, portable media players, toys, hand tools and other consumer electronic devices. [39,40] As is shown in Figure 1-2, in the boxes at center, these applications require high power to harness energy in transit systems during braking and provide it during the start-up (up to 1 MW [35]), and to obtain devices requiring less time of charging. Also, the applications require high energy capacity to make micro-energy harvesting worthwhile (up to 0.1 kWh [35]) and to guarantee durable supply of energy.

The other potential application of EES devices are the electric cars, as is shown in Figure 1-2, in the boxes at bottom, they require systems that provide enough power to start the car, maintain it moving, and replenish it in less time. And store enough energy to move the car for long times. [41–43] Summarizing, EES devices could be applied in i) reliable and high-quality energy supply, ii) portable electronic applications and energy harvesters, and iii) electric

vehicles. These applications have different power and energy requirements, which could be attained with different designs and scaling of EES. But devices with both high energy and power density are desirable for all those applications.

FIGURE 1-2- REQUIREMENTS OF DIFFERENT ENERGY STORAGE APPLICATIONS.



SOURCE: Author. (Data from [35,42]).

Batteries and supercapacitors (SCs) do not satisfy individually the requirements, batteries have high energy density but low power density, while SCs have high power but low energy density. [13,44] For example, SCs can provide the high-power requirement of a car, but its actual energy density is not enough to give them the autonomy required. So, it is desirable to improve EESs to meet the requirements of modern applications. [42,43,45] An interesting approach to meet those requirements is the construction of devices with materials that offers high energy and power density. [13,46,47] The next section presents the working principles of EESs, identifying key factors for their performance.

1.2 FUNDAMENTALS OF ENERGY STORAGE

“A quantity of it is decomposed exactly proportionate to the quantity of electricity which has passed.”

“Although we know nothing of what an atom is; and though we are in equal, if not greater, ignorance of electricity... yet there is an immensity of facts which justify us in believing that the atoms of matter are in some way endowed or associated with electrical powers, to which they owe their most striking qualities.”

Michael Faraday, *Trans. Roy. Soc. London*, 124, p. 91 and 116, 1834

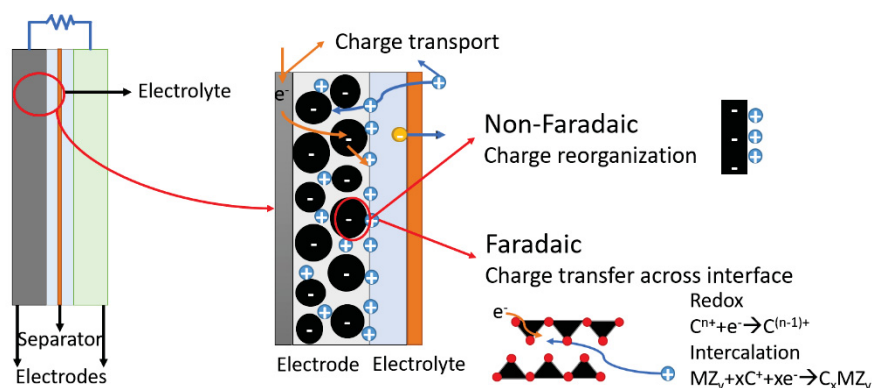
Electrochemistry is concerned with the interrelation of electrical and chemical effects. As it was intuited by Michael Faraday there is a close relationship between chemistry and electricity enclosed in the atoms that make up the matter, which as now we know is composed by a nucleus and electrons. An electrochemical cell allows to study and to harness the

interconversion of electricity and chemical compounds, it is composed mainly by two electrodes and one electrolyte. In the EESs, electrical charge is stored through the processes occurring at the electrodes, the electrolyte, and the electrode/electrolyte interface. The understanding of that processes is key to identify important factors in the functioning of EESs and guide the design of storage devices with better performance. [48–50] But also, the task is challenging since it is a multi-physics and a multidimensional problem. Its complexity is mainly found in the interrelated electrical and chemical processes occurring at different scales mainly at the interfaces, which are the key elements of any electrochemical system. [48–50] Currently, the storage processes are classified into two main mechanisms and the devices are classified according to these mechanisms. Next section presents some fundamentals of energy storage processes.

1.2.1 Working Principle of Electrochemical Energy Storage

An electrochemical energy storage device is mainly composed of two electrodes and one electrolyte separating the electrodes as illustrated in Figure 1-3. The charge storage processes occur at the electrodes, and the electrolyte allows the passage of ions but not electrons. A solid electrolyte or a porous and isolating material soaked on liquid electrolyte are used as separator between electrodes in the compact energy storage devices. It maintains the electrodes isolated allowing to establish a different chemical environment in each electrode, hence a difference of potential between them can be established driving the electron flow between electrodes which is compensated by the movement of corresponding ions toward the electrode. [11,44,51] Besides, two basic types of charge storage processes can occur at electrodes, as shown in Figure 1-3:

FIGURE 1-3- SCHEME OF ELECTROCHEMICAL ENERGY STORAGE DEVICE AND THE DIFFERENT CHARGE STORAGE MECHANISMS OCCURRING AT ELECTROLYTE/ELECTRODE



SOURCE: Author.

i) Rearranging of charge at the electrode-electrolyte interface, when the device is charged by imposing an external voltage, one electrode is charged positive and the other negatively attracting electrolyte ions of opposite charge, as illustrated in Figure 1-3. So, the ions move in the electrolyte to regions close to the electrode resulting in a configuration with negative and positive charges lying in separate planes, which is known as the electrical double layer (EDL). Finally, when the device is discharged by connecting to an external circuit, the ions leave the electrode. Processes that do not involve electron transfer across the interface, like this, are named non-faradaic processes, and it should be noted that with them the energy is stored in an electrostatic way. [11,14,44,52]

ii) Chemical changes, species electrochemically active can be oxidized ($R \rightarrow O + e^-$) or reduced ($O + e^- \rightarrow R$) at the electrodes involving electron transfer from or to the reagent. When an EES is discharged, the electrochemical reactions occur spontaneously at the electrodes (or electrode-electrolyte interface) producing a potential difference between them that drives a current through the external circuit and delivers energy. In principle, the battery reactions could be reversed if they are thermodynamically reversible, and the original chemical constituents regenerated by applying an external voltage, so reversing the current flow in a process known as charging. These processes, involving electron transfer across electrochemical interface, are named faradaic processes, and it should be noted that in this case, energy is stored as chemical energy [11,14,44,52].

1.2.2 Classification of Electrochemical Energy Storage Devices

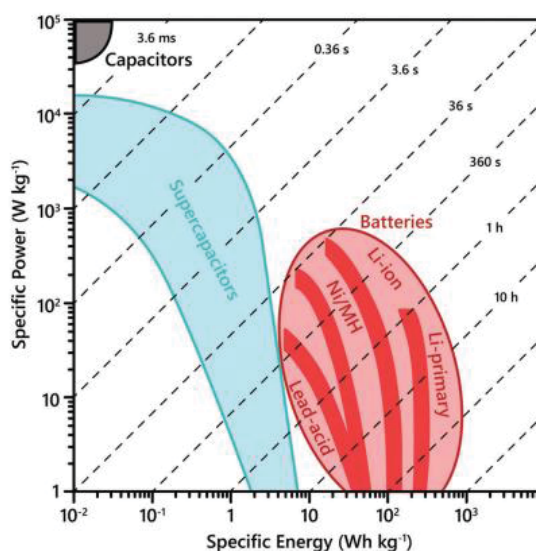
Typical SCs are based on non-faradaic storage process (EDL formation) and they are named electrical double layer capacitors (EDLCs). As they do not have chemical changes, the charge stored is limited to that accommodated in the electrical double layer, and the energy stored correspond to that involved in the EDL formation, for that reason the electrode materials mostly used are the carbons with high surface area. [10,11,52,53] In the batteries, the charge storage process is essentially faradaic, also there are double-layer formation, but it is not the main mechanism. As they have chemical changes, the charge stored should be corresponding to the electron charge transferred in the reaction, and the energy stored corresponds to that involved in the chemical transformation. [10,11,52,53] Therefore, it could be expected that batteries attain higher energy density than SCs, since a chemical transformation usually involves higher energy change than charge reorganization.

On the other hand, non-faradaic processes are fast since they do not involve great extent of reorganization in the system. It only involves the movement of electrons in the electrode and charges at surface. So, the rate of charge storage or delivery is high, hence their power density is high. [11,52] Whereas faradaic processes can be slow since it involves

electron transfer across electrochemical interface. Also, it could involve phase transitions, formation, breaking or reorganization of bonds and normally requires the diffusion of charges within the electrode. So, the rate of charge storage or delivery is limited. [11,52] The characteristic time for the EDL charging typically is around of milliseconds, [15,54] whereas time constant for redox reactions could be in the order of hundred milliseconds or higher depending on the extent of system changes upon reaction (phase changes, molecules/atoms reorganization). [15,54] Therefore, it could be expected that EDLCs attain higher power density than batteries.

The differences expected for batteries and SCs for the sake of its different charge storage mechanisms are illustrated in the Ragone plot shown in Figure 1-4. Batteries are located at right bottom of the plot, corresponding to high energy density (typically from 10 to 100 Wh kg⁻¹) and low power density (typically below 300 W kg⁻¹), whereas SCs are located at left top of the plot corresponding to low energy density (typically below 8 Wh kg⁻¹) and high power density (typically up to 10000 W kg⁻¹). [44,53,55] The plot also illustrates the characteristic operation times (charge-discharge times) for that devices, SCs are mostly below 30 seconds, whereas the batteries go from minutes to hours. [15,44,55]

FIGURE 1-4. RAGONE PLOT SHOWING THE ENERGY AND POWER DENSITY OF CURRENT ELECTROCHEMICAL ENERGY STORAGE SYSTEMS.



SOURCE: Reprinted from [55].

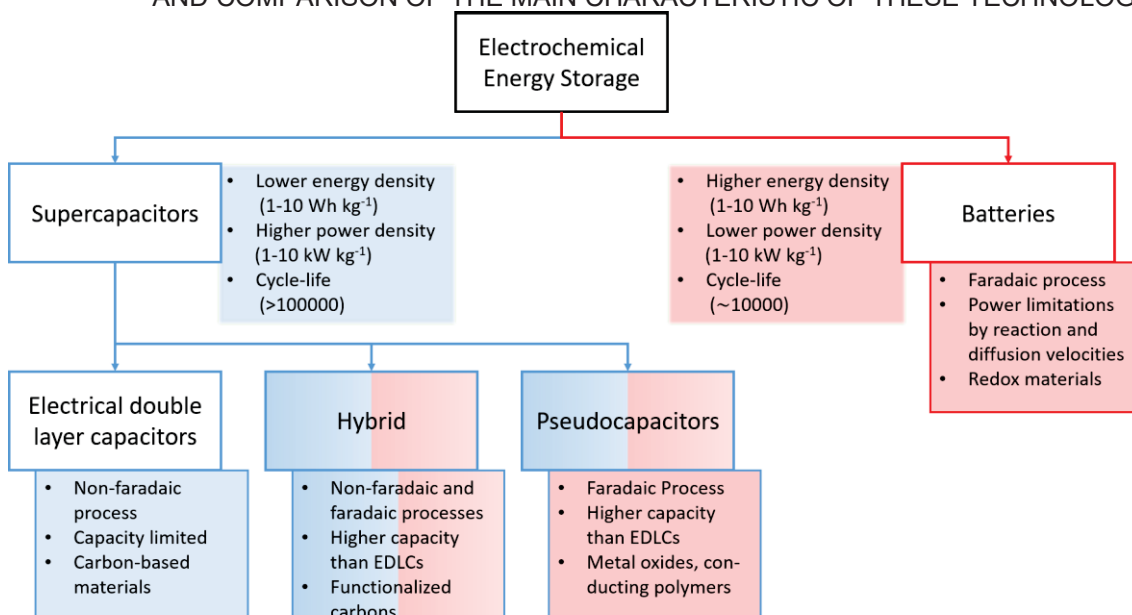
Some electrode materials, such as metal oxides and some conducting polymers, exhibit faradaic processes like in batteries, but they have a capacitive electrochemical behavior, so they are named pseudocapacitive. [15,52,56–58] Specific chemical adsorption, surface redox reactions and some intercalation reactions are some of the faradaic processes that lead to pseudocapacitance. Reversible electrochemical reactions occur within significantly shorter time, that is, fast reactions that are not limited by diffusion toward active sites.

[15,52,56–58] Devices using that electrodes are named pseudocapacitors, they are considered other type of supercapacitor along with EDLCs and they are promising to achieve energy densities like that of batteries and power densities like that of EDLCs. [15,52]

Considering all the above mentioned, electrode materials could be classified according to their storage mechanisms and their characteristics into capacitive, battery-like, and pseudocapacitive electrodes. Additionally, the hybrid materials combine two or more materials at molecular level. Particularly, the combination of a capacitive and conductive material with a battery-like or pseudocapacitive material should enable the harnessing of both faradaic and non-faradaic processes. So, each hybrid material could behave like a battery or like a capacitor depending on various factors and they should be labeled according to the behavior exhibited.

The electrochemical energy devices are classified in a similar way as shown in Figure 1-5. the two main categories are the batteries and supercapacitors. The main characteristics of the SCs are their high power and low energy density which are characteristic of non-faradaic mechanism present in EDLCs. The energy density of SCs can be increased without so much decreasing of the power density or modification of their capacitive behavior including materials with faradaic processes like in pseudocapacitors and hybrid devices as shown in Figure 1-5. The lasts could use a capacitive electrode and a faradaic (or pseudocapacitive) electrode or also hybrid electrodes. [44,53].

FIGURE 1-5. GENERAL CLASSIFICATION OF ELECTROCHEMICAL ENERGY STORAGE DEVICES AND COMPARISON OF THE MAIN CHARACTERISTIC OF THESE TECHNOLOGIES



SOURCE: Author. (Data from [44,53])

Summarizing, there are two basic mechanisms to store energy in EESs, each one confers particular characteristics to the devices. The EDLCs relies on non-faradaic processes (EDL formation), so they exhibit high power density and limited energy density as compared

with batteries which relies on faradaic processes (including redox reaction, ion intercalation, and specific chemical adsorption). Some devices exhibit intermediate characteristics between batteries and EDLCs, such as the pseudocapacitors and hybrid devices. Pseudocapacitors are based on faradaic processes but exhibit a capacitive behavior, and hybrid devices combines capacitor and battery like materials in the same cell or in the same electrode. They seem promising to attain high energy and power density, either by the fast kinetics of the faradaic process in a pseudocapacitive material or by the synergy between different kind of electrode materials. [44,53,59] Next section broaden the vision about electrode materials reviewing some rational strategies to get better energy storage electrode materials.

1.3 STRATEGIES TO IMPROVE THE ELECTROCHEMICAL ENERGY DEVICES

“When we get to the very, very small world... we have a lot of new things that would happen that represent completely new opportunities for design.”

Richard Feynman, *There's Plenty of Room at the Bottom*, 1959

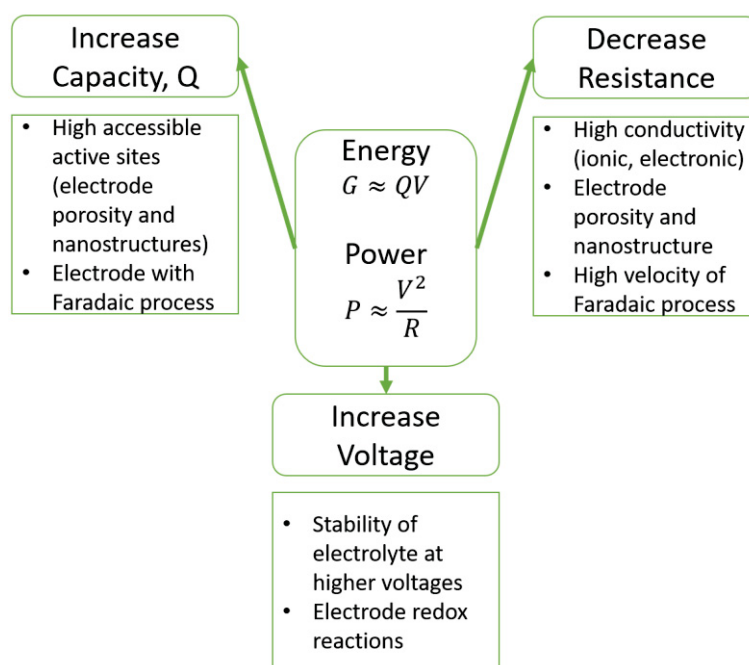
The functioning of technological devices depends largely on the material basis of those technologies, particularly the processes occurring in them. For all the electrochemical devices is important to understand the electrochemical transformations and the role of materials properties in those transformations.[60–62] This understanding, along with the capability to construct materials with some control of their arrangement on the nanoscale (ideally construct materials “atom” by atom”), is crucial to design strategies to circumvent technical obstacles exploiting the greater range of possible properties of the materials manipulated at nanoscale. So, in order to outline some strategies to improve electrochemical energy devices, we retake the key factors of energy device and review the possibilities offered by nanotechnology and chemical synthesis to create materials on “atomic” level tuning their interactions and bonds.

Retaking the fundamentals of EES functioning above mentioned, it can be remarked that the energy stored by the EDL depends mainly on the total charge capacity (Q) accommodated in this structure and its distribution. Besides, the total capacity Q stored by the electrochemical reaction depends on the reaction itself and the total quantity of material involved in the transformation. [10,11,13] So, as it is shown in Figure 1-6, it is expected the stored energy (G) be proportional to Q , which is influenced by issues such as accessible surface area and/or active sites of electrodes, and the nature of electrochemical reaction. [10,13] The porosity and structure of electrodes influence the accessible area and the charge distribution at electrode electrolyte interphase, in fact the capacity shows high dependence on pore size.

The power density is related with the rate of charge storage or delivery, which is high for non-faradaic processes since they only involve charge movement with low extent of

reorganization in the system, that is, the processes have low resistance (R_{el}). Whereas faradaic processes are slower and thus have higher associated R_{el} . They involve electron transfer along with the diffusion of electrolyte ions to specific sites, and they could be accompanied by higher reorganization in the system, including the modification of bonds and phase transitions of electrode materials. [10,11,13,15] Therefore, as it is summarized in Figure 1-6, it is expected that the power (P) be inversely proportional to R_{el} , which is influenced by the kinetics of faradaic processes and the velocity of electron and ion transport within the electrode. The last depends on electrode porosity and structure, and the electrical and ionic conductivity of electrodes and electrolyte respectively [10,13].

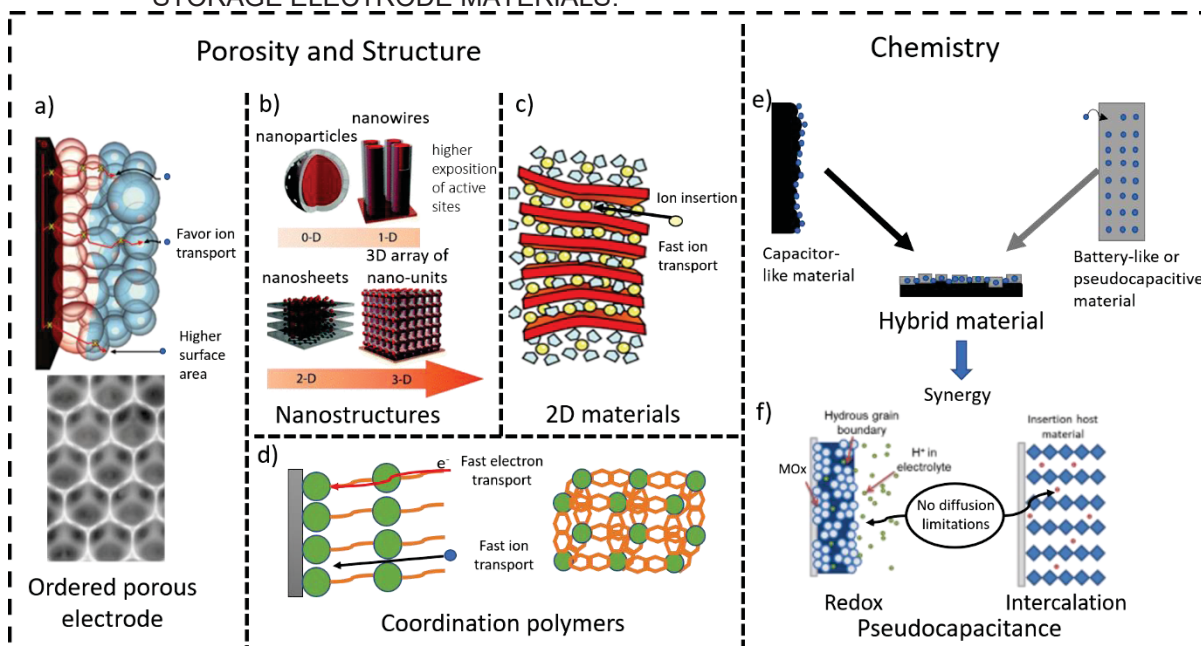
FIGURE 1-6. SCHEME SUMMARIZING THE KEY FACTORS TO IMPROVE THE ENERGY AND POWER DENSITY OF ELECTROCHEMICAL ENERGY STORAGE SYSTEMS.



SOURCE: Author.

The device voltage (V) is another important factor that contributes to the increasing of the energy and power density of these devices, which depends on electrode redox reactions and is limited by the stability of the electrolyte. Thus, increasing the operation voltage is regarded as a promising strategy to improve the energy and power density. It can be achieved by selecting a proper electrolyte with a large operating voltage, for instance, the development of organic electrolytes, ionic liquids, and solid electrolytes with high operating voltage and ionic conductivity is an active research line to improve EESs. In the light of the aforementioned, some ways to increase the power and energy density attainable in EES are the increasing of the operating voltage and conductivity of the electrolytes, and the improvement of i) porosity, ii) structure and iii) composition of the electrode materials. The strategies for electrode development are summarized in the Figure 1-7 and described in the following paragraphs.

FIGURE 1-7 - STRATEGIES FOR CONSTRUCTION OF HIGH-PERFORMANCE ENERGY STORAGE ELECTRODE MATERIALS.



a) Porous electrodes. b) nanostructured electrodes. c) 2D layered materials. d) Coordination polymers and redox organized films. e) Hybrid materials. f) Pseudocapacitive materials.

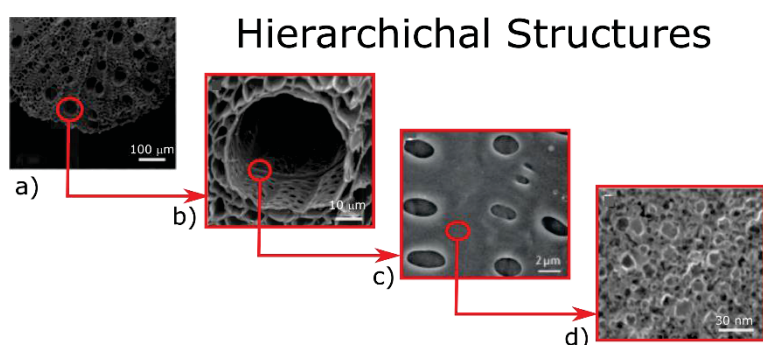
SOURCE: Author. a) adapted from LIU et al. [63] b) adapted from LIU et al. [64] c) adapted from KAJITAMA et al. [65] f) adapted from FLEISCHMANN et al. [15]

One of the main proposals in electrode development research area is optimize the porosity of the electrodes. As is shown in Figure 1-7a, the main idea is to synthesize electrodes with hierarchical interconnected porous structures and pore size tuned to fit the size of ions of the electrolyte which may improve the ion transport and increase the surface area exposed, therefore, the electrode performance at high rates. [10,13,53,66,67] Some of the proposals to increase surface area are the developing of electrodes based on porous carbons or hierarchical metal organic frameworks (MOFs), and the use of conductive foam supports and porous templates to growth active materials on them. [10,13,53,66,67] A valuable concept in the design of porous electrodes is the structural hierarchy. That is, materials exhibiting structure on more than one length scale, so the materials are composed from structural elements with structures itself. [63,68,69] So, the materials should exhibit meso-, micro- and nanopores as illustrated in Figure 1-8.

Besides, the construction of tailored structures that facilitate the ions transport toward active sites is other proposal. [10,67,70–72] Nanostructured and layer-structured materials are some ideas to obtain shortened transport pathways and higher accessible active sites by mass unit, as indicated in Figure 1-7b and c. [62,64] As illustrated in Figure 1-7c, 2D materials such as graphene composed by sheets held together by weak van der Waals interactions can be used to create electrodes consisting of an arrangement of layers of atomic dimension with inserted ions.[70–72] The interlayer space may work as a channel with higher ionic transport

efficiency, whereas the layers may offer high density of redox active or intercalation sites and high electrical conductivity, leading to better performance at high rates. However, a drawback of this materials is the restacking of the layers, which decreases the ionic transport efficiency and the accessibility to layer sites. [72–76]

FIGURE 1-8- ILLUSTRATION OF HIERARCHICAL POROSITY: SCANNING ELECTRON MICROSCOPY IMAGES OF THE CROSS SECTION OF CALCINED 3D HIERARCHICAL POROUS C/SnO_x COMPOSITE DERIVED FROM MEDULLA OF SUAEDA GLAUCA STEMS.



a) High-density array of parallel channels (diameters of $\sim 50 \mu\text{m}$). b) Magnification in a channel with abundant micropores across the cell wall and surrounded by micropores ($\sim 5 \mu\text{m}$). c) Magnification in the channel sidewall showing abundant micropores ($\sim 1\text{--}5 \mu\text{m}$). d) Further closeup view of cell wall structure revealing a high density of nanopores ($\sim 1\text{--}10 \text{nm}$).

SOURCE: adapted from DUAN et al. [68,77]

Likewise, electrodes with tailored structures could be fabricated using molecules or units with nanostructures. The synthesis of functional materials from nanoscale units requires contributions from nanotechnology and supramolecular chemistry, it has been called “nanoarchitectonics”. [78,79] The materials fabricated in this way enable the control of their properties and functionalities through the design of the shape formed during the assembly of the atoms or molecules. So, an active material with organized structures at nanoscale can be synthesized, such as nanowires and nanosheets (see Figure 1-7b), which favor the exposition of active sites and shorten the charge transport pathways.

Other example is the fabrication of nano-architected materials through the design of the constituent units and the control of their assembly. So, redox coordination compounds could be used as constituent unit since they present a rich electrochemical behavior that can be tuned by ligands and redox active metals chosen. In turn, the designed moieties could have properties facilitating the assembly to form coordination polymers or organized films (see Figure 1-7d). [80–82] Those films can be grown using layer-by-layer, Langmuir-Blodgett, self-assembly and film deposition methods. [78–81,83,84] The obtained structures may present advantages in the charge transport owing to the electronic coupling and the organization of constituent molecules. [82,85] However, special care should be paid to the structure stability

and the design of effective ionic pathways that facilitate the interaction of redox centers with balancing counter-ions.

Despite the optimizing of porosity and structure of the electrodes is an effective way to increase the power density, the energy density is not profoundly increased. Unless the electrode includes “faradaic materials”. As is the case of many layered materials or organized redox films which present chemical adsorption, intercalation, or redox reactions. In fact, the developing of new electrode materials with pseudocapacitive properties and hybrid materials combining a capacitive and pseudocapacitive material are other strategies to improve the energy storage electrode performance. [13–15,52] Since pseudocapacitive electrode materials encompasses fast faradaic processes which may have higher Q than the EDL formation process, and higher velocity than the processes involved in typical batteries. Therefore, the development of materials with pseudocapacitance could be promising to obtain EESs with improved energy and power density.

Pseudocapacitance is promising to obtain EESs with improved energy and power density. The main pseudocapacitive materials developed up to date are conducting polymers and the metal oxides, being RuO_2 and MnO_2 the pseudocapacitive metal oxides more recognized. Their capacity arises from fast and reversible charge transfer reactions involving the double bonds in polymer networks or the change of metal oxidation state with the concomitant doping/adsorption of a counter-ion [86–88] The presence of structural water, porosity and nanostructures is crucial because the structure may facilitate ion transport and provide an interconnected network with more accessible sites. [13,86,87] The main drawbacks of these materials is their poor stability and the poor electronic conductivity. [86–90] Some additional details about the pseudocapacitive materials developed up to now is offered in the chapter 2.

The use of conductive and mechanically stable compounds is proposed to increase the electrical conductivity and the stability of the electrodes, it could be linked at nanoscale level to fabricate a hybrid material. [15,59,70,91] Moreover, the hybrid materials are very attractive because of the possibility of using a pseudocapacitive or “Faradaic” material and a capacitive one, and thus, exploit two different mechanisms for charge storage. Even more interesting, hybrid materials show improved properties due to synergy between materials. [59] The hybrid materials more studied up to now are those composed by nanocarbons and a pseudocapacitive material. Carbon nanostructures offer high surface area and conductivity, whereas the pseudocapacitive material contribute to increase the electrode capacity with their faradaic processes. However, the synthesis of hybrid material does not always result in better performance, since there are other critical factors such as electron transfer across the interfaces within hybrid material which should be optimized in the electrode design. [13,14,44,53,59,67]

Summarizing, the improvement of electrodes for EES devices can be achieved considering several aspects in the electrode design and fabrication such as i) the design and synthesis of materials with optimized porosity to increase exposition of active centers and favor charge transport. ii) the design of structures, such as nanosheets and nanowires, organized thin films and layered structures. They favor the exposition of active material, the electronic conduction, intercalation mechanism and ion transport, iii) the search for new materials that enable pseudocapacitive mechanisms, particularly the presence of fast redox or intercalation reactions (iv) the combination of materials exhibiting different desirable properties to obtain a material with improved properties due to the synergy between them. Considering all the previous, and particularly that the pseudocapacitive materials are characterized by the presence of fast redox reaction accompanied with counter-ion doping/adsorption into material structure. This work considers metal complexes, such as triruthenium acetate clusters as a new energy storage electrode chemistry.

Triruthenium clusters are a kind of material exhibiting fast redox reaction which can be harnessed to store energy, but they scarcely explored as energy storage electrodes. They have general formula $[\text{Ru}_3\text{O}(\text{CH}_3\text{CO}_2)_6\text{L}_3]$ with L indicating a ligand group (N-Heterocycles, thiols, CO, H₂O and other Lewis base). [18–20,23,92] The interest in triruthenium clusters as energy storage material arises from its rich electrochemical behavior, exhibiting 4 or 5 electrochemically reversible and monoelectronic redox pairs in a potential range from 2.5 to -1.5 V measured with standard hydrogen electrode (SHE). [19,22,23] Also, the values of redox potential peaks obtained in cyclic voltammetry depend on the electron transfer properties of axial ligands L. [21] Also, it is observed electronic delocalization in the Ru₃O core facilitating electrical conduction. [16,17]

So, this work aimed to develop electrodes with high capacity at high rates based on triruthenium clusters using some design strategies as the fabrication of organized/nanostructured films and their hybridization with other materials. $[\text{Ru}_3\text{O}[(\text{CH}_3\text{CO}_2)_6]\text{Py}_2\text{L}]$, Py is pyridine and L an appropriate ligand which allows the fabrication of organized structures or the integration with other materials. For example, amphiphilic ligands allow to obtain amphiphilic clusters that self-organize on water surface. Ligands with thiol and amino groups allow to integrate the triruthenium cluster with highly conductive materials as gold and carbon nanostructures. All these electrodes may have high performance owed to the contribution of fast faradaic processes of triruthenium clusters and the designed electrode structures.

1.4 OBJECTIVES

1.4.1 Aim

Develop electrodes based on triruthenium acetate clusters with high capacity at high rates and apply it in electrochemical capacitors.

1.4.2 Objectives

- (1) Evaluate the electronic and electrochemical properties of three different asymmetric triruthenium acetate clusters $[\text{Ru}_3\text{O}[(\text{CH}_3\text{CO}_2)_6]\text{Py}_2\text{L}]$ with L: 1) 4-aminopyridine, 2) 4-mercaptopyridine and 3) 4-(4-dodecyloxyphenylazo)pyridine using cyclic voltammetry, spectroscopic techniques, and density functional theory.
- (2) Synthesize novel hybrid nanomaterials by the immobilization of 4-aminopyridine derivative ruthenium clusters on graphene using an adapted route for covalent functionalization of graphene oxide.
- (3) Develop strategies to fabricate thin film electrodes with different structures based on triruthenium clusters and their hybrid materials with graphene on conducting substrates using as base the Langmuir-Blodgett, dip-coating, and drop-coating methods which may be favorable to fabricate film from material dispersions.
- (4) Evaluate the energy storage performance of the electrodes fabricated with typical electrochemical methods, calculating the specific capacitance and the capacitance retention at high discharge rates.
- (5) Demonstrate the functioning of the energy storage electrode materials based on triruthenium clusters in a single cell supercapacitor device measuring the device capacitance at different discharge rates.
- (6) Explain the electrochemical properties of materials synthesized using electronic structure calculations and macroscopic models based on electrochemical kinetic theory.

2 DESIGN OF ENERGY STORAGE ELECTRODES

This project aims to develop electrodes based on triruthenium cluster, which seems promising as energy storage material. Previously, it was outlined some strategies to achieve highly efficient energy storage electrodes which could be used in this work, stating that i) the pseudocapacitive materials and the hybrid materials are promising. ii) The assembly of nanoscale units to prepare organized and porous structures should be an effective strategy to obtain efficient electrodes. So, this section deepens some key points to this work. First, a literature review about pseudocapacitance concept is presented wrapping up the understanding of pseudocapacitive mechanisms. Then, some pseudocapacitive material proposals are reviewed remarking the key factors in their electrochemical behavior and pointing out strategies to get better electrodes. Finally, the strategy of material hybridization and electrode structure design are reviewed emphasizing in 2D layered structures and the Langmuir-Blodgett (LB) technique as powerful method for controlling nanoscale components organization within a 2D plane.

2.1 PSEUDOCAPACITANCE

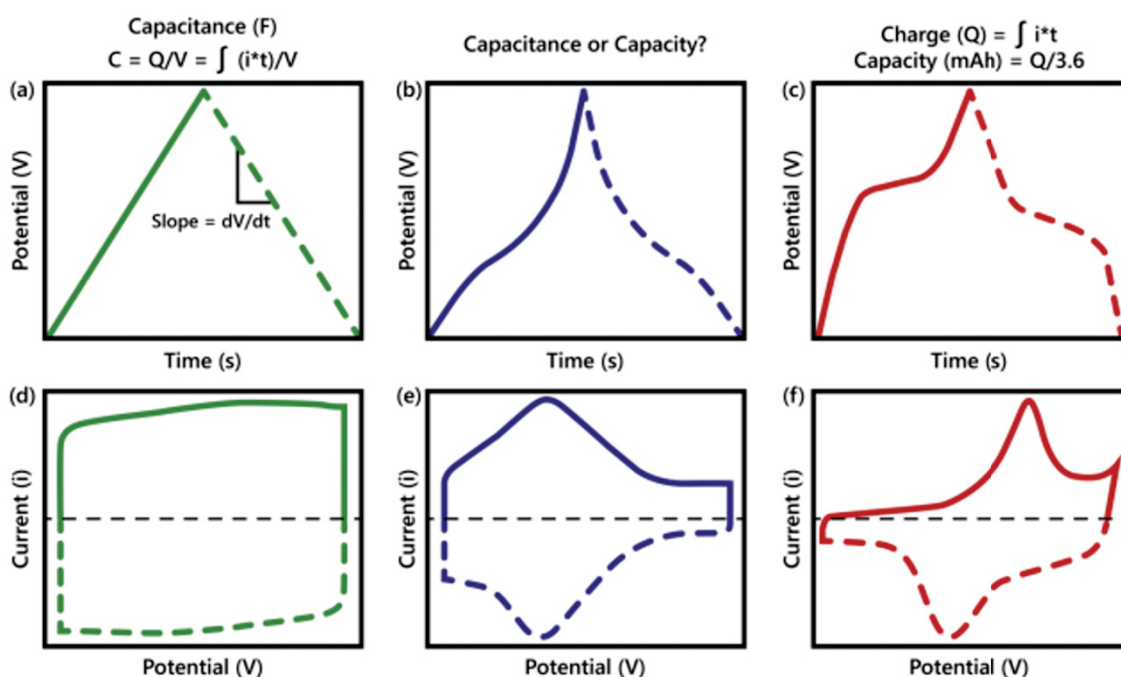
The concept of pseudocapacitance in the energy storage field was originally used by Conway [93] to describe surface Faradaic processes exhibiting a capacitive electrochemical response. Currently, the development of new materials with behavior between that of batteries and capacitors can blur the limit between capacitor and batteries leading to wrongly consider some materials as pseudocapacitive. Therefore, a material should be labeled as pseudocapacitive with care. Truly pseudocapacitive materials exhibit symmetrical charge-discharge curves roughly triangular, symmetric redox peaks with little to no separation in the voltammograms, so the voltammograms are roughly rectangular-shaped; and peak current with linear trend respect to the scanning rate (characteristic of surface-controlled processes) as is shown in Figure 2-1. [55] Additionally, the Nyquist plots resulting from electrochemical impedance spectroscopy may show capacitive behavior, that is a line close to the vertical at low frequencies, and an arc-line at high frequencies characteristic of interfacial charge transfer processes. [55]

The pseudocapacitive behavior is typically attributed to highly reversible electrochemical reactions with no diffusion limitations, then the electrochemical characteristics helping to identify it are the electrochemical reversibility and the predominance of “surface-controlled” kinetics. [15] As observed in Figure 2-1 symmetric cyclic voltammograms and charge-discharge profiles evidence the electrochemical reversibility and absence of diffusion limitations. Other way to quantify the contribution of “surface-controlled” processes, that is

processes without diffusion limitations, is to track the changes of total charge stored q_T (as estimated by cyclic voltammetry) with the sweep rate. [55] It allows to estimate the charge stored owed to diffusion-controlled (q_i) and surface-controlled (q_o) processes to q_T since the former may be proportional to $k_D v^{-1/2}$, so $q_T = q_o + q_i = q_o + k_D v^{-1/2}$. [94]

When $v^{-1/2}$ tends to 0 (so $v \rightarrow \infty$) q_o can be calculated, whereas when $v \rightarrow 0$ q_T could be estimated (see how in section 3.4.1 page 65) since all processes, capacitive and diffusive, may occur at low scan rates. Similarly, the relationship between current i and the scan rate v is given by the sum of the capacitive (i_C) and diffusive (i_D) currents ($i = i_C + i_D = k_C v + k_D v^{1/2}$). [14,95,96] i_C is proportional to the sweep rate (current flowing in a capacitor). i_D follows the Randles–Ševčík equation. i vs. v data at determined potentials can be fitted to this model to estimate the capacitive and diffusive contributions to the total current in the electrode. In a more simplified approach, the current is written as a power law ($i = av^b$). Electrodes dominated by capacitive/surface processes should exhibit b values close to 1, and the electrodes dominated by diffusion-controlled processes should exhibit b values close to 0.5. [97] b -Values between 0.5 and 1 indicate a transition area with mixed control or finite-length diffusion which should be considered carefully. [15,95,98,99] However, values between 0.85 and 1 indicate that surface/capacitive processes are predominant. [15,55]

FIGURE 2-1- TYPICAL BEHAVIOR IN THE ELECTROCHEMICAL CHARACTERIZATION OF A, D) CAPACITIVE, B, E) PSEUDOCAPACITIVE AND C, F) BATTERY-LIKE ELECTRODES.



a-c) Typical charge-discharge profiles and d-f) typical cyclic voltammograms.

SOURCE: reprinted from MATHIS et al.[55]

The pseudocapacitive behavior is typically attributed to reversible electrochemical reactions occurring in electrode species, so that there are no diffusion limitations in the solid electrode structure or the electrochemical interface. [15,57] Typically, the processes occurring in the pseudocapacitive materials are i) monolayer adsorption, ii) surface redox reaction or iii) intercalation without solid state diffusion limitations. [15,56] Pseudocapacitance for these processes was defined in terms of some property y proportional to the charge accepted Q , which is a function of electrode potential E . So, a capacitance C_ϕ could be mathematically defined as a quantity proportional to the derivative of y respect the potential ($C_\phi \propto dy/dE$). [56] For example, Conway developed an expression for adsorption pseudocapacitance considering that the electro-sorption of species on electrode surfaces can be described by a Langmuir-type isotherm (i.e. H^+ on Pt). Therefore, for a generic electro-sorption of a cation A^+ on a surface site M ($A^+ + M + e^- \leftrightarrow MA_{ads}$) the following relationship arises [100]:

$$\frac{\theta}{1-\theta} = KC_A e^{\left(\frac{FE}{RT}\right)} \quad 2.1$$

C_A is the concentration of the cation in solution, θ is the surface coverage of MA_{ads} , K is the ratio of the forward and reverse reaction rate constant, F is the Faraday constant, R is the ideal gas constant, V is the electrode potential, and T is the temperature. Systems that can be thermodynamically described in the way above shown can exhibit adsorption pseudocapacitance if they are fast with no mass transfer limitations. So, these processes are electrochemically reversible and remains in quasi-equilibrium. In fact, rearranging equation 2.1 an expression with the form of the Nernst equation can be derived:

$$E' = E^0 + \frac{RT}{F} \ln \left(\frac{1}{KC_A} \frac{\theta}{1-\theta} \right) \quad 2.2$$

E' is the equilibrium potential of the electro-sorption process and E^0 is the standard potential of the redox couple, if the charge required for the formation of A monolayer on M in process is q the pseudocapacitance C_ϕ can be defined as:

$$C_\phi = q \frac{d\theta}{dE} = \frac{qF}{RT} \frac{KC_A e^{\left(\frac{FE}{RT}\right)}}{\left[1 + KC_A e^{\left(\frac{FE}{RT}\right)}\right]^2} = \frac{qF}{RT} \theta(1-\theta) \quad 2.3$$

This result indicates that a purely Langmuir-type electro-sorption process exhibit a pseudocapacitance C_ϕ which is function of E . C_ϕ initially must increases when E increases to reach the maximum when E is zero (so $\theta = 0.5$) and must decrease with further E increasing (θ approaches to 1). The C_ϕ is only spread out over a small range of E (120 mV), so a single process of adsorption have no practical energy storage application. [56] A factor which can spread C_ϕ out on a wider range of potential is the lateral repulsive interaction between adsorbates as θ increases.[15,56,93] It can be described by introducing a lateral interaction parameter γ which modifies the adsorption energy ΔG^0 with a term proportional to coverage

as in the Frumkin isotherm ($\Delta G^0 = \Delta G^0 + \gamma\theta$). Also, the deposition of adsorbates at successive states giving rise to multiple peaks can lead C_ϕ to spread out on a wider range of potential.

Conway generalized his approach to other mechanisms by replacing the surface coverage with the lattice occupancy (for intercalation) or oxidized/reduced molecule concentration (for surface redox). [56] Additionally, it is remarkable that the essential thermodynamical aspect in his approach to pseudocapacitance is the relationship of potential to the activity relation $\theta/1 - \theta$. This aspect is dominant for highly electrochemically reversible processes, so the critical difference of pseudocapacitive redox processes as compared to batteries is their high degree of kinetic reversibility and the absence of mass transfer limitations.[57] In fact, some nanostructured materials that undergo redox or intercalation reactions exhibited electrochemical features of pseudocapacitance, which is attributed to short diffusion length and to the presence of most of active sites on the surface, so the time required to ion diffusion is small.[15] But the same material could exhibit a battery-like behavior when is fabricated as thicker electrodes.[101]

Further research on materials exhibiting pseudocapacitance should be conducted to deepen the understanding of pseudocapacitance fundamentals. This task requires modeling and theory along with experimental studies involving in-situ characterization, which can reveal key factors in the mechanism of operation of these materials. This understanding should assist the design of new electrode materials for EES devices with improved efficiency. The next section presents some materials exhibiting pseudocapacitance, such as transition metal oxides, which are model materials for the understanding of pseudocapacitance. Rather than present an exhaustive list of pseudocapacitive materials, the materials are presented briefly mentioning the current understanding of the functioning mechanism.

2.2 DEVELOPMENT OF MATERIALS FOR ELECTRODES

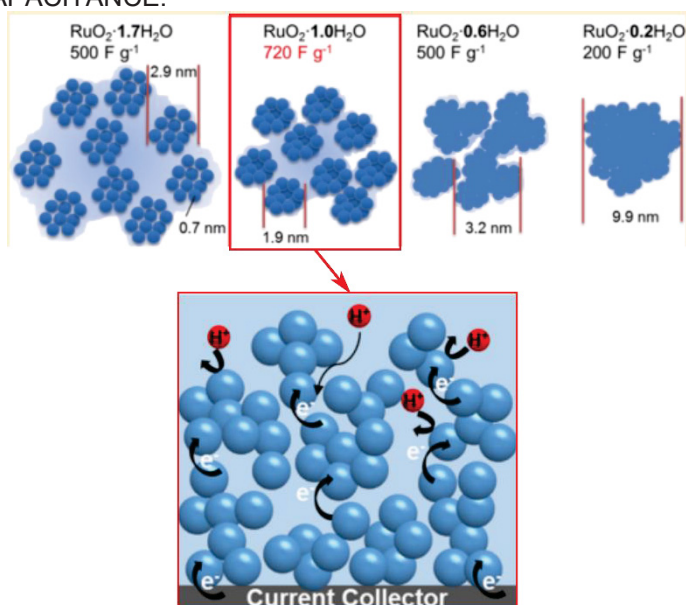
2.2.1 *Pseudocapacitive Materials*

One of the main pseudocapacitive materials developed up to date are the metal oxides (MO_x). RuO_2 and MnO_2 are the pseudocapacitive metal oxide most recognized, RuO_2 have high theoretical specific capacitance (2000 F g^{-1} [13,87]) that arises from fast and reversible charge transfer reactions between Ru^{2+} and Ru^{4+} while H^+ ions are adsorbed on the surface. MnO_2 also have relative high theoretical specific capacitance (1100 F g^{-1}) that arises from redox reactions between Mn^{3+} and Mn^{4+} and the ion intercalation or adsorption. [13,44,86,87] The presence of structural water and presence of nanostructures is crucial for high performance of metal oxides. In fact, the $\text{RuO}_2 \cdot n\text{H}_2\text{O}$ capacitance in acidic electrolytes varied with the water content [102,103] and the presence of nano-crystallites favors the

reactions mediated by RuO_2 surface. [104,105] As above mentioned, the structure may provide an interconnected network facilitating the charge transport (electronic and ionic) and the sites accessibility.[13,44,86,87] A probable advantageous structure is that formed by interconnected MO_x nano-crystallite with significant electronic conductivity surrounded by water as shown in Figure 2-2. That structure may favor the electron and proton conductivity. Precisely, the main drawback of MO_x are their poor electronic conductivity. [10,86,87]

Another transition metal oxides such as V_2O_5 [106–110], and spinel crystal structure oxides with formula AB_2O_4 are also important for EES. V_2O_5 is an interesting material because of several oxidation states of vanadium and its low cost, but its durability is limiting. [106] However, its durability is improved synthesizing it as nanotubes [107] or nanosheets [108]. The AB_2O_4 compounds such as Mn_3O_4 , [111,112] Fe_3O_4 , [113,114] Co_3O_4 [115–117] and NiCo_2O_4 [118,119] offer a robust crystalline structure with three dimensional diffusion pathways, their capacity arises from reactions involving the redox pair $\text{M}^{3+/2+}$. [86,112] However, Co_3O_4 and NiCo_2O_4 can exhibit battery-type behavior due to the formation of oxyhydroxides (involving phase transitions) during the charge storage process. [86,119] The low electronic conductivity and the lack of available accessible sites of AB_2O_4 materials can hinder the performance of this material, [116,117] so composite materials [116] and layered structures [117] are proposed to improve its performance. Moreover, the preparation of these materials in nanoscale form is expected to emphasize their pseudocapacitive behavior over the battery-like behavior. [86]

FIGURE 2-2- SCHEMATIC OF $\text{RuO}_2 \cdot \text{H}_2\text{O}$ HYDROUS STRUCTURE AND ITS INFLUENCE ON MATERIAL CAPACITANCE.



The scheme shows as the loss of the hydrous structure leads to lowered material capacitance and remarks the improved charge transport in hydrous structure.

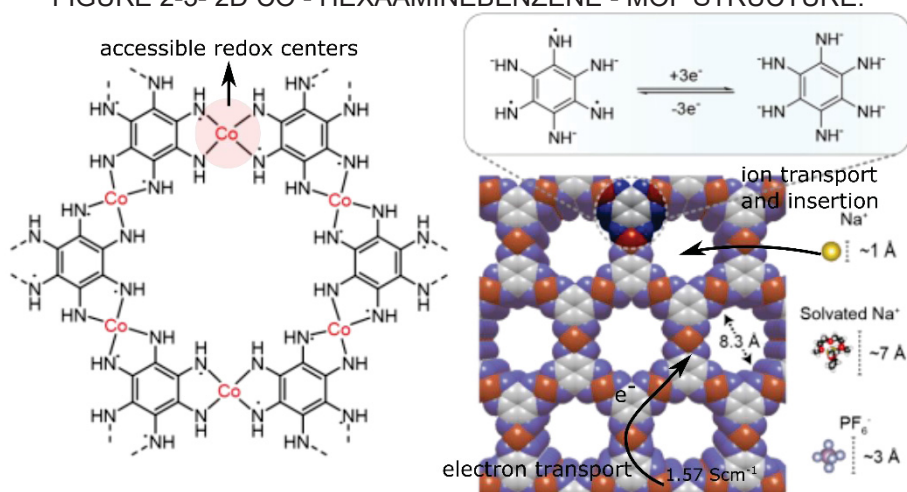
SOURCE: adapted from FLEISCHMANN et al.[15] and YOSHIDA et al.[104]

Conducting polymers are widely explored as electrode material for supercapacitors. They have a backbone chain of alternating double- and single-bonds, so overlapping π -orbitals create a system of delocalized electrons, which result in interesting electronic properties. They present reversible redox reactions involving generally double bonds in polymer networks, and simultaneous polymer doping with a counter-ion. Conducting polymer commonly admit 1 dopant counter-ion per 2 or 3 monomers. [88] The conducting polymers most studied as pseudocapacitive electrodes are polythiophene, polypyrrole and polyaniline (PAni). [88,90] The main drawback of conducting polymers is their poor durability caused by swelling and shrinking of conducting polymers when dopant counter ions are inserted [88,90,120].

Other organic polymers bearing redox active groups such as carbonyl [121] (i.e. quinones,[122–125] imides [126–129]) have been described. These polymers are structures grafted with active sites, where redox reaction may occur with the concomitant counter-ion doping and electron transport through the polymer. Their synthesis involves the preparation of a polymerizable group with a redox-active group followed by the polymerization. [89] Additionally, the synthetic versatility of these materials allows to design electrodes with high density of redox site and significant electron conductivity through the modification of their chemical structure, which may result in a higher energy storage efficiency. Some other advantages of organic materials are the abundant sources and their suitability for flexible and lightweight devices. [89] Whereas the material conductivity and stability are the main characteristics to improve.

Likewise, electrodes based on coordination compounds with redox properties have been proposed. Metal coordination materials are formed by ligands and metal atoms linked through coordination bonds. Coordination materials based on ferrocene,[89,130,131] hexacyano-metalates (HCMs),[132–134] and other complexes with ruthenium,[135] iron,[136–138] nickel [139,140] and cobalt [141,142] have been investigated, particularly the “coordination polymers” with repeating coordination units extending in 1, 2, or 3 dimensions such as MOFs and HCMs. [132,143,144] These materials are promising since the transition metals in coordination compounds present electrochemically reversible reactions that can be harnessed in energy storage applications. Also, the choice of ligands would allow to integrate the compounds with other materials and obtain designed structures with high porosity, surface area and improved ion transport as shown in Figure 2-3 . [83,132,143,144] However, strategies to promote charge transport are desirable to obtain better electrodes. [143,144]

FIGURE 2-3- 2D CO - HEXAAMINEBENZENE - MOF STRUCTURE.



The Figure illustrates the chemical structure of a metal coordination material with three-electron reversible reaction, remarking that the ion and electron transport is favored through the formation of nanopores and the electronic coupling of metal center and ligands.

SOURCE: adapted from PARK et al. [145]

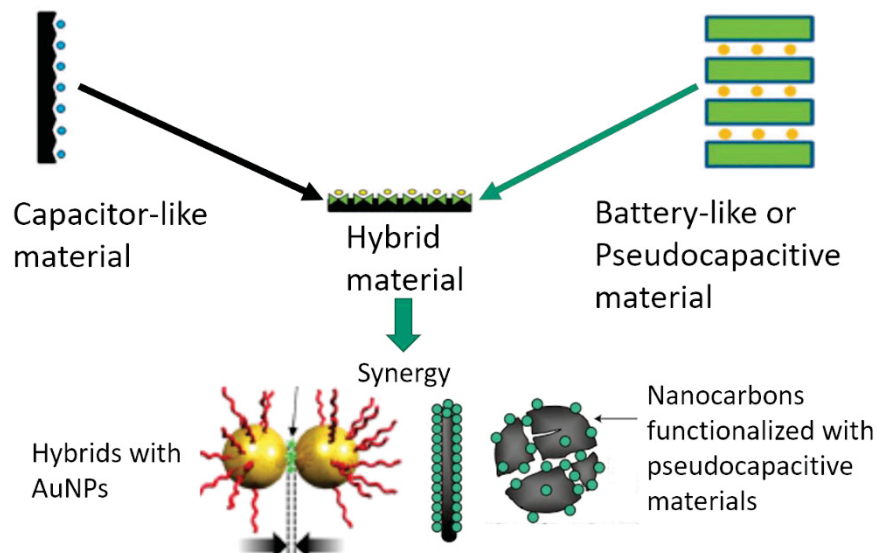
The mixing of active material with capacitive, conductive, and mechanically stable compounds is proposed to increase the capacity, the electrical conductivity and the stability of the electrodes. But there are some critical factors for the conductivity of hybrid material electrodes. Such as the electron transfer across the interfaces within hybrid material, and the electrical integration of electrode with other cell elements, such as electrolyte and current collector. These issues influence the internal resistances and should be considered in the electrode design. [13,14,44,53,59,67] Some proposals of hybrid materials are reviewed in the next section.

2.2.2 Hybrid Materials

The hybrid materials integrate at least two materials at molecular level. They have drawn great attention in the last years due to the possibility of integrating a pseudocapacitive material with a capacitive material to exploit the two different mechanisms for charge storage in a single material as depicted in Figure 2-4. [59] The carbon nanocomposites have been largely investigated in the recent years. Carbon materials, particularly nanostructures as carbon nanotubes (CNTs) and graphene (G) are mostly used due to its high electrical conductivity, controllable porosity and structure, high surface area and ease of the integration with other materials (e.g. redox components) [9,44,76,87,146]. For example, the combination of carbon structures with transition metals oxides or conducting polymers, such as CNTs/RuO₂, [147] G/ RuO₂, [148–150] G/MnO₂, [151–153] CNTs/V₂O₅, [154] graphene with polyaniline (G/PAni) [155] and CNTs/PAni [156–158] increased the capacitance and power

density of the composite electrodes due to the synergy effect between the electric double layer and pseudocapacitive charge storage processes.

FIGURE 2-4- SCHEMATIC REPRESENTATION OF THE HYBRIDIZATION BETWEEN CAPACITOR AND BATTERY – LIKE MATERIALS.



SOURCE: adapted from DUBAL et al., [59] SIMON and GOGOTSI,[66] and KO et al.[159]

Some other works have developed other composites based on carbon structures but combined with metal hydroxides and metal complexes. For example the combination of graphene with hydroxides $G/Ni(OH)_2$ [160–163] and $G/NiCo(OH)_2$ [164–166] improved the performance and stability of $Ni(OH)_2$ and $NiCo(OH)_2$. Likewise coordination compounds have been combined with carbon structures obtaining CNTs/HCMs, [167,168] G/MOFs [169–172] and G or CNTs with metal phthalocyanine complexes. [139,173] The combination of G and CNTs with metal phthalocyanine complexes resulted in an electrode with superior performance due to the contribution of capacitive and pseudocapacitive mechanisms of constituent materials. [173] Likewise the addition of graphene to MOFs with transition metals (manganese[169], copper[170] and nickel[171,172]) improved the electrode capacitance due to the contribution of porous and interconnected structure of the composite material and the metal redox center distributed through MOFs. Besides, CNTs improved the stability of HCMs getting a promising performance as battery electrode. [167]

Metallic nanocomposites also have been studied since metallic nanostructures show high conductivity, high surface area and new functionalities leading to higher performance of the supercapacitor electrodes. [159,174–176] In fact, the deposition of silver nanoparticles on carbon cloth electrode led to increase its capacitance 300%, [177] and the use of gold nanoparticles to decorate CNTs led to performance increasing respect to bare CNTs. The performance increasing could be partly attributed to the small size of nanoparticles increasing the total surface area of the electrode. [175] Additionally, nanoporous gold substrates were fabricated using methods as de-alloying [178] or ligand-mediated layer-by-layer assembly of

gold nanoparticles. [159] Pseudocapacitive materials as MnO_2 or Fe_3O_4 nanoparticles were deposited on the fabricated nanoporous gold substrates to obtain electrodes with superior performance owing the energy storage capabilities of metal oxides and high electrical conductivity provided by gold. [159,178]

Nanocomposites of gold and MnO_2 have been described, the nanocomposites were designed with different nanostructures such as MnO_2 nanowires decorated with gold nanoparticles, [179] core-shell Au-Co nanoparticles [176] and coaxial nanowires with MnO_2 nanowire coating a gold nanowire.[180] They provided clear proof that metal oxide/metal hybrid structures have the potential to function efficiently as energy storage electrodes. [176,180] Likewise, nanocomposites of gold and conducting polymers were synthesized by in-situ polymerization on the gold nanoparticle surface. The high conductivity of the metal core and the thin polymer layer may promote the efficient charge transport. [174,181]

Summarizing, the key factors of the pseudocapacitive material functioning is the presence of redox reaction accompanied with counter-ion doping/adsorption into material structure. So, the high rates of redox reaction and ion transport within electrode structure are important aspects for their performance. Likewise, the electrical conductivity and the surface area are relevant properties. Therefore, conductive materials with high surface area (hence high capacitance) are mixed with pseudocapacitive ones to obtain hybrid material with enhanced properties. However, as mentioned, the electrode architecture of hybrid materials requires a careful design to promote fast electron transfer in the whole hybrid material, fast ion transport to active sites, and high exposition of active sites. So, in addition to the materials chemistry, the porosity, structure, and interactions within the material should be optimized to obtain materials with reduced charge pathways and high surface area. Particular attention may be paid to the interfacial interactions, that is electrode-electrolyte and electrode-current collector, which are determinant in the electrode performance. [48–50] Some of those mentioned structural aspects are reviewed in the next section.

2.3 ELECTRODE STRUCTURES

A viable strategy to obtain electrodes with better performance at high rates is promote the surface-controlled rather than diffusion-controlled kinetics through the nanostructuring of the electrode material. So that large part of the reaction sites is accessible on the near-surface region, which reduce the kinetic limitation. [15,101] Furthermore, nanostructures can lead to the suppression of phase transitions in intercalation processes and the shortening of diffusion length which reduce the kinetic limitations for charge storage. However, the challenge is to maintain the nanoscale material properties in the commercially viable thick electrodes, promoting the electronic and ionic transport throughout the whole electrode.

1D nanostructured materials such as carbon nanotubes, transition metal oxide nanowires and conducting polymer nanowires and nanofibers are interesting structures for energy storage electrodes. They can be entangled with each other enabling the possibility to assemble flexible composite film electrodes with high mechanical strength. Also, they can be used as the building blocks in electrode arrays. For example, the In_2O_3 nanowire-CNTs composite with long and flexible nanowires assembled on CNTs films forms an electrode. [182] CNT paper prepared by a simple filtration method was used as a matrix for MnO_2 nanowires which was electrodeposited onto the CNT paper to obtain a free-standing electrode. [183,184] G-PAni nanofiber composite electrodes were fabricated obtaining a composite film with layered structure and higher conductivity. [185] Those electrodes show an increment of their capacitance which can be attributed to the high exposition of sites in 1D nanostructured materials and the synergic effects of the conductive carbon material and the pseudocapacitive material (transition metal oxide or conducting polymer).

Besides, the 2D nanostructures or materials grown epitaxially are a promising structure, these 2D atomic crystals such as graphene, dichalcogenide, layered oxides, metal carbides or metal nitrides (MXene) exhibit a chemical unit repeating along a plane with strong bonds and a layered structure held by weak forces. [74] This structure is advantageous since each monolayer is ideally a sheet of atomic dimensions with high electronic conductivity and several accessible sites able to undergo redox reaction, whereas the interlayer space may offer a short path for ion diffusion and is used to insert counterions which can intercalate or adsorb on specific sites, in this way the redox reaction occurring on the layer sites is balanced. For example, MXenes [186–188] show high capacity even at high rates due to the set of properties above mentioned. It was demonstrated that a high capacitance can be achieved because of the interlayer composition/structure with water and cations pre-intercalated in the hydrogels and “clay” electrodes. [186–188] The appropriated interaction of electrolyte components and MXene interlayer chemistry allow to insert/disinsert ions easily, that is a shallow ion insertion with short diffusion path. [189]

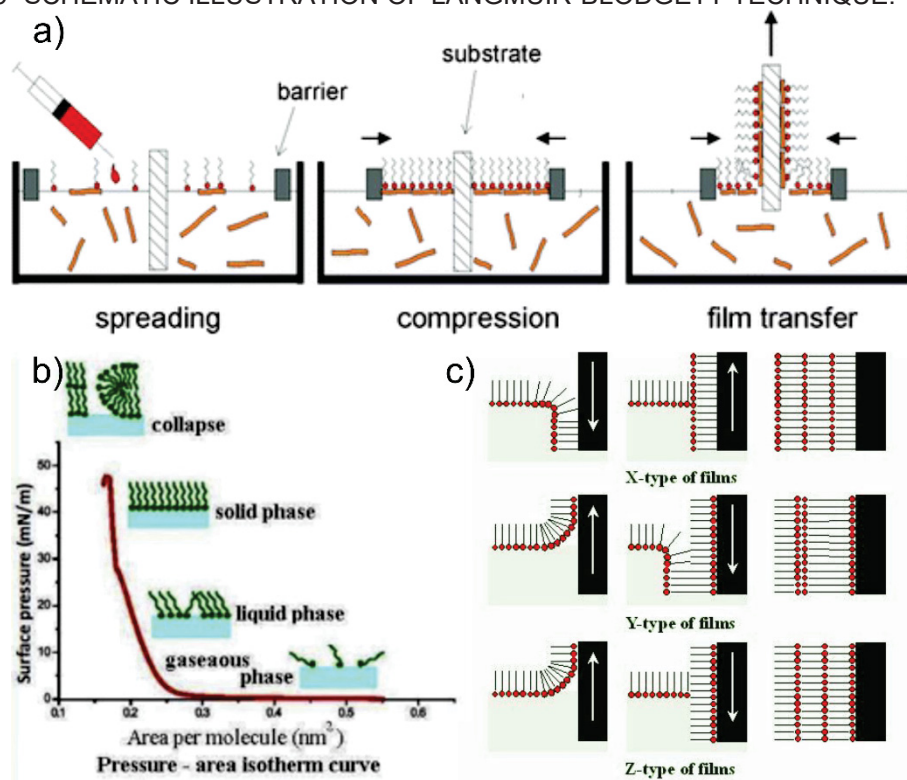
Another 2D materials of great interest for EES are the nanostructured and exfoliated transition metal dichalcogenides, particularly MoS_2 . [190] It is of great interest due to its layered structure which undergoes ion intercalation without phase transition. Graphene is other 2D material of great interest by its electronic conductivity and its structure which may promote ultrahigh specific surface area if each graphene sheet is exploited. In contrast with other 2D materials containing transition metals, graphene may not exhibit significant faradaic process (redox reaction, intercalation). However, a pseudocapacitive process attributed to interactions with oxygen groups was reported for graphene oxide (GO). [191] This characteristic could be harnessed fabricating GO partly reduced to restore their electronic conductivity without losing the pseudocapacitive feature.

The understanding of energy storage mechanism in those materials allows the design of different electrode structure which helps to improve the capacitance of energy storage electrodes. For example, it was found that the surfaces of MXene sheets have oxygen groups able to react with H^+ , additionally the fast diffusion of cations and H^+ between MXene sheets without large lattice deformation may enable a higher rate (power) supercapacitor. [192–194] These factors, the redox reaction and fast diffusion, are key in MXene electrodes excellent performance. In this sense, structures with hydrated and cation pre-intercalated such as hydrogel structures may lead to improved power capabilities. Usually, thicker electrodes have diffusion limitations due to more entangled diffusion paths. However, the design of structure with long-range organization could enable fast ion diffusion in electrodes with higher thickness. Such as was demonstrated in previous work, electrodes with aligned or microporous structures exhibiting long-range organization allows certain control on ion diffusion. [187,195,196]

A basic strategy for controlling organization within a 2D plane is the LB method, which is a way of making supramolecular assemblies with a controlled layered structure through the transfer of material monolayer formed in air-liquid interface upon the compression of the monolayer. The technique was first developed by Katharine Blodgett who deposit stearic acid on glass, transferring monolayers of the amphiphilic molecules on water surface (Langmuir films) to a substrate [197], so the technique became known as Langmuir-Blodgett. Usually, two main steps are involved: i) *The preparation of the Langmuir-film*, amphiphilic materials (with hydrophilic and hydrophobic parts) dispersed in a volatile solvent are carefully spread onto ultrapure water subphase lying in a Langmuir trough as it is shown in Figure 2-5a. After some minutes, the solvent is evaporated and the amphiphilic molecules are self-organized at air-water interface orienting the hydrophilic region towards water and the hydrophobic part away from water. [198–201] Typically the initial concentration is low such that there are not significant interactions among units, but the area occupied by molecules can be reduced, so the units can interact as it is shown in Figure 2-5a.

The behavior of the film under compression is monitored recording the surface pressure (Π) which is defined as: $\Pi = \sigma_0 - \sigma$ with σ_0 surface tension of liquid without molecules and σ with molecules [198,199]. The recording of Π variation with the area (A), known as $\Pi - A$ isotherm, allows to identify different regions (see Figure 2-5b). First a region analogous to “gas phase” with little increasing of Π is observed due to separated and “non-interacting” molecules. Then a region corresponding to “liquid” phase with a sustained increment of Π is observed with A decreasing due to significant interaction among molecules. Finally, Π increase more sharply with further decrease in A due to the close-packed arrangement like in a “solid phase”. If the film is further compressed a discontinuity in the increment of pressure can be observed which indicates the collapse of the film. It is remarkable that isotherm curve depends on the condition of subphase-pH, temperature and the spread molecule [198].

FIGURE 2-5- SCHEMATIC ILLUSTRATION OF LANGMUIR-BLODGETT TECHNIQUE.



a) Steps of the fabrication, b) typical pressure-area isotherm ($\Pi - A$), c) types of films deposition.
SOURCE: Adapted from HUSSAIN et al [198] and RAS et al. [202]

ii) *Langmuir film transfer to the substrate* (or fabrication of LB film), it is made maintaining a fixed pressure at any value and submerging or emerging the substrate in the subphase while it is held vertically perpendicular to the Langmuir film. It is convenient to use a pressure value lying in solid phase to obtain well organized and packed films. Whereas the substrate is chosen according to the needs, and it can be treated to get hydrophobic or hydrophilic surfaces to influence the adherence of the molecules to the substrate. That is, if the substrate is hydrophilic the polar part of the molecule in the first monolayer is oriented toward the substrate, so the transference of first monolayer is more effective with the substrate emerging from the subphase. Whereas in a hydrophobic substrate is more effective begin submerging the substrate. Subsequent depositions can proceed during each submersion and emersion of the substrate, this deposition is named Y-type deposition, in which films have a head-to-head and tail-to-tail configuration. However, the single layers also can be transferred only during immersion (X-type deposition) or only at emersion (Z-type deposition) as depicted in Figure 2-5c leading to head-to-tail configuration with hydrophobic (X-type deposition) or hydrophilic part (Z-type deposition) in contact with the surface. [198] Ideally the LB technique offers the possibility to control each step of the preparation, which should result in the achievement of films with controlled layered arrangements.

Considering the above described, electrodes based on redox metal complexes with fast redox reactions and highly conducting materials exhibiting an organized structure could

be constructed to promote a pseudocapacitive behavior which is promising to obtain energy storage devices with high energy and power density. The presence of highly accessible redox sites, improved ionic and electronic conductivity within the electrode are key for the electrode performance.[72,136] Suitable strategies to improve the electrode conductivity and obtain organized structures are the hybridization of conductive materials with metal complexes and the fabrication of organized layered films using self-assembly or LB techniques.

These electrodes typically present low energy density (per unit of area) because of low material loading, so they could be suitable for energy storage units in microelectronics, transparent and flexible devices. In fact, some thin film electrodes for energy storage based on redox transition metal complexes and metal oxides have been proposed in previous works, such as iron based supramolecular polymer,[136] ruthenium complexes,[135] nickel complex,[203] and metal organic frameworks based on zirconium[204] or nickel[205]. All these works remark the reduction of the resistance associated to ion diffusion achieved by the structure of those films and the higher performance of electrodes with metal complexes exhibiting pseudocapacitive redox processes. [135,136,203,206–208] Herein, electrodes based on triruthenium acetate clusters were developed as hybrid materials and organized layered films. So, the next section presents a review on those metal complexes remarking their electrochemical properties.

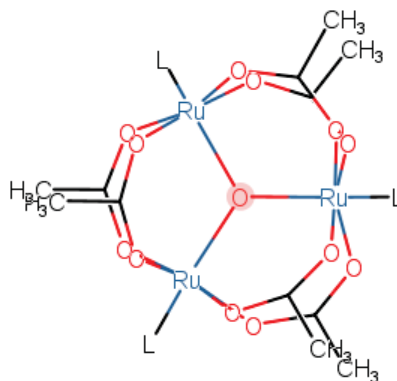
2.4 OXO-CENTERED TRIRUTHENIUM ACETATE CLUSTERS

Triruthenium acetate clusters have interesting electronic, magnetic, and physico-chemical properties that can be tuned through design of its structure and composition at molecular level. They have as general formula $[\text{Ru}_3\text{O}[(\text{CH}_3\text{CO}_2)_6]\text{L}_3]$ with L indicating a ligand group, it is H_2O or methanol in the first step of the synthesis and can be exchanged by N-heterocycles, thiols, CO, and other Lewis base to add some functionalities. [18,20,92] A general scheme of these complexes is shown in Figure 2-6, it can be observed that ruthenium ions seem to form a trigonal structure with an oxygen located in the center as bridging ligand binding the ruthenium ions at the vertices. Also, ruthenium ions are connected by three double carboxylate bridges which held the triangular structure. The proximity of ruthenium metals allows strong electronic interactions, mainly via the central oxygen atom, stabilizing a whole series of successive oxidation states associated with the three ruthenium simultaneously. [16,17] Additionally, the ligands L are bind axially to the centered oxygen atom.

Ru-Ru and Ru-O bond lengths are not sensitive to the changes in the formal oxidation states of the metal ion, implying a strong electronic delocalization within the Ru_3O core and reflecting their high stability. [19] Ru-L bond lengths are considerably higher than the Ru-O and Ru-Ru, indicating the lower bond strength with the ligands which may facilitate their exchange.

Therefore, $\text{Ru}_3\text{O}(\text{CH}_3\text{CO}_2)_6$ core unit has considerable stability to reaction with various ligands, the substitution of acetate is difficult and needs vigorous reaction conditions. [209] Whereas ligand substitution allow to form compounds with tuned stability of the possible oxidation states, so clusters may exhibit mixed valency chemistry. [19,210,211] Additionally, ligand substitution affords an excellent way of tuning the redox properties in the cluster and provides a feasible approach to design ligand-linked triruthenium cluster oligomers. [19,211,212]

FIGURE 2-6- SCHEMATIC REPRESENTATION OF TRIRUTHENIUM ACETATE CLUSTERS.



SOURCE: Author. Marvin was used for drawing, Marvin version 21.8, ChemAxon (<https://www.chemaxon.com>)

The interest in oxo-centered ruthenium clusters as is energy storage material arises from its electrochemical and electronic properties. They have a rich electrochemical behavior, exhibiting 4 reversible and monoelectronic redox pairs in a potential range from 2.0 to -1.5 V measured with SHE as reference and 4 of these redox pairs are separated by 1V. [19,22,23] Furthermore, the introduction of redox-active axial ligands which can interact mediated by the Ru_3O core could contribute to the design of versatile multielectron redox systems, whose redox peak potentials are influenced by the different interactions present in the cluster. [22] In fact it is found a linear relationship between redox potential (E°) of the cluster and the pKa of N-heterocyclic ligands. [21]

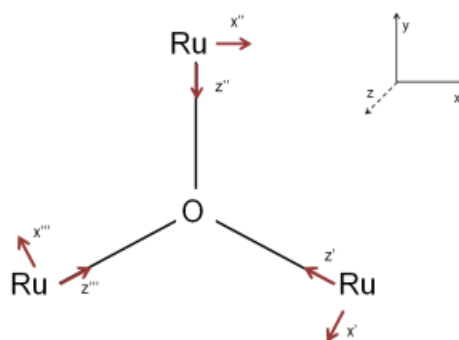
This dependence of the redox potentials indicates that the reduced form of the cluster is stabilized by the presence of ligands with higher electron acceptor character. Additionally, the stabilization is more evident at lower redox potentials (from -0.8 to -1.3 V) corresponding to lower ruthenium oxidation states.[21] It could be understood, considering that the metal core is stabilized by σ bonding and π back-bonding, the last plays a significant role to stabilize the lower oxidation states of ruthenium core since it can withdraw negative charge “excess” of the metal. Therefore, the cluster reduction at lower potentials is facilitated by π back-bonding effects of the ligand.

The dependence of the E° as a function of the ligand properties was studied by Alexiou and Toma [213] using the linear correlation with the ligand parameter E_L proposed by Lever

($E^\circ = S_M \sum E_L + I_M$). S_M indicates the relative stabilization of the reduced state (metal with lower oxidation state) by the ligand. I_M involves several contributions such as the ionization energy in the gas phase, electronic repulsion, and solvation energy. [214] Remarkably, these studies showed higher S_M for the redox pair involving lower oxidation states of ruthenium. [19,213] It corroborates Lever's appointment, that S_M is greater for redox couples stabilized by acids through back-donation. [214] Whereas I_M follows a trend with respect to the average oxidation number, that reflect the trends in successive ionization potentials of the Ru_3O core identical to that observed for successive ionization energies of atoms. [19]

The electronic properties of the triruthenium clusters also are very interesting, they are originated by the metal center interactions through the oxygen and carboxylate bridges. The interactions and electronic transitions have been discussed based on the qualitative molecular orbital scheme proposed by Cotton and Norman [18] and further detailed by Baumann et al. [23] for the Ru_3O unit. According to this model, the Ru_3O system is considered as unit with D_{3h} symmetry, and the axis system at each ruthenium site (see Figure 2-7) was chosen to facilitate the discussion in terms of each Ru orbital. It does not lie along the coordinate axis of molecular orbitals which for the D_{3h} point group is set with the C_3 axis that coincides with z axis as illustrated in Figure 2-7.

FIGURE 2-7- AXIS SYSTEM (X, Y, Z) USED TO CONSTRUCT THE QUALITATIVE MOLECULAR ORBITAL DIAGRAM OF THE Ru_3O UNIT AND THE LOCAL AXIS (X', Y', Z') OF EACH RUTHENIUM ATOM.

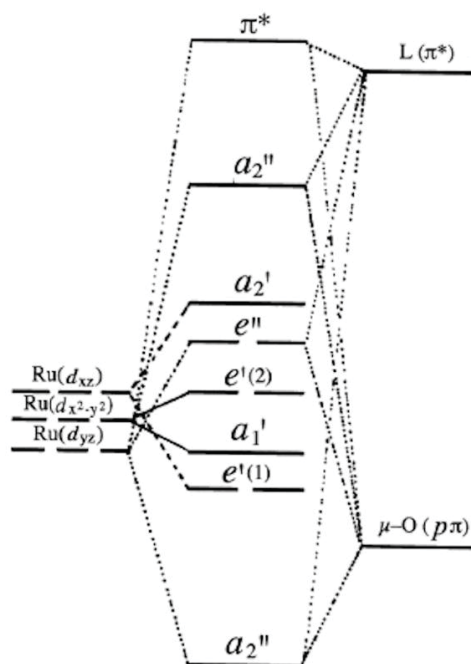


SOURCE: reprinted from NAIDEK [215]

The central oxygen is sp^2 hybridized to account the Ru_3O σ -bonding. This leaves a single p orbital of π symmetry which interact with one d_{yz} orbital in the metal giving rise to one bonding and one antibonding a_2'' molecular orbital (MO), the other two d_{yz} orbitals yields to two non-bonding e'' MOs as shown in the diagram of Figure 2-8. The d_{xz} orbital in each metal is able to interact with the same type of d-orbital on each of the other two atoms giving rise to metal-metal orbitals, two degenerated $e'(1)$ MOs and the non-degenerated a_2' MO. The formation of metal-metal orbitals is also suggested by DFT calculations performed in this work, in which some frontier orbitals with delocalized character are extended over the three ruthenium atoms (see Figure 4-4). The remaining d orbitals ($d_{x^2-y^2}$) have appropriate symmetry

to interact with each other, but they are far apart, such interaction remove the degeneracy of d orbitals yielding to $e'(2)$ and a_1' MOs, so these orbitals involve mostly region around one of the ruthenium atoms. The π -axial ligands can interact with the ruthenium d orbitals at the three Ru sites resulting in molecular orbitals of a_2'' and e'' symmetry as indicated in Figure 2-8.

FIGURE 2-8- QUALITATIVE MOLECULAR ORBITAL FOR THE $[\text{Ru}_3\text{O}[(\text{CH}_3\text{CO}_2)_6]\text{L}_3]$ IN D_{3h} SYMMETRY.



SOURCE: TOMA et al. [19]

According to the diagram proposed, the $[\text{Ru}_3\text{O}[(\text{CH}_3\text{COO})_6]\text{L}_3]$ complexes with $\text{Ru}_3^{\text{III,III,III}}\text{O}$ oxidation state, have the electronic configuration $(a_2'')^2(e'(1))^4(a_1)^2(e'(2))^4(e'')^4(a_2')^1$ with an empty a_2'' orbital. The broad absorption band observed in electronic spectra at low energies can be ascribed to the symmetry-allowed $e'' \rightarrow a_2''$ and $a_1' \rightarrow a_2''$ intracluster transitions, and to the $e(1)' \rightarrow a_2'$ electric dipole forbidden intracluster transition in D_{3h} symmetry which is activated by cluster distortions. The energies of the band increase for cluster with lower oxidation state reflecting a gradual rise of the occupied d orbitals as the number of electrons increases. Another band at intermediate energies is strongly sensitive to the ruthenium oxidation states and the nature of the axial ligands can be ascribed to the charge-transfer transition from the occupied Ru^{II} d orbitals of e'' symmetry to the lowest unoccupied π^* orbitals of the axial ligands.

Additionally, in the case of the totally reduced $\text{Ru}_3^{\text{II,II,II}}\text{O}$ cluster species, the d orbitals are completely filled and no metal-metal band is observed. Consequently, the interaction between central oxygen and the three ruthenium atoms stabilizing the system is no longer possible, facilitating the transfer of the oxygen ion to the proton donor species in the solvent. Summing up, it was shown above that the triruthenium clusters are systems presenting multiple

possible electronic transitions with energy in the visible and UV-vis region. The peripheral ligand influences greatly the energy of these transitions, conferring interesting optical properties for these complexes.

The properties found for this kind of compound lead to propose different applications for it, from optoelectronic devices to catalysts.[19] Among the applications proposed in the literature are its use as heat shields, since they can absorb light in the near-infrared region their performance depends of the oxidation state of ruthenium in the clusters [216]. Optoelectronic applications as logic gates [217] where a triruthenium carboxylate cluster is used as acceptor of electrons from TiO₂ semiconductor layer, and the electron transfer is modulated with optical sources [218]. Or electrochromic switching devices [219,220] used for smart glasses or electrochromic display devices. The mentioned application is owed to the redox properties and the spectra alterations of near infrared regions in the redox process.

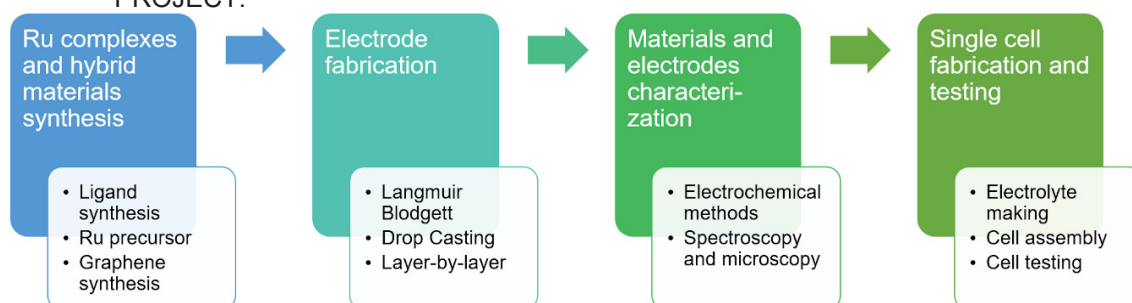
Also, they have been used as effective catalyst for oxidation of alcohols achieving a selectivity of 100% for carbonyl products [221,222], cyclohexene and cyclohexane [223], olefin hydrogenation [224] and hydration of nitriles reaching conversions up to 99% [225]. The catalyzed oxidation reactions, commonly involve the formation of radical $[Ru_3O]^+$ upon interaction with peroxide, also the catalytic performance can be tuned for the ligand groups L used [226]. Their photochemical properties also have been harnessed to design controlled photo-releasers of molecules as NO which could be used as therapeutical or antimicrobial agent. [227]

Summarizing triruthenium-acetate clusters exhibit reversible redox reactions with tunable redox potential using of different ligands (such as N-heterocyclic compounds). Also, they exhibit strong electronic coupling and delocalization conferring interesting electronic properties. These properties are appealing and could be exploited for its use in supercapacitor electrodes. So, this project aims to develop electrode materials based on $[Ru_3O(CH_3CO_2)_6Py_2L]$, L is an appropriate ligand which allows the fabrication of organized structures or the integration with other conductive components leading to hybrid materials. For example, mercaptopyridine (SHPy) and aminopyridine (NH₂Py) ligands allow to integrate the triruthenium cluster with highly conductive materials as gold and carbon nanostructures, respectively. 4-(4-dodecyloxyphenylazo) pyridine (AzoPy) allows to obtain an amphiphilic cluster with self-assembly properties. All these electrodes may have high performance owed to the contribution from fast faradaic processes of triruthenium cluster, the capacitive contribution of carbon and the designed electrode structures.

3 MATERIALS AND METHODS

Figure 3-1 shows the steps followed in this work. First, it was necessary to synthesize the ruthenium complexes, the graphene and hybrid nanomaterials based on ruthenium. After, thin films electrodes were fabricated with the materials synthesized using drop casting and Langmuir Blodgett (LB) techniques. The materials and the electrodes fabricated were characterized with spectroscopy and microscopy techniques and tested as electrodes for energy storage. Finally, a single energy storage cell was constructed and tested. Details of complexes and hybrid nanomaterial synthesis and characterization are described in the following sections.

FIGURE 3-1- FLOW DIAGRAM FOR EXPERIMENTAL ACTIVITIES CARRIED OUT DURING THE PROJECT.



SOURCE: Author.

3.1 MATERIALS SYNTHESIS

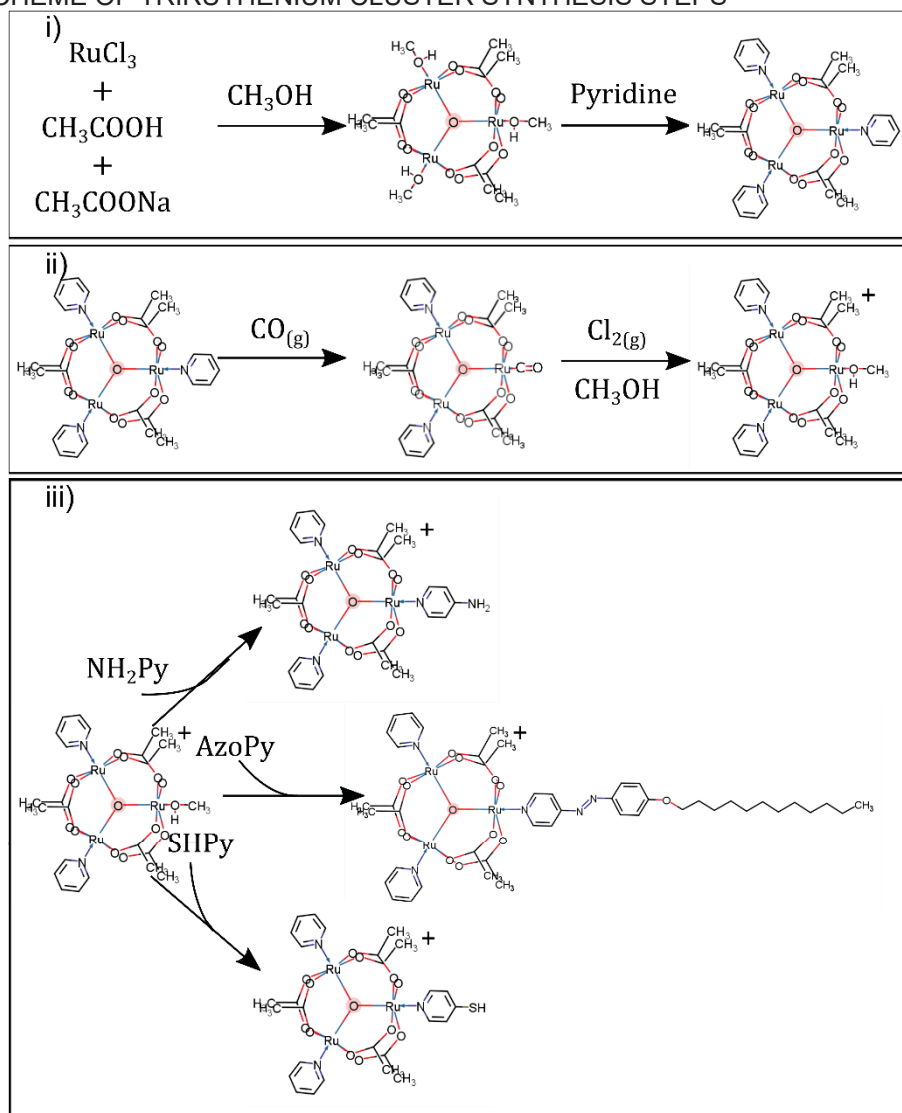
All reagents and solvents were of analytical grade purchased from commercial sources. Precursor reagents employed for triruthenium cluster synthesis were ruthenium chloride (RuCl_3 , Sigma-Aldrich, 45–55% Ru content), sodium acetate (Sigma-Aldrich, >99%), acetic acid (Dinamica), pyridine (Carlo Erba, >99.8%), 4-aminopyridine (Sigma-Aldrich, >99%), phenol (Sigma-Aldrich, >99%), 1-bromododecane (Sigma-Aldrich, >97%) and 4-mercaptopyridine (Sigma-Aldrich, 95%). Pyridine (Py) ligand was treated with potassium hydroxide and distilled. For reduced graphene oxide (rGO) synthesis were used the graphite (Nacional Grafite; 99.84%; Graflake 99.58%), NaNO_3 (Vetec, 99%), H_2SO_4 (Biotec, 95–98%), KMnO_4 (Synth) and H_2O_2 (Neon). For the graphene functionalization N-hydroxy-succinimide (NHS) and 1-ethyl-3-(3-dimethylaminopropyl) carbodiimide (EDC) were obtained from Sigma-Aldrich with 97% and 99% purity respectively.

3.1.1 Synthesis of Triruthenium Clusters

Briefly, the synthesis route for $[\text{Ru}_3\text{O}(\text{CH}_3\text{CO}_2)_6\text{Py}_2\text{L}]$ is illustrated in Figure 3-2. The ligand L is one of the following 4-aminopyridine, 4-mercaptopyridine or 4-(4-

dodecyloxyphenylazo) pyridine (L=NH₂Py, SHPy or AzoPy). The route requires i) the synthesis of ruthenium acetate and the replacement of all ligands by Py ii) after one Py ligand is changed by methanol according to the methods followed previously in our group [23,219], iii) finally the methanol ligand is changed by the ligand of interest NH₂Py, SHPy or AzoPy. The AzoPy ligand was synthesized previously in our group and the other ligands were obtained from commercial suppliers.

FIGURE 3-2- SCHEME OF TRIRUTHENIUM CLUSTER SYNTHESIS STEPS



i) synthesis of [Ru₃O(CH₃CO₂)₆Py₃] and ii) [Ru₃O(CH₃CO₂)₆Py₂CH₃OH] iii) and for [Ru₃O(CH₃CO₂)₆Py₂L].

SOURCE: Author. Marvin was used for drawing, Marvin version 21.8, ChemAxon (<https://www.chemaxon.com>).

3.1.1.1 Synthesis of Ru₃O(CH₃CO₂)₆Py₃

Triruthenium acetate cluster [Ru₃O(CH₃CO₂)₆(CH₃OH)₃] was previously synthesized from reaction of RuCl₃ (1.0170 g, 4.9031 mmol) with 54% excess sodium acetate (1.2500 g

15.237 mmol) dissolved in a round bottom flask using a mixture of 25 mL ethanol and 25 mL acetic acid and maintained with constant reflux for 4 hours and 30 minutes. The obtained mixture was filtered to remove excess reagents sedimented after left it resting overnight. The solvent of filtrate was removed using a rotary evaporator obtaining an oily liquid which was washed with methanol and again evaporated, the washing with methanol was done 4 times until a dry solid was obtained. Finally, solid was suspended in methanol, precipitated with the addition of acetone, filtered, washed with diethyl ether, and dried in desiccator containing CaCl_2 . 0.9820 g of solid was obtained (1.2760 mmol, 77.5% yield).

After, CH_3OH ligand was substituted by Py from the reaction of the $\text{Ru}_3\text{O}(\text{CH}_3\text{CO}_2)_6(\text{CH}_3\text{OH})_3$ (0.9820 g, 1.2760 mmol) and excess pyridine (4.0 mL, 49 mmol) dissolved in 19 mL of methanol (MeOH) in a round bottom flask and maintained under reflux for 20 minutes. Then 4 mL of hydrazine (N_2H_4) was slowly added while the mixture was stirred for 15 minutes and cooled in ice bath. After left at rest, an olive-green solid corresponding to $[\text{Ru}_3\text{O}(\text{CH}_3\text{CO}_2)_6\text{Py}_3]$ was recovered by filtration, washed with diethyl ether, water and methanol and dried in desiccator containing CaCl_2 . 0.6120 g of an olive-green color powder was obtained (0.6719 mmol, 56% yield).

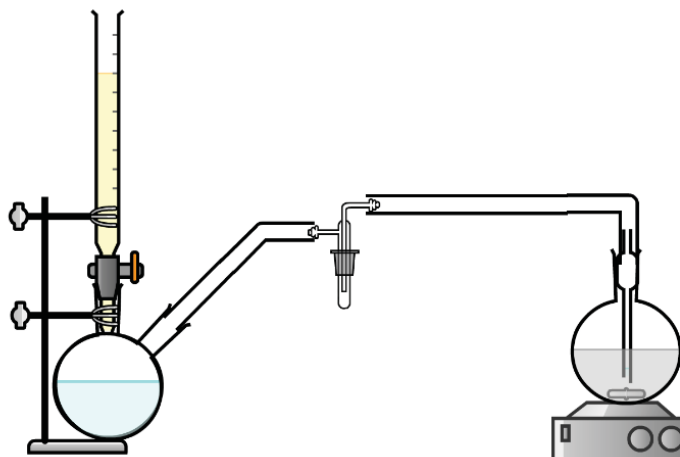
3.1.1.2 Synthesis of $\text{Ru}_3\text{O}(\text{CH}_3\text{CO}_2)_6\text{Py}_2\text{CH}_3\text{OH}$

A solution of $[\text{Ru}_3\text{O}(\text{CH}_3\text{CO}_2)_6\text{Py}_3]$ (0.6120 g, 0.6719 mmol) in a mixture with 24 mL of benzene and 8 mL of methanol contained in a round-bottom flask was bubbled with carbon monoxide for 6 hours. It was generated after dripping sulfuric acid contained in a two-necked round-bottom flask containing formic acid with the aid of a burette as is shown in the Figure 3-3. The CO generated replaced one pyridine ligand of the cluster, and the color of mixture was changing from olive-green to navy blue. The solvent in the mixture was removed by rotary evaporation until reach $\frac{3}{4}$ of initial volume and left at rest in the freezer by 2 hours. Then solid was recovered by filtration, washed with diethyl ether, and dried in desiccator with CaCl_2 , obtaining 0.2900 g (0.3373 mmol, 50% yield).

The obtained solid was suspended in 19 mL of DCM and bubbled with $\text{Cl}_{2(g)}$, generated from the reaction between KMnO_4 and HCl , to oxidize the triruthenium cluster allowing to replace the CO by solvent molecules which led the suspension to change from dark blue to green. The experimental set-up used for $\text{Cl}_{2(g)}$ bubbling was like the used for $\text{CO}_{(g)}$ bubbling. The suspension solvent was removed by rotary evaporation, then solid was resuspended in 14 mL of MeOH and heated under reflux for 30 minutes. Finally, 0.2290 g of NH_4PF_6 (1.4052 mmol) dissolved in 4 mL of CH_3OH was added, the mixture was left at rest overnight in the freezer. 0.2965 g of $[\text{Ru}_3\text{O}(\text{CH}_3\text{CO}_2)_6\text{Py}_2\text{CH}_3\text{OH}]^+\text{PF}_6^-$ (0.2939 mmol, 87% yield), which we

named MeOHRu, was recovered by filtration, washed with diethyl ether and dried in desiccator containing CaCl_2 .

FIGURE 3-3- DIAGRAM OF THE BUBBLING PROCESS



SOURCE: Author.

3.1.1.3 Synthesis of $[\text{Ru}_3\text{O}(\text{CH}_3\text{CO}_2)_6\text{Py}_2\text{NH}_2\text{Py}]^+\text{PF}_6^-$

$[\text{Ru}_3\text{O}(\text{CH}_3\text{CO}_2)_6\text{Py}_2\text{NH}_2\text{Py}]^+\text{PF}_6^-$ (NH_2Ru) was synthesized based on the synthesis procedure of similar compounds [23]. Briefly, MeOHRu (0.0662 g, 0.0656 mmol) and excess NH_2Py ligand dissolved in 21 mL of 6:1 DCM:MeOH solvent. The obtained mixture was stirred during 30 hours at room temperature in the dark, then 0.0340 g of NH_4PF_6 (0.2086 mmol) was added and the mixture was stirred for further 18 hours. After, 20 mL of diethyl ether was added, and the mixture was left at rest in the freezer for 24 hours. The solvent of the mixture was partly removed using a rotary evaporator without heat, and finally 0.0580 g of NH_2Ru (0.0542 mmol, 78% yield) was recovered by filtration, washed with diethyl ether, and dried in desiccator containing CaCl_2 .

3.1.1.4 Synthesis of $[\text{Ru}_3\text{O}(\text{CH}_3\text{CO}_2)_6\text{Py}_2\text{AzoPy}]^+\text{PF}_6^-$

$[\text{Ru}_3\text{O}(\text{CH}_3\text{CO}_2)_6\text{Py}_2\text{AzoPy}]^+\text{PF}_6^-$ was synthesized according to previous work [215]. Briefly, MeOHRu (0.0703 g, 0.0697 mmol) dissolved in 17 mL of DCM was mixed with ~3.8 times excess ligand 4-(4-dodecyloxyphenylazo) pyridine (0.0922, 0.2509 mmol) dissolved in 30 mL of DCM in a round bottom flask. The system was kept under reflux for 24 hours in the dark, after NH_4PF_6 (0.0338 g 0.2074 mmol) dissolved in 10 mL of ethanol was added and the mixture was maintained with constant reflux for further 1 hour. Then, the solvent of the mixture was removed by rotary evaporation. The solid product was purified by column chromatography, using α -cellulose column and a mixture of hexane with acetone (9:1 v/v) as

eluent. The eluent removes excess of ligand AzoPy and other impurities, so a descending yellow substance was observed. The remaining solid product was eluted with DCM and the solution was evaporated and the remaining solid was dried at desiccator with silica gel and CaCl_2 obtaining 0.0734 g of product (0.0546 mmol, 81% yield).

3.1.1.5 Synthesis of $[\text{Ru}_3\text{O}(\text{CH}_3\text{CO}_2)_6\text{Py}_2\text{SHPy}]^+\text{PF}_6^-$

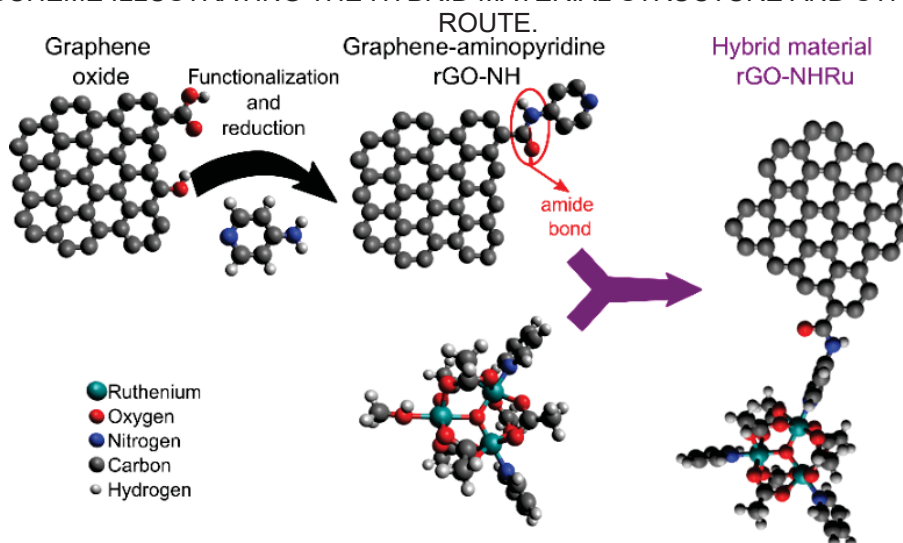
$[\text{Ru}_3\text{O}(\text{CH}_3\text{CO}_2)_6\text{Py}_2\text{SHPy}]^+\text{PF}_6^-$ was synthesized according to the synthesis procedure of similar compounds [228]. MeOHRu (0.0787 g, 0.0780 mmol) dissolved in 5 mL of DCM was mixed with excess ligand SHPy (0.0870 g, 0.7827 mmol) dissolved in 10 mL of MeOH in a round bottom flask. The mixture was stirred and maintained in an ice bath for 48 hours. After that, the mixture was filtered through celite to remove ligand excess, then the filtered was evaporated in a rotary evaporator without applying heat and filtered again through celite. After, hexane was added to the mixture and left at rest 15 minutes, it was observed the formation of two phases a yellow phase at the upper part and a dark green phase at the bottom, the yellow part was poured in a beaker. The procedure was repeated two times more, then the green phase was left at rest overnight. 0.0600 g of solid was recovered by filtration, washed with hexane and dried in desiccator containing CaCl_2 .

3.1.2 Synthesis of Graphene-Triruthenium Cluster Nanocomposite

Graphene-triruthenium cluster hybrid material was synthesized in three steps. First, graphene oxide was covalently functionalized with NH_2Py , after it was reduced and finally the triruthenium cluster was coordinated to functionalized reduced graphene oxide. Functionalization and reduction of graphene oxide was carried out by Grupo de Catálise e Cinética with a method similar to the described in [229–231]. Briefly, GO was obtained using a modified Hummers method [232]. Then, GO was functionalized using the couple agents EDC (2.85 g, 15 mmol) and NHS (1.7 g, 15 mmol) which were added to 50 mL of GO dispersion (0.05 mg mL^{-1}) and stirred in an ice bath for 2 hours. After removing the ice bath, NH_2Py (1.05 mmol) was added and stirred for 24 hours, so a solid was recovered by filtration and washed with distilled water. Some of the remaining oxygen groups of functionalized GO were removed reducing with NaBH_4 (480 mg) which was added to the solid dispersed in 25 mL of distilled water and stirred during 24 h at room temperature. The final solid was dried in an oven at 70°C and the sample was named rGO-NH. In this compound aminopyridine is bonded to graphene through amide bond between carboxyl groups in GO and amine group in NH_2Py as is shown in Figure 5-1.

After, the hybrid material was synthesized mixing 5 mL of rGO-NH dispersion (1 mg mL⁻¹) in distilled water and 5 mL of MeOHRu dispersion (4 mg mL⁻¹, 0.020 mmol) in methanol. The obtained mixture was stirred for 48 h. at room temperature. Then solid was recovered by successive centrifugation steps at 4000 RPM, the liquid phase was replaced by 8 mL of methanol upon each centrifugation step. Finally, the solid phase (rGO-NHRu) was isolated and dried at desiccator. The precursor MeOHRu was used since methanol is a labile ligand which can be replaced as ligand by pyridine groups anchored to graphene sheets, resulting in the linking of ruthenium center to pyridinic nitrogen as is shown in Figure 3-4.

FIGURE 3-4- SCHEME ILLUSTRATING THE HYBRID MATERIAL STRUCTURE AND SYNTHESIS



SOURCE: Author. Avogadro2 was used for drawing, Avogadro2 in version 1.91, (<https://www.openchemistry.org/projects/avogadro2/>). [233]

3.2 ELECTRODES AND SINGLE CELLS FABRICATION

Thin film electrodes were fabricated using drop-casting, dip coating and Langmuir-Blodgett technique with the materials synthesized. Drop-casting method was used to fabricate thin films of rGO-NHRu, rGO-NH and NH₂Ru. Langmuir-Blodgett technique was used to fabricate thin films of amphiphilic triruthenium complex AzoRu which can self-assemble in the water-air interface. Langmuir-Blodgett technique also was used to fabricate graphene oxide films, since GO also has amphiphilic character. It is composed of a largely hydrophobic basal plane with hydrophilic edges. So, it could mimic molecular surfactants, in fact, stable thin films of GO at water-air interface and toluene-water interface have been fabricated. In this case, organic solvent non soluble in water helps to “pick up” GO from its aqueous dispersion.

3.2.1 Drop casted films

A glassy carbon disc electrode with 0.3 cm of diameter (area 0.07 cm²) was cleaned rinsing it with abundant distilled water and drying with a fresh lab wipe. After the electrode was polished with carbon diamond suspension on a pad surface. Finally, the electrode was submerged on distilled water and gently shake to remove residual particles and dried at 70 °C for 15 minutes. After, rGO-NHRu, rGO-NH and NH₂Ru were drop casted on the glassy carbon disc electrode. For that, active material was suspended in distilled water (1 mg mL⁻¹) by ultrasonic bath for 25 min. Then, 5 μL of dispersion were deposited onto a glassy carbon disc previously cleaned and dried in an oven at 70 °C for 10 minutes, after 5 μL more were deposited and dried at 70 °C for 30 minutes.

3.2.2 Langmuir Blodgett films

The preparation of the LB films of GO was carried out based on the suggested in previous works [234,235], methanol was added to aqueous graphene oxide dispersion in order to obtain 1:4 H₂O:methanol ratio reaching ~0.08 mg mL⁻¹ GO dispersion. The films were prepared using a Nima Technology 311D trough system, 1.8 mL of GO dispersion was spread onto an ultrapure water subphase dropwise using a glass micro-syringe, so GO LB film was fabricated using Z-type deposition method, that used upward stroke at pressure of 10 or 20 mN m⁻¹ and a dipping speed of 5 mm min⁻¹ for GO.

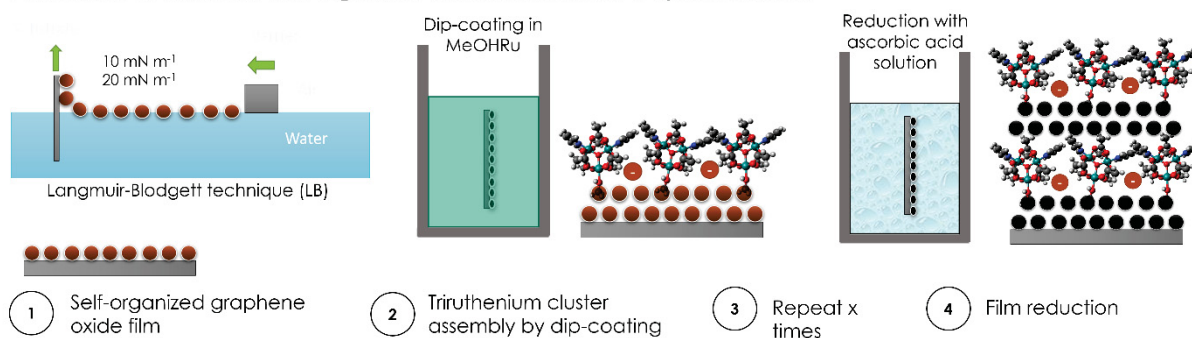
Whereas 50 μL of AzoRu (0.5 mg mL⁻¹) in DCM was spread on water surface, so the triruthenium cluster LB films were fabricated using a Y-type deposition method that involved the monolayer transfer during each immersion and emersion of the substrate at pressure of 23 mN m⁻¹ and a dipping speed of 10 mm min⁻¹. The deposition pressures were chosen considering the pressure-molecular area ($\Pi - A$) isotherms at ~25 °C and the dipping speeds were chosen based on the conditions reported on other works. [219,236]

The electrode containing the hybrid material was fabricated by the LB method to deposit the layers of graphene oxide and the dip-coating method to deposit the triruthenium cluster. As is shown in Figure 3-5 the film was grown in a layer-by-layer fashion, first one graphene oxide layer was deposited using the Langmuir-Blodgett technique and the film was dried at 65 °C for 3 minutes, then one triruthenium cluster layer was deposited by dip coating method immersing the film in a MeOHRu dispersion in methanol for 5 minutes, after the film is dried at 65 °C for 2 minutes, washed with water and dried at 65 °C for 3 minutes. It is expected the triruthenium cluster coordinate with oxygen groups swapping the methanol ligand to obtain the hybrid LB film. The process is repeated to grow the film depositing the desired number of layers.

Finally, the films were reduced immersing it in an aqueous solution of ascorbic acid (2 mg mL^{-1}) at 90°C during 75 minutes obtaining rGO and rGORu LB films. Ascorbic acid is a mild and environmental friendly reductant that could match hydrazine efficiency for graphene oxide reduction. [237,238] The materials were deposited on different substrates such as tin-doped indium oxide (ITO), quartz, gold or silicon to conduct different characterizations of the films. The substrates were previously cleaned with alternated washings of DCM and isopropanol, and finally treated with isopropanol to create hydrophilic sites at the surface.

FIGURE 3-5- SCHEME ILLUSTRATING THE FABRICATION OF THIN FILM ELECTRODES BASED ON GRAPHENE AND TRIRUTHENIUM CLUSTER.

Fabrication of electrode with organized structure based on a hybrid material



SOURCE: Author.

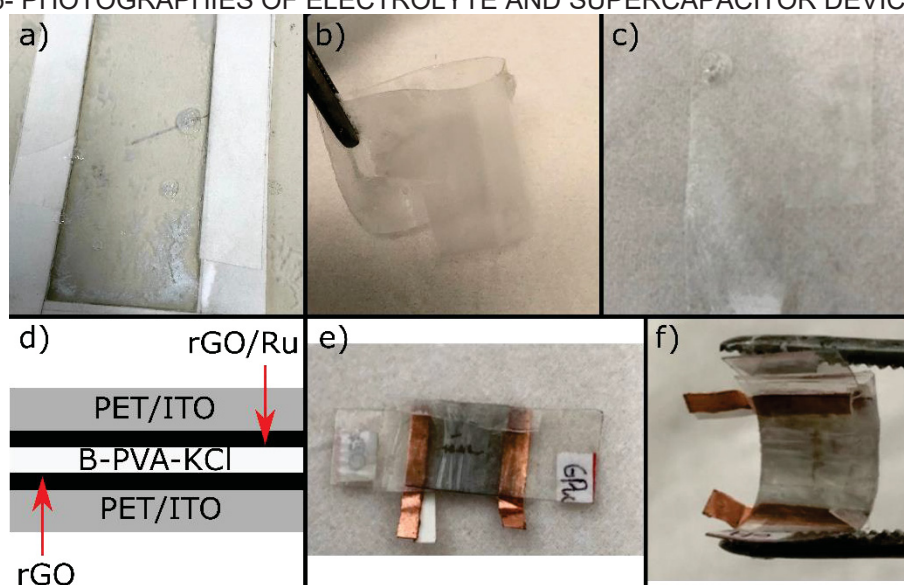
3.2.3 Single cell fabrication

The asymmetric flexible all-solid-state supercapacitors were assembled in a sandwich-type style. ITO coated Polyethylene terephthalate (PET) film was used as substrate for the fabrication of LB films of rGO and rGORu with 12 ML and AzoRu with 18 ML. The approximated dimension of the region with deposited material was $0.8 \times 0.8 \text{ cm}$. The number of layers were chosen so the charge stored in each electrode were similar, as recommended for the construction of supercapacitors ($q_+ = q_-$). [70,239,240] According to previous results that is expected that the stored charge ranges between 0.32 and 0.38 mC cm^{-2} . "acid boric crosslinked" PVA-KCl gel (B-PVA-KCl) was used as electrolyte, the as prepared B-PVA-KCl film was placed between the electrodes and wetted with a water drop, after verifying that the film was completely wetted and retained its mechanical integrity the two electrodes were sandwiched together face to face with care to avoid direct electrical contact between electrodes as illustrated in the scheme of Figure 3-6d. The assembly was wrapped with parafilm and held together with a paper clip during the experiments. Some photos of the single cell device are shown in Figure 3-6e and f.

B-PVA-KCl electrolytes were prepared according to procedures found on literature. [241–243] 0.5 g of PVA was dispersed on 10 mL of distilled water and the mixture was stirred for 20 minutes and kept at 60°C . 0.12 g of KCl and 0.03 g of H_3BO_3 were dissolved in 1.5 mL

and added dropwise on the PVA dispersion and stirred for further 15 minutes at 60°C. Heater was turned off and the stirring was maintained for 10 minutes. Care should be taken with the stirring and solvent evaporation to avoid bubble formation during gelification. The gel obtained was used to fabricate films with blade casting technique. A drop of B-PVA-KCl was poured on a cleaned glass surface with adhesive tape as guides, with a blade the drop was spread on the surface delimited with the adhesive tape as shown in Figure 3-6a. The gel was dried overnight at room temperature obtaining a thin flexible electrolyte easy to handle as shown in Figure 3-6b and c. A piece of B-PVA-KCl film with the required dimensions (it was a little bigger than electrode dimensions) were cut just before of device assembly and wetted to restore their binder and conductive properties. Care may be taken with the handling and wetting of the film, since film tends to roll up on itself and too much water can damage the film.

FIGURE 3-6- PHOTOGRAPHIES OF ELECTROLYTE AND SUPERCAPACITOR DEVICES.



Photographs of a) fresh B-PVA-KCl electrolyte film b) and c) dry and bended B-PVA-KCl electrolyte film. d) scheme of the single device showing electrical contacts. Photographs of e) single cell device and f) the same device bended.

SOURCE: Author.

3.3 MATERIALS AND ELECTRODES CHARACTERIZATION

3.3.1 Structural characterization

Elemental analysis of triruthenium clusters was performed in a 2400 CHN Series II Elemental Analyzer from Perkin-Elmer-USA at the analytical center of the Institute of Chemistry at Universidade de Sao Paulo. Mass spectra of triruthenium cluster were recorded using a Thermo Scientific LTQ XL linear ion trap mass spectrometer using electro spray ionization (ESI-MS). Hydrogen-1 nuclear magnetic resonance spectroscopy ($^1\text{H-NMR}$) of triruthenium cluster was performed using a Bruker DPX 200 MHz (4.7 tesla) spectrometer and

deuterated chloroform or methanol with tetramethylsilane as solvents. Fourier-transform infrared spectroscopy (FTIR) of ruthenium complexes, graphene and hybrid materials were acquired in the range from 4000 to 400 cm^{-1} with 4 cm^{-1} of resolution using the FTIR Bruker Vertex 70 spectrophotometer and the materials prepared as powders dispersed in KBr pellets. The spectra of LB films were acquired from 4000 to 600 cm^{-1} with 8 cm^{-1} of resolution using the same spectrophotometer and the Bruker A518 accessory for grazing incidence at 80° and a polarization accessory. Ultraviolet-visible spectra of ruthenium complexes dispersed in DCM, graphene and hybrid materials dispersed in water and LB films on quartz were obtained from 190 to 1100 nm using the UV-vis HP Agilent 8453 spectrophotometer and a quartz cuvette with 1 cm of pathlength. The values of extinction coefficient (ϵ) of ruthenium complexes were calculated using the Beer-Lambert law, five spectra acquired consecutively with different concentrations and ϵ was obtained as the slope of absorbance vs. concentration curve.

Raman spectra of drop-casted thin films, and AzoRu LB film were obtained in a Witec alpha300 R confocal Raman imaging system using a 633 nm excitation laser, the laser beam was focused on the sample using objective magnification 100× in three different points. The morphology and distribution of Ru in the drop casted electrode with graphene and the hybrid material was studied with SEM and EDS, which were performed in a TESCAN VEGA 3 SEM system. It was used 12 kV voltage to obtain the SEM images, and 30 kV voltage and an Oxford accessory to obtain EDS spectra. The samples were prepared by drop casting on Cu adhesive tape (same as described in section 3.2). Raman and SEM techniques were carried out at CME – Centro de Microscopia Eletrônica at UFPR. X-ray diffraction (XRD) measurements of thin films were recorded at x-ray diffraction laboratory of chemistry department-UFPR on a Shimadzu XRD-6000 diffractometer using Cu-K α radiation (1.5418 Å), in glancing angle mode at 40 kV and 30 mA with a step of 0.02° and scanning during 5 s per point on aluminum substrate.

X-ray photoelectron spectroscopy (XPS) measurements of functionalized graphene and hybrid material powder samples were performed at physics department of Universidade do Estado de Santa Catarina on a K-Alpha ThermoScientific system using Al K α radiation and an X-ray spot of 300 μm . Measurements in three different points were performed in each sample to check uniformity, and a flood gun was used to avoid charging of the sample. Survey spectra were obtained in the range 0.0–1350.00 eV with an energy step size of 1.00 eV and a pass energy of 200.00 eV, and high-resolution spectra of the N 1s (392.00–410.00 eV) region were acquired with an energy step of 0.10 eV and a pass energy of 50.00 eV. All spectra were charge-corrected to the C 1s main peak at 284.8 eV. The N1s peaks were fitted with Gaussian functions and a least square algorithm, and the fittings were acceptable, as indicated by the determination coefficients of 0.984 and 0.970 for rGO-NHRu and rGO-NH respectively.

3.3.2 Electrochemical characterization

Cyclic voltammetry (CV) was performed for solution of triruthenium clusters dissolved in acetonitrile with concentration 0.001 mol L^{-1} and tetrabutylammonium perchlorate 0.100 mol L^{-1} . It was used a platinum disc with 3 mm diameter as working electrode, a platinum wire as counter-electrode and Ag/Ag⁺ reference electrode prepared with an Ag wire and AgNO₃ 0.01 mol L^{-1} in acetonitrile. The acetonitrile used in these experiments was treated with calcium hydride and distilled in presence of calcium hydride just before use. The potential values were converted to SHE based on “internal reference redox system” which is assumed to be independent of the solvent as is explained in [244]. Additional measurements were performed in narrower regions to explore the different redox peaks.

Electrochemical impedance spectroscopy (EIS), CV and charge discharge (CD) measurements of the fabricated electrodes were carried out using a potentiostat/Galvanostat Ivium Compactstat and a three-electrode cell. It was used a platinum wire as counter-electrode, Ag/AgCl electrode prepared with Ag wire and NaCl 3 mol L^{-1} in water as reference electrode and the thin films electrodes as working electrodes. An aqueous solution of KCl 0.5 mol L^{-1} was used as supporting electrolyte. All samples were cycled for at least 20 CV cycles to check stability prior to performance test, and the test was replicated in new electrodes. 3 CV and CD cycles were performed at different scan rates (ν) or charging/discharging currents respectively, the scan rates and charge/discharge currents were chosen in order to test discharge times from 1-5 s to 90-120 s. EIS was carried out at frequency range from 10^{-2} to 10^5 Hz at chosen fixed potential and potential amplitude of 0.01 V.

3.4 ESTIMATION OF ENERGY STORAGE PROPERTIES

3.4.1 Cyclic Voltammetry

It provides information about:

Voltage window, Electrolyte degradation or electrode oxidation usually restricts the voltage window. CV allows to measure the voltage window by testing different voltage limits and observing that is obtained a signal without including any undesired irreversible reactions.[245]

Capacity, the dominating process in the electrode (or device) determine the shape of the voltammogram obtained, a typical squared voltammogram is usually obtained for capacitive electrodes, whereas peaks and increasing currents is obtained for electrodes with redox processes. Some materials with charge transfer processes present a roughly squared voltammogram, these materials are pseudocapacitive. [245] The specific charge stored q is calculated from cyclic voltammetry integrating the area below the curve:

$$q = \int_{E_1}^{E_2} \frac{I}{m\nu} dE \quad 3.1$$

With m the electrode mass or area, since it is recommended to present the values obtained as specific quantities. q is obtained in coulombs by mass or area unit, the quantity can be expressed in mAh dividing by 3.6 (1mAh = 3.6 C). Additionally, a common procedure is to suppose that the charge stored during anodic and cathodic sweep is similar, so calculate the area enclosed by the cyclic voltammogram and divide the obtained value by two. The specific capacitance C_s can be calculated for capacitive materials as:

$$C_s = \frac{q}{E_2 - E_1} \quad 3.2$$

Kinetics, when redox peaks are present, it can be analyzed parameters as the difference between cathodic (E_{pc}) and anodic (E_{pa}) redox peak potentials ΔE_p , ratio between current peaks and current peaks dependence on ν . The last parameter allows to determine if the reversible redox process is diffusion controlled, verifying the i dependence on $\nu^{1/2}$. For hybrid energy storage materials, it is useful to analyze the i dependence on ν assuming a power-law relationship. $i = a\nu^b$. The b value is calculated as the slope from a linear fit of $\text{Log}(i)$ vs. $\text{Log}(\nu)$ data. i is calculated as the sum of the anodic and cathodic current peaks or at specified potential. Electrode is dominated by capacitive/surface processes when b is close to 1, and by diffusion processes when b is close to 0.5. [55,97]

Trassati et al. [94] proposed to analyze the pseudocapacitive energy storage process by dividing the charge storage capacity in two contributions, one associated to the more accessible sites (q_o) and other to the less accessible sites (q_i) which depends on diffusion and is proportional to $\nu^{-1/2}$.

$$q_T = q_o + q_i \quad 3.3$$

Diffusion controlled current contributing to q_i is $i = k\nu^{1/2}$ so:

$$q_{inner} = \int_{E_1}^{E_2} \frac{k\nu^{1/2}}{\nu} dE = a\nu^{-1/2} \quad 3.4$$

Consequently,

$$q_T = q_o + a\nu^{-1/2} \quad 3.5$$

A plot of q vs. $\nu^{-1/2}$ allows us to estimate the q_o as the intercept of the fitting to the linear plot of q vs. $\nu^{-1/2}$ data. Note that q_o is the value of q when $a\nu^{-1/2} = 0$, that is, when $\nu \approx \infty$. Care must be taken since not ever q vs $\nu^{-1/2}$ provides a linear plot for all values of $\nu^{-1/2}$ as pointed out by Shao et al. [246] In this case, it should be considered the linear region that includes the high scan rates of interest. q increases with ν decreasing, at the limit when $\nu = 0$, all the possible charge is stored (q_T). So, extrapolating to $\nu = 0$ an appropriate function

of q on v , q_T can be estimated. From the last equation is expected that $1/q \propto v^{1/2}$, so it is proposed:

$$1/q = 1/q_T + cv^{1/2} \quad 3.6$$

$1/q_T$ corresponds to the intercept calculated from the linear fit of q Vs. $v^{1/2}$ data. Note that $1/q_T \neq 1/q_o$. Finally, it is possible to calculate q_i subtracting q_o to q_T .

$$q_i = q_T - q_o \quad 3.7$$

A related analysis [14,95,96] proposed to divide the total current obtained at determined potential value in two contributions:

$$i(V) = k_D v^{1/2} + k_C v \quad 3.8$$

According to this model a plot of $i/v^{1/2}$ vs. $v^{1/2}$ should be linear and provides estimations of k_D and k_C . These values calculated in all the potential range allowed us to quantify the total contribution of diffusion limited and capacitive processes, the i_C contribution to the total current can be defined as:

$$\%i_C = k_C v / (k_D v^{1/2} + k_C v) \quad 3.9$$

3.4.2 Charge-discharge measurements

It provides information about:

Capacity, the shape of charge discharge curves indicates the dominating process in the electrode. A linear shape is characteristic of capacitive processes whereas curved features is characteristic of faradaic processes. Electrodes with redox processes exhibit a potential almost constant during charging/discharging when redox process occurs, then it changes abruptly when electrode is charged/ discharged. [245] Specific charge stored in an electrode with mass/area m can be calculated from discharge part of CD curve as:

$$q = \frac{I\Delta t}{m} \quad 3.10$$

The specific charge stored is expressed in mAh units dividing q by 3.6 ($1C = 3.6 mAh$). The specific capacitance C_s of materials with linear discharge curve, can be calculate as:

$$C_s = \frac{q}{E} = \frac{I\Delta t}{m\Delta E} \quad 3.11$$

Cyclability, Cycles of charge discharge are repeated several times (usually 4000 cycles or more) using a determined charge/discharge current, the capacity variation with each cycle is monitored.

3.4.3 Electrochemical Impedance Spectroscopy (EIS)

EIS is a powerful analytical technique which allows covering a large timescale (various frequency regimes). Electrochemical processes have different characteristic time constant, so the electrochemical response in determined frequencies regimes is dominated by some processes according to their characteristic time constant. Therefore, the contribution of different processes could be inferred with EIS. Moreover, it is performed on systems at stationary state using small sinusoidal perturbations, that is, a signal with a bias potential/current and small amplitude is applied at several frequencies after to stabilize the system. So, a usual electrical analysis can be performed and presented as indicated below.

Nyquist and Bode plots, The results are commonly presented with Nyquist and Bode plots. The Nyquist plot presents the imaginary impedance (Z'') vs. the real impedance (Z'), whereas the Bode plot presents the impedance modulus vs. frequency and phase vs. frequency. The plots help in the qualitative discussion regarding the frequency response of the system since they allow to identify processes with different time scale dominating the cell response and the characteristic time constants for the transitions between the processes.

Equivalent Circuit, the results can be analyzed using an analogous electrical circuit behaving like the studied electrochemical cell to understand processes occurring at the system. The experimental data are fitted to the circuit model, so one could get reasonably good fittings with many equivalent circuits. For that reason, this modeling tool should be used with care to maintain a reasonable relationship between equivalent circuit and the electrochemistry of the system. One should use appropriate equivalent circuit models for extracting associated resistive, charge transfer, diffusive, and capacitive parameters for a given electrochemical cell. In this work EIS results were fitted to a simple equivalent circuit model consisting in a Randles circuit in series with a constant phase element, and the EIS Spectrum Analyser software was used to find the better parameter values.[247]

Complex capacitance, another way to analyze impedance data is to calculate the complex capacitance $C(\omega)$. It was calculated assuming that the impedance measured in the system is completely attributed to an unique capacitive element so $Z(\omega)$ can be expressed in terms of the impedance $z(\omega)$ as in equation 3.12 [248,249]:

$$Z(\omega) = Z'(\omega) + jZ''(\omega) = \frac{1}{j\omega C(\omega)} \quad 3.12$$

So $C(\omega)$ is expressed as in equation 3.13

$$C(\omega) = \frac{1}{\omega(jZ'(\omega) - Z''(\omega))} = \frac{-Z''(\omega)}{\omega|z(\omega)|^2} - j \frac{Z'(\omega)}{\omega|z(\omega)|^2} = C'(\omega) - jC''(\omega) \quad 3.13$$

$C'(\omega)$ and $C''(\omega)$ are the real and imaginary part of the capacitance from equation 3.13 we can define those terms as follows:

$$C'(\omega) = \frac{-Z''(\omega)}{\omega|Z(\omega)|^2} \quad 3.14$$

$$C''(\omega) = \frac{Z'(\omega)}{\omega|Z(\omega)|^2} \quad 3.15$$

$C'(\omega)$ at low frequencies gives the capacitance value of the whole system which should be comparable with the obtained with galvanostatic measurements. Whereas $C''(\omega)$ could be related with energy dissipation [248,249], also, the maxima in the $C''(\omega)$ plot points out the critical frequencies at which the impedance associated to capacitive and resistive processes are comparable. So, this characteristic frequency indicates the system transition from a behavior mostly resistive at high frequencies to one mostly capacitive at low frequencies because of the reaching of the electrolyte full access in the electrode. Also, it is the frequency of the median charge storage and can be defined as a merit factor, as higher the frequency, more suitable the electrode is for high-power applications.

3.5 SOFTWARE

Density functional theory (DFT) calculations were performed with Orca version 4 [250] using the Ahlrichs split valence basis set (def2-SVP) [251] and the triple zeta valence basis set (def2-TZVP) for ruthenium atom [251]. The spin-unrestricted wave function for the open-shell structures, effective core potentials for Ru atoms [252], the RI-J approximation for Coulomb integrals [253] and COSX approximation for the Hartree-Fock exchange integration step, and Grimme's DFT-D3 dispersion correction [254] was used. The BP86 functional was used for a first geometry optimization and so the PBE0 [255] hybrid functional was used to further geometry optimization step, frequency calculations, single-point energy calculation and simplified time-dependent DFT (sTD-DFT). Additionally, a larger integration grid was used for single-point energy calculation and sTD-DFT for higher accuracy in derived properties. The orca_asa program [256] was used for the quantum-assisted simulation of resonance Raman intensities, which proceeds via normal mode vibration scan and use the independent mode, displaced harmonic oscillator model for the prediction of resonance Raman intensities.

Besides, the set of equations that constitutes the model for electrochemical behavior simulation and some further analysis of datasets requiring data fitting was performed with MATLAB, the codes are made available as [appendix](#). Whereas graphics and further data analysis of experimental data were prepared with Origin 8 software. Graphics with 2D representations of molecules were prepared using marvinsketch, whereas the 3D representations of molecules were prepared using visual molecular dynamics or Avogadro and Inkscape.

4 TRIRUTHENIUM CLUSTERS PROPERTIES

Triruthenium acetate clusters, $\text{Ru}_3\text{O}(\text{CH}_3\text{CO}_2)_6\text{Py}_2\text{AzoPy}$, $\text{Ru}_3\text{O}(\text{CH}_3\text{CO}_2)_6\text{Py}_2\text{NH}_2\text{Py}$ and $\text{Ru}_3\text{O}(\text{CH}_3\text{CO}_2)_6\text{Py}_2\text{SHPy}$ were synthesized. The reacting mixture change its color respect to precursors, and it was separated to isolate the compound of interest. As it is shown in next sections, the structural characterization indicates its formation.

4.1 STRUCTURE AND CHEMISTRY OF TRIRUTHENIUM CLUSTERS

AzoRu was successfully synthesized as suggested by the structural characterization. The mass spectra of AzoRu obtained with the electrospray ionization in positive mode revealed a positive ion with $m/z = 1199.60$ which is the mass expected for $[\text{Ru}_3\text{O}(\text{CH}_3\text{CO}_2)_6\text{Py}_2\text{AzoPy}]^+$ (see Figure A-1 in Appendix A), also were observed low intensity peaks at $m/z = 1120.71$ and $m/z = 832.60$ which were attributed to the cluster without a pyridine ligand ($[\text{Ru}_3\text{O}(\text{CH}_3\text{CO}_2)_6\text{PyAzoPy}]^+$) and AzoPy dissociated ($[\text{Ru}_3\text{O}(\text{CH}_3\text{CO}_2)_6\text{Py}_2]^+$) respectively. Also, a composition of 41.12%C, 4.27%H and 5.41%N was found with the elemental analysis which are close enough to the theoretical composition as indicated by the relative errors below 6.56%.

The NH_2Ru ESI-MS in the positive mode revealed a cation with $m/z = 926.53$ which is the mass expected for $[\text{Ru}_3\text{O}(\text{CH}_3\text{CO}_2)_6\text{Py}_2\text{NH}_2\text{Py}]^+$ (see Figure A-2 in Appendix C). This cation can be broken into a cation with $m/z = 846.56$ attributed to the triruthenium cluster with a Py dissociated (Figure A-3). This molecule can be subsequently broken mainly into a cation with $m/z = 767.58$ attributed to the dissociation of the other Py ligand, and cations with $m/z = 531.78$ and 437.81 (Figure A-3) attributed to the loss of 4 acetate ligands in addition to the Py ligand and the further loss of NH_2Py ligand respectively. A composition of 29.71%C, 3.02%H and 5.56%N was found with the elemental analysis which are close enough to the theoretical composition as indicated by the relative errors below 6.36% suggesting the successful synthesis of the desired compound.

The $^1\text{H-NMR}$ of AzoRu in deuterated chloroform (CDCl_3) (Figure A-5) exhibited a wide peak from 1.231 to 1.454 parts per million (ppm) attributed to the hydrogens in CH_2 part of dodecyl chain of AzoPy which should have similar chemical environment. Furthermore, considerably large peaks were observed at 4.873 and 4.989 ppm attributed to hydrogens of the acetates indicating two different chemical environments for the acetates, one between AzoPy and Py ligands and other between two Py groups. Also, it was noted that the chemical shift of hydrogens in pyridine groups were significantly lower than in free pyridine molecules, particularly those closer to Ru_3O core (shift from 8.78 to 0.72 ppm for AzoPy ligand and from 8.54 to -0.124 ppm for Py). It indicates that the chemical environment is more shielded for the

ligands in the complex. Interestingly, this shift to lower ppm is observed for paramagnetic complexes with charge +1, which is consistent with magnetic interactions between the acetate and the unpaired spin density localized within the Ru₃O core. [23]

Similarly, the ¹H-NMR of NH₂Ru in CDCl₃ solvent with 18 μL of deuterated dimethyl sulfoxide (CD₃)₂SO (Figure A-6) exhibited considerably large peaks at 4.333 and 4.129 ppm attributed to hydrogens of methyl group in acetates which have two different chemical environments. Also, the chemical shift of hydrogens in pyridinic groups of the complex were lower than in the free ligands, particularly those closer to Ru₃O core (shift from 7.987 to 0.934 ppm for NH₂Py ligand and from 8.54 to -0.178 ppm for Py), due to the interaction of the ligands with the unpaired electron within the Ru₃O core. Summarizing, the results suggest that AzoRu and NH₂Ru were formed as indicated by the two peaks for acetate (characteristic of asymmetric clusters), and the shifting of the ligand peaks to lower ppm respect to free ligands.

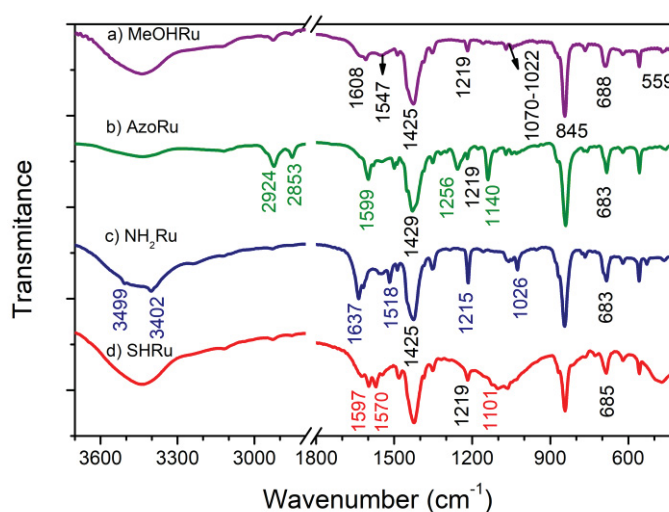
The SHRu ESI-MS in positive mode revealed several peaks (Figure A-4), the most intense corresponds to a positive ion with m/z = 941.50, which is the mass expected for [Ru₃O(CH₃CO₂)₆Py₂SHPy]⁺ with SHPy ligand deprotonated. Also, a less intense peak is observed at 974.40 which was attributed to the same cation associated to a methanol molecule respectively. Other intense peaks are observed at 832.59 and 753.62, the former was attributed to the cation with the SHPy ligand dissociated and the last may results from the further dissociation of Py ligand. Both peaks are close to peaks with lower intensity at 862.53 and 785.50 respectively which may result from the mentioned fragments but associated to a methanol molecule. The peaks at 1051.39 and 1081.34 were attributed to the triruthenium cluster with 4-4'-Dipyridyl disulfide (DPyDS) instead of SHPy and the same compound but associated to a methanol molecule respectively.

The ¹H-NMR of Ru₃O(CH₃CO₂)₆Py₂SHPy in methanol CD₃OD solvent is depicted in Figure A-7. It was observed three large peaks at 0, 3.304 and 4.915 ppm corresponding to the reference compound TMS, CD₃OD and water respectively. Also, the considerably large peaks at 4.443 and 4.601 pp, were attributed to hydrogens of methyl group in acetate, the two peaks indicate two different chemical environments for acetate groups, one between SHPy and Py ligands and the other between two Py groups as it is pointed out in the structure embedded. The other peaks were assigned considering the spectra of SHPy and Py ligand. In general, the peaks in cluster spectrum are shifted to lower values with respect to free ligands spectra, indicating that these hydrogens have higher electronic shielding in the clusters. The peaks in SHPy shifts from 7.65 and 7.45 to 7.58 and 7.16 ppm respectively. Also, it is noted that the shifting of peak attributed to free ligands is larger for hydrogen closer to Ru center, indicating that the chemical environment change is more significant close to Ru center. For example, the hydrogens closer to Ru in Py suffer a high shifting from 8.54 to 0.22 ppm.

Also, it was observed peaks located from 8.25 to 8.42 ppm, similar peaks were found at 8.54 ppm in the $^1\text{H-NMR}$ spectrum of SHPy with a lower intensity than the peaks attributed to SHPy. They were attributed to the presence of DPyDS since it is reported a peak in 8.55 and 7.25 ppm for DPyDS in CDCl_3 .^[257] The presence of this compound sounds reasonable since it can be formed through interaction between sulfurs in thiol group to form disulfide. So, the peaks were attributed to DPyDS coordinated to Ru cluster. The other peak of DPyDS probably was overlapped with peak of SHPy at 7.17 ppm.

The FTIR spectra of triruthenium clusters are shown in Figure 4-1, MeOHRu (a), AzoRu (b), NH_2Ru (c), and SHRu (d). Bands common to all complexes are indicated with black labels and the characteristic bands of each complex are indicated with colored labels. Bands were assigned according to literature^[258] and DFT calculations, the detailed assignation can be seen in the [Appendix A](#). The band at 846 and 562 cm^{-1} observed in the spectra of cationic compounds were attributed to PF_6^- counterion. The characteristic large band at $\sim 1425\text{ cm}^{-1}$ present in all spectra was attributed to δCH_3 , $\nu\text{C-C}$ in acetate groups, and δCH accompanied by collective ring vibrations in Py ligands. According to DFT calculations, δCH_3 is located at $\sim 1400\text{ cm}^{-1}$, $\nu\text{C-C}$ in acetate groups at $\sim 1425\text{ cm}^{-1}$ and ring stretching in Py ligand is located between 1450 and 1470 cm^{-1} . Furthermore, the ring stretching in pyridyl and phenyl groups of AzoPy are located between 1443 and 1490 cm^{-1} , these vibrations have a relatively high contribution respect to the other vibrations in the same region, which could explain the band shifting to 1429 cm^{-1} and the wider band in AzoRu spectra (Figure 4-1b) respect to the other complexes.

FIGURE 4-1 - IR SPECTRA OF SYNTHESIZED TRIRUTHENIUM CLUSTERS



a) precursor of $[\text{Ru}_3\text{O}(\text{CH}_3\text{CO}_2)_6\text{Py}_2\text{MeOH}]\text{PF}_6$ (purple), b) $[\text{Ru}_3\text{O}(\text{CH}_3\text{CO}_2)_6\text{Py}_2\text{AzoPy}]\text{PF}_6$ (green), c) $[\text{Ru}_3\text{O}(\text{CH}_3\text{CO}_2)_6\text{Py}_2\text{NH}_2\text{Py}]\text{PF}_6$ (blue) and d) $[\text{Ru}_3\text{O}(\text{CH}_3\text{CO}_2)_6\text{Py}_2\text{SHPy}]\text{PF}_6$ (red). Spectra of samples prepared as KBr pellets were recorded in transmittance mode.

SOURCE: Author.

The band around to 1600 cm^{-1} observed in all the complexes corresponds to symmetric ring stretching in pyridinic ligands, this band is slightly modified in the other complexes due to other close vibrations in the NH_2Py , AzoPy or SHPy ligands. Some other vibrations in pyridinic ligands also contribute to other bands observed in the spectra, for example the pyridine ring stretching contributes to the band at 1547 cm^{-1} which also have contributions of $\nu\text{C-O}$ in carboxylate. The $\gamma\text{-CH}$ vibration mode of pyridines contributes to the band at 683 cm^{-1} which is mainly attributed to $\nu\text{Ru-O}$ in the Ru_3O core, δCH in pyridinic ligands contributes to the band at 1219 cm^{-1} as well as the band located between 1022 and 1070 cm^{-1} which also have contributions of the ring breathing vibration mode of pyridinic ligands.

Besides, the AzoRu spectrum (Figure 4-1b) exhibited two peaks in 2939 and 2865 cm^{-1} which are attributed to $\nu\text{C-H}$ in methyl and methylene groups of the long chain of AzoPy ligand. Whereas peaks in 1261 and 1157 cm^{-1} are attributed to $\nu\text{C-O-C}$ in phenyl-ether group, δCH in Py and τCH_2 vibrations. The NH_2Ru spectrum (Figure 4-1c) showed two peaks in 3498 and 3393 cm^{-1} which were attributed to $\nu\text{N-H}$ and a peak in 1636 cm^{-1} corresponding to δNH_2 bending in NH_2Py . Besides, the peak in 1215 cm^{-1} has contributions of δCH in NH_2Py in addition to the δCH in Py . The SHRu spectrum (Figure 4-1d) exhibited peaks at 1597 , 1570 and 1102 cm^{-1} attributed to ring deformation in SHPy and DPyDS , and $\nu\text{C-S}$ in SHPy respectively.

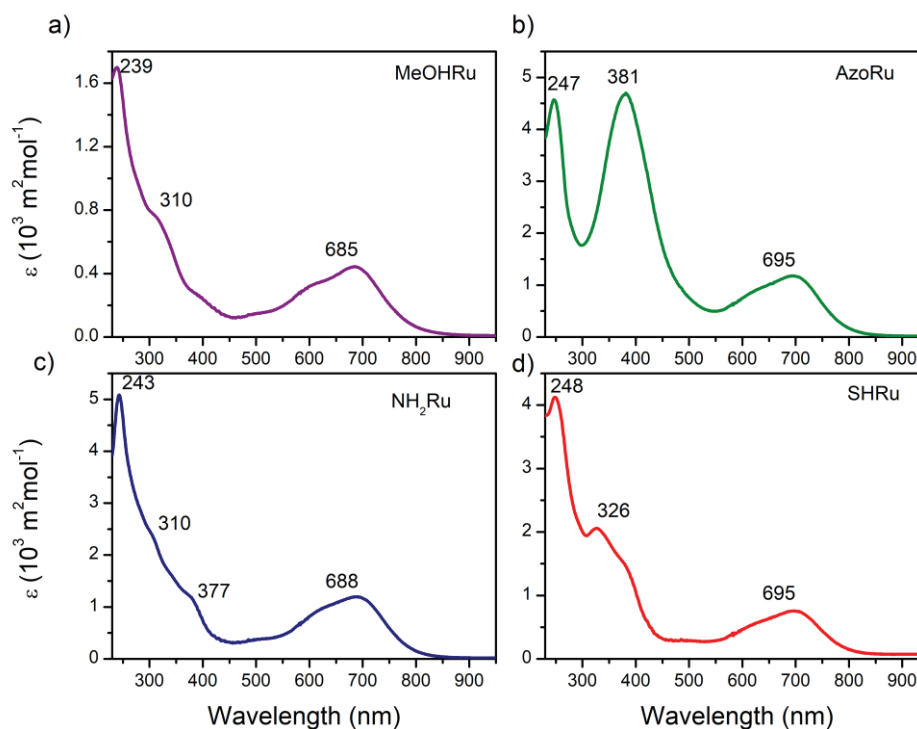
4.2 ELECTRONIC PROPERTIES OF RUTHENIUM CLUSTERS

Spectroscopy in the UV and visible region of the different complexes solution in DCM was performed. The spectra showed composite absorption bands, which must be originated from a series of closely spaced molecular electronic transitions. All the spectra, depicted in Figure 4-2, showed a wide band extended between 800 and 550 nm , which is a characteristic band of triruthenium clusters with charge $+1$. [23] This band was ascribed to several intra-cluster transitions (IC) in the Ru_3O core, the maximum extinction coefficient value was observed at $\lambda_{max} = 685\text{ nm}$ for MeOHRu , 688 nm for NH_2Ru , and 695 nm for AzoRu and SHRu as is indicated with the corresponding labels in the Figure 4-2. The little differences in λ_{max} confirms that the influence of the ligands in this band is small since those electronic transition involves mainly d-orbitals in triruthenium clusters. The spectra also exhibited a band in the high energy region with maximum in 239 nm for MeOHRu , 243 nm for NH_2Ru , 247 nm for AzoRu and 248 nm for SHRu , this band was attributed to intraligand (IL) electronic transitions involving pyridine groups of ligands, including $\pi \rightarrow \pi^*$ transition.

MeOHRu and NH_2Ru spectra (Figure 4-2a and c) lack of evident band in the region from 500 to 300 nm , but the absorption increased in this region and showed some shoulders attributed to the sum up of several closely spaced electronic transitions involving metal ligand

charge transfer (MLCT). In contrast, AzoRu (Figure 4-2b) exhibited a large band with λ_{max} at 381 nm, similar to the obtained in previous work for the same compound [215,219]. As it was proposed in that work, the band in 381 nm is associated with intra-ligand transitions (IL) and MLCT. DFT calculations revealed that from 489 to 390 nm the excited states are composed for electronic transitions involving MLCT from Ru₃O core to Py ligand. Also, the transition with the largest oscillator strength is located at 359 nm and arises from IL transition from phenylazo group to π^* orbitals in the ligand. Additionally, we found that from 330 to 310 nm the excited states involved the IL transition from phenyl group to π^* orbitals and MLCT from Ru₃O core to Py ligands. SHRu (Figure 4-2d) also exhibited a band with a defined maximum at 326 nm, this band is ascribed to IL and MLCT transitions. MLCT probably occurs around 400 nm, as was suggested in previous work[23], and the IL transition in SHPy probably occurs close to 326 nm, since the UV-vis of SHPy exhibit a band with λ_{max} at 338 nm.

FIGURE 4-2 – UV-VIS SPECTRA OF TRIRUTHENIUM CLUSTERS DISPERSED IN DICHLOROMETHANE



a) [Ru₃O(CH₃CO₂)₆Py₂MeOH]PF₆ (purple), b) [Ru₃O(CH₃CO₂)₆Py₂AzoPy]PF₆ (green), c) [Ru₃O(CH₃CO₂)₆Py₂NH₂Py]PF₆ (blue) and d) [Ru₃O(CH₃CO₂)₆Py₂SHPy]PF₆ (red).

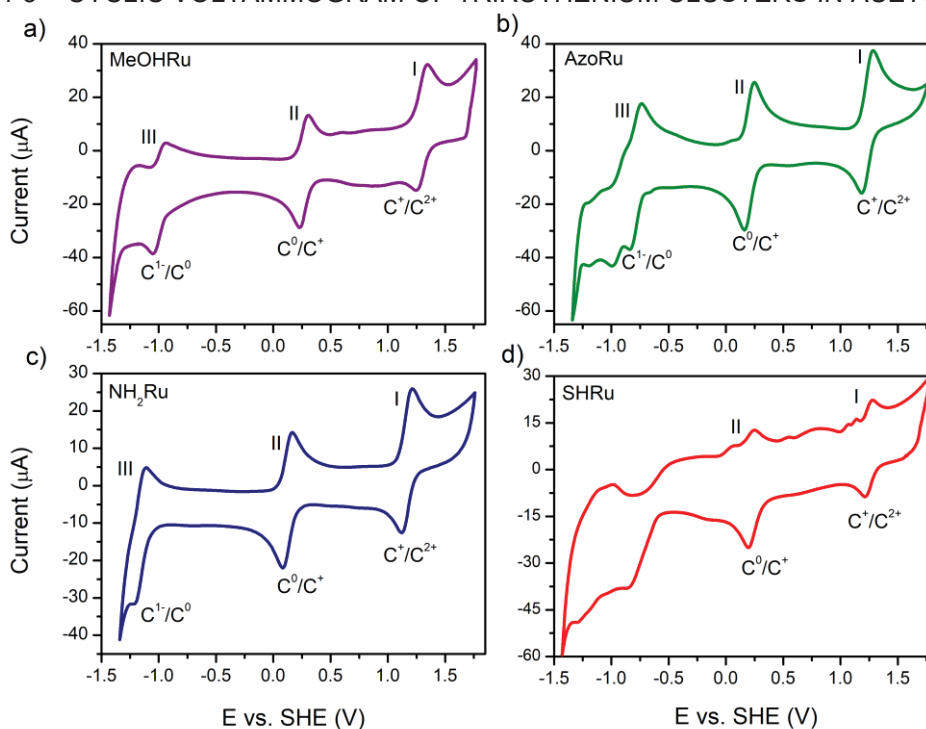
SOURCE: Author.

4.3 ELECTROCHEMICAL PROPERTIES OF RUTHENIUM CLUSTERS

Electrochemical behavior of triruthenium clusters was characterized through cyclic voltammetry of the compounds in acetonitrile solution. The results of second scan between -1.34 and 1.76 V with scan rate (v) of 100 mV s⁻¹ are shown in Figure 4-3. MeOHRu, AzoRu, NH₂Ru and SHRu exhibited three or two redox peaks (labeled as I, II and III) separated

approximately by 1V, some of them exhibited a distorted redox peak at low potential values. MeOHRu (a) have three peaks with half-wave potential ($E_{1/2}$) of 1.290 (I), 0.260 (II), and -0.990 V (III), which were attributed to redox pair $\text{MeOHRu}^{+/2+}$, $\text{MeOHRu}^{0/+}$ and $\text{MeOHRu}^{1-/0}$ respectively. $E_{1/2}$ was calculated as the average of anodic and cathodic potential peak ($E_{1/2} = (E_{pa} + E_{pc})/2$). The difference between oxidation and reduction potential peak (ΔE_p) was on average 0.080 V for the process I and II and 0.085 V for the process III. The ΔE_p of process III could be affected by the parasitic reduction current observed at low potentials. Also, the variation of oxidation and reduction peak current (i_{pc} and i_{pa}) with the v was analyzed. The i_p vs. v data was fitted to a power model ($i = av^b$), the results (Table 4-1) revealed that the value of b of all peaks were close to 0.5 as is expected for reversible and quasi-reversible redox processes of electroactive species in solution, which should be only limited by diffusion.[14,96,97]

FIGURE 4-3 – CYCLIC VOLTAMMOGRAM OF TRIRUTHENIUM CLUSTERS IN ACETONITRILE



Voltammograms at 100 mV s^{-1} of a) $[\text{Ru}_3\text{O}(\text{CH}_3\text{CO}_2)_6\text{Py}_2\text{MeOH}]\text{PF}_6$ (purple), b) $[\text{Ru}_3\text{O}(\text{CH}_3\text{CO}_2)_6\text{Py}_2\text{AzoPy}]\text{PF}_6$ (green), c) $[\text{Ru}_3\text{O}(\text{CH}_3\text{CO}_2)_6\text{Py}_2\text{NH}_2\text{Py}]\text{PF}_6$ (blue) and d) $[\text{Ru}_3\text{O}(\text{CH}_3\text{CO}_2)_6\text{Py}_2\text{SHPy}]\text{PF}_6$ (red) dispersed in acetonitrile (0.001 mol L^{-1}) with tetrabutylammonium perchlorate (0.100 mol L^{-1}) as supporting electrolyte.

SOURCE: Author.

AzoRu voltammogram (Figure 4-3b) have three redox peaks with $E_{1/2}$ at 1.230 (I), 0.210 (II), and -0.785 V (III), which were attributed respectively to redox pair $\text{AzoRu}^{+/2+}$, $\text{AzoRu}^{0/+}$ and $\text{AzoRu}^{1-/0}$. ΔE_p was 0.085 V (I), 0.070 V (II) and 0.100 V (III), the higher ΔE_p of process III can be related with other redox process observed at lower potentials. The process

is probably related with a reaction in the ligand AzoPy which present a redox process with $E_{1/2} \sim -1.0$ V, also we can observe separately a reversible peak at $E_{1/2} = -1.27$ V when the potential window was accordingly reduced. Also, the b values obtained from i_p vs. v data fitting were close to 0.5 for all the peaks (Table 4-1). Besides, NH_2Ru voltammogram (Figure 4-3c) have three redox peaks with $E_{1/2} = 1.165$ (I), 0.125 (II), -1.160 V (III) the oxidation and reduction peaks were similar. The processes were attributed to $\text{NH}_2\text{Ru}^{+2+}$, $\text{NH}_2\text{Ru}^{0/+}$ and $\text{NH}_2\text{Ru}^{1-/0}$. ΔE_p was on average 0.090 V (I and II) and 0.100 V (III). Also, the b value obtained from i_p vs. v data fitting were close to 0.5 for all the peaks.

TABLE 4-1 B-VALUES FROM CURRENT PEAK VARIATION WITH SCAN RATE FOR THE TRIRUTHENIUM CLUSTERS.

Complex	Process I	Process II	Process III
NH_2Ru	0.55	0.6	0.50
AzoRu	0.56	0.53	0.47
SHRu	0.58	0.74	---
MeOHRu	0.60	0.59	0.57

SOURCE: Author

Finally, SHRu voltammogram (Figure 4-3d) showed two well defined redox peak with $E_{1/2}$ at 1.240 (I) and 0.220 V (II). The processes I and II could be attributed to SHRu^{+2+} and $\text{SHRu}^{0/+}$, ΔE_p is on average 0.070 V and the oxidation peak showed a shoulder which was not observed when the potential window was reduced to study each peak separately. So, it could be related with processes occurring at lower potentials. The results of SHRu were not discussed deeply since the structural characterization suggested presence the undesired species in the sample, so the synthesis with other conditions is recommended. Summarizing, the described results suggest that all the complexes exhibited electrochemically reversible redox processes. Since the ΔE_p ranges from 0.07 and 0.10 V independent of the scan rate from 15 to 400 mV s^{-1} . Additionally, the i_p variation is roughly proportional to $v^{1/2}$ as is expected for electrochemical reversible processes of electroactive species in solution.

Besides, the $E_{1/2}$ of the redox processes changed significantly with the exchange of axial ligands in the triruthenium cluster compounds, as was previously pointed out by other authors, evidencing an important influence of the ligands in the stability of the different redox states of the complexes. As can be seen in Table 4-2 the $E_{1/2}$ of Process III had the higher variation, and AzoRu exhibited the highest $E_{1/2}$ (-0.785 V) of all the compounds studied, demonstrating that the reduction of the neutral complex is the most favorable. AzoRu^{1-} is more stable than the other 1 – compounds, which could be explained by the higher π -back-bonding effect of AzoPy, because it has higher π acceptor character than the other ligands studied and it can be reduced at relative low potentials ($E_{1/2} \sim -1.0$ V). [215] Whereas NH_2Ru presented the lowest $E_{1/2}$, revealing that $\text{NH}_2\text{Ru}^{1-}$ is less stable character than the other 1 – compounds.

As general trend, NH₂Ru exhibited the lowest $E_{1/2}$ potentials as compared to the other triruthenium clusters as listed in Table 4-2.

TABLE 4-2 HALF-WAVE POTENTIAL OF TRIRUTHENIUM CLUSTERS.

Complex	Process I (V)	Process II (V)	Process III (V)
NH ₂ Ru	1.165	0.125	-1.230
Py ₃ Ru ^a	1.220	0.190	-1.080
AzoRu	1.230	0.210	-0.785
SHRu	1.235	0.220	---
MeOHRu	1.290	0.260	-0.990

^a Ru₃O(CH₃CO₂)₆Py₃

SOURCE: Author

DFT calculations of the electronic structure of triruthenium clusters revealed that the lowest unoccupied molecular orbital (LUMO) of AzoRu was located in AzoPy ligand as it is shown in Figure 4-4. Confirming that it offers accessible antibonding π -states to stabilize reduced species through π -back-bonding mechanism. Whereas antibonding π -states with lower energy than pyridine ligands are absent in NH₂Py ligand, so reduced states in NH₂Ru are less stable. Even more it seems that π -states of pyridine ligands of NH₂Ru were higher in energy than in other compounds as noted in Figure 4-4 and Table 4-3. MeOHRu exhibited similar electronic structure that the symmetric cluster Ru₃O(CH₃CO₂)₆Py₃ (Py₃Ru) which could explain the little shift in the $E_{1/2}$ of process III. Besides SHRu exhibited an unoccupied orbital located in the SHPy ligand (LUMO+1) with lower energy than antibonding π -states of pyridine suggesting that SHPy ligand could offers accessible antibonding π -states to stabilize reduced species through π -back-bonding mechanism. However, this cannot be confirmed by experimental data since the compound generated during redox process III was not clearly observed. Summarizing this trend confirms that π -back-bonding is an important mechanism in the stabilization of the reduced cluster in each redox pair, hence higher π acceptor character of ligands should lead to higher redox potentials.

TABLE 4-3 ENERGY AND LOCATION OF FRONTIER MOLECULAR ORBITALS ACCORDING TO DFT CALCULATIONS

	NH ₂ Ru	Py ₃ Ru ^a	AzoRu	SHRu	MeOHRu
	Energy in eV	Energy in eV	Energy in eV	Energy in eV	Energy in eV
HOMO-2	-5.00 (Ru ₃)	-5.10 (Ru ₃)	-5.17 (Ru ₃)	-5.15 (Ru ₃)	-5.16 (Ru ₃)
HOMO-1	-4.92 (Ru ₃)	-4.97 (Ru ₃)	-5.01 (Ru ₃)	-4.96 (Ru ₃)	-5.02 (Ru ₃)
HOMO	-4.91 (Ru ₃)	-4.97 (Ru ₃)	-5.00 (Ru ₃)	-4.95 (Ru ₃)	-4.93 (Ru ₃)
LUMO	-2.63 (Ru ₃ O)	-2.60 (Ru ₃ O)	<u>-2.64(AzoPy)</u>	-2.58 (Ru ₃ O)	-2.53 (Ru ₃ O)
LUMO+1	<u>-0.98 (Py)</u>	-1.02 (Py)	-2.60 (Ru ₃ O)	<u>-1.05 (SHPy)</u>	-1.02 (Py)
LUMO+2	<u>-0.94 (Py)</u>	-1.01 (Py)	-1.04 (Py)	-1.02 (Py)	-0.99 (Py)

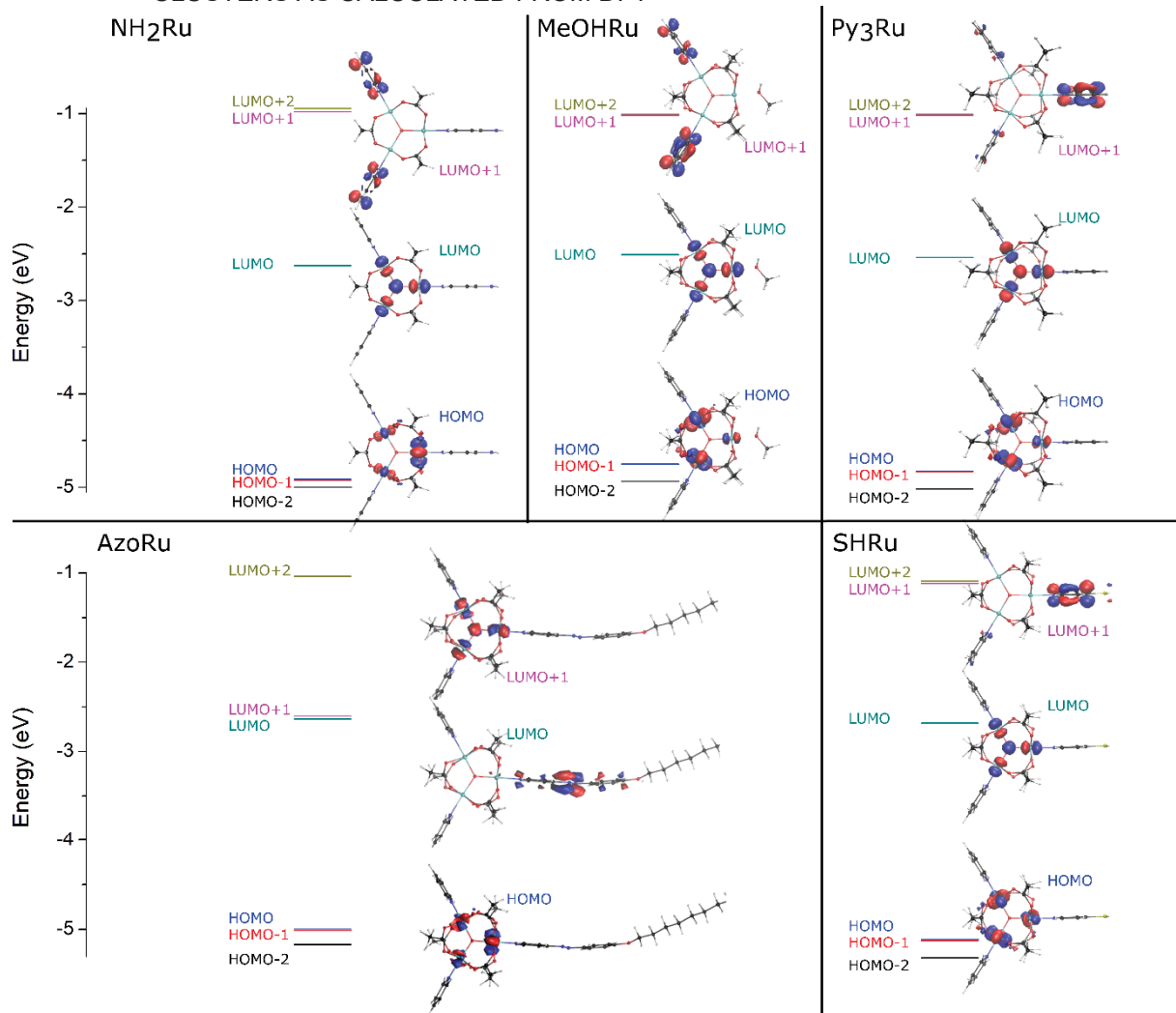
^a Ru₃O(CH₃CO₂)₆Py₃. In parenthesis the fragment where is located the molecular orbital.

SOURCE: Author

It is worth mentioning that the highest occupied molecular orbital (HOMO) of all neutral compounds studied is mostly located in the ruthenium atoms, as well as other occupied molecular orbitals (HOMO-1 and HOMO-2). The lowest unoccupied molecular orbitals are

located in the ruthenium atoms and the central oxygen atom, or pyridinic ligands. This electronic structure explains the rich optical behavior of this kind of material which can have different electronic transitions involving IC transitions among d-states in ruthenium atoms, MLCT transitions, and intraligand transition between π -states of pyridinic ligands.

FIGURE 4-4- FRONTIER MOLECULAR ORBITAL DIAGRAM OF THE DIFFERENT TRIRUTHENIUM CLUSTERS AS CALCULATED FROM DFT



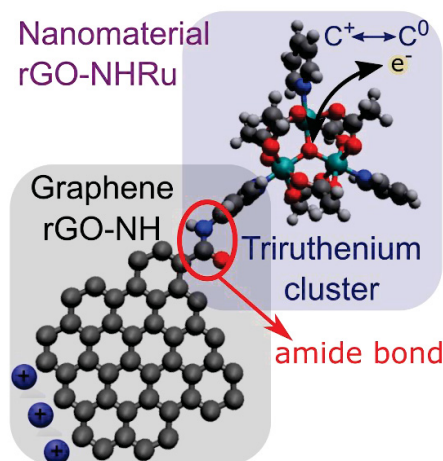
SOURCE: Author

AzoRu, and SHRu complexes present one electrochemically reversible redox process in the range from 0 to 1 V vs. SHE, which could be harnessed in energy storage electrodes. So, electrodes based on those complexes were fabricated taking advantage of their specific properties. In addition to the highly reversible redox peak, NH₂Ru have an amino group which facilitate the chemical interaction with graphene oxide and the fabrication of hybrid material with ruthenium clusters. Whereas AzoRu have amphiphilic properties because of its long hydrocarbon chain, so it can auto-organize in water-air interfaces allowing the construction of organized films which could enhance their performance as energy storage electrode.

5 HYBRID MATERIALS: GRAPHENE MODIFIED WITH TRIRUTHENIUM CLUSTER

As was mentioned in chapter 2, electrode materials exhibiting high double layer capacitance (high surface area) and electron transfer processes should result in energy storage devices with higher performance. Therefore, hybrid materials combining capacitor-like materials, as nanocarbons, [9] and redox components with pseudocapacitive behavior are suitable strategy to achieve higher performance.[59,259] The μ -oxo centered triruthenium-acetate clusters is an interesting class of compounds with reversible and fast redox reactions, strong electronic coupling among ruthenium atoms,[19,22,260] and ligands which could be easily exchanged through substitution reactions to build molecular materials. [211] So, an hybrid material with triruthenium cluster and graphene was synthesized based on previous experiences of graphene oxide functionalization of Grupo de Catálise e Cinética at UFPR through formation of highly stable amide bonds including groups as imidazole [261], thiols [230,262] and pyrrole. Several works combining carbon materials with pseudocapacitive or battery like materials (i.e. conducting polymer, metal oxides, MOFs) have been synthesized. However, as far as we know, energy storage electrodes based on carbon nanostructures with triruthenium cluster have not been described yet.

FIGURE 5-1- SCHEME ILLUSTRATING THE HYBRID MATERIAL STRUCTURE OF GRAPHENE AND TRIRUTHENIUM CLUSTER.



SOURCE: Author. Avogadro2 was used for drawing, Avogadro2 in version 1.91, (<https://www.openchemistry.org/projects/avogadro2/>). [233] Partly reprinted from [263]

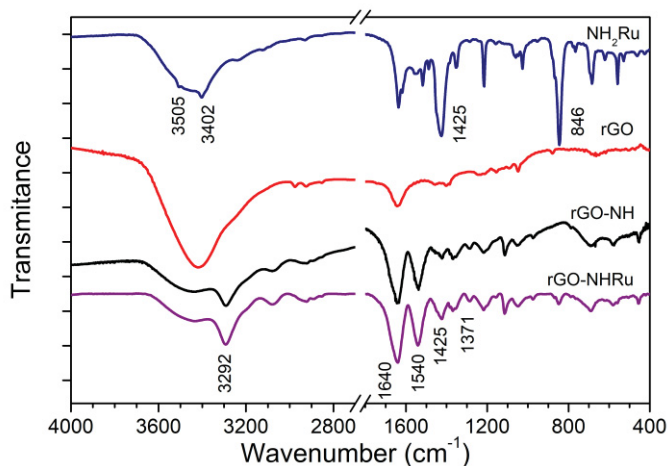
This chapter describes the novel electrode material based on reduced graphene oxide modified with triruthenium cluster chemically attached to graphene by 4-aminopyridine (NH_2Py) ligand. As is shown in Figure 5-1 NH_2Py binds to graphene oxide (GO) forming an amide group with carboxyl groups in GO resulting in a functionalized graphene which was subsequently reduced (rGO-NH). Then, the triruthenium cluster is linked through N-pyridyl of

NH₂Py resulting in the nanomaterial (rGO-NHRu). The electrochemical performance of material was tested and compared with isolated blocks (rGO-NH and NH₂Ru) to explore its function as energy storage electrode.

5.1 STRUCTURE OF GRAPHENE MODIFIED WITH TRIRUTHENIUM CLUSTER

The functionalization of graphene oxide with 4-aminopyridine (rGO-NH) is mainly evidenced in the FTIR spectra (see Figure 5-2) by the presence of bands at 3292, 1540 and 1371 cm⁻¹ attributed to ν N-H in amide group, ν C-N in aromatic and aliphatic part of amide bond respectively. Moreover, it is not observed the band associated with ν N-H in amine group observed in NH₂Ru spectrum at 3505 cm⁻¹ and 3402 cm⁻¹. These results evidenced the formation of amide bond upon functionalization of graphene with 4-aminopyridine. Additionally, the bands at 1640 cm⁻¹ can be partly attributed to ν -CO remaining in the reduced graphene. The rGO-NH and rGO-NHRu FTIR spectra were very similar, but rGO-NHRu spectrum had a change in the band around 1425 cm⁻¹, which can be associated with the δ C-H and ν C-C in acetate bridges of ruthenium cluster, in fact NH₂Ru spectrum presents an intense band around 1425 cm⁻¹.

FIGURE 5-2- IR SPECTRA OF TRIRUTHENIUM CLUSTER, GRAPHENE AND GRAPHENE-TRIRUTHENIUM CLUSTER HYBRID MATERIAL.



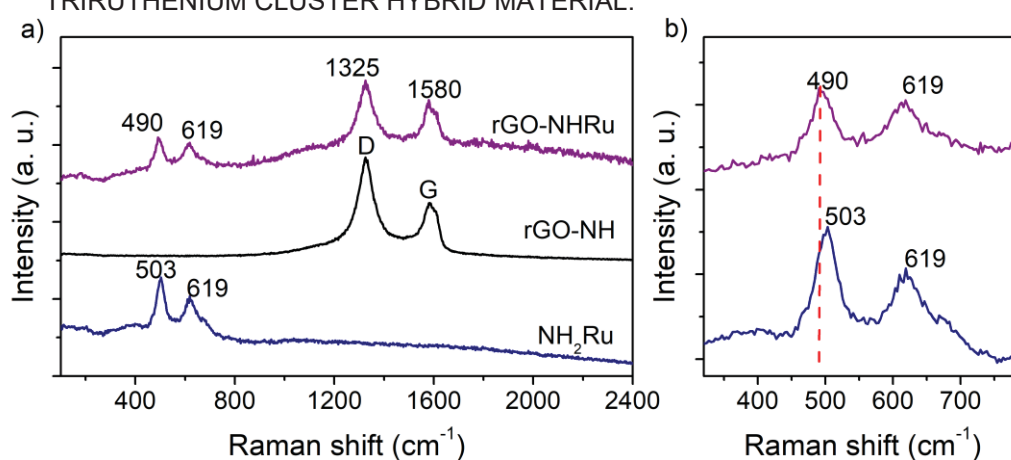
Spectra of NH₂Ru, rGO rGO-NH and rGO-NHRu samples prepared as KBr pellets were recorded in transmittance mode.

SOURCE: Author

The differences mentioned above slightly suggest that triruthenium cluster was linked with functionalized graphene. In order to further investigate the vibrational structure, Raman spectra (Figure 5-3), were acquired with 632.8 nm excitation laser, which coincides with the intracuster band present in the triruthenium cluster. [18,23,264] The rGO-NH spectrum (Figure 5-3a) presented two intense bands at 1325 and 1580 cm⁻¹ named as D and G, from the simple molecular view of carbon material corresponds to the bond stretching of all pairs of sp² carbon

atoms and to a breathing mode of sp^2 carbon atoms in rings, respectively. [265] The D band is a Raman forbidden vibrational mode that becomes active in the presence of defects in the graphene honeycomb structure due to vacancies, heteroatoms or symmetry broken in the edges of flakes. [265–268] 2b shows that D band is more intense than G band suggesting the presence of a large number of defects in the sample. The functionalized rGO structure is characterized by nanometric “graphene islands” surrounded by defect areas [266] and remaining oxygenated groups present at the borders. This characteristic is probably responsible for the D band intensification observed in the spectra of Figure 5-3a.

FIGURE 5-3- RAMAN SPECTRA OF TRIRUTHENIUM CLUSTER, GRAPHENE AND GRAPHENE-TRIRUTHENIUM CLUSTER HYBRID MATERIAL.



a) complete spectra from 100 to 2400 cm^{-1} obtained with a 632.8 nm laser excitation, b) zoom in the region between 300 and 800 cm^{-1}

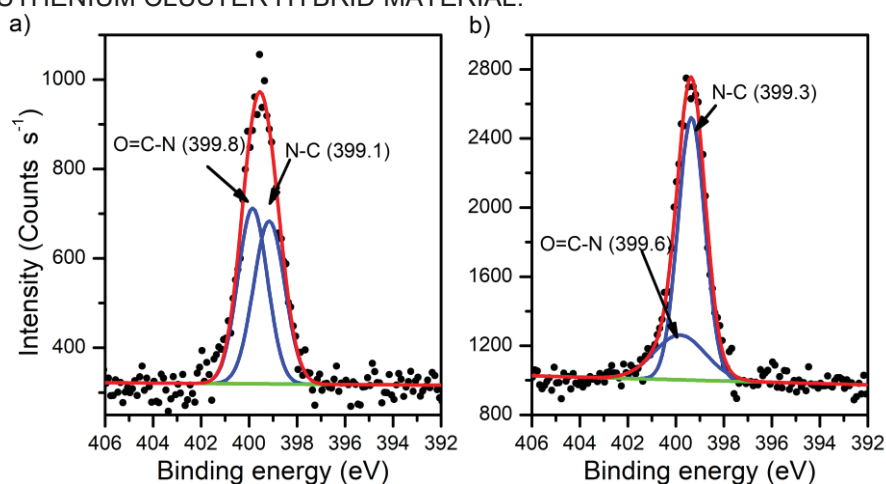
SOURCE: Author. Reprinted from [263]

In addition to the D and G band, rGO-NHRu spectrum presented two bands at 490 and 619 cm^{-1} , which also are present in NH_2Ru spectrum. However, the former band is shifted to 503 cm^{-1} in NH_2Ru as is clearly displayed in Figure 5-3b. The bands observed are result of the intensifying of core-cluster related vibrations by Raman resonant effect, since the laser excitation wavelength (632.8 nm) coincides with a broad absorption band which promotes electronic transitions involving ruthenium atoms as was above described (see Figure 4-2c). The bands were attributed with the aid of quantum-based resonant Raman simulation. The band at 490 cm^{-1} is attributed to ν_{Ru-N} (N is the pyridinic nitrogen of NH_2Py) and the band at 619 cm^{-1} to ν_{Ru-O} (O is the central oxygen), which is reasonable since it is expected the Ru-N bond be weaker than Ru-O bond. Therefore, the band shifting to lower energies in rGO-NHRu could be explained by the weakening of Ru-N bond due to the amide bond in rGO-NHRu.

The presence of ruthenium cluster also was evidenced by high-resolution XPS spectrum of the N1s band (Figure 5-4). The N1s band in rGO-NHRu is located at slightly lower binding energies respect to rGO-NH, which is probably related to the presence of pyridyl

nitrogen in a higher amount than amide nitrogen. The N1s band was fitted to three gaussian functions using MATLAB (see code in annex) to separate both components, two of those functions correspond to pyridinic and amide nitrogen, and the other one is a baseline curve. The fittings are good enough as indicated by the determination coefficients of 0.970 and 0.984 for rGO-NH and rGO-NHRu respectively. The two Gaussian functions are located at 399.1 and 399.8 eV in the rGO-NH sample, the former was attributed to pyridyl nitrogen[269–271] and the latter to amide nitrogen.[269,272] The two peaks have a similar intensity and wide, so the ratio between the areas of N-pyridyl and N amide peaks is close to 1 (0.98). In rGO-NHRu, the peak positions are similar to those of rGO-NH (399.6 and 399.3), but the peak associated with N amide is less intense, therefore the area of the N-pyridyl peak is ~3.10 times of the N-amide peak, which indicates that the amount of N-pyridyl is approximately 3 times the amount of N-amide in rGO-NHRu.

FIGURE 5-4- HIGH RESOLUTION XPS SPECTRA OF N1S BAND OF GRAPHENE AND GRAPHENE-TRIRUTHENIUM CLUSTER HYBRID MATERIAL.



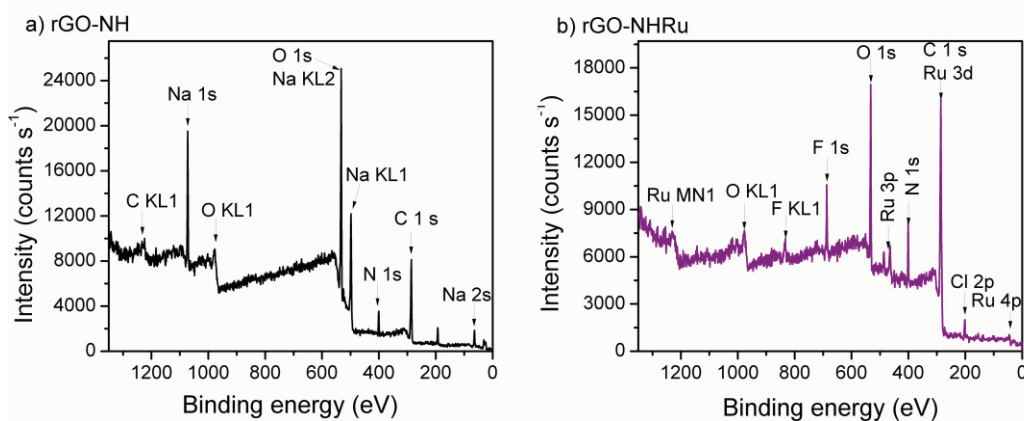
XPS N1s band of a) rGO-NH and b) rGO-NHRu.

SOURCE: Author. Reprinted from [263]

XPS survey spectra showed in revealed ruthenium presence of 2 at.% (or 13 wt.%) in the hybrid material rGO-NHRu as is shown in Figure 5-5, the composition estimation could have some uncertainty due to the overlapping of Ru 3d and C 1s region (see Figure 5-5). rGO-NHRu XPS survey spectra also exhibited bands corresponding to C, O, N, F and Cl the last two elements may correspond to counterions of the cationic triruthenium cluster. EDS analysis also evidenced the presence of ruthenium in the hybrid nanomaterial, the Table 5-1 summarize the results of EDS and XPS spectra obtained from different areas of the sample. It shows that rGO-NHRu contains approximately 9.2 % wt. of Ru, assuming that all the ruthenium is present as triruthenium cluster, it means that 28.0% of total weight of rGO-NHRu corresponds to the triruthenium cluster. Whereas rGO-NH exhibited bands corresponding to C, O and N. The estimated composition from the exploratory XPS and EDS spectra are also shown in Figure 5-5. In rGO-NH the O:C ratio estimated with XPS (1:1) is higher than that estimated by EDS

(3:8). Besides, in rGO-NHRu the Ru:C ratio estimated with XPS (1:34) is higher than that estimated by EDS (1:61). So, content of oxygen groups and ruthenium was higher in the surface of material.

FIGURE 5-5- XPS SURVEY SPECTRA OF GRAPHENE AND GRAPHENE-TRIRUTHENIUM CLUSTER HYBRID MATERIAL



SOURCE: Author. Reprinted from [263]

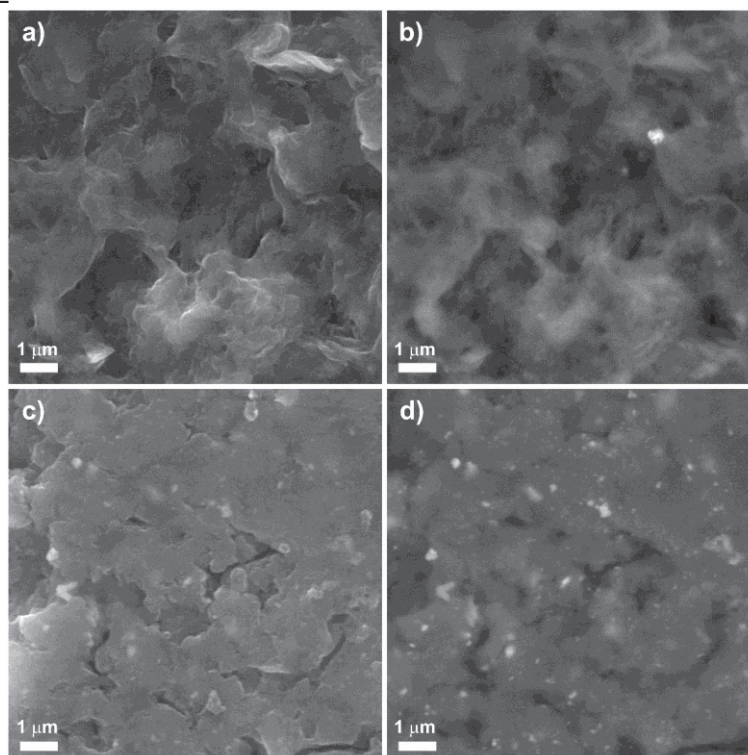
TABLE 5-1- CHEMICAL COMPOSITION OF GRAPHENE-TRIRUTHENIUM CLUSTER HYBRID MATERIAL FROM EDS AND XPS.

	Element	EDS				XPS	
		areas		clear points	dark points	%wt.	#atoms
		%wt.	#atoms	%wt.	%wt.		
rGO-NHRu	C	66.1	61	56.6	65.6	50.3	34
	O	24.7	17	26.5	23.5	16.4	8
	N	---	---	---	---	7.8	5
	Ru	9.2	1	15.4	8.8	12.6	1
rGO-NH	C	55.1	8	---	---	42.2	6
	O	24.5	3	---	---	39.1	6
	N	---	---	---	---	7.0	1

SOURCE: Author

The SEM image of obtained with backscattered electrons (BSE) is shown in Figure 5-6. It exhibited little clear areas distributed in all the sample with higher ruthenium content than the dark ones. As was determined by punctual EDS, clear areas contain an average of 15.4% wt. of Ru and dark areas 8.8 %. Both zones contain Ru, so it seems that Ru is distributed in all sample. In contrast the BSE image of rGO-NH (Figure 5-6b) do not shows that little clear areas, and the contrast observed between clear and dark zones is due to morphology. In fact, SEM image obtained with secondary electrons (SE) of rGO-NH (Figure 5-6a) also exhibited coinciding jagged features and clear zones. Whereas rGO-NHRu image do not exhibit so many jagged features neither that contrast between dark and clear zones. It evidences that rGO-NH material has an irregular texture and rGO-NHRu sample seems more compact. So, it could be expected a higher surface area in the rGO-NH film.

FIGURE 5-6- SEM IMAGES OF GRAPHENE AND GRAPHENE-TRIRUTHENIUM CLUSTER HYBRID MATERIAL

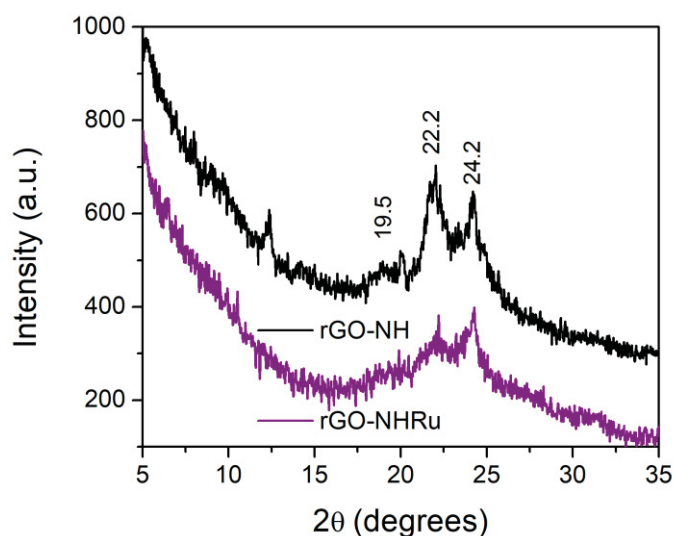


SEM Image of rGO-NH obtained with secondary electrons and b) backscattering electrons. c) SEM Image of rGO-NHRu obtained with secondary electrons and d) backscattering electrons. The SEM images were obtained using an electron beam energy of 12 keV.

SOURCE: Author. reprinted from [263].

The XRD pattern of reduced graphene oxide functionalized with aminopyridine (rGO-NH) exhibited peaks at 19.5° , 22.2° and 24.2° corresponding to interplanar spacings of 4.55, 4.00 and 3.73 \AA (see Figure 5-7). These peaks were previously described in other works reporting properties of graphene functionalized with cysteamine and pyrrole derivative. [262,273,274] Functionalization of graphene oxide led to the modification of the large interplanar spacing of 7.89 \AA (peak at 11.2°) observed for graphene oxide and the appearance of three new peaks between 18° and 25° , suggesting new structural organizations due to the chemical modification. Presumably, new 3D structural organization is formed because of interactions involving other functional groups, in fact it was reported that GO functionalized with aminopyridine [275] and 2,6-diaminopyridine [276] exhibited heavily stacked structure, which was attributed to physical cross-linking of graphene layers after the functionalization. [276] The diffractogram of ruthenium cluster modified graphene rGO-NHRu exhibited no significant changes, the only notable difference is the less intense and wider peak at 22.2° as compared with rGO-NH indicating less organized structure and irregular stacking.

FIGURE 5-7- X-RAY DIFFRACTOGRAM OF GRAPHENE AND GRAPHENE FUNCTIONALIZED WITH TRIRUTHENIUM CLUSTER.



5.2 ENERGY STORAGE IN DROP-CASTED ELECTRODES BASED ON GRAPHENE MODIFIED WITH TRIRUTHENIUM CLUSTER

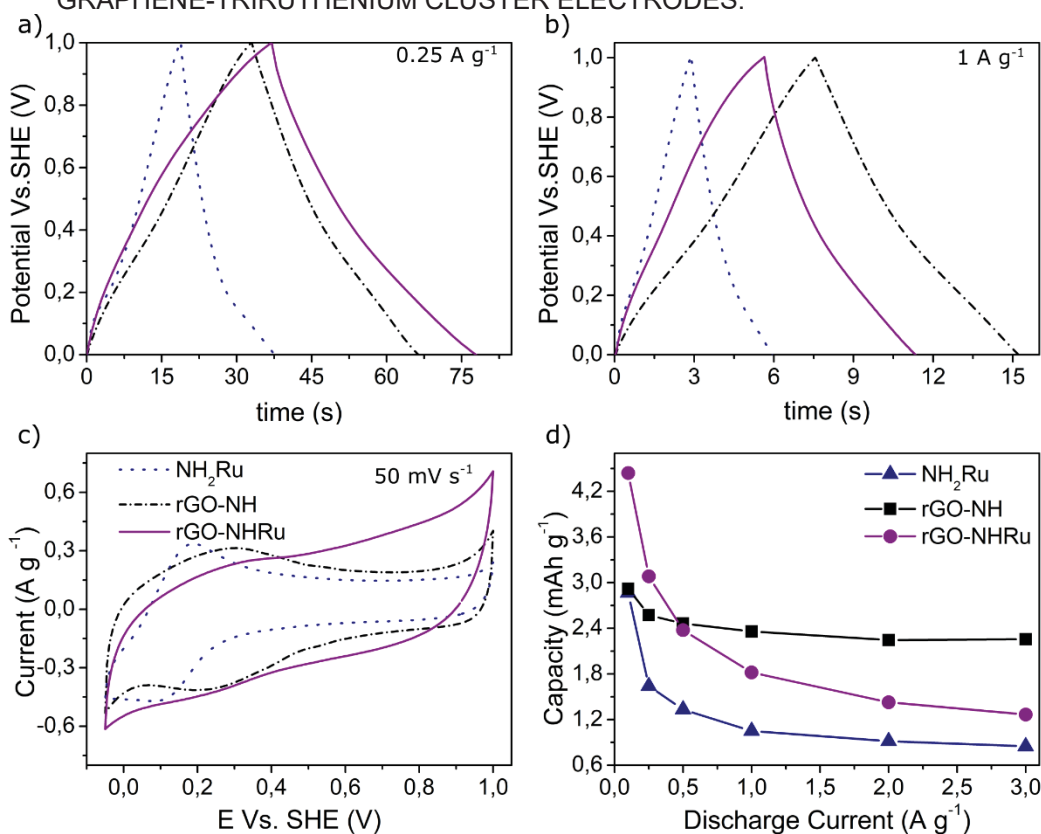
5.2.1 Electrochemical Behavior of Graphene-Triruthenium cluster Electrodes

The electrochemical performance of the electrodes fabricated by drop casting of rGO-NH, NH_2Ru and rGO-NHRu was tested with cyclic voltammetry (CV), charge-discharge (CD) measurements and electrochemical impedance spectroscopy (EIS). The voltammogram at scan rate of 50 mV s^{-1} , and the fourth CD cycle profiles at 1 and 0.25 A g^{-1} are shown in Figure 5-8. The CD profile (Figure 5-8a and b) of NH_2Ru (dotted blue line) presented a linear shape at potentials higher than 0.2 V and a curved variation around 0.2 V since it is required more charge to change the potential at that value due to redox reaction. The voltammogram (Figure 5-8c) of NH_2Ru showed a redox peak with $E_{1/2} = 0.14 \text{ V}$ which was attributed to $[\text{Ru}_3\text{O}(\text{CH}_3\text{CO}_2)_6\text{Py}_2\text{NH}_2\text{Py}]^{+1/0}$ redox reaction. Whereas, from 0.3 to 1 V the voltammogram is flat.

The rGO-NH CD profile (dashed line) was triangular shaped and voltammogram presented a rectangular shaped curve evidencing that its behavior is mostly dominated by double layer capacitance. But a feature like a broad redox peak at $E_{1/2} = 0.270 \text{ V}$ was also observed, this peak was attributed to a pseudocapacitive process arising from redox reactions of oxygen surface groups with hydrogen ions ($\text{C}_x\text{O} + \text{H}^+ + \text{e}^- \rightarrow \text{C}_x\text{OH}$), especially epoxy and alkoxy ones. [277,278] Also, it was suggested a similar redox reaction involving alkali metal atoms and epoxy groups to form a stable complex. [191] This peak was observed before by other authors in graphene [191] and nano-porous carbons. [279,280] This pseudocapacitive

process was noticed in the CD profile as a slightly curved feature at potentials lower than 0.4 V (Figure 5-8a and b). Furthermore, rGO-NH reached higher currents than NH_2Ru at potentials higher than 0.6 V, where both voltammograms are almost flat, revealing the higher double-layer capacitance of rGO-NH.

FIGURE 5-8- ELECTROCHEMICAL BEHAVIOR OF TRIRUTHENIUM CLUSTER, GRAPHENE AND GRAPHENE-TRIRUTHENIUM CLUSTER ELECTRODES.



a) Charge discharge profiles at 0.25 A g^{-1} and b) 1 A g^{-1} . c) voltammogram at 50 mV s^{-1} . d) capacity calculated from discharge curve at different specific discharge currents. Results for triruthenium cluster NH_2Ru (dotted blue line), aminopyridine functionalized graphene rGO-NH (dashed black line) and graphene-triruthenium cluster (rGO-NHRu) are shown.

SOURCE: Author

The rGO-NHRu CD profile (Figure 5-8a and b purple line) shows a roughly triangular shape which is asymmetrical, similar profiles were obtained for other electrode materials combining redox and capacitive materials [154,281]. The asymmetrical feature is consistent with the steep increases in reduction and oxidation currents observed in the voltammogram. The oxidation current could be related with triruthenium cluster oxidation. The reduction current at potential lower than 0.4 V resembles the peak of rGO-NH at same potentials and could be also related with presence of oxygen groups and the further increment of the reduction current at lower potentials could be partly attributed to redox process in ruthenium cluster. Furthermore, redox processes of rGO-NHRu were more evident at low scan rates and discharge currents as can be observed in Figure 5-9. The anodic current increased at lower potentials when lower scan rates were used. Also, at low specific current (Figure 5-8a) a CD cycle last more for rGO-

NHRu, whereas at high specific current (Figure 5-8b) last more for rGO-NH. Hence, the capacities calculated from discharge curve at different specific currents were higher in rGO-NHRu only at specific discharge currents lower than 0.5 A g^{-1} as show in Figure 5-8d. Additionally, Figure 5-8d shows that the rGO-NHRu and NH_2Ru capacity decreased significantly with the increase of discharge current. These trends illustrate that rGO-NHRu charge storage is limited by slow processes probably related with redox process diffusion limited by ions transport through the electrode.

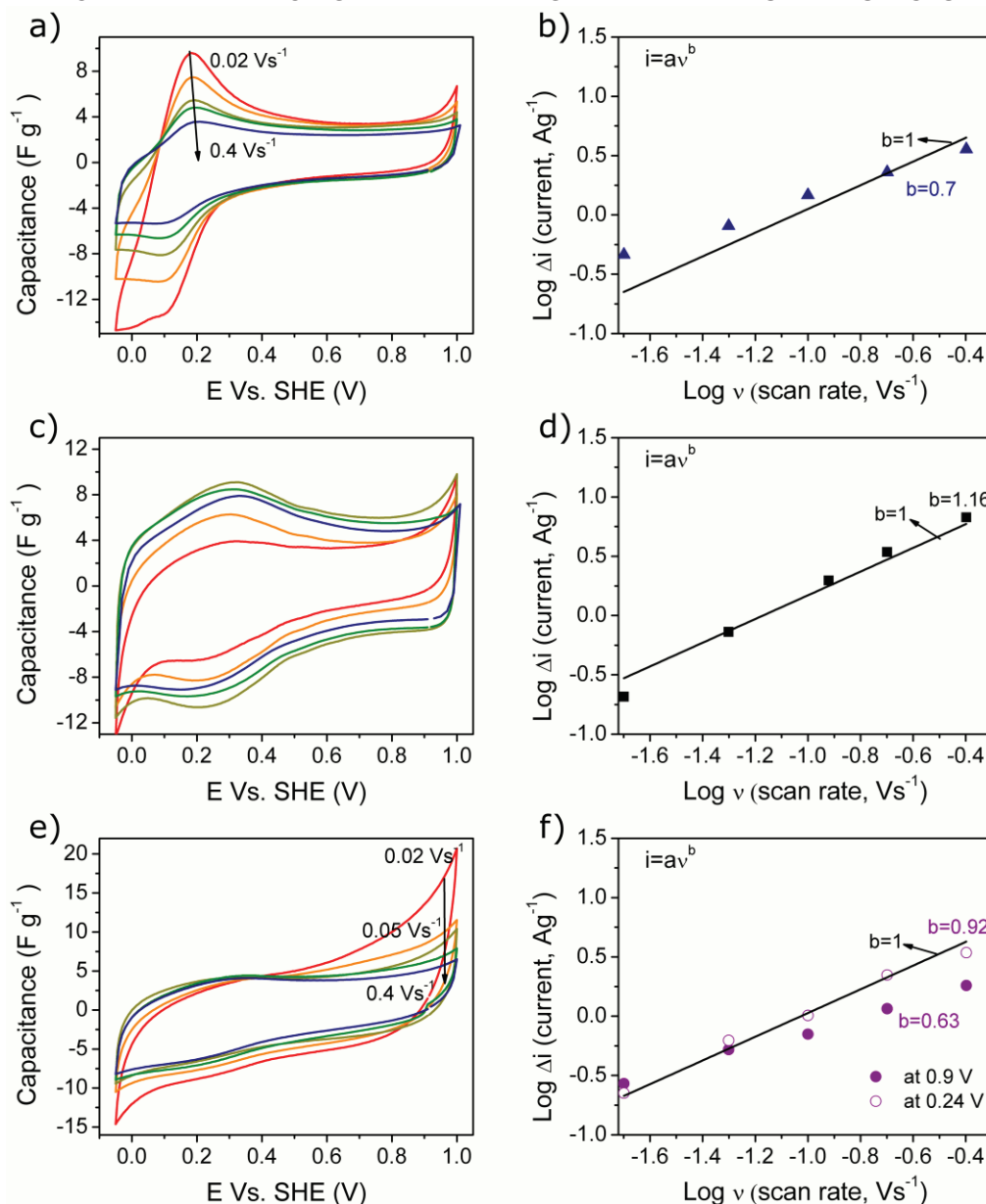
Our results suggest that the triruthenium cluster combined with graphene lead to an electrode with improved capacity at low specific discharge current (11.1 F g^{-1} at 0.25 A g^{-1}) as compared with rGO-NH. At high specific discharge current the capacity is limited (5.1 F g^{-1} at 2 A g^{-1}) probably due to charge transport process limitations. The performance is poor compared to other G/Metal oxides or G/MOFs materials, that report a significant performance improvement with respect to the component materials and capacitances ranging from 125 to 758 F g^{-1} . [148,151,170–172] This large range in the capacitances values resulted from several factors. For hybrid materials using metal oxides is reported that capacity increases with the metal oxide load and the specific surface area.[148,151] Likewise. the improved performance of hybrid materials with MOFs were attributed to the high surface area and the nickel or copper content. [170–172] Considering this, the dense and less porous rGO-NHRu morphology with respect to rGO-NH, and the structure with only 9% ruthenium content are important factors that accounts for rGO-NHRu low performance.

5.2.2 Analysis of Charge Storage on Graphene-Triruthenium cluster Electrodes

The analysis of the current variation with v in CV (see Figure 5-9) also suggests some charge transport limitations in the hybrid material. The current dependence on v was analyzed assuming a power-law dependence of i on v ($i = av^b$) as indicated in section 3.4. Also, the charge storage capacity contributions from surface sites (q_{outer}) and the less accessible sites (q_{inner}) was estimated according to the proposed by Trassati et al. [94] (see section 3.4). For rGO-NHRu, it was analyzed the dependence of i on v at 0.24 V (flat region in the CV) and 0.9 V (steep anodic current region in the CV). At 0.24 V the material had capacitive behavior ($b=0.92$) and at 0.9 V the process was limited by diffusion ($b=0.63$) and the calculated q_{inner} was 47% as is shown in Figure 5-10. Likewise, redox peak of NH_2Ru became broader and separation between oxidation and reduction peak (ΔE_p) became larger with v increment (from 0.09 to 0.14 V) as is observed in Figure 5-9a. Also, the value of b was 0.7 , and the q_{inner} was 57% as is shown in Figure 5-10. Therefore, the charge storage mechanism may be also limited by diffusion processes. Besides, the ΔE_p of rGO-NH had a minimum increment of 0.05 V when v was increased from 0.02 to 0.4 V as is observed in Figure 5-9c, b value was close to 1, and

q_{inner} was just 14% as is shown in Figure 5-10, then charge storage mechanism of graphene is not limited by diffusion processes.

FIGURE 5-9- ANALYSIS OF CURRENT VARIATION WITH THE SCAN RATE IN CYCLIC VOLTAMMETRIES OF GRAPHENE AND GRAPHENE-TRIRUTHENIUM CLUSTER.



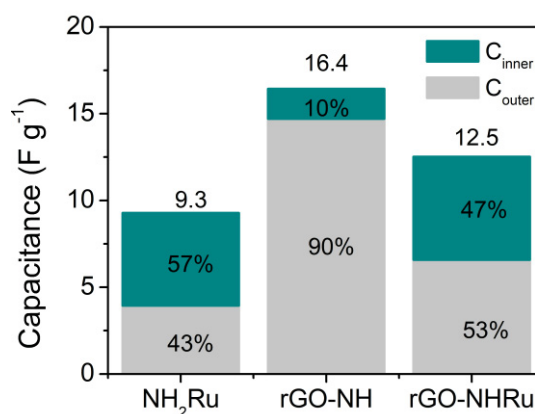
a) Cyclic voltammetry and b) $\log i$ vs $\log v$ plots for NH_2Ru . c) and d) for rGO-NH. e) and f) for rGO-NHRu. The $\log i$ vs $\log v$ plots use the peak currents of the materials, or the current reached at 0.24 and 0.9 V in the case of rGO-NHRu.

SOURCE: Author. Reprinted from [263]

It should be noted that rGO-NH reached an average specific capacitance of $\sim 8.8 \text{ F g}^{-1}$ (average considering all specific discharge currents tested), which is lower than other graphene materials reported, which ranges from 75 to 150 F g^{-1} . [148,151,276] However, rGO-NH showed an excellent capacitive performance with insignificant loss of capacitance at high discharge rates. The performance of graphene materials varies significantly depending on the

experimental conditions. For example, higher values of capacitance are reported when acid electrolyte is used in the electrochemical experiments. [148,276] Furthermore, the aggregation of graphene sheets during electrode fabrication leads to lower ion accessible surface area and longer ion diffusion paths, diminishing the capacitance [282,283] as was demonstrated in other studies in which graphene with higher specific surface area and improved porosity had higher capacitance than graphene with compact structure. [283] We noticed by SEM images that the graphene materials synthesized in this work are compact and probably with lower accessible surface area than other described in the literature. [148,151,276,282,283] Also, some studies reported that rGO functionalized with aminopyridine has a disordered structure, [275] and exhibits significant lower surface area than rGO (21.5 vs. 295.4 m² g⁻¹). [276]

FIGURE 5-10- ESTIMATED INNER AND OUTER CAPACITANCE OF TRIRUTHENIUM CLUSTER, GRAPHENE AND GRAPHENE-TRIRUTHENIUM CLUSTER ELECTRODES.



The capacitance values shown correspond to the total capacitance achieved at very low scan rates or specific discharge currents.

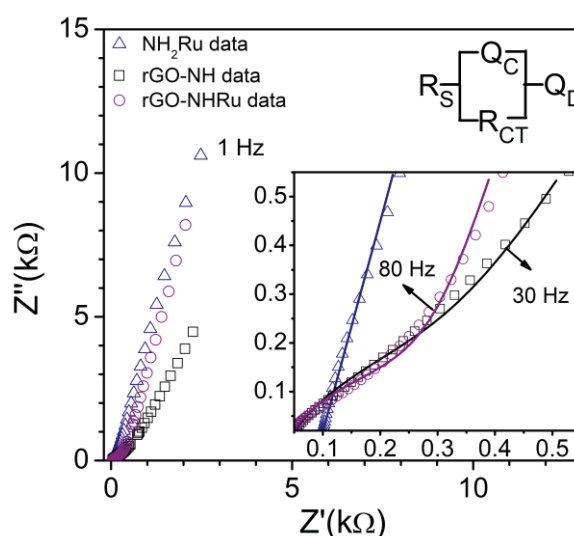
SOURCE: Author.

5.2.3 EIS of Graphene-Triruthenium cluster Electrodes

EIS was carried out at 0.24 V to obtain additional insights on the electrochemical processes occurring at electrodes. At 0.24 V, the triruthenium cluster (C⁺⁰) redox peak may occur. The Nyquist plot presented in Figure 5-11 suggest the presence of processes with different characteristic time constants. At very high frequencies, resistive processes, related with ionic (electrolyte) conductivity, electronic conductivity and contacts of all components, of the cell dominate the EIS response [284–286]. The real impedance value (Z') is directly related with the resistance of the processes mentioned. Triruthenium cluster have higher resistance ($R_s = 96 \Omega$) than rGO-NH and rGO-NHRu, which presented similar resistances ($R_s = 40 \Omega$). A small arc line was observed at high frequencies, which is associated to the double layer capacitance and resistive process due to charge transfer at interface. The small arc line suggests small charge transfer resistances at 0.24 V.

rGO-NH and rGO-NHRu exhibited an evident 45° line at intermediate frequencies, whereas such line was absent in the NH₂Ru Nyquist plot. It indicates that ions diffusion is more important in graphene materials than in NH₂Ru, since 45° line in the Nyquist plot is associated to the ion transport in the porous network of the electrode.[284–286] At low frequencies a tilted line close vertical was observed due to a capacitance that dominates the spectrum.[284–286] This line began at relative higher frequencies (ca. >20 Hz), which is characteristic of very thin film electrodes. However, lower frequency was observed in the Nyquist plot of rGO-NH, indicating that this material has longer diffusion paths than NH₂Ru and rGO-NHRu.

FIGURE 5-11- NYQUIST PLOT OF TRIRUTHENIUM CLUSTER, GRAPHENE AND GRAPHENE-TRIRUTHENIUM CLUSTER OBTAINED AT 0.24 V (VS. SHE).



A zoom in the high frequency region is shown in the inset figure. Frequencies at which transition between resistive to capacitive response are pointed out in the inset. Circuit model proposed is shown at right top of the figure, the data from model is shown as solid lines.

SOURCE: Author.

A simple equivalent circuit model was proposed to rationalize the different responses of the materials (see inset in Figure 5-11). The proposed circuit shown in the inset of Figure 5-11 have three elements connected in series: i) a resistance R_S associate to electrolyte conductivity, electronic conductivity and contacts of all components; R_S is evidenced at very high frequencies. ii) A parallel arrangement of a constant phase element Q_C , representing the electrical double layer, and a resistance R_{CT} , representing the charge transfer process. Which is associated to interfacial processes and evidenced at high frequencies in the initial arc of the Nyquist plot. iii) A constant phase element Q_D that represents the low frequency capacitive behavior as result of a quasi-stationary state with non-consuming species. That is, the diffusion layer has a length comparable with the characteristic physical dimensions of the electrode, [285,287] and the diffusion layer is no longer "semi-infinite" within the experimental frequency range.[287]

Interestingly, fitting results indicated: i) Q_C was higher in rGO-NH ($2.6 \cdot 10^{-5} \Omega^{-1} s^n$) than rGO-NHRu ($1.7 \cdot 10^{-5} \Omega^{-1} s^n$), whereas the values of n are similar. So, we can infer that rGO-NH has higher accessible area than rGO-NHRu. ii) Q_D was higher for rGO-NH ($5.5 \cdot 10^{-5} \Omega^{-1} s^n$) than for rGO-NHRu ($2.5 \cdot 10^{-5} \Omega^{-1} s^n$) and NH₂Ru ($1.9 \cdot 10^{-5} \Omega^{-1} s^n$) suggesting longer ion paths in rGO-NH which is probably related with a rougher surface. Also, it is remarkable that the response due to Q_C and R_{CT} is almost unnoticed in NH₂Ru plot indicating that the values of double layer capacitance and charge transfer resistance are very low at 0.24 V. More accurate fitting was achieved considering only R_S and Q_D , the results of the fitting are shown in Table 5-2.

TABLE 5-2- ESTIMATED PARAMETERS OF CIRCUIT MODEL FOR TRIRUTHENIUM CLUSTER GRAPHENE AND GRAPHENE-TRIRUTHENIUM CLUSTER ELECTRODES.

	NH ₂ Ru	rGO-NH	rGO-NHRu
$R_S (\Omega)$	96.5	40	36
$R_{CT} (\Omega)$		256	256
$Q_C (\Omega^{-1} s^n)$	1.9×10^{-5}	5.5×10^{-5}	2.5×10^{-5}
α_C	0.86	0.71	0.85
$Q_D (\Omega^{-1} s^n)$		2.64×10^{-5}	1.74×10^{-5}
α_D		0.70	0.70

In addition to storage capacity, the electrochemical stability of the electrode is another important parameter. Cycling stability was tested during 5000 cycles of charge discharge at constant current of 3 Ag^{-1} between 0 and 0.75 V cutoff potentials. NH₂Ru exhibited a slight decay of the capacity after 5000 cycles retaining 90% of the initial capacity. On the other hand, rGO-NH and rGO-NHRu retained their charge capacity practically unaltered even after 5000 cycles, being superior in this aspect than other hybrid materials [169,170,288]. Summarizing, the hybrid material consisting of rGO covalently functionalized with aminopyridine and coordinated to the triruthenium cluster exhibited capacitive behavior. Its capacity arises from double layer and pseudocapacitive processes present in rGO-NH and the redox reaction of triruthenium cluster. However, the coordination with ruthenium cluster apparently leads to a more compact structure, likely due to interplay of charges in the cluster and graphene flakes which contributes to aggregation. The modification in the structure limits its storage capacity at higher specific discharge currents, since nanomaterials morphology is the main factor that rules their performance. Consequently, the hybrid material studied in this chapter should have a promising usage as energy storage electrode if enhancements in its structure would be provided, such as increments in the porosity and surface area.[283] Further studies are necessary to better characterize how the electrodes fabrication could leads to higher ion accessible surface area and more effective ion diffusion paths.

6 ELECTRODE STRUCTURES: LANGMUIR BLODGETT ELECTRODES OF AMPHIPHILIC RUTHENIUM COMPLEXES

As was before mentioned electrochemical energy storage devices functioning relies on the processes occurring in the electrode-electrolyte interface (e.g. ion transport, chemical/structural changes, and electron transfer across the interface),[48,50,289,290] so tailored interfaces would be of interest for energy storage devices. The self-assembly of specific molecular geometries via supramolecular chemistry could be harnessed to fabricate tailored interfaces.[291] For example, highly organized thin films incorporating transition metal complexes with desired redox properties, with high exposition of redox sites and short ion pathway distances. [72,136]

Interfaces with these properties would be appealing as energy storage electrodes in energy storage devices for microelectronics, transparent and flexible devices. Since those electrodes could present a pseudocapacitive behavior due to the presence of electrochemically reversible redox processes not limited by diffusion within the electrode. [15,70] However, those electrodes typically present low energy density (per unit of area) because of low material loading that limits its application to microelectronics. Particularly, the Langmuir-Blodgett technique allow the achievement of organized interfacial structures through the transfer of molecules/materials previously organized on the water-air interface. [79,198,292] In addition to the self-assembly in the water-air interface, the compression process changes the organization of the materials, hence the properties of the film.[79,198,292]

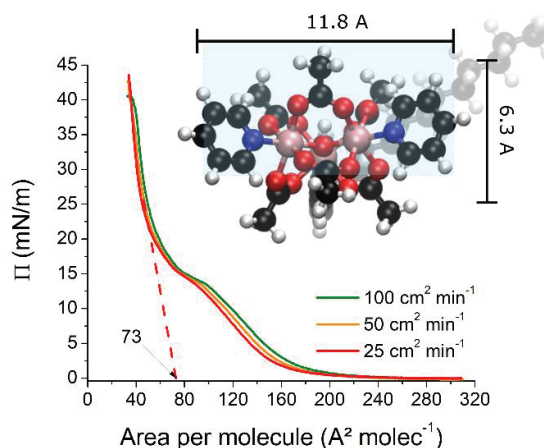
6.1 STRUCTURE OF RUTHENIUM COMPLEXES LANGMUIR-BLODGETT FILMS

Langmuir-Blodgett films fabrication involves the compression of the film with a moving barrier forcing the interaction and reorganization of the molecules within the monolayer. The behavior of this monolayer during the compression was monitored by recording the surface pressure (Π) and the area per molecule. $\Pi - A$ isotherms of AzoRu for several barrier speeds are shown in Figure 6-1. The behavior observed is similar to the found previously for the same complex. [219] Some differences were observed probably due to the lower temperature used in previous work (20 °C) as compared with the actual work (25 °C).

It was observed a slight increase of the surface pressure from $\sim 220 \text{ \AA}^2$ per molecule, indicating some interactions between cluster moieties. The pressure increment is higher from $\sim 160 \text{ \AA}^2$ as result of stronger interaction because of shorter distance between triruthenium clusters. A plateau at 13.5 mN m^{-1} was observed from $\sim 96 \text{ \AA}^2$ to $\sim 80 \text{ \AA}^2$, it was attributed to the coexistence of two phases during the transition from a liquid-like phase, in which molecules

have more freedom to move around in the monolayer, to a condensed phase with molecules organized in a close-packed arrangement. [293] The condensed phase was characterized by a sharp increment of surface pressure with the area, characteristic of monolayers with low compressibility. It is worth to remark that the monolayer film formed at the liquid–air interface was very stable, it collapsed at more than 35 mN m^{-1} . Furthermore, the isotherms at different barrier speeds were overlapped in great part, only little changes are observed when pressure start to increase in the liquid-like phase as shown in Figure 6-1.

FIGURE 6-1- $\Pi - A$ ISOTHERM FOR AMPHIPHILIC TRIRUTHEMIUM CLUSTER AT DIFFERENT BARRIER SPEEDS.



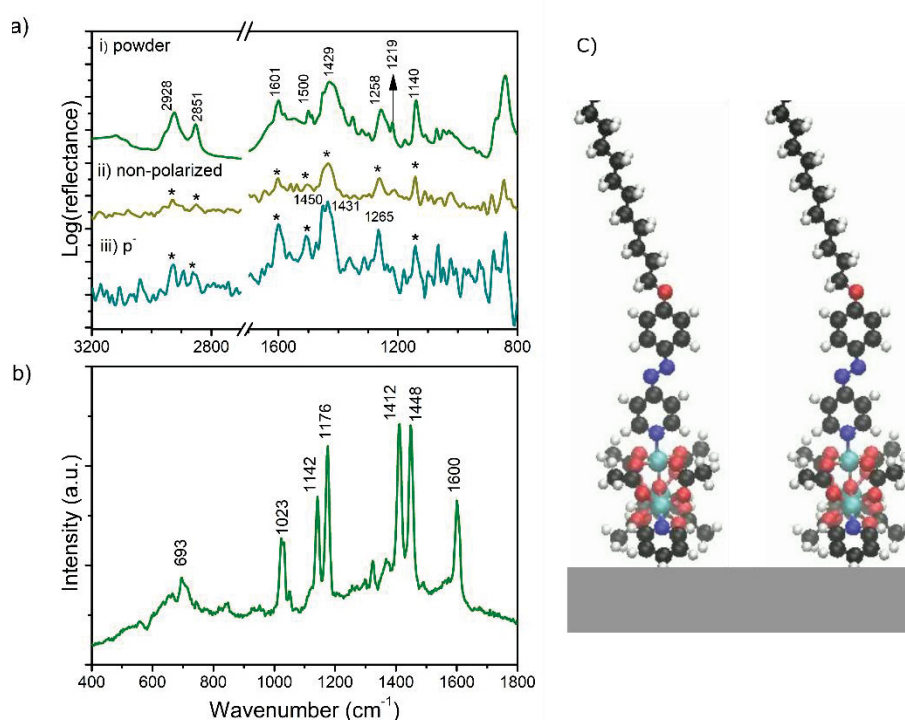
The area per molecule of 73 \AA^2 is pointed out in the figure. The inset shows the part of the molecule which is probably in contact with water and its dimensions according to molecule geometry from DFT. SOURCE: Author.

Based on the $\Pi - A$ curve, we decided to deposit films at surface pressure of 23 mN m^{-1} , condition in which AzoRu film is stable and highly packed. The estimated average area per molecule in the condensed phase was $73 \pm 2 \text{ \AA}^2$, which is close to the estimated area of the molecule in contact with water (74 \AA^2) if aromatic group in AzoPy ligand is normal to the surface. The area was calculated from the optimized geometry of complex in gas phase (Figure 6-1– Inset) obtained with DFT. The characterization of LB films fabricated on gold substrates with infrared reflection absorption spectroscopy (IRRAS) also suggested that aromatic rings in AzoPy ligand are normal to the surface. This technique allows to identify vibrations with dipole moment perpendicular to metal surface, since only the electric field perpendicular to the surface do not vanish near to metal. [294] Recording the p^- polarized light (incidence perpendicular to the surface) orientation of molecules could be inferred.

The IRRAS spectra (p^- polarized and non-polarized) of LB film with 13 “monolayers” (ML) on gold substrates is shown in Figure 6-2a, along with the spectrum of the AzoRu powder. Bands around $1140, 1258, 1429, 1500, 1601, 2851$ and 2928 cm^{-1} were observed as in powder spectrum, but some bands are intensified in the film spectrum obtained using p^- polarized light. For example, the bands around 2928 and 2851 cm^{-1} corresponding to $\nu\text{C-H}$ in the long chain

of ligand AzoPy have lower relative intensity in the film spectrum. This can be explained by partial alignment of the dipole moment of the vibration with metal surface normal plane resulting of the hydrocarbon chain in a titled position. The band at 1258 cm^{-1} is sharper and shifted to 1265 cm^{-1} in the film spectrum. This band result from several vibrations in AzoPy ligand, such as $\nu\text{C-O-C}$ stretching in phenyl ether group, δCH in pyridyl and phenyl groups and τCH_2 in the long chain of AzoPy. According to DFT calculations the τCH_2 vibrations are located at 1250 cm^{-1} and δCH at 1265 cm^{-1} , so the sharpening and shifting of the band can be related to lower contribution of τCH_2 vibrations with respect to δCH vibration. Then, the plane of pyridyl and phenyl rings are probably aligned to the normal plane whereas the long chain is titled.

FIGURE 6-2- INFRARED REFLECTION ABSORPTION AND RAMAN SPECTRA OF AMPHIPHILIC TRIRUTHENIUM CLUSTER LB FILM.



a) Infrared reflection absorption spectra of triruthenium cluster LB films, the non-polarized and p-polarized signals are shown. Infrared spectrum of powder sample is shown as a reference and the asterisks indicates the vibrations corresponding to the bands labeled in powder sample spectrum b) Raman spectrum of amphiphilic triruthenium cluster LB film obtained with Laser excitation of 632.8 nm . c) Scheme illustrating the orientation of the AzoRu cluster in the film.

SOURCE: Author.

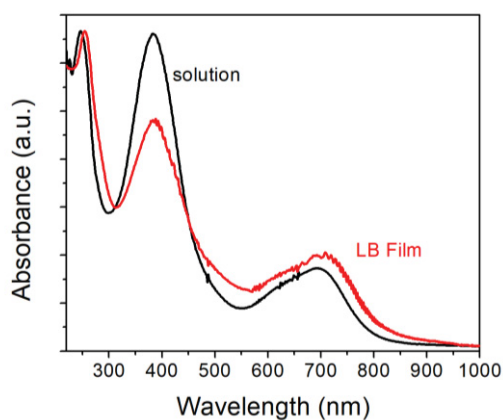
Additionally, the band around 1429 cm^{-1} is sharper and have other significant peak at 1450 cm^{-1} in the film spectrum. The band result from δCH_3 and $\nu\text{C-C}$ in acetate groups, and ring stretching of pyridyl and phenyl groups of AzoPy ligand. According to DFT calculation the δCH_3 vibration is located at 1401 cm^{-1} , $\nu\text{C-C}$ in acetate groups is located at 1428 cm^{-1} whereas ring stretching in AzoPy ligand L is located at 1443 cm^{-1} . Then the sharpening and the peak at 1450 cm^{-1} can be explained by a higher contribution of $\nu\text{C-C}$ in AzoPy corroborating to the

alignment of phenyl rings plane with the normal plane. Furthermore, the bands around 1601 cm^{-1} and 1500 cm^{-1} seem more intense in film spectrum. These two bands result from contributions of ring stretching in pyridine ligands and pyridyl and phenyl group of AzoPy. It reinforces that the plane of pyridyl and phenyl rings should be aligned to the surface normal.

Raman spectrum obtained with laser excitation of 632.8 nm is shown in Figure 6-2. Some intense bands at 693 , 1023 , 1142 , 1176 , 1412 , 1448 and 1600 cm^{-1} were observed. It was notorious the presence of more intense Raman bands as compared with NH_2Ru spectrum (see Figure 5-3), which is attributed to azobenzene group presence leading to enhanced Raman scattering. [295]. The band at 693 cm^{-1} was attributed mainly to $\nu\text{Ru-O}$ in the Ru_3O core. The others band were attributed mostly to vibrations in pyridinic ligands, particularly AzoPy ligand. Band at 1023 cm^{-1} was mainly attributed to ring breathing mode and δCH in pyridinic ligands. The δCH vibration in Py and AzoPy also contributes to the bands at 1142 and 1176 cm^{-1} . Whereas the bands at 1412 and 1448 cm^{-1} were attributed to the $\nu\text{C-C}$ in acetate groups and ring stretching in AzoPy ligand. Likewise, band at 1600 cm^{-1} also is attributed to the ring stretching in AzoPy ligand.

The UV-vis spectra of AzoRu dispersed in dichloromethane and LB films deposited on quartz (Figure 6-3) were similar but lower intensity of band at 382 nm in the film spectrum was observed. The main electronic transition involved is $\text{azo}(\pi) \rightarrow \text{phen}(\pi^*)$, which have a transition moment parallel to long axis of phenylazo group. The reduction in peak intensity is a second order effect arising from weak interactions of transition moments organized side-by-side. [296–298] Therefore the lower band intensity at 382 nm was partly attributed to weak interactions between phenylazo groups organized side-by-side but with a significant distance between them due to the presence of large Ru_3O core.

FIGURE 6-3- UV-VIS SPECTRA OF AMPHIPHILIC TRIRUTHENIUM CLUSTER LB FILM.

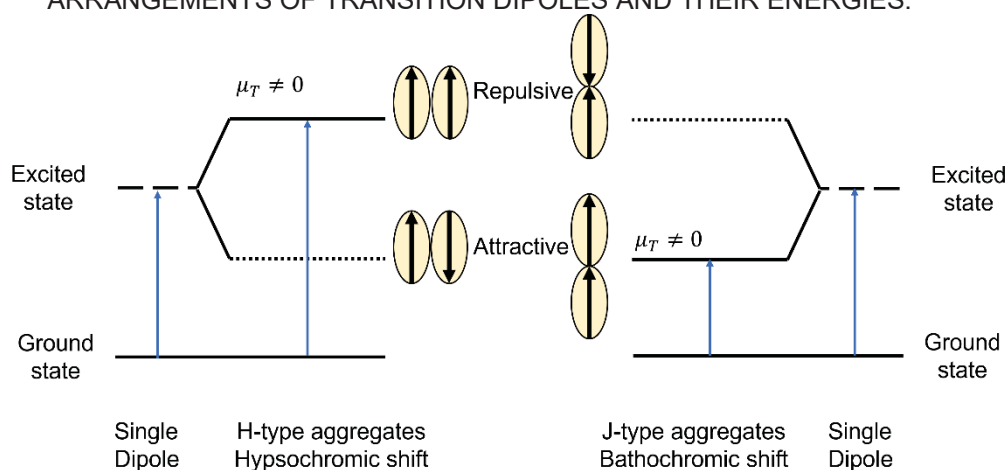


UV-vis spectra of amphiphilic triruthenium cluster LB film and dissolved in dichloromethane, the spectra were normalized to the highest peak for better comparison of peak shifting and relative intensities.

SOURCE: Author.

Another factor contributing to lower intensity could be the exciting electric field propagating along normal plane with respect to the surface, so the electronic transitions with dipoles parallel to the surface are disfavored. Besides the bands at higher and lower wavelengths exhibited a bathochromic shift of 12 and 8 nm respectively, the wide band at 696 nm was attributed to intracluster transitions and the band at 247 nm is associated with $\pi \rightarrow \pi^*$ in pyridine ligands. According to the exciton model illustrated in Figure 6-4, [298–300] the strong interaction between the transition dipole moment of two different chromophores lead to lower energy (bathochromic shift) when its orientation favors the attractive interaction between dipoles and a band is observed if the net moment is different to zero. So, dipoles should be collinear as in the named J-type aggregates (see Figure 6-4). Whereas higher transition energies (hypsochromic shift) are expected when its orientation favors the repulsive interaction between dipoles and an absorption band is observed if the net moment is different to zero. So, dipoles should be side by side with the same orientation as in H-type aggregates.

FIGURE 6-4- SCHEME OF EXCITON MODEL SHOWN THE DIFFERENT GEOMETRICAL ARRANGEMENTS OF TRANSITION DIPOLES AND THEIR ENERGIES.



Dotted line indicates that the state is not allowed since the total dipolar moment μ_T is zero.

SOURCE: Author. Based on [298]

According to this model, the Ru_3O cores in the films should be aggregated in a such way that they are close, and their transition dipole moments are mainly collinear. However, that dipole moments probably are not frequently aligned, since the band shifting observed in the spectra at Figure 6-3 is small. The characterizations suggest that mostly of the AzoRu molecules in each layer of film are organized with the aromatic groups of AzoPy aligned with the surface normal and with significant distance between them since the Ru_3O core acts as spacer between the ligands. Moreover, the Y-type deposition process was used (deposition during both submersion and emersion) starting with the substrate emersion, so it is expected a tail-to-tail and head-to-head configuration with the Ru_3O cores, which are expected to be more hydrophilic than the AzoPy tails, facing the substrate.

However, the shape of the transfer ratio shows that the material deposited during emersion is significantly higher than during submersion, suggesting that most of the material is deposited when substrate upstroke. Therefore, we can expect lower “coverage” in layers formed when substrate lifted down, those layers may have some of the tails inserted between molecules of previous layers as suggested previously, [215] inducing some disorder in molecules organization with only some parts within the film exhibiting a tail-to-tail and head-to-head configuration. This configuration may propitiate interaction between transition dipole moment as that of J-type aggregates, which is slightly evidenced in UV-vis spectra. Moreover, the proximity of Ru₃O cores may lead to strong repulsive interactions when there are several neighbors oxidized molecules because of their positive charge, so a mixed presence of both reduced and oxidized molecules could be thermodynamically favored.

6.2 ENERGY STORAGE IN LANGMUIR-BLODGETT FILMS OF AMPHIPHILIC TRIRUTHENIUM CLUSTERS

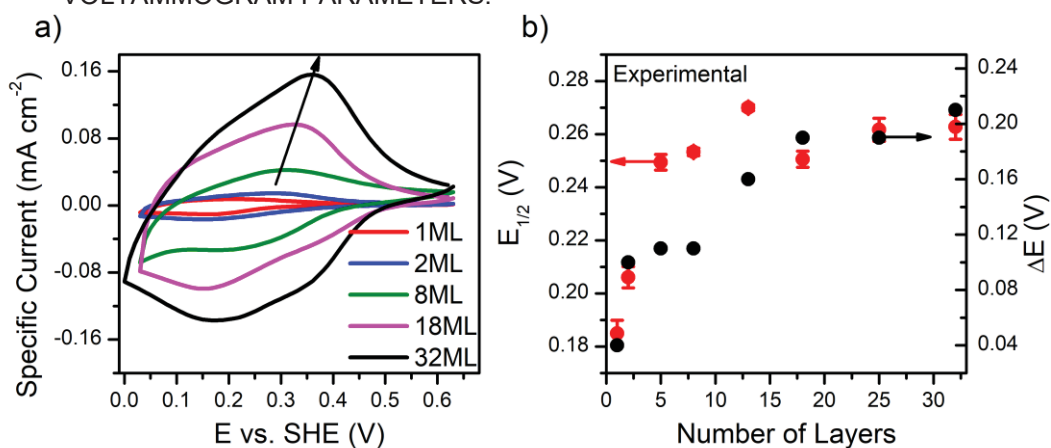
6.2.1 *Electrochemical Behavior of Amphiphilic Triruthenium Cluster Electrodes.*

The electrochemical performance of the AzoRu electrodes fabricated by LB technique was tested by cyclic voltammetry (CV) and electrochemical impedance spectroscopy (EIS). The voltammograms at 50 mVs⁻¹ for AzoRu LB films with different number of layers (Figure 6-5) exhibited a faradaic process related to the redox pair [Ru₃O (C₂H₃O₂)₆ (Py)₂ AzoPy]⁺⁰. The redox peaks were wide, the estimated peak width at half of peak current varied from 0.20 V to 0.25 V as the number of layers increased. The wide peaks could be partly explained by the interactions between oxidized and reduced molecules within the film as is described by the model proposed in this work which is presented in the next chapter (page 106). Also, it was observed a notorious increment in the anodic peak potential as the number of layers increased, a similar result was reported previously by Naidek et al.[219] Whereas the cathodic peak potential presented a strange trend, it was shifted from 0.17 V to ~0.21 V as the number of layers increases, from 13 **ML** a further increase of the number of layers led to shift the potential to lower potentials ~0.16 V for 32 **ML**. Additionally, a further increase in reduction current at lower potential was observed in some voltammograms, suggesting the presence of other reduction current at these potentials, which may affect the cathodic peak position and shape.

The described trend could be explained by variations in $E_{1/2}$ and ΔE with the number of layers. $E_{1/2}$ goes from 0.18 V for films with 1 **ML** to 0.26 V for films with 18 **ML** or more as is shown in Figure 6-5 (red circles). These values are different to the value estimated for the compound in solution (0.21 V), the $E_{1/2}$ shifting could be explained by the presence of sites with different redox potential or the difference in the stability of the reduced and oxidized

molecules in the film. Oxidized molecules may be less stable in thicker films due to their cationic nature, so the reduction process is more favorable hence redox potential is higher in thicker electrodes. It was additionally discussed in next chapter with the aid of a mathematical method (see page 106). On the other hand, ΔE_p goes from 0.03 V for 1 **ML** to 0.21 V for 32 **ML** as is shown in Figure 6-5 (black circles). Note that even in electrodes with 1 **ML** there are some limitations in the charge transfer between molecules and the substrate. Since electrodes with surface modified by permanently absorbed redox molecule should not present peak separation ($\Delta E_p = 0$) in the ideal case. Also, the results suggests that redox reaction is limited by charge transport in thicker films, which is probably related to electron transfer process between triruthenium clusters in the film.

FIGURE 6-5- CYCLIC VOLTAMMOGRAM OF LANGMUIR BLODGETT ELECTRODES AND SOME VOLTAMMOGRAM PARAMETERS.



(a) Cyclic voltammogram at 50 mV s⁻¹ for electrodes with different number of monolayers (**ML**). (b) Half wave potential $E_{1/2}$ and potential difference between peaks ΔE variation with number of layers.

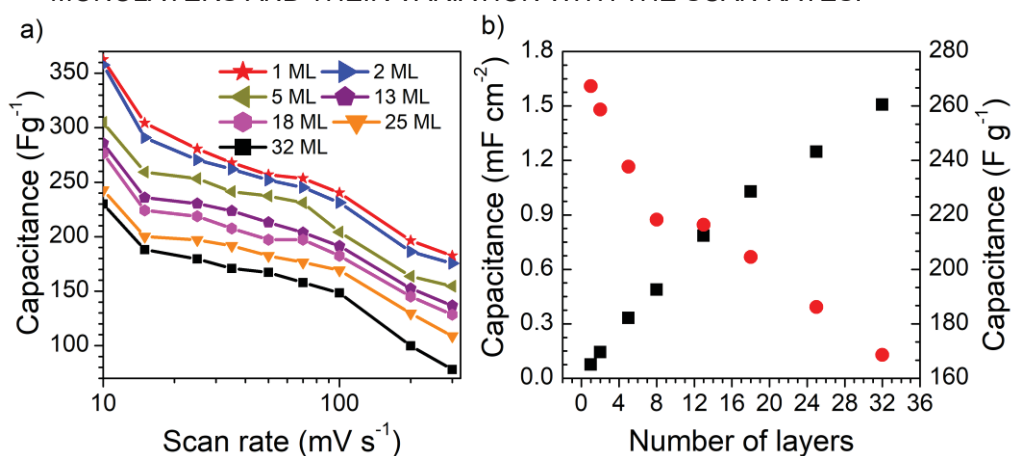
SOURCE: Author. Partly Reprinted from [301]

Summarizing, the electrochemical response of AzoRu films was influenced by interactions modifying the stability of oxidized and reduced molecules in the film. It can be remarked that i) oxidized molecules in layers far from substrate are less stable because of the repulsive force between oxidized molecules (cationic) or counter-ion intercalation in the oxidized film. So, the reduction process is more favorable hence redox peaks are shifted to higher potential in thicker electrodes. ii) The interaction between reduced and oxidized molecules is more favorable leading to wide redox peak. iii) The ΔE_p increases significantly as the film thickness increases, indicating limitations in charge transfer within the film.

Despite those limitations in the charge transport, AzoRu films could be interesting for energy storage electrodes because of wide redox peaks which could confer a capacitor-like behavior to an electrode entirely based on a redox reaction. The capacitances were calculated from CV at different scan rates. Figure 6-6a shows that capacitance by mass unit decreased with scan rate, the decreasing was moderated from 15 to 100 mVs⁻¹ and higher from 100 to

200 mVs^{-1} . Also, the capacitance by mass unit decreased with the number of layers, the decreasing seems more significant from 13 **ML** as is clearly visualized in Figure 6-7b, here is shown the capacitance per unit of area which increase with the number of layers as expected, but that increment is lower from 13 **ML**. This trend indicates that the effective quantity of material in the electrodes lowers as the thickness increases, indicating that the permeation of electrolyte to all sites of electrode is more difficult and some molecules could be electrically isolated hindering its contribution to energy storage. Probably, the loss of organization in the multilayers films results in a less effective use of electrode mass.

FIGURE 6-6- CAPACITANCE OF THE ELECTRODES WITH DIFFERENT NUMBER OF DEPOSITED MONOLAYERS AND THEIR VARIATION WITH THE SCAN RATES.



(a) Capacitance of the electrodes with different number of deposited monolayers calculated from cyclic voltammetry at different scan rates. (b) Average specific capacitance (per unit of area and mass unit) and its variation with the number of layers.

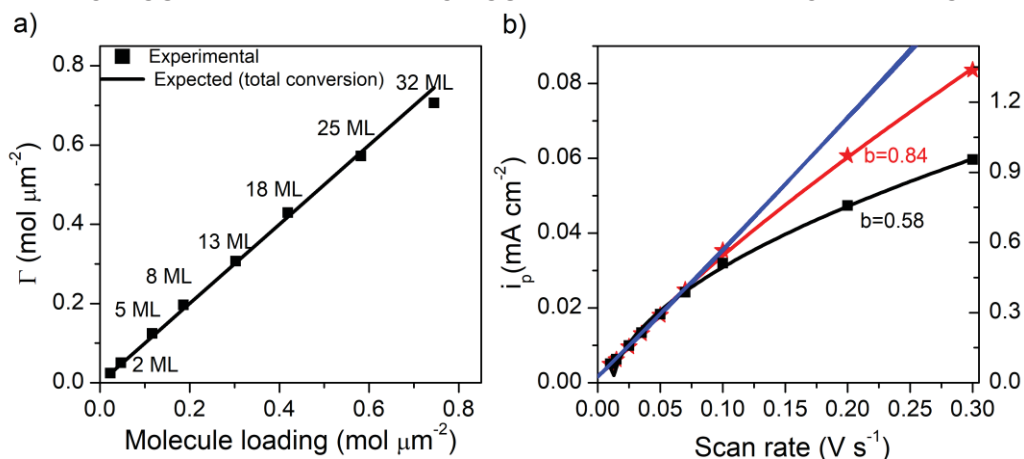
SOURCE: Author. Partly reprinted from [301]

6.2.2 Analysis of Charge Storage on Amphiphilic Triruthenium Cluster Electrodes.

The comparison between the molecule loading (Γ) obtained from the area below oxidation peak in the CV and from the $\Pi - A$ isotherm tests observed in Figure 6-7 confirms that thicker electrodes have less effective use of electrode mass, since the electrochemical active molecules Γ is lower than the expected if all molecules in the film reacts. The analysis of variation of peak current (i_p) with v reveals that it varies linearly from 10 to 100 mVs^{-1} for electrodes with few layers (up to 13 **ML**), which is characteristic of capacitive behavior [55]. This trend deviates as the number of layers further increases, for electrodes with 32 **ML** the peak current deviates from this linear behavior at v higher than 50 mVs^{-1} as is observed in Figure 6-7b. It indicates that some diffusion processes limit the current in thicker electrodes, the b value estimated by data fitting to $i_p = av^b$ (considering all scan rates tested) was lower for thicker electrodes, b varied from 0.84 for 1 **ML** film to 0.56 for 32 **ML** film, confirming the higher contribution of diffusion limited processes to the current in thicker electrodes. [14,96,97]

When only the scan rate values up to 100 mV s^{-1} were considered, we found that the values of b are close to 1 for electrodes up to 13 **ML**, thicker electrodes have values close to 0.80.

FIGURE 6-7- COMPARISON OF MOLECULE LOADING WITH THE ELECTROCHEMICALLY ACTIVE MOLECULES AND ANALYSIS OF CURRENT PEAK VARIATION WITH SCAN RATE.

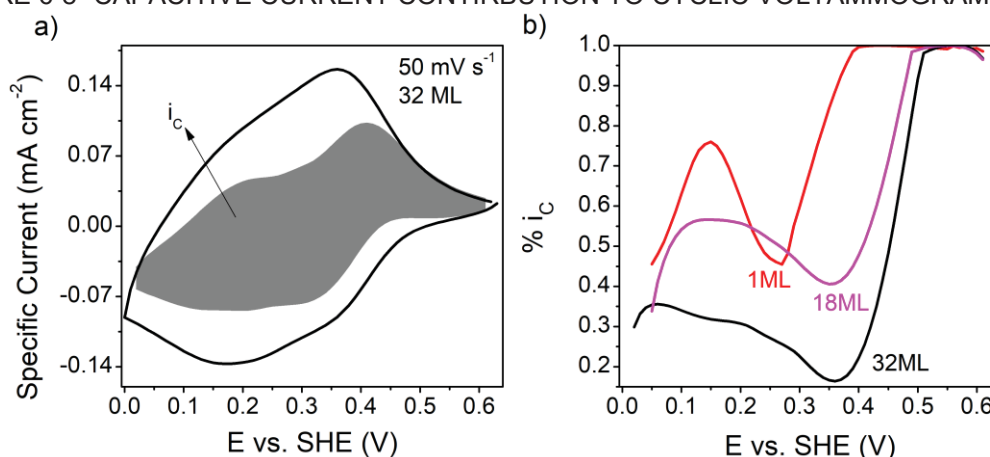


a) Surface concentration of the electrochemical active molecules Γ obtained from integration of oxidation peak in cyclic voltammograms compared with the expected loading obtained from surface pressure π vs. area plots. b) Current peak variation with scan rate for 1 **ML** film and 32 **ML** film.

SOURCE: Author.

In other analysis of current peak variation with scan rate [14,95,96] is proposed to divide the total current obtained at determined potential value in two contributions $i(V) = k_D v^{1/2} + k_C v$ as was shown in equation 3.8 of methods section. The values estimated depends on the potential and we noticed that at some potentials the points corresponding to higher scan rates deviates from the linear trend. The estimation of these values in all the potential range allowed us to estimate the total contribution of diffusion limited and capacitive processes. The Figure 5a show the total current (experimental voltammogram) and the “capacitive current” ($i_C = k_C v$) for the electrode with 32 **ML**. It is noticed that between 0 and 0.4 V there are an important contribution from diffusion limited current to the total current, in contrast from 0.4 V the total current has only capacitive contribution. It is better observed in Figure 6-8b, where the i_C contribution to the total current ($\%i_C k_C v / (k_D v^{1/2} + k_C v)$) is depicted for electrodes with different thickness. It is also noticed a lower capacitive contribution in the 0 to 0.4 V range for electrodes with higher thickness. This trend reinforces the performance deterioration for thicker electrodes because of charge transport limitations.

FIGURE 6-8- CAPACITIVE CURRENT CONTRIBUION TO CYCLIC VOLTAMMOGRAM.



a) Cyclic voltammogram of LB film with 32 ML at 50 mVs⁻¹ showing the “capacitive current i_c ”. b) The estimated contribution of capacitive current at 50 mV s⁻¹ for films with different thickness.

SOURCE: Author.

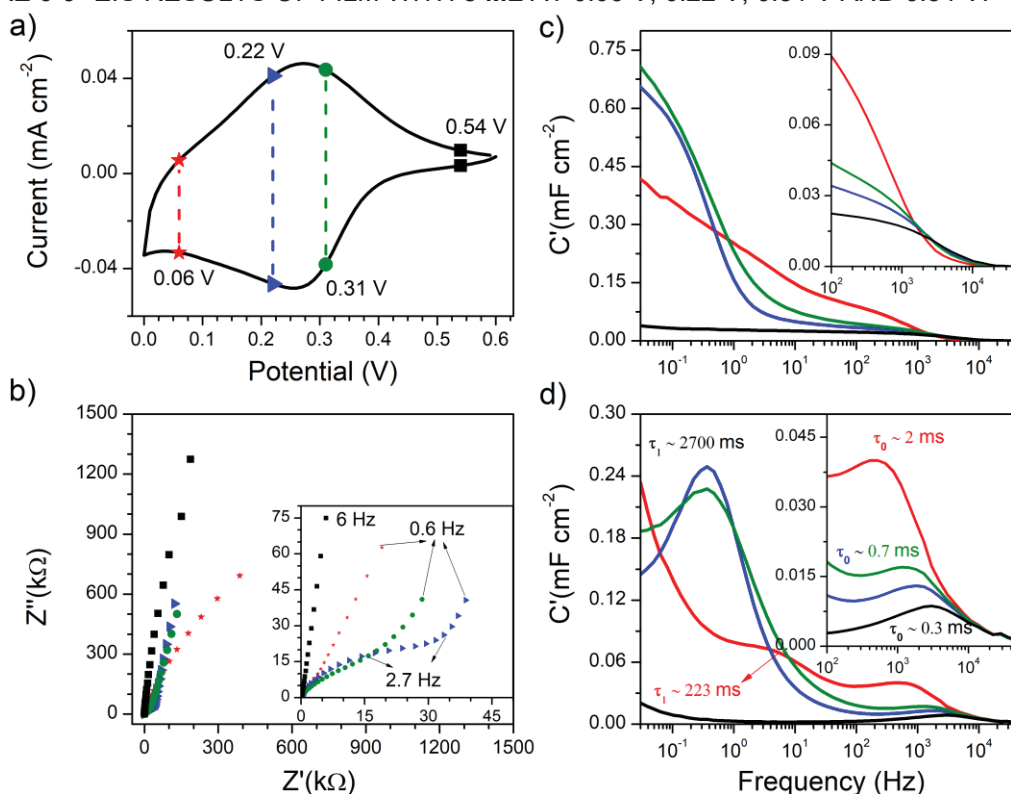
Specific capacitance of 204 Fg⁻¹ (or 1.02 mF cm²) was obtained for the electrode with 18 monolayers of AzoRu at 50 mV s⁻¹ which is a value higher or similar than the reported for other thin film electrodes involving ruthenium complexes (31.3 F g⁻¹[206] and 95.3 F g⁻¹[135]), iron based metallo-supramolecular polymer (131 F g⁻¹ [136]), and metal organic frameworks (90 F g⁻¹ [204]). But it is lower than the reported for a cobalt complex hybridized with polypyrrole (412.7 F g⁻¹ [203]). We report the capacitance values despite we have a faradaic electrode, considering that the voltammogram is close to that of a pseudocapacitive material (roughly squared with wide and symmetric peaks) within determined potential window (from 0.05 to 0.35 V). When the separation between the redox peaks is low and potential window is delimited around to redox peaks values, the voltammogram becomes closer to a capacitor-like voltammogram[55]. It should be remarked that the capacitance value makes sense only for electrodes with capacitive behavior which exhibit only one capacitance value (or with small deviations) in all the potential window. In this case, the electrodes at scan rates from 10 to 100 mV s⁻¹ could be considered pseudocapacitors in a potential window from 0.05 to 0.3 V or 0.35 V (redox peak width) as was shown by the analysis of current peak variation with the scan rate. Further analysis of the charge storage processes within electrodes was performed using EIS, which is discussed next.

6.2.3 EIS of Amphiphilic Triruthenium Cluster Electrodes.

The Figure 6-9 shows the EIS results for the AzoRu film of 8 ML at several potentials, which are pointed out in the voltammogram (Figure 6-9a). The potentials chosen were 0.22 V and 0.31 V which are close to $E_{1/2}$ (0.265 V), and 0.06 V and 0.54 V which are far from $E_{1/2}$. When the periodic perturbation in the potential is applied, some electrochemical processes occur, such as charge reorganization and transfer across the film-solution interface, ion

diffusion within the film and electron transfer reaction within the film. The last occurs if the potential perturbation values are enough to change the redox state of the molecules in the film. Those processes have distinct and characteristic time constants, so different frequency domains [249,285,287].

FIGURE 6-9- EIS RESULTS OF FILM WITH 8 ML AT 0.06 V, 0.22 V, 0.31 V AND 0.54 V.



a) cyclic voltammogram pointing out the potentials tested 0.06 V, 0.22 V, 0.31 V and 0.54 V, (b) Nyquist plot with an inset showing high frequencies region (c) capacitance and (d) complex capacitance plots vs. frequency with insets showing high frequency region.

SOURCE: Author. Reprinted from [301]

Figure 6-9b shows the real ($Z'(\omega)$) and imaginary ($Z''(\omega)$) part of impedance at several frequencies. Two regions were identified, the first characterized by an initial arc-line starting with $Z''(\omega)$ close to zero at very high frequencies and finishing at determined frequency with the transition to the second region which is characterized by a tilted line close to vertical, the mentioned features are more evident in the inset of Figure 6-9b for potentials close to the $\text{AzoRu}^{0/+}$ half-wave potential (blue and green line). The approaching to the real axis at very high frequencies indicates that the response is dominated by a resistive element attributed to charge transport in electrolyte. [249,285,287] The initial arc-line at high and intermediate frequencies is associated to the capacitive process of charge reorganization at interface in parallel to resistive processes associated with the redox reaction [249,287]. Consequently, the increasing of the real impedance in that arc-line is only evident when the potential tested is close enough to $E_{1/2}$ (blue, green, and red lines) whereas at potentials far from $E_{1/2}$ the resistive

process is not observed. A little perturbation at 0.54 V should not lead to significant reduction of the molecules which should be completely oxidized at that potential.

At low frequencies, a tilted line close vertical was observed in Nyquist plot indicating that the phase shift is close to 90 degrees. This capacitive behavior was attributed to the reaching of a quasi-stationary state with non-consuming species. That is, electroactive species and ion concentrations are stationary, and the diffusion layer has a length comparable with the characteristic physical dimensions of the electrode. So the diffusion layer is no longer "semi-infinite" within experimental frequency range and the electrode acts as blocking surface (non-consuming or adsorbing species). [285,287] This characteristic was observed for all the potentials tested, but when the potential was close to $E_{1/2}$ the tilted line began at lower frequencies (as low as 2.7 Hz). Additionally, the tilted line deflects on real axis at very low frequencies when the potential tested is far from $\text{AzoRu}^{0/+}$ half-wave potential. This phase shift decreasing suggests the presence of a resistive process, perhaps a leaking current or ion transfer to the film.

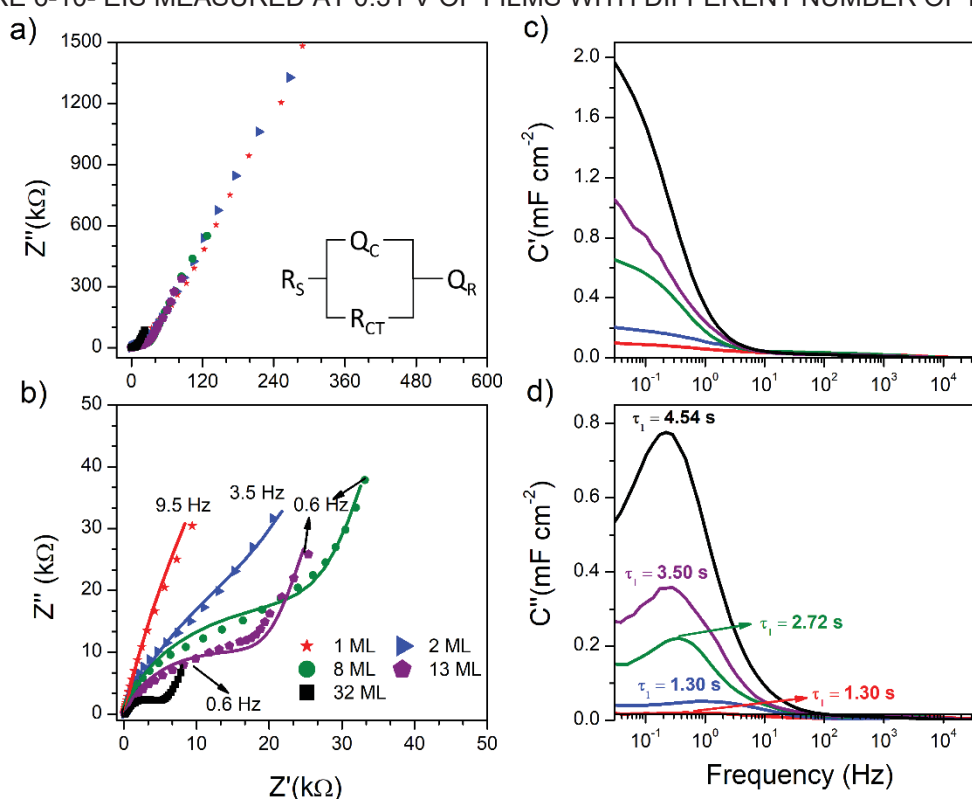
The real ($C'(\omega)$) and imaginary ($C''(\omega)$) part of the complex capacitance was calculated using equation 3.15 and are shown in Figure 6-9c and d respectively. $C'(\omega)$ gives the capacitance value of the whole system, whereas $C''(\omega)$ could be related with energy dissipation. [248,249] Also, the maxima in the $C''(\omega)$ plot points out the critical frequencies at which the system transits from a mostly resistive behavior at high frequencies to one mostly capacitive at low frequencies. A local maximum in $C''(\omega)$ at high frequencies was observed between 500 and 1500 Hz (see inset in Figure 6-9d) which was attributed to non-Faradaic processes (EDL rearranging). Peak frequency f points out a characteristic time constant $\tau = 1/f$. Interestingly the peak attributed to EDL exhibited a time constant τ_0 significantly higher at 0.06 V (2 ms vs. 0.7 ms) indicating the presence of a high time constant value process, maybe ion exchange at film interface since at this potential the film is totally reduced. Likewise, the capacitance value is higher at 521 Hz, it is 0.09 mF cm² at 0.06 V, 0.05 mF cm² at 0.22 and 0.31 V, and 0.03 mF cm² at 0.54 V. These results revealed that this process has higher capacitance.

When the potential is close enough to the half-wave potential of $\text{AzoRu}^{0/+}$, another maximum is observed in $C''(\omega)$ around 0.4 Hz corresponding to a time constant τ_1 value of 2700 ms. It could be attributed to the Faradaic process within the film, the capacitance value at that frequency region increases significantly when potentials are close to half-wave potential corroborating the important contribution of redox reaction to the charge storage. Interestingly at 0.06 V it is observed a shoulder around 4.5 Hz corresponding to τ_1 of 223 ms, suggesting again the presence of other process at lower potentials (positive polarization).

The EIS measured at 0.31 V for electrodes with different number of deposited layers is shown in Figure 6-10. The results for all the electrodes are similar to the previously described,

it is observed an initial arc-line starting close to the real axis ($Z''(\omega)$ close to zero) at very high frequencies and finishing at determined frequency with the transition to the second region which is characterized by a tilted line close to vertical (see Figure 6-10a and b). But the initial arc-line is more evident and the transition to the second region is observed at lower frequencies in thicker electrodes, indicating that the characteristic time of total consumption of the species, is higher for thicker electrodes. The shifting of the maximum $C''(\omega)$ to lower frequencies (or higher τ_1) as the number of layer increase (see Figure 6-10d) confirms that the Faradaic process needs longer times to occur in thicker electrodes. These results could be related with higher difficulty for electron diffusion through thicker films.

FIGURE 6-10- EIS MEASURED AT 0.31 V OF FILMS WITH DIFFERENT NUMBER OF LAYERS



(a) Nyquist plot with the equivalent circuit proposed for data interpretation, (b) inset of Nyquist plot at higher frequencies (c) capacitance and (d) complex capacitance plots vs. frequency. The Figure b) show the results from fitted circuit model as lines.

SOURCE: Author. Reprinted from [301]

EIS results were fitted to an equivalent circuit model exhibited in the inset of Figure 7a using the EIS Spectrum Analyser software. [247] The model consists in a resistance R_S in series with an "interfacial" impedance and a constant phase element Q_R . R_S is associated to electrolyte conductivity, electronic conductivity, and contacts of all components. The interfacial impedance consists in a parallel array of a constant phase element Q_C , representing the non-faradaic processes (EDL), and a resistance quantifying the strength of electronic coupling of the redox sites to the substrate and Q_R represent the capacity attributed to the redox reaction. The impedance of the constant phase element is defined as $Q^{-1}(j\omega)^{-n}$, which is equal to

capacitor impedance when $n=1$, so it could be considered as a non-ideal capacitance when the n value is higher than 0.75 and lower than 1.

The results of the fitting are provided in Table 6-1, it is worth to remark that the n value varied from 0.85 to 0.90 for the constant phase element representing the redox capacitance, also the Q_R value increased for higher thickness (1 **ML**: 1.2, 2 **ML**: 2.6, 8 **ML**: 7.4, 13 **ML**: 11 and 32 **ML**: 51 $\mu\Omega^{-1} s^n$), indicating the higher redox capacity of the thicker electrodes. Despite the Q_R value is not exactly the capacitance value, it is expected that the trend found would be maintained for the capacitance values since the n values are similar. The R_S is low and similar for all the electrodes (131 - 144 Ω), and R_{CT} oscillates between 21 000 and 43 000 Ω as thickness increases but their parameter estimation errors are considerably high (higher than 10%), probably the data without completely defined initial arc-line contributed to the poor determination of this parameter.

TABLE 6-1- ESTIMATED PARAMETERS VALUES OF CIRCUIT MODEL ELEMENTS AND THEIR RESPECTIVE ESTIMATION ERRORS.

Electrode	$R_S(\Omega)$		$Q_C(\mu\Omega^{-1}s^n)$		n_C		$R_{CT}(k\Omega)$		$Q_R(\mu\Omega^{-1}s^n)$		n_R	
		%error		%error		%error		%error		%error		%error
1 ML	89	3.9	2.3	5	0.87	0.9	43	15	1.2	3	0.90	0.4
2 ML	132	10	2.0	7	0.81	0.9	25	17	2.6	7	0.88	1
8 ML	142	11	1.4	6	0.86	2	27	13	7.4	11	0.90	2
13 ML	161	11	1.3	7	0.82	1	21	13	11	13	0.85	3
32 ML	143	9	5.4	5	0.71	0.8	7	10	51	7	0.87	3

The fitting was performed with Levenberg-Marquard algorithm for nonlinear least squares as implemented in EIS spectrum analyzer. [247]

SOURCE: Author.

Summarizing, AzoRu LB film electrodes store energy mainly through redox reaction. The heterogeneous electron transfer and charge transfer between molecules is fast enough to lead to pseudocapacitive behavior at determined condition, as it is expected for electroactive molecules with fast redox reaction bounded to the surface. Additionally, the redox peak of AzoRu LB electrodes is significantly wide, so the pseudocapacitive behavior is extended in a relevant potential window and could be harnessed. However, this behavior is deteriorated at high scan rates (higher than 100 $mV s^{-1}$) and for thicker electrodes as evidenced by the larger ΔE and the larger characteristic time constant τ_1 . It was attributed to ion transport limitations and higher difficulty for electron transfer through thicker films. Those limitations led to lower capacitance at high rates and lower gravimetric capacity in thicker films. Therefore, electrodes with improved charge transport within the film should lead to thicker redox film with better performance at high scan rates. The next chapter offer additional insights in electrochemical behavior of AzoRu LB film electrodes through mathematical modeling.

7 UNDERSTANDING ELECTROCHEMICAL BEHAVIOUR OF THIN FILMS BASED ON IMOBILIZED REDOX MOLECULES

A mathematical model was developed to aid in the interpretation of AzoRu CV results, the model describes an electroactive film on a conductive substrate conformed by n number of layers with the same quantity of molecules, which present a monoelectronic redox reaction at a determined potential.

7.1 MODEL DEVELOPMENT

The system here studied, shown in Figure 7-1, consists in a conductive substrate with n layers of molecules which undergoes the reaction written in equation 7.1

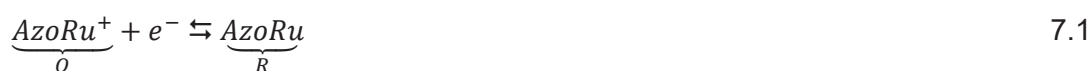
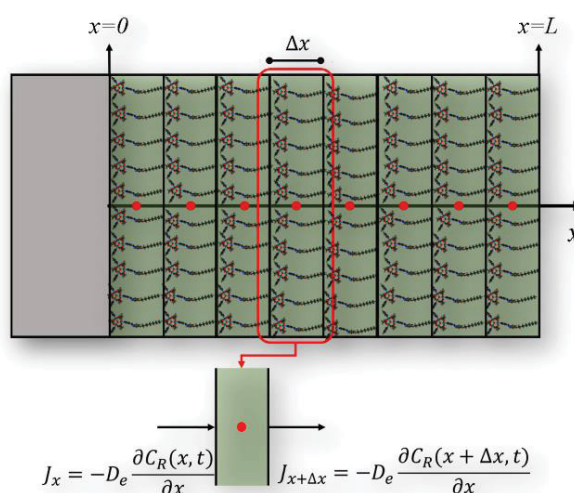


FIGURE 7-1- SCHEME OF FILM ELECTRODE MODEL WITH EIGHT LAYERS.



The axis x , in which diffusion occurs, is shown along with the boundaries. The substrate is shown as a gray rectangle and each layer of the film as a green rectangle. Each layer is considered as a finite "volume" of thickness Δx and with a node point located at centre of the "volume". An inset of one layer is shown along with the equations of the molar fluxes (J_i) in the boundaries of that layer which is defined as the diffusion coefficient (D_e) times the gradient of R concentration (C_R) along x axis.

SOURCE: Author. Reprinted from [301]

The molecules are in fixed positions in each layer, the electrons and counterions could be diffused through the film, rather along thickness direction (x direction) generating an apparent diffusion of R specie. For example, if all the species are initially reduced, upon application of appropriated potential difference to the system, the reduced species just outside of the current collector are oxidized. The charge gradient generated acts as a driving force promoting the electron diffusion towards the support. This phenomenon was considered as the

diffusion of reduced species from the film to the support instead of generation/consumption of species in that way was considered the dependence of the electron transfer reaction in each layer on the redox states of the adjacent layers.

7.1.1 Mass Balance

A matter balance of reduced species R was applied in determined control volume $\Delta x \Delta y \Delta z$, considering that only the diffusion along the x direction is significant to describe the electrochemical behavior of the system and non-generation or consumption of species in the layer. So, the moles entering or leaving the volume control is expressed as the molar flux J times the area $\Delta y \Delta z$ crossed by the flux. And the balance can be derived as in Equation 7.2 considering that the flux is described by the Fick's law ($J_x = -D_e \frac{\partial C_R}{\partial x}$) and surface concentration can be defined as $\Gamma_R = C_R \Delta x$:

$$(J_x - J_{x+\Delta x}) \Delta y \Delta z = \Delta x \Delta y \Delta z \frac{\partial C_R}{\partial t}, \text{ with } J_x = -D_e \frac{\partial C_R}{\partial x}, \Gamma_R = C_R \Delta x$$

$$\frac{\partial \Gamma_R(x,t)}{\partial t} = D_e \frac{\partial^2 \Gamma_R(x,t)}{\partial x^2} \text{ note that } \Gamma_R(x,t) = \frac{C_R(x,t)}{\Delta x} \quad 7.2$$

The solution of the partial differential equation 7.2 requires boundary conditions and one initial condition. The formers were determined by mass balance in the first layer ($x = 0$) and the last layer ($x = L$). In $x = 0$ there are generation or consumption of R and no flux of R in the $x = 0$ boundary. The reaction rate r_R in moles per unit of area, is described as a first order reaction with k_f and k_b as the rate parameters for reduction and oxidation reactions respectively and using the surface concentration just outside of the current collector ($x = 0$). Then, the R balance can be written as in equation 7.3.

$$\Delta x \Delta y \Delta z \frac{\partial C_R(0,t)}{\partial t} = -J_{x+\Delta x} \Delta y \Delta z + R_R, \text{ with } J_{0+\Delta x} = -D_e \frac{\partial C_R(\Delta x,t)}{\partial x}, r_R = \frac{R_R}{\Delta y \Delta z}, \Gamma_R = C_R \Delta x$$

$$\frac{\partial \Gamma_R(0,t)}{\partial t} = \frac{D_e}{\Delta x} \frac{\partial \Gamma_R(\Delta x,t)}{\partial x} + r_R \quad 7.3$$

$$\text{with } r_R = k_f \Gamma_O(0,t) - k_b \Gamma_R(0,t) \quad 7.3'$$

Whereas the condition in $x = L$ is determined by a balance in the last layer, which involves no flux of R in the $x = L$ boundary. So, the balance can be written as in equation 7.4.

$$\Delta x \Delta y \Delta z \frac{\partial C_R}{\partial t} = J_x \Delta y \Delta z, \text{ with } J_x = -D_e \frac{\partial C_R(x,t)}{\partial x}, \Gamma_R = C_R \Delta x$$

$$\frac{\partial \Gamma_R(L,t)}{\partial t} = -\frac{D_e}{\Delta x} \frac{\partial \Gamma_R(L,t)}{\partial x} \quad 7.4$$

Additionally, one initial condition is required to define completely the problem. The initial condition first is assumed to be a fraction of Γ^S as is written in equation 7.5, then a stationary

value of Γ_R is calculated simulating the application of a constant potential with value equal to the initial potential value of the CV, finally CV is simulated.

$$\Gamma_R(x, 0) = a \Gamma^S \quad 0 \leq a \leq 1 \quad 7.5$$

7.1.2 Constituent Equations and Additional Considerations

The partial differential equation problem specified by expressions 7.2-7.5 depends on Γ_O and Γ_R (see equation 7.3). So, we need one more equation to solve the problem. The equation is given by the total mass balance, we can expect that the total concentration of molecules in each layer Γ^S remains constant. Then, the surface concentration of reduced (Γ_R) and oxidized (Γ_O) species are related as in equation 7.6:

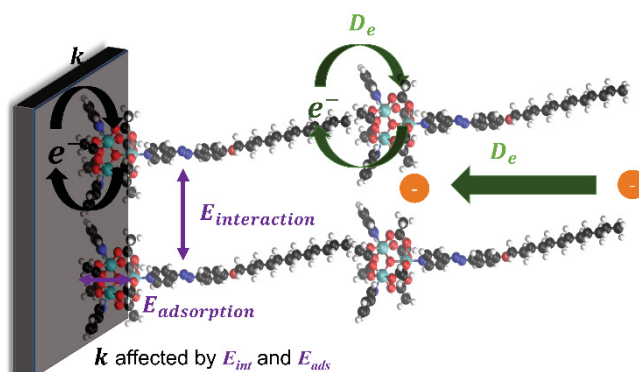
$$\Gamma_R(t) + \Gamma_O(t) = \Gamma^S \quad 7.6$$

Additionally, kinetic and diffusion parameters need to be specified. The diffusion parameter is assumed as a constant value D_e . The one monolayer thickness Δx , required in equations 7.3 and 7.4, was estimated from the optimized geometry obtained with DFT, as the “vertical” distance between CH_3 in the long chain tail of AzoPy ligand and CH_3 in the acetate opposed to the AzoPy ligand, so the film thickness L is obtained multiplying Δx by the number of layers. Whereas kinetic parameter is an Arrhenius type expression modified to include the effects of overpotential ($\eta = E - E^0$) on the energy barrier for electron transfer, just like in Butler-Volmer kinetics (see equation 7.7). Below is shown the equation defined for an electroactive specie in solution with one step electron transfer:

$$\begin{aligned} k_f &= A_f e^{-\frac{\Delta G_{f0}^*}{RT}} e^{-\alpha \frac{F\eta}{RT}} = k^0 e^{-\alpha \frac{F\eta}{RT}} \\ k_b &= A_b e^{-\frac{\Delta G_{b0}^*}{RT}} e^{(1-\alpha) \frac{F\eta}{RT}} = k^0 e^{(1-\alpha) \frac{F\eta}{RT}} \end{aligned} \quad 7.7$$

Typically, ΔG_{f0}^* and ΔG_{b0}^* are related to the energy barrier for reduction and oxidation reactions when the electrode potential is E^0 (at equilibrium), the barrier is defined as the energy difference between the transition state and the reactants ($G_{\text{TS}} - G_R$). A_f and A_b are related to the frequency of attempts of those reactions. α indicates how much the reduction reaction is affected by η , and k^0 is the reaction rate constant when the interface is at equilibrium ($\eta = 0$) and $C_R = C_O$. These expressions were modified to describe the redox reaction of molecules fixed in a film. Then, the energy barriers for reduction (ΔG_f^*) and oxidation (ΔG_b^*) are redefined to include the interaction between neighbor molecules and with the substrate, interactions arising when molecules are in the film, such as is shown in Figure 7-2.

FIGURE 7-2- SCHEME SHOWING PARAMETERS CONSIDERED IN KINETIC MODEL AND IN CHARGE TRANSPORT DESCRIPTION



SOURCE: Author. Based on [301]

Interaction with substrate, in a first approximation we consider that the activation energy is modified by the interaction energy of the molecule (R or O) with the substrate ΔG_i^{ads} . So, the activation energy for molecules fixed to the substrate (ΔG_{fs}^* or ΔG_{bs}^*) is as equation 7.8:

$$\begin{aligned}\Delta G_{fs}^* &= \Delta G_{f0}^* - \Delta G_O^{ads} \\ \Delta G_{bs}^* &= \Delta G_{b0}^* - \Delta G_R^{ads}\end{aligned}\quad 7.8$$

The equation 7.8 could be rationalized assuming that ΔG_{f0}^* is the energy activation for the electroactive specie in solution. So, when molecules are fixed to the substrate, reactants energy (and hence the energy barrier) is changed by a value equal to reactant adsorption energy. Note that an attractive interaction of O with substrate (negative ΔG_O^{ads}) which stabilize it leads to the increase of energy barrier for the reduction reaction ΔG_{fs}^* .

Also, when we consider the equilibrium case ($k_f \Gamma_O = k_b \Gamma_R$) we can derive with the aid of equations 7.7 and 7.8:

$$\frac{\Gamma_O}{\Gamma_R} = \frac{k_b}{k_f} = e^{\Delta G_R^{ads} - \Delta G_O^{ads}} e^{\frac{nF(E-E^0)}{RT}} \Rightarrow E = E^0 + \frac{\Delta G_O^{ads} - \Delta G_R^{ads}}{nF} + \frac{RT}{nF} \ln \frac{\Gamma_O}{\Gamma_R}\quad 7.9$$

Equation 7.9 show that the potential in which $\Gamma_O = \Gamma_R$ is shifted according to the difference between adsorption energies of oxidized and reduced molecules $\Delta E_{ads} = \Delta G_O^{ads} - \Delta G_R^{ads}$. Note that if the oxidized molecules are more stable (more negative ΔG_O^{ads}), the potential is shifted toward negative values. In contrast if the reduced molecules are more stable the potential is shifted toward positive values.

Lateral interactions, Lateral interactions change the stability of oxidized and reduced molecules within the film. It is reasonable to think that the energy barrier for the oxidation or reduction is modified by those interactions. Some isotherm models as Temkin or Frumkin isotherm, express that the energy of adsorption change with that interaction, hence it is function of the surface concentration. Assuming that the changes in adsorption energy is linearly related to Γ_i , just as is assumed in other previous works, [93,302,303] the adsorption energy within film can be written as in equation 7.10:

$$\begin{aligned}\Delta G_{film,O}^{ads} &= \Delta G_O^{ads} - \gamma\Gamma_O \\ \Delta G_{film,R}^{ads} &= \Delta G_R^{ads} - \gamma\Gamma_R\end{aligned}\quad 7.10$$

Note that γ indicates how the adsorption energy of species vary with coverage changes. If the interaction is attractive at high Γ_O or Γ_R , the Gibbs adsorption energy should be more negative, so γ should be positive. Whereas a repulsive interaction at high Γ_O or Γ_R lead to less negative Gibbs adsorption energy, so γ should be positive. So γ can be seen as a balance of interactions between two O or two R molecules (“self-interaction”) and between R and O molecules (“crossed interaction”). When “self-interaction” is less favorable than “crossed-interaction” γ becomes negative since the interaction is less favorable at high Γ_O or Γ_R . We can redefine the energy barrier according to the idea expressed in the equation 7.11:

$$\begin{aligned}\Delta G_{fs}^* &= \Delta G_{f0}^* - \Delta G_{film,O}^{ads} = \Delta G_{f0}^* - \Delta G_O^{ads} + \gamma\Gamma_O \\ \Delta G_{bs}^* &= \Delta G_{b0}^* - \Delta G_{film,R}^{ads} = \Delta G_{b0}^* - \Delta G_R^{ads} + \gamma\Gamma_R\end{aligned}\quad 7.11$$

Using this definition for the energy barrier, the Butler-Volmer equations (equation 7.7) can be modified as in equation 7.12

$$\begin{aligned}k_f &= A_f e^{-\frac{\Delta G_{f0}^*}{RT}} e^{\frac{\Delta G_O^{ads} - \gamma\Gamma_O}{RT}} e^{-\alpha\frac{F\eta}{RT}} = k^0 e^{-\frac{\Delta G_{film,O}}{RT}} e^{-\alpha\frac{F\eta}{RT}} \\ k_b &= A_b e^{-\frac{\Delta G_{b0}^*}{RT}} e^{\frac{\Delta G_R^{ads} - \gamma\Gamma_R}{RT}} e^{(1-\alpha)\frac{F\eta}{RT}} = k^0 e^{-\frac{\Delta G_{film,R}}{RT}} e^{(1-\alpha)\frac{F\eta}{RT}} \\ \text{with } \Delta G_{film,O} &= \gamma\Gamma_O - \Delta G_O^{ads} \text{ and } \Delta G_{film,R} = \gamma\Gamma_R - \Delta G_R^{ads}\end{aligned}\quad 7.12$$

Summarizing, the kinetic parameters above defined depends on k^0 , α which are parameters defined for Butler-Volmer kinetics; ΔG_O^{ads} and ΔG_R^{ads} account the interaction with substrate; γ accounts the interactions between molecules. Also, they are function of the temperature T , the overpotential η and the surface concentration Γ . Molecules within the film interacts permanently with the substrate but the interaction of molecules in “external” layers should be screened by “internal” layers. So, in a first approximation the interactions are accounted by ΔG_i^{ads} calculated as the mean value of all layers in the film ($\sum_{k=1}^n \Delta G_i^{ads}(k)/n$).

The electrochemical response depends on the electron flux from the film to current collector which, according to Faraday law, is proportional to the generation of O and R consumption, which can be expressed in terms of surface concentration Γ variation as in Equation 7.13. As can be noted the current from oxidation is defined as positive, that is, when electrons flow from the film to the current collector (working electrode).

$$\frac{i}{n_eFA} = \frac{\partial\Gamma_O}{\partial t} - \frac{\partial\Gamma_R}{\partial t} = \frac{(i_a - i_c)}{n_eFA}\quad 7.13$$

The model presented was expressed in terms of dimensionless variables $\theta_R = \Gamma_R/\Gamma^S$, $z = x/L$, and $t' = t/t_f$. With t_f the total time of duration of electrochemical experiment. The dimensionless equations were discretized in the spatial domain to implement the

computational simulation of the model conveniently. In this process emerged a dimensionless factor $\frac{D_e t_f}{L^2 \Delta z^2}$. It is a dimensionless quantity relating the mean squared displacement traveled by the charge during the whole time of the experiment ($l_e^2 = D_e t_f$) and the squared length of one monolayer ($\Delta x^2 = L^2 \Delta z^2$), which we named Kn_{ML} . An analogous expression could be defined to the whole film dividing for the length L of the film instead of $L\Delta z$, so $Kn = \frac{D_e t_f}{L^2}$. Considering that the t_f for one cycle in the cyclic voltammetry is defined as two times the potential window divided by the scan rate $t_f = 2(E_2 - E_1)/v$. Then, $Kn = \frac{2D_e(E_2 - E_1)}{L^2 v}$ depends on the scan rate, film thickness and diffusion coefficient for the charge and is a parameter which allows to compare the charge transport rate within the potential perturbation rate.

7.2 RESULTS FROM MODEL AND ANALYSIS

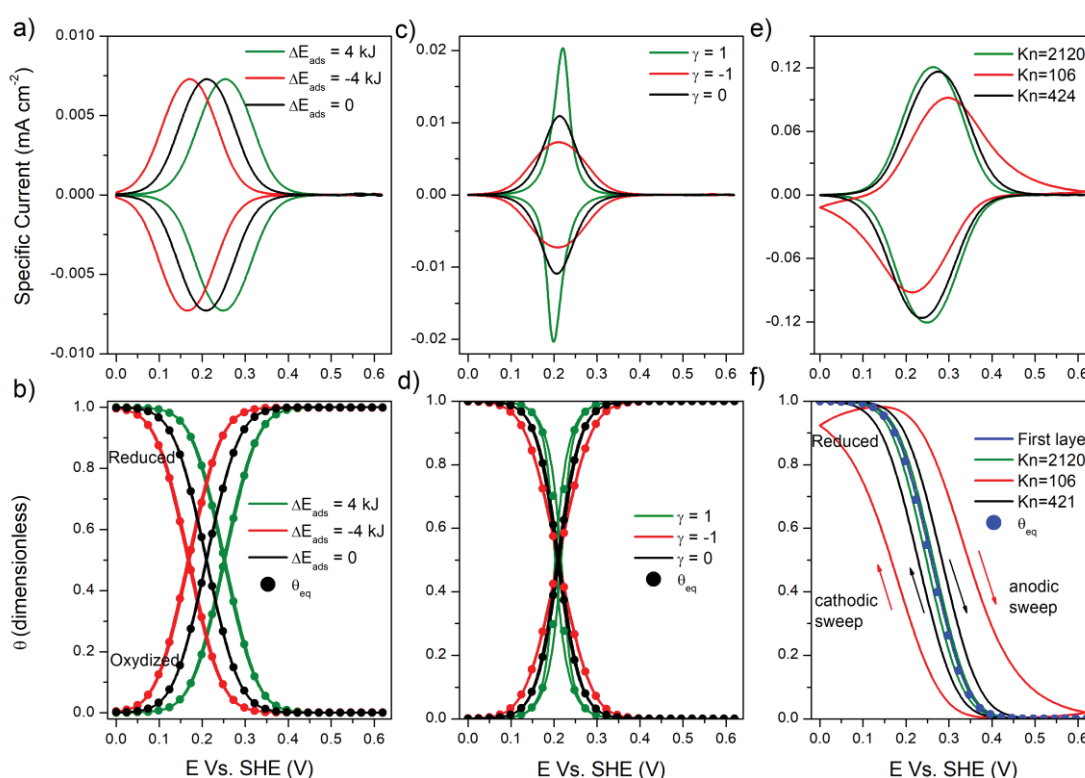
7.2.1 Effects of Main Parameters on Electrochemical Behavior

The model proposed describe the shifting in $E_{1/2}$, the peak width and the separation between peaks through parameters such as ΔE_{ads} , γ and Kn . The shifting in $E_{1/2}$ depends on the difference between the adsorption energy of reduced and oxidized species ($\Delta E_{ads} = \Delta G_O^{ads} - \Delta G_R^{ads}$). As it was above demonstrated (see equation 7.9), the $E_{1/2}$ shifting is negative when the adsorbed oxidized species in the film are more stable than adsorbed reduced species. So, we can expect voltammogram peaks are shifted to lower potentials as is shown in Figure 7-3a. This shifting is consequence of the stability of molecules in the film, as the oxidized species are more stable the reduction of the species is more difficult so we need lower potentials to reduce the surface species (see red line in Figure 7-3), we also noticed that the parameters used lead to electrochemically reversible case and the surface coverage is the same as the expected for the Nernstian case. In contrast, the $E_{1/2}$ shifting is positive when the adsorbed reduced species in the film are more stable than adsorbed oxidized species indicating that it is easier to reduce the oxidized species.

The interactions between oxidized and reduced molecules within the film could lead to wider or narrower peaks in the voltammogram, since it leads to a dependence of the electrochemical reaction kinetics on the surface concentration. [93,303,304] When the reaction is fast enough (behaves as electrochemically reversible reaction) the parameter γ accounting by the interactions among molecules have a great effect on the peak width. A negative γ value indicates that the “crossed interaction” is energetically more favorable than the “self-interaction”, so we can expect that the surface concentrations of reduced and oxidized species tend to be similar in a wider potential window as can be seen in the Figure 7-3d (red line),

consequently the peak in voltammogram is wider. In contrast, a positive γ value indicates that the “crossed interaction” is energetically less favorable, so we can expect that the potential window with similar coverage of reduced and oxidized species be narrower as can be seen in the Figure 7-3d (green line), consequently the peak in voltammogram is narrower. It indicates that controlling the interactions between the molecules on the film would change the electrochemical response from a voltammogram with sharp redox peaks to a more “squared shaped” voltammetry.

FIGURE 7-3- SIMULATED CYCLIC VOLTAMMOGRAM AND COVERAGE IN ONE MONOLAYER VARYING ADSORPTION ENERGY, INTERACTION BETWEEN MOLECULES AND THE CHARGE DIFFUSION PARAMETERS.



a) Cyclic voltammogram and b) coverage for electrode of 1 **ML** varying the adsorption energy difference $\Delta E_{ads} = \Delta G_O^{ads} - \Delta G_R^{ads}$. c) Cyclic voltammogram and d) coverage for electrode of 1 **ML** varying the interaction parameter between molecules γ . e) Cyclic voltammogram and f) coverage for electrode of 13 **ML** varying the electron diffusion parameter Kn .

SOURCE: Author.

Finally, the description of charge transport within the whole film and the kinetic parameter k^0 allows to account part of the peak separation ΔE . A relatively small k^0 value led to non-ideal ΔE values even in 1 **ML** film and low scan rates, whereas the electron diffusion parameter have important effects in ΔE for thicker electrodes. The dimensionless parameter $Kn = l_e^2/L^2$ which compare the mean squared displacement of the charge and the dimension of electron allows to rationalize the trends in ΔE . The l_e^2 is proportional to the diffusion parameter D_e and inversely proportional to the scan rate ($Kn = \frac{2D_e(E_2-E_1)}{L^2 v}$). So, lower D_e leads

to lower displacement hence lower Kn , consequently the charge could be no transported fast enough to species in the layers far from substrate as compared with the experiment time. So, we can expect that ΔE increases as the value decreases, lower Kn values indicate that the displacement of charge in the time of the experiment is shorter and getting closer to the film thickness. Therefore, in the cathodic sweep, the electron diffusion from substrate to all the layers is slow respect to the potential perturbation and the quantity of reduced species (θ_R) in the last layer would look delayed in the potential respect to the first layer as is observed in Figure 7-3 (red line). Whereas at high Kn , θ_R in the last layer would be similar to that in the first layer as is observed in Figure 7-3 (green line).

7.2.2 Interpretation of Experimental Results According to the Model

The results previously described allows us to explain and reproduce the main experimental findings making educated guesses for the model parameters shown in Table 7-1. The theoretical voltammogram shown in displayed current and potential peaks similar to the experimental values. Also, the peaks width is like the experimental, the wider peaks is partly explained by the favored interaction between oxidized and reduced molecules within the film respect to the interactions between oxidized molecules (negative Γ). The oxidized molecules are cations which probably have repulsive interactions between them. Despite of the reproduction of peak widths some differences are evidenced in the slope of the anodic and cathodic peaks, probably related with capacitance which were no included in our model and charge transport issues which could be better described. Charge transport was described by the homogeneous parameter D_e , but the films have inhomogeneities due to aggregates and molecules filling the spaces between neighboring molecules. Those factors may change the electron transfer between molecules of adjacent layers.

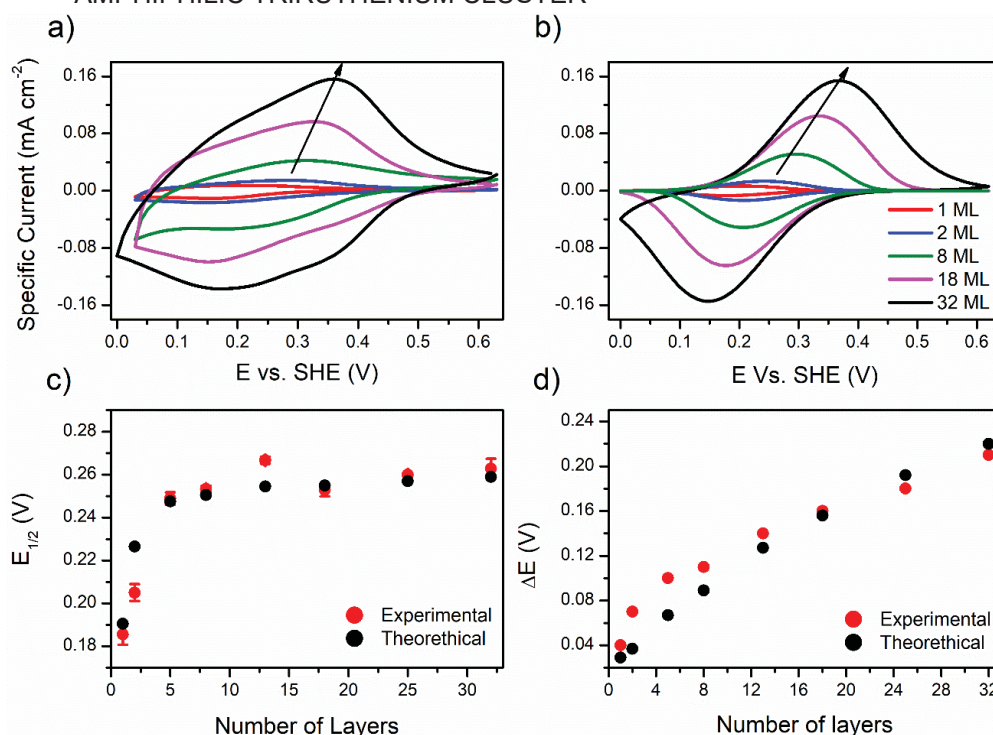
TABLE 7-1- PARAMETER VALUES FOR SIMULATION OF VOLTAMMOGRAMS SHOWN IN FIGURE 7-4.

Parameter	Value	Parameter	Value	Parameter	Value
k^0	8 s^{-1}	Kn_{ML}	954	E^0	0.21 V
α	0.5	Γ_s	$0.23 \text{ nmol cm}^{-2}$	E_1	0 V
$\gamma\Gamma_s/RT$	-1.25	$\Delta x = L\Delta z$	$2.6 \times 10^{-7} \text{ cm}$	E_2	0.62 V
$\Delta G_O^{ads}(1)$	-6.9 kJ	$\Delta G_O^{ads}(k)$	-0.4 kJ	ν	0.05 V s^{-1}
$\Delta G_R^{ads}(1)$	-5.0 kJ	$\Delta G_R^{ads}(k)$	-5.0 kJ	T	298 K

The Figure 7-4 shows that simulated ΔE and $E_{1/2}$ followed a trend very similar to the experimental one. Therefore, the experimental trend in $E_{1/2}$ was attributed to the variation in adsorption energy of the molecules in the first monolayer with respect to the subsequent deposited layers. In the first monolayer the oxidized molecules would be more stable than the reduced molecules, that is, the interaction of positively charged oxidized AzoRu with ITO

substrate is stronger than that of the neutral reduced molecules, it led to $E_{1/2}$ of 0.18 V which is lower than $E_{1/2}$ of species in solution 0.21 V. Whereas in the subsequent layers the oxidized molecules would be less stable than the reduced molecules probably because of higher effect of electrostatic repulsion between ruthenium clusters groups or counter-ion intercalation in the oxidized film. Then $E_{1/2}$ increases as the number of layers increases getting closer asymptotically to a value of 0.26 V.

FIGURE 7-4- EXPERIMENTAL AND THEORETICAL CYCLIC VOLTAMMOGRAM OF LB FILMS OF AMPHIPHILIC TRIRUTHENIUM CLUSTER



Cyclic voltammogram at 50 mV s⁻¹ obtained a) experimentally and b) theoretically for the electrodes with different number of monolayers (ML). Comparison between experimental and theoretical variation of c) $E_{1/2}$ and d) ΔE_p .

SOURCE: Author

Besides, the experimental trend observed for ΔE_p was attributed partly to the magnitude of the electron transfer rate within the film. A relatively small k^0 value led to non-ideal ΔE values even in 1 ML film, whereas electron diffusion limitations explain the trend in ΔE for thicker electrodes. As was mentioned the Kn value ($Kn = l_e^2/L^2$) helps to rationalize the trend in ΔE . The mean squared displacement of the charge within the film l_e^2 in determined time interval have a characteristic value film depending on their structure and chemistry. As the film thickness increases the Kn value decreases, since the film thickness get closer to the path length traveled by the charge in the time of the experiment. Therefore, in the cathodic sweep, the charge transport from substrate to all the layers is slow respect to the potential perturbation leading to higher separation between peaks as film thickness increases. The Kn

value also helps to explain the higher ΔE_p as the scan rate increases. Since higher scan rates involve lower time intervals for the charge displacement, hence lower l_e^2 .

The trends in $E_{1/2}$ and ΔE_p obtained with the model also allow us to explain the apparently chaotic trend of the cathodic peak potential (E_{PC}) described on the previous chapter. The increasing of both led to an E_{PC} increase as thickness increases, and from 13 **ML** to an E_{PC} decreasing as thickness further increases. Comparing the values calculated from the model for E_{PC} , $E_{1/2}$ and ΔE_p with the experimental ones, we note a general agreement between both values obtaining errors below 9%. But some points have greater errors such as the ΔE_p values for electrodes with 2, 5 and 8 **ML**. Summarizing, the electrochemical response of the AzoRu films was influenced by interactions modifying the stability of oxidized and reduced molecules in the film. i) we propose that the oxidized molecules in layers far from substrate are less stable because of the repulsive force between oxidized molecules or counter-ion intercalation in the oxidized film. So, the reduction process is more favorable (redox peaks at higher potential) in thicker electrodes. ii) The interaction between reduced and oxidized molecules is favored leading to wide redox peak. iii) The ΔE_p trend is explained by the magnitudes of charge transfer rates.

TABLE 7-2- REDUCTION PEAK POTENTIAL, HAL-WAVE POTENTIAL AND PEAK SEPARATION OBTAINED EXPERIMENTALLY AND FROM SIMULATIONS.

Electrode	E_{PC} (V)	E_{PC} model	$E_{1/2}$ (V)	$E_{1/2}$ model	ΔE (V)	ΔE model
1 ML	0.17	0.176	0.190	0.191	0.04	0.03
2 ML	0.18	0.208	0.215	0.225	0.07	0.04
5 ML	0.20	0.214	0.250	0.246	0.10	0.07
8 ML	0.20	0.206	0.255	0.251	0.11	0.09
13 ML	0.19	0.191	0.265	0.255	0.14	0.13
18 ML	0.18	0.177	0.255	0.257	0.16	0.16
25 ML	0.17	0.161	0.260	0.259	0.18	0.19
32 ML	0.16	0.149	0.260	0.261	0.21	0.22

7.3 CLUES FROM MODEL TO IMPROVE REDOX FILM ELECTRODES

The model proposed suggests that when the path length traveled by the charge in the time of the experiment is so short that it approaches to the film thickness, we observed a delay in the reduction/oxidation of layers far from substrate and consequently a separation between voltammogram peaks. It is observed when charge transfer within the film is slow (low D_e) or the scan rate is too high. Therefore, electrodes with higher accessible redox active sites per unit of area, improved electron transfer and ion diffusion within the film (which is interrelated with electron transfer) should lead to thicker redox film with better performance at high scan rates. The electrodes could be improved through nano-porous supports or giving a porous structure to the active film through porous templates. This strategy has been previously applied to metal oxides leading to higher volume-based capacity at high rates owed to the higher

accessible sites and the formation of ion transport channels for fast charge transport within the electrode.[110,178,196,305]

Some feasible strategies to obtain LB films with improved energy storage performance are i) the modification of the conditions for LB films fabrication to obtain films with different organization and appropriated channels for ion diffusion and better electronic conduction within the film. ii) The choosing of film components (molecules and materials) to tune the electronic coupling between materials within the film and between the current collector and the materials within the film leading to improved electron transfer.[85,306] For example, the including of a molecule which interacts with the ruthenium cluster through orbitals energetically and spatially more accessible could improve the charge transfer from ruthenium complexes to the substrate and lead to a ΔE_p close to zero as was previously demonstrated by our research group [307].

Therefore, the challenge would be construct thick films with high capacity at high rates i) through the engineering of metal complexes using ligands and integrating it with other materials to obtain fast redox reactions and to enhance the electron transport process, ii) the design of film structure to obtain organized structure which facilitate the ion diffusion within the film. Additionally, the choosing of a substrate that enhances the heterogeneous electron transfer rate would contribute to the improvement of thicker electrodes performance. Additionally, the model here presented could be improved including the explicit description of counter-ion movement within electrolyte, at film-electrolyte interface, and within the film which would be important to optimize the interface electrode electrolyte and the film structure to decrease the performance limitations attributable to charge transport in the system.

8 ELECTRODE STRUCTURES: ELECTRODES BASED ON RUTHENIUM COMPLEXES HYBRID LANGMUIR-BLODGETT HETEROSTRUCTURES

The performance of energy storage electrodes can be improved enhancing the charge transport through the whole film. As was above suggested, organized structures may favor the ion transport through films and the integration with other materials or molecules, such as conductive materials, may improve the electron transport. Hybrid 2D heterostructures are assemblies of different materials held together mostly by non-covalent interactions, which allow to exploit the synergy between two or more materials and to tune the properties of the materials.[308–310] Moreover, they could be assembled into ordered architectures with channels or ions insertions. However, it remains as a challenge to be addressed because of restacking problem owing to interactions between sheets, which lead to decrease the accessible area or conducting channels. [73]

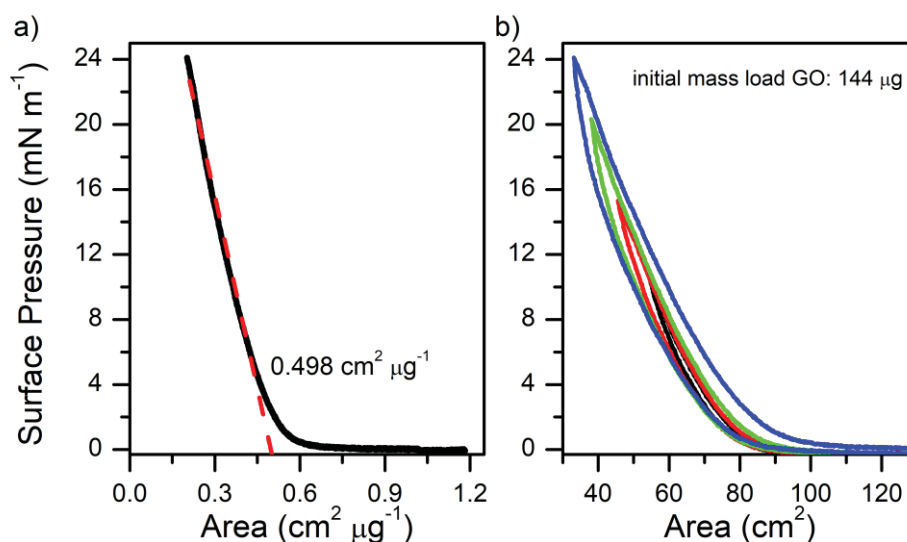
The previous sections just suggested that despite of the combination of capacitive and faradaic energy storage of graphene and triruthenium cluster could exhibit higher capacity, the graphene flakes aggregation induced by the presence of triruthenium cluster limits its storage capacity at higher specific discharge currents. Likewise, the difficulty for electron transport through thick films of amphiphilic triruthenium cluster, probably due to poor conductivity of the material or electronic coupling between molecules, limits the storage capacity of thick films at higher specific discharge currents. Therefore, electrodes with enhanced electron transport and ion diffusion are required, which can be achieved through materials choosing and film structure design as was suggested in the section 7.3.

Herein, we developed a hybrid heterostructured film based on graphene and triruthenium cluster fabricated with a layer-by-layer strategy alternating each material and using the Langmuir-Blodgett technique. Particularly, the Langmuir-Blodgett technique was used since it allow to control the interfacial structures. [79,198,292] It is expected to obtain an electrode with both capacitive and faradaic energy storage, an improved conductivity due to graphene presence, a less aggregated structure due to the use of LB technique to obtain thin films of exfoliated graphene oxide and the layer-by-layer strategy which intercalates triruthenium cluster cations between graphene layers, and better electron transfer in the whole film due to the expected coordination between graphene and triruthenium cluster through oxygen groups. This strategy was motivated by the previous findings described in this thesis and our previous experience with heterostructured Langmuir-Blodgett films based on organic amphiphilic molecules exhibiting charge storage through capacitive mechanism and amphiphilic ruthenium complex exhibiting charge storage through redox mechanism described in our other work. The characterization results of hybrid heterostructured film are presented in this section.

8.1 STRUCTURE OF HETEROSTRUCTURED GRAPHENE MODIFIED WITH TRIRUTHENIUM CLUSTER

The behavior of “monolayers” formed at water-air interface was monitored by recording the surface pressure (Π) and the area per molecule during the compression. The $\Pi - A$ isotherm of GO at $50 \text{ cm}^2 \text{ min}^{-1}$ is shown in Figure 8-1, it was obtained a behavior similar to the reported in previous work. [234,235] Initially the pressure remained constant during compression indicating non-significant interaction between graphene sheets spread on water surface. When area was further decreased the surface pressure started to rise slowly, likely due to electrostatic repulsion between graphene flakes which are getting close. Finally, the pressure increasing was more notorious with further area decreasing, probably because of higher proximity between graphene sheets which must have high packing like in a solid-state phase. Apparently, pressure increased at constant rate and it was not observed collapse or a sharp increment at high pressures in contrast to monolayers of hard colloids. [311] Probably because of the reorganization and overlapping of graphene sheets, close enough graphene sheets might overlap, fold on themselves or wrinkle when area is diminished such as reported in previous works, [234–236,312] and even more with a further decrease in area, the graphene sheets can be restacked. [236]

FIGURE 8-1- ISOTHERM FOR GRAPHENE OXIDE FILMS



a) Surface pressure vs. area plot showing the area per molecule of 0.50 \AA^2 . b) Isotherm cycles at different maximum pressures (24, 20, 15 and 10 mN m^{-1}).

SOURCE: Author.

The $\Pi - A$ isotherm did not clearly show the transition between solid-state graphene film and the wrinkled or “crashed” film. But on some occasions when were reached pressures higher than 20 mN m^{-1} , we observed the formation of little darker regions on water surface which remained upon open the barrier. Also, when pressures higher than 20 mN m^{-1} are

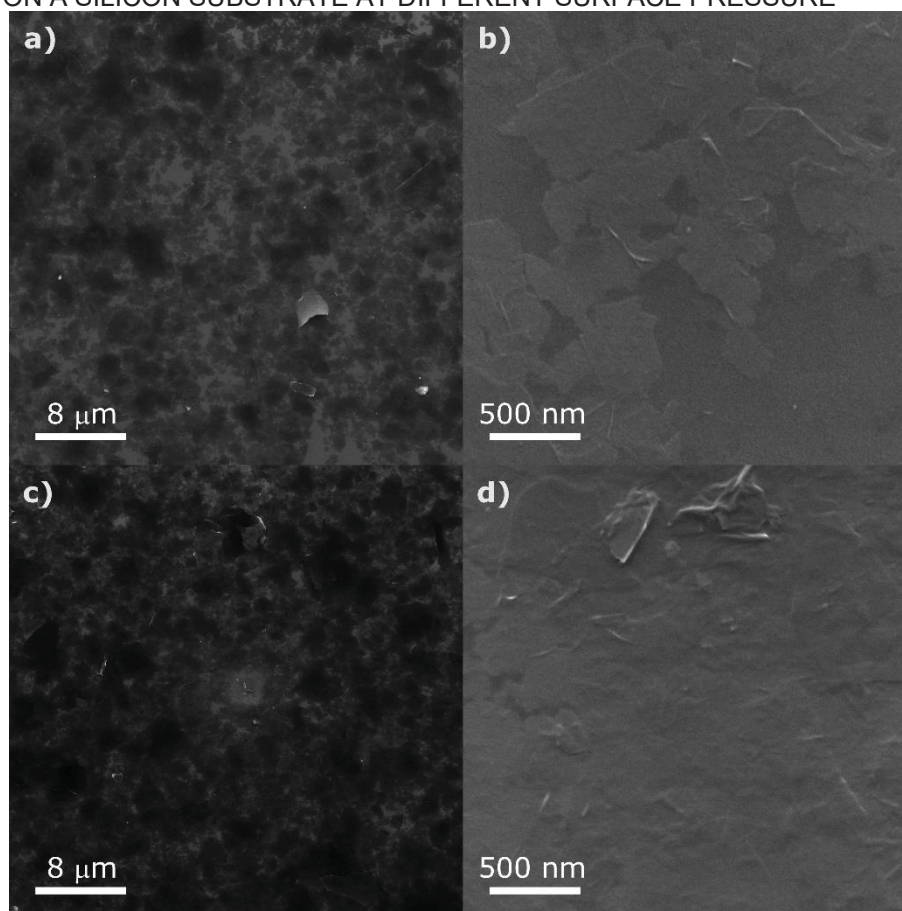
reached, GO films isotherms have a notable hysteresis as can be observed in Figure 8-1b, material is accumulated in the trough edges and consequently the isotherm is shifted to lower areas when the film is compressed again. Similar phenomenon was observed before with rGO flakes with different sizes, which tend to attach and form a big cloudy region near the edge of LB trough when they were spread on water. [236] So, the evidence mentioned suggests that the graphene oxide can restack, and form aggregated films when the pressure increase so much.

The multilayer films obtained at 10 and 20 mN m^{-1} (Figure 8-2a and c) exhibited similar morphology, with agglomerated material in some regions (darker regions) and other with less material (clearer regions), so they should have an irregular surface. However, films obtained at 20 mN m^{-1} exhibited higher packing density than the obtained at 10 mN m^{-1} as indicated by the higher presence of dark regions in the respective SEM image (Figure 8-2c). Moreover, they were more compact and with higher presence of folded and wrinkled graphene sheets (Figure 8-2b and d), as expected since it is more compressed. The image for the film obtained at 20 mN m^{-1} (Figure 8-2d) looked like one unique wrinkled piece whereas the image for the film obtained at 10 mN m^{-1} (Figure 8-2b) exhibited some smooth regions and layers at different depth could be identified. Based on the above results we decided to deposit GO films at surface pressure of 20 mN m^{-1} expecting to obtain films with high packing, a higher pressure was not chosen because it would create higher material aggregation and overlapping, and material accumulation at edges. The estimated material area per mass unit was $0.50 \text{ cm}^2 \mu\text{g}^{-1}$ as pointed out in Figure 8-1a which corresponds to a material loading in one monolayer of $\sim 2.00 \mu\text{g cm}^2$.

The GO films obtained were dipped in a dispersion of MeOHRu in methanol expecting the anchorage of the cluster in graphene oxide through electrostatic interactions of coordination of the cluster with oxygenated groups on GO to obtain GORu. Either path is likely to occur, the electrostatic force between the cationic ruthenium cluster MeOHRu and the dipole moment of oxygenated groups in graphene, or the coordination of oxygenated group in graphene with one of the ruthenium atoms in MeOHRu upon oxygen deprotonation and methanol ligand displacement.

The UV-vis spectra of GO and GORu is shown in Figure 8-3a. GO spectrum exhibited a distinctive band at 238 nm attributed to $\pi \rightarrow \pi^*$ transitions at the bonds of the aromatic rings within graphene oxide sheets and a shoulder at ~ 300 nm attributed to $n \rightarrow \pi^*$ transitions in C=O bonds. [313–316] The GO film functionalized with triruthenium cluster exhibited a similar spectrum, but it was slightly modified. The shoulder at 300 nm was less evident and the band at 238 nm was shifted to 230 nm, it was attributed to electronic transitions in the cluster involving pyridine ligands which have an intense band between 320 and 200 nm with maximum at 239 nm.

FIGURE 8-2- SEM IMAGES OF GRAPHENE OXIDE LB FILMS WITH 4 MONOLAYERS DEPOSITED ON A SILICON SUBSTRATE AT DIFFERENT SURFACE PRESSURE



a) Low magnification and b) high magnification SEM image of GO LB film obtained at 10 mN m^{-1} . c) Low magnification and b) high magnification SEM image of GO LB film obtained at 20 mN m^{-1} .

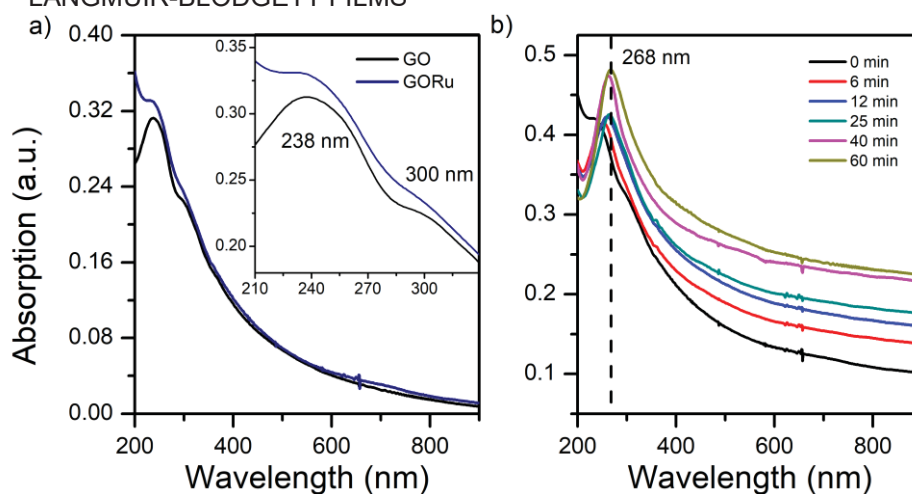
SOURCE: Author.

GO and GORu films were reduced submerging them in ascorbic acid solution (2 mg mL^{-1}) at $90 \text{ }^\circ\text{C}$. The reduction was accompanied by UV-vis spectroscopy, recording the spectrum before reduction process and after determined times elapsed. The films were removed from the ascorbic acid solution to record the UV-vis and submerged again. As can be observed in Figure 8-3b the band maximum, located initially at 238 nm (black line), was gradually shifted to higher wavelengths. After 12 minutes (blue line) the band maximum was located at 260 nm and the shoulder at 300 nm was not noted. With further time, the absorption close to 200 nm was diminished, the intensity of the maximum was increased and shifted to 268 nm as can be observed in the spectrum recorded after 60 minutes (dark yellow line). The absorption in the whole spectral region increased gradually, which is attributed to the increase in the opacity and roughness of the film evident to the naked eye. These results suggest the restoring of sp^2 -conjugated structure of graphene due to the partial removing of oxygen groups in the graphene sheets. [313–315]

As shown in Figure 8-3b, the chemical reduction of GORu seems complete after 60 min, in contrast GO reduction seemed to take shorter time (30 min). Probably due to the

presence of the triruthenium cluster in GORu which also could be reduced simultaneously competing with graphene and can limit the access of ascorbic acid to oxygenated sites on graphene delaying the chemical reduction of graphene oxide. Besides, it was noted that rGORu spectrum have a minimum at 211 nm, whereas rGO spectrum have no minimum. It could be attributed to electronic transitions of pyridine ligands in the rGORu sample, since pyridine present a band at 200 nm. Suggesting the presence of the triruthenium cluster in the reduced samples.

FIGURE 8-3- UV-VIS SPECTRA OF GRAPHENE AND GRAPHENE TRIRUTHENIUM CLUSTER LANGMUIR-BLODGETT FILMS



a) UV-vis spectra of graphene oxide and graphene oxide-triruthenium cluster (GORu) LB films, the inset shows a zoom in between 210 and 330 nm. b) GORu UV-vis spectra change as function of reduction time.

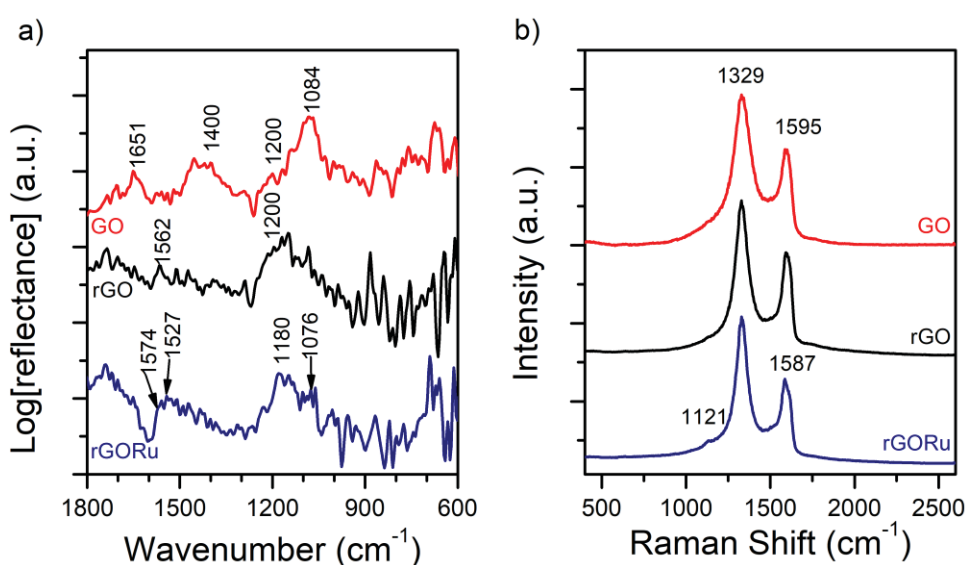
SOURCE: Author.

The IRRAS spectra for GO LB film with 8 ML (Figure 8-4a) displayed typical bands of graphene oxide, such as the $\nu\text{C}=\text{O}$ bond vibration in carboxyl groups at 1651 cm^{-1} , hydroxyl and carboxyl groups deformation vibrations at 1400 cm^{-1} , $\nu\text{C}-\text{O}$ bond vibration in epoxy and alkoxy groups at 1200 and 1080 cm^{-1} respectively. which account for the abundant oxygen containing groups on the GO films, according to previous studies that show the presence of carboxyl, epoxy, and hydroxyl groups in graphene oxide samples. [238,315,317,318] The broad and intense band at 1080 cm^{-1} and 1400 cm^{-1} presented significant lower intensity in the spectra of reduced samples, whereas the band at 1200 cm^{-1} remained, also a band at 1562 cm^{-1} appeared, it was attributed to $\text{C}=\text{C}$ bond stretching vibration in graphitic domain. These results confirm the restoration of sp^2 structure of carbon atoms within graphene sheets and the removal of oxygen-containing functional groups to a certain degree, some fraction of these groups, particularly epoxy groups may remain.

The Raman spectra of graphene materials (Figure 8-4b) also confirmed the successful reduction of graphene oxide films. The spectra are characterized by the D and G band at 1329 and 1595 cm^{-1} respectively. The D band is activated by the presence of defects or other

functional group whereas G band arises from C-C bond stretching in sp^2 carbon systems. [265,267,319,320] We noted that the D band in the reduced samples are narrower as indicated by the lower value of full width at half maximum in rGO (75 cm^{-1}) and rGORu (70 cm^{-1}) as compared with GO (100 cm^{-1}). Indicating lower structural disorder in the reduced samples. [319] Moreover, the G band presented higher relative intensity on rGO than GO as indicated by the ratio between D and G bands (I_D/I_G) which is lower for rGO samples (1.45) than for GO (1.56). It can be attributed to larger sp^2 C-C domains in rGO after removal of oxygen-containing groups.

FIGURE 8-4 - INFRARED REFLECTION ABSORPTION AND RAMAN SPECTRA OF GRAPHENE AND HETEROSTRUCTURED GRAPHENE-TRIRUTHENIUM CLUSTER LB FILM.



a) Infrared reflection absorption spectra and b) Raman spectra recorded at excitation wavelength of 632.8 nm of graphene oxide, reduced graphene oxide and reduced graphene oxide – triruthenium cluster LB films

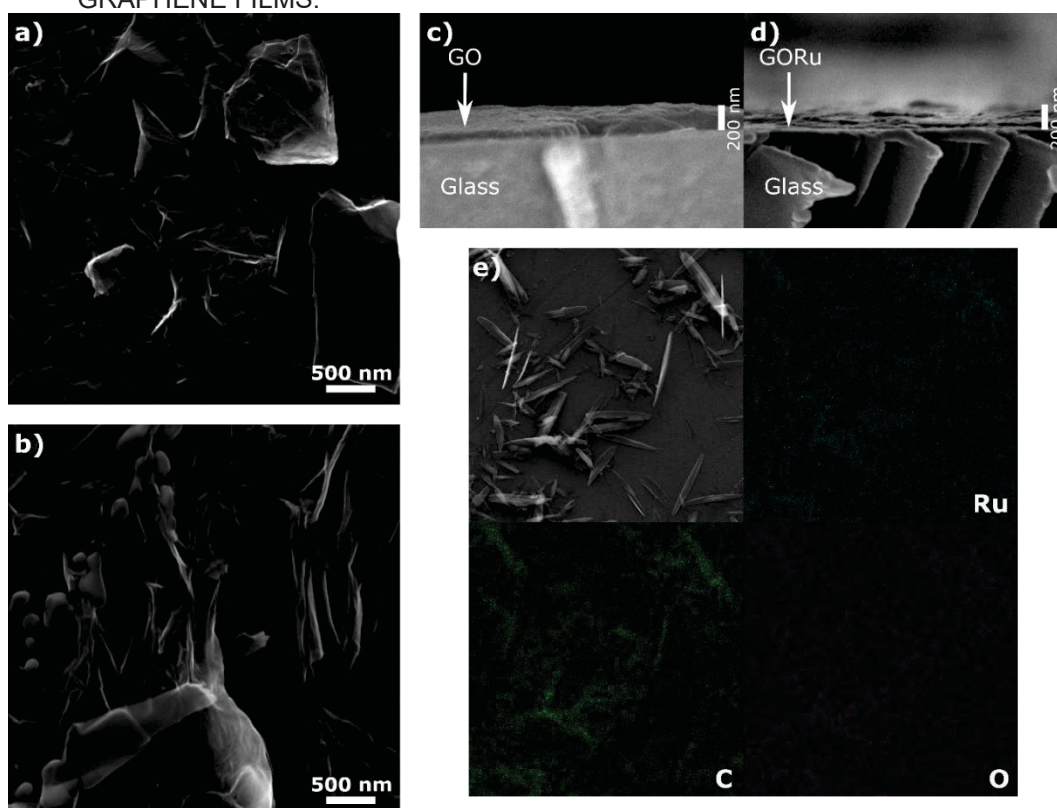
SOURCE: Author.

Infrared spectrum of hybrid heterostructured film (rGORu) observed in Figure 8-4a was like that of rGO but presented some differences. The band at 1562 cm^{-1} was modified by the presence of other close vibrations at 1574 cm^{-1} and 1527 cm^{-1} , attributed to ring stretching vibration in pyridine and carboxyl bond stretching in acetate groups of the triruthenium cluster. The band at 1200 cm^{-1} also was modified and the maximum shifted to 1180 cm^{-1} which was attributed to in plane δ -CH vibrations in pyridine ligands at this region. Likewise, a new band related with δ -CO in acetates and out of plane δ -CH vibrations in pyridine was observed at 690 cm^{-1} . Raman spectrum of rGORu (Figure 8-4b) exhibited the D and G bands, but the G band seemed asymmetrical with higher intensity at lower wavenumbers, so the band maximum is slightly shifted from 1595 to 1587 cm^{-1} , it could be attributed to the presence of vibrations related with ring stretching of pyridine ligands of the triruthenium cluster at 1580 cm^{-1} . Besides,

the low intensity shoulder was observed at 1120 cm^{-1} , which could be attributed to in plane δ -CH and breathing mode ring stretching in pyridine ligands.

These results suggest the presence of triruthenium cluster in the hybrid heterostructured film and the successful reduction of graphene within the films and the EDS spectroscopy confirmed the presence of ruthenium in the rGORu sample, it was distributed homogeneously in the whole sample, although there are some agglomerations of triruthenium cluster on the film surface as showed in the EDS map (Figure 8-5e). It was noted some crystals on surface with higher concentration of Ru. In this case the triruthenium cluster is not anchored by amide bond to graphene in the hybrid material (rGO-NHRu) discussed in chapter 5, but the triruthenium cluster could be anchored through electrostatic interactions or coordination between oxygenated groups in graphene and ruthenium atom upon release of labile methanol ligand. The bands corresponding to triruthenium cluster were masked by graphene bands. These bands were not so intense since the energy of excitation laser (632.8 nm) did not overlap the absorption band of triruthenium cluster, so Raman resonant effect was not observed like in the rGO-NHRu material. The triruthenium cluster may be reduced, so the band observed at 685 nm for cationic compound is absent and shifted to higher wavelengths. [21]

FIGURE 8-5- SEM IMAGES AND EDS MAP OF THE HYBRID HETEROSTRUCTURED FILM AND GRAPHENE FILMS.



a) SEM image of rGO and b) rGORu LB films on Si substrate. c) SEM image of the transversal section of GO and d) GORu LB films on glass substrate. e) EDS map of rGORu LB films on Si substrate.

SOURCE: Author

The morphology of rGORu surface is like that of GO and rGO, with high packing density, the presence of sheets folded due to graphene overlapping, and with some big pieces of graphene aggregates (Figure 8-5b). Also, there are some crystals of triruthenium cluster on rGORu surface as indicated by some clearer features with irregular stick shape and some needle-shaped crystal which were attributed to an organic salt crystal. Besides, the SEM image of the transversal section of the hybrid heterostructured film exhibited several heterogeneous thin layers stacked with clearer regions than GO film, which was attributed to the presence of triruthenium cluster as salt (Figure 8-5d). Whereas GO film looked more homogeneous like mountains of material (Figure 8-5c). It suggests that the GORu film has alternated layers of triruthenium and graphene. Additionally, we noted that films are irregular with regions with less material, so lower thickness, also GO films had higher thickness than GORu films, indicating that the triruthenium cluster affects the subsequent transfer of GO and have a shrinking effect on graphene, which could be attributed to electrostatic attraction between graphene and triruthenium cluster.

8.2 ENERGY STORAGE IN HYBRID HETEROSTRUCTURED LANGMUIR-BLODGETT FILMS

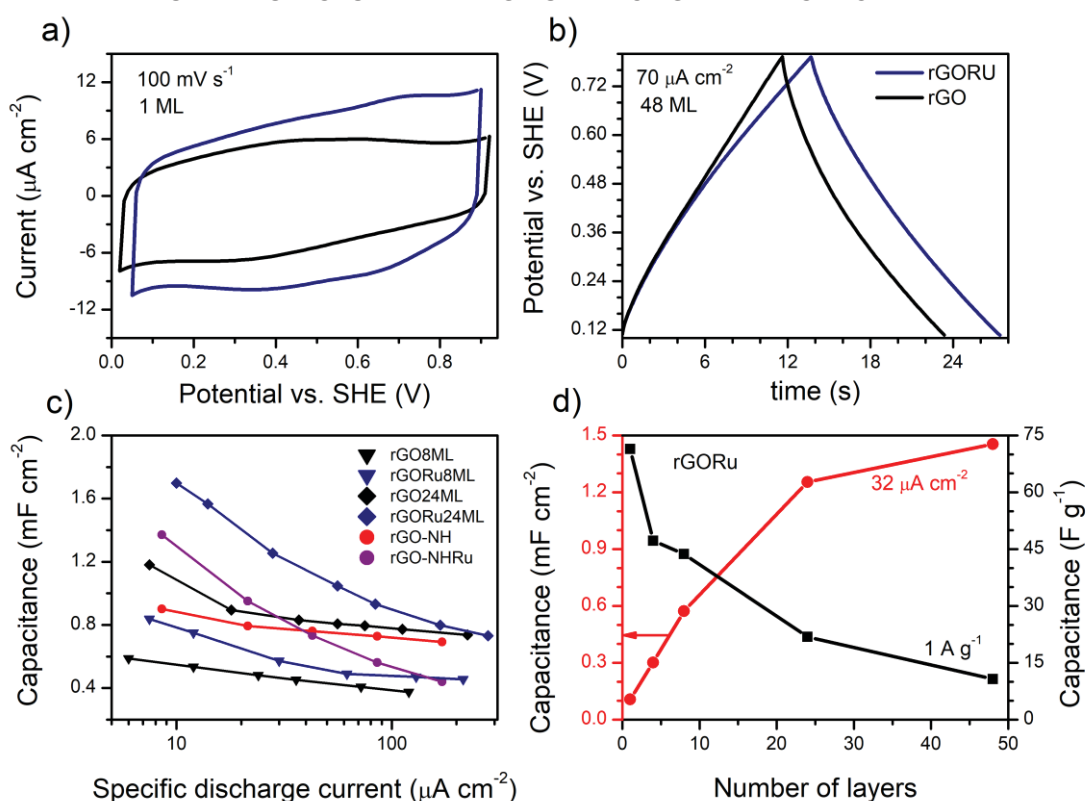
8.2.1 *Electrochemical Behavior of Hybrid Langmuir-Blodgett Electrodes*

The electrochemical performance of the electrodes fabricated by Langmuir-Bodgett technique of rGO and rGORu was tested with cyclic voltammetry, charge-discharge measurements, and electrochemical impedance spectroscopy. The rGO and rGORu CD profile was triangular shaped and voltammogram presented a rectangular shaped curve evidencing that their behaviors are mostly dominated by double layer capacitance (Figure 8-6a and b). A feature like a broad redox peak with $E_{1/2}$ around 0.4 V was also observed, this peak was attributed to a pseudocapacitive process arising from interactions of oxygen groups in graphene with alkali metal from supporting electrolytes. [191,279,280] Additionally, rGORu exhibited an additional broad redox peak at higher potentials with $E_{1/2}$ -0.72 V (Figure 8-6a), that process could be related with the presence of triruthenium cluster on the film. The rGORu CD profile is asymmetrical (Figure 8-6b), similar profiles were obtained for other electrode materials combining redox and capacitive materials. [154,281] The asymmetrical feature is consistent with the oxidation peak observed in the voltammogram. Furthermore, the oxidation current peak of rGORu was slightly more evident at low scan rates as shown in Figure 8-7.

The presence of that additional redox peak led to a higher capacitance in rGORu than in rGO as can be seen in Figure 8-6c comparing blue (rGORu) with black lines (rGO). Likewise, the dependence of the redox process with the scan rate led to a higher capacitance decrease

at high discharge rates in rGORu than in rGO. This effect was more evident in thicker electrodes as noted in Figure 8-6c, the profile of capacitance variation with the specific discharge current plot of 24 **ML** films (Figure 8-6c - blue diamonds) resembled the shape of drop-casted electrodes contrasting with the profile of 8 **ML** electrode (Figure 8-6c - blue triangles) which is almost constant at high discharge currents. The results suggest that redox peak in rGORu have some diffusion limitations which are more evident in thicker electrodes. However, the limitations are not so high as in the rGO-NHRu drop-casted electrode, so the capacitance per unit of area of rGORu electrode with 24 **ML** is higher than in the rGO-NHRu drop-casted electrode as shown in Figure 8-6c, even though that it should have less mass. The estimated mass of graphene per unit of area in rGORu of 24 **ML** is $48 \mu\text{g cm}^{-2}$ (load of one monolayer estimated from isotherms is $2 \mu\text{g cm}^{-2}$) whereas the graphene in drop-casted electrode is $\sim 86 \mu\text{g cm}^{-2}$ (considering that the total material load is $9 \mu\text{g}$, 70% of rGO-NHRu is graphene and the electrode area is 0.07 cm^2).

FIGURE 8-6- ELECTROCHEMICAL BEHAVIOR OF GRAPHENE AND HYBRID GRAPHENE-TRIRUTHENIUM CLUSTER LANGMUIR BLODGETT ELECTRODES.



a) voltammogram at 100 mVs^{-1} of 1 **ML** electrodes. b) Charge discharge profiles at $70 \mu\text{A cm}^{-2}$ of 48 **ML** electrodes. c) Capacitance variation at different specific discharge currents of electrodes with 8 **ML** and 24 **ML**, drop-casted electrodes are shown for comparison. d) capacitance variation with the number of layers in the rGORu electrode at $32 \mu\text{A cm}^{-2}$ and 1 A g^{-1} .

SOURCE: Author

The capacitance per unit of area of hybrid LB electrodes increased with the number of layers as expected since the electrode mass-loading also increased (Figure 8-6d). But this

increasing was less significant for greater number of layers. For example, the capacitance of 48 **ML** electrode was only 1.16 times that of 24 **ML** electrode, which suggest that the use of the material is less effective in thicker electrodes, so the capacitance by mass unit of thicker electrodes is significantly lower as seen in Figure 8-6d (black line). Also, it is possible that a less effective material transfer for thicker electrodes during LB deposition contribute to the observed trend. Considering the results an electrode with ~8 **ML** could offer high capacitance per unit of area and an effective use of material

The specific capacitance of rGORu with 8 **ML** was 0.710 mF cm⁻² (44.38 F g⁻¹) at 16 μ A cm⁻² (1 A g⁻¹). The 64% of the capacitance was retained at high discharge current of 216 μ A cm⁻² (13.5 A g⁻¹). Its performance was notably superior to the drop-casted electrodes rGO-NHRu at high discharge current. rGO-NHRu exhibited a capacitance of 0.951 mF cm⁻² (11.1 F g⁻¹) at ~21 μ A cm⁻² (0.25 A g⁻¹) and retained only 41% of its capacitance at high discharge current of 257 μ A cm⁻² (3 A g⁻¹). The performance of rGORu with 8 **ML** is superior or near the reported for other hybrid electrodes as rGO/RuO₂ and rGO/RuO₂/PVK (PVK: polyvinylcarbazole) which exhibited a capacitance of 30 and 75 F g⁻¹ at 1 A g⁻¹ and of 26 and 45 Fg⁻¹ at 10 A g⁻¹. [321] But it was inferior to other electrodes such as the material derived from carbonization of nickel metal organic frameworks (NiMOF) with rGO, [172] prussian blue (PB) [322] and phthalocyanine (PC) [173] with rGO, which exhibited a capacitance of 330, 225 and 193 F g⁻¹ at 1 A g⁻¹ and a capacitance retention of 84%, 68% and 77% respectively.

TABLE 8-1- CAPACITANCE OF HYBRID GRAPHENE-TRIRUTHENIUM CLUSTER ELECTODES COMPARED WITH OTHER WORKS.

I (A g ⁻¹)	rGORu-1ML	rGORu-8ML	rGO-NHRu	rGO/RuO ₂ [321]	rGO/RuO ₂ /PVK[321]	rGO/Ni-MOF[172]	rGO/PB [322]	rGO/PC [173]
1	82.6	44.4	6.6	30	75	330	225	193
2	71.5	35.8	5.1	28	75	308	194	180
5	63.9	30.6	4.6 ^c	27	54	294 ^d	175	164
10	60.6 ^a	28.5 ^b	---	26	45	277	154	150

^areal specific discharge current is 9 A g⁻¹. ^breal specific discharge current is 14 A g⁻¹. ^creal specific discharge current is 3 A g⁻¹. ^dreal specific discharge current is 4 A g⁻¹.

SOURCE: Author.

The superior performance of those electrodes could be attributed to several aspects. For example, the electrode derived from carbonization of NiMOFs with rGO exhibited abundant hollow carbon microrods with corrugated graphene sheets and hierarchical porosity nature leading to a considerably high surface area, these characteristics led to high capacitance and higher capacitance retention. [172] The electrode synthesized by GO reduction on iron foil in acid media and presence of KFe(CN)₆ propitiated the simultaneous growth of PB nanocubes and rGO film, forming electrodes with a porous interconnected graphene sheets of tens of microns covered by PB nanocubes of 80 nm tightly connected to graphene which may prevent the graphene restacking, this structure allowed fast electron transport through heterojunctions

and fast ion diffusion through the porous structure. [322] The PC-rGO aerogel fabricated with an hydrothermal process exhibited $\pi - \pi$ interactions between graphene sheets and PC and interconnected 3D sponge-like structure with high porosity instead of sheet stacked architecture, so the amount of electrochemically active sites is greater. [173]

The strategy here used to obtain structures facilitating the charge transport in the whole film was partly successful since it led to better performance with respect to drop-casted electrodes. The 2D organization with interconnected wrinkled graphene sheets probably helped to improve the electron transport and ion diffusion through the whole film. However, it did not lead to achieve a capacitance as high as other works, since the material did not present hierarchical pores, porous nanoarchitecture, or interconnected 3D network reported in those works which may increase the accessible active area of the electrodes, particularly in thicker electrodes and further improve the ion diffusion in the whole electrode. So, the structure induced by the wrinkled graphene was not enough to provide fast ion diffusion paths and did not prevent the graphene restacking, however it could be improved using graphene of high lateral size which could be easier deformed leading to higher roughness and porosity. [236] Other relevant aspect is the electrolyte used in those works since the use of basic electrolytes and ionic liquids can improve the electrode performance. [172,173] It would be an interesting alternative using ionic liquids or organic electrolytes.

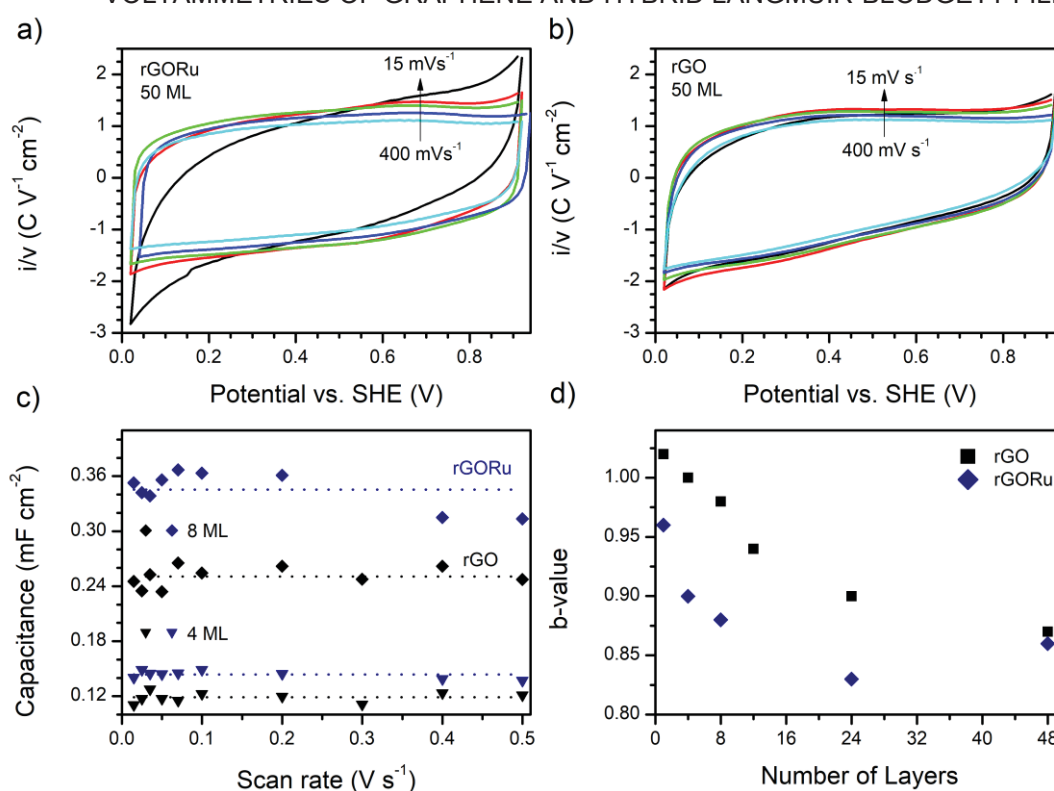
rGO LB films reached specific capacitance of 0.401 mF cm^{-2} (25.1 F g^{-1}) at $36 \mu\text{A cm}^{-2}$ ($\sim 2 \text{ A g}^{-1}$), whereas the drop-casted rGO-NH electrode exhibited a capacitance of 0.693 mF cm^{-2} (8.1 F g^{-1}) at $171 \mu\text{A cm}^{-2}$ ($\sim 2 \text{ A g}^{-1}$). The specific capacitance by mass unit of the LB film is significantly higher than in rGO-NH electrode, however this value is lower than other graphene materials reported, that range from 90 to 140 F g^{-1} . [148,276,323,324] The performance of graphene materials varies significantly depending on the experimental conditions. For example, higher values of capacitance are reported when acid electrolyte is used in the electrochemical experiments due to pseudocapacitive hydrogen adsorption. [148,191,276,279,280] Furthermore, the aggregation of graphene sheets leads to lower ion accessible surface area diminishing the capacitance. [282,283] So, synthesize graphene with higher specific surface area and improved porosity is challenging and strategies as the fabrication of hydrogels and aerogels have been proposed. [173,283]

8.2.2 Analysis of Charge Storage on Hybrid Langmuir Blodgett Electrodes

The analysis of the current variation with v in CV summarized in Figure 8-7 suggests little charge transport limitations and a behavior predominantly capacitive in the rGO and rGORu LB electrodes. The voltammogram “normalized” dividing the specific current by the scan rate (i/v) depicted in Figure 8-7a show that the i/v peak of rGORu at higher potentials

slightly decreased as scan rate increased, probably due to some charge transport limitation. The rGO voltammogram in Figure 8-7b also shows this trend, but it is moderated. Additionally, current dependence on v was analyzed assuming a power-law dependence of i on v ($i = av^b$) as indicated in section 3.4. The b -value obtained from oxidation current peak analysis was 1 for the 1 ML electrodes, and it decreased for electrodes with higher number of layers, the decreasing is greater for the rGORu electrodes as can be seen in Figure 8-7d. rGO-Ru reach a minimum b -value of 0.83 for the 24 ML electrode. This value is higher than 0.8, so the behavior could be considered capacitive but far from ideal.

FIGURE 8-7- ANALYSIS OF CURRENT VARIATION WITH THE SCAN RATE IN CYCLIC VOLTAMMETRIES OF GRAPHENE AND HYBRID LANGMUIR-BLODGETT FILMS.



Cyclic voltammetry of a) rGORu and b) rGO LB film with 48 layers. c) capacitance variation with the scan rate for rGORu and rGO LB films with 4 and 8 layers. d) variation of b -values with the number of layers in rGO and rGORu films. The y-axis in voltammograms is the current divided by the scan rate.

SOURCE: Author.

Besides the b -value of rGO electrodes with less than 12 layers is higher than 0.94 indicating a capacitive behavior close to ideal, the thicker electrodes with 24 and 48 layers showed a less ideal capacitive behavior as indicated by the b -values of 0.9 and 0.87. The variation in the charge stored with the scan rate presented a random distribution around to the mean value and did not show a clear trend as depicted in the plot of capacitance vs scan rate of Figure 8-7c. It appears to be horizontal, so the analysis of charge storage capacity contributions led to conclude that most of the charge arises from surface sites q_{outer} since the

q is similar at slow and high scan rates. An estimation of the q_{outer} and q_{inner} as the indicated in section 3.4 was not reported because the simulated curve does not fit well the experimental data.

In summary, graphene Langmuir-Blodgett electrodes fabricated in this work exhibited performance superior to the rGO-NH and rGO-NHRu drop-casted electrodes. It could be attributed to higher accessible area and improved charge transport in LB electrodes. Also, the capacitance by mass unit decayed at higher thickness and the capacitance have a higher decay at high rates, indicating a less effective use of the material and slower charge transport. It is expected that the using of other electrolytes and further optimization of the fabrication process, particularly the reduction of the films, improve the performance of rGO and rGORu electrodes. These results confirms that the nanomaterials morphology is a main factor in the electrode performance, different strategies could be tested to get new architectures that increases the accessible surface area and shortens ion diffusion paths.[282,283]

8.2.3 EIS Hybrid Langmuir Blodgett Electrodes

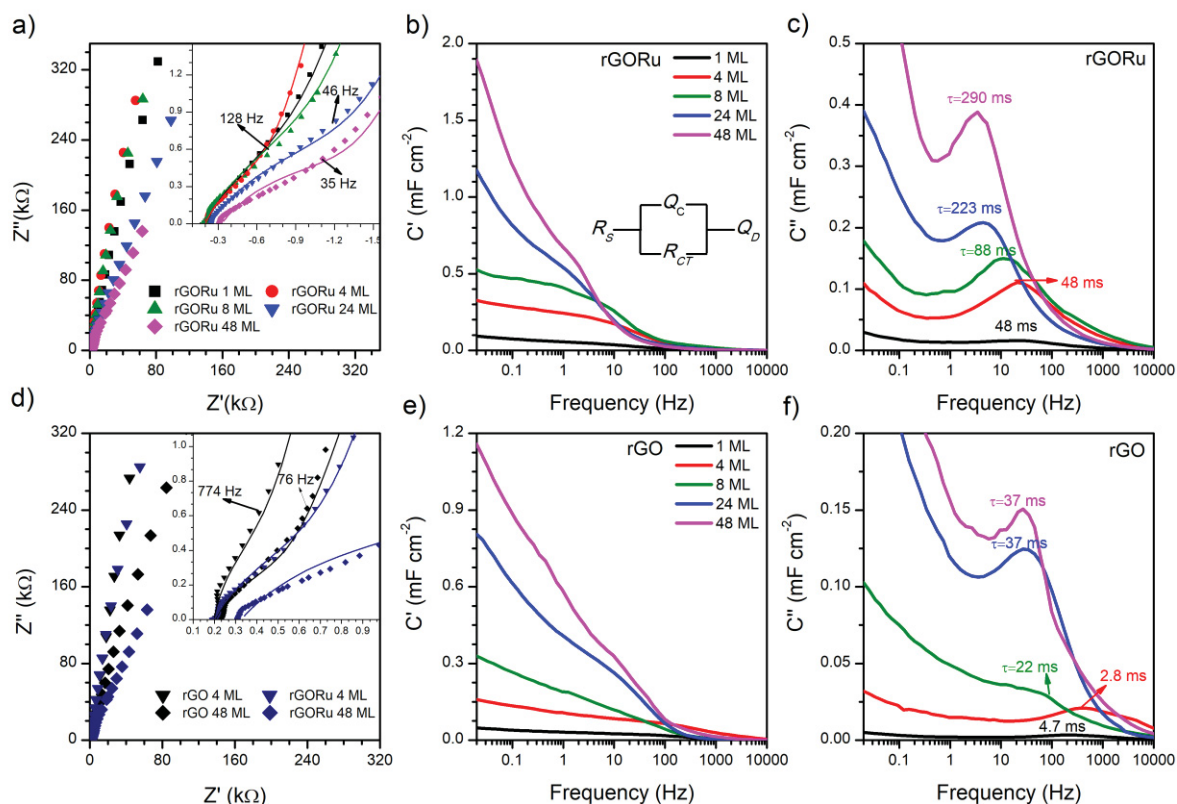
EIS was carried out at 0.8 V to obtain additional insights on the electrochemical processes occurring at electrodes. Around to 0.8 V is observed the oxidation peak in the hybrid electrodes. The Nyquist plot of rGORu is shown in Figure 8-8a and in the inset is shown the high frequency region, the comparison with the Nyquist plot of rGO can be seen in Figure 8-8e. At very high frequencies the imaginary impedance was close to zero, so the resistive processes related with the conductivity and electrical contacts of all components may dominate the spectrum. [284–286] The real impedance value at these frequencies (Z') is directly related with the resistance of the processes mentioned, according to the modeling with equivalent circuits the resistance value R_s was $\sim 200 \Omega$ for all the electrodes, only the resistance of rGORu with 48 ML was significantly higher ($R_s = \sim 327 \Omega$). The R_s values of the LB electrodes on ITO was significantly higher than the drop-casted electrodes on glassy carbon (40Ω), which probably is associated with the substrate conductivity.

At high frequencies was observed an arc line associated to the double layer and resistive process at interface. At lower frequencies the imaginary impedance increases rapidly, which is characteristic of capacitive process. The initial slope of the arc line depends on the capacitive process, then the arc-line deflects on the real axis depending on the resistive process. The arc-line was more extended on the real axis in rGORu spectra (see inset in Figure 8-8e) than in rGO spectra, which could be related with predominance of resistive processes associated with the charge transfer and ions rearranging in the interface as is expected by the presence of the triruthenium cluster. Moreover, the arc-line was also more extended on the

real axis for the spectra of thicker electrodes indicating higher charge transfer limitations on thicker electrodes (see inset in Figure 8-8a).

This part of Nyquist plot is captured in the equivalent circuit model mainly by the impedance of charge transfer resistance R_{CT} which is parallel to a constant phase element Q_C representing the double layer capacitance, as can be observed in the inset of Figure 8-8b this array is in series with the resistance R_S representing electronic and contact resistance and a constant phase element Q_D representing the low frequency capacitance in quasi-stationary state when all processes have occurred. The R_{CT} values obtained from equivalent circuit model fitting are higher in rGORu materials, a value of 1230 Ω was obtained for rGORu with 48 ML whereas a value of 365 Ω was obtained for rGORu with 4 ML. Likewise, it was observed that R_{CT} tends to increase as the number layer increases as can be observed in Table 8-2.

FIGURE 8-8- EIS RESULTS OF GRAPHENE AND HYBRID LANGMUIR BLODGETT FILMS.



Nyquist plot of a) hybrid rGORu LB electrodes and d) its comparison with rGO LB electrodes. The inset shows a zoom at high frequencies, the data from model is shown as lines. Real capacitance vs. frequency plots of b) hybrid rGORu LB electrodes and e) rGO LB electrodes. Imaginary capacitance vs. frequency plots of c) hybrid rGORu LB electrodes and f) rGO LB electrodes.

SOURCE: Author

A titled line close to vertical was observed at low frequencies, it was attributed to capacitive processes dominating the spectrum. This behavior is characteristic of bounded diffusion processes observed within a thin slice of material/solution as membranes, or electrochemical supercapacitors. [284–286] It was attributed to the reaching of a quasi-stationary state with non-consuming species. That is, electroactive species and ion

concentrations are stationary, and the diffusion layer has a length comparable with the characteristic physical dimensions of the electrode. [285,287] This line began at relative high frequencies for all electrodes tested (ca. >35 Hz), which is characteristic of very thin film electrodes. However, the frequency for rGORu was lower than for rGO, likewise the frequency decreased as thickness increased. It suggests higher charge transfer resistance in rGORu and thicker films.

TABLE 8-2- ESTIMATED PARAMETERS VALUES OF CIRCUIT MODEL ELEMENTS AND THEIR RESPECTIVE ESTIMATION ERRORS.

Electrode	$R_s(\Omega)$		$Q_C(\mu\Omega^{-1}s^n)$		n_C		$R_{CT}(\Omega)$		$Q_R(\mu\Omega^{-1}s^n)$		n_R	
	value	%error	value	%error	value	%error	value	%error	value	%error	value	%error
rGORU-1ML	200	23	9.5	8	0.70	6	904	8	5.8	0.2	0.88	0.1
rGORU-4 ML	201	8	10	15	0.74	3	576	6	8.7	1	0.88	0.3
rGORu-8 ML	174	14	12	11	0.67	3	1304	4	7.4	0.9	0.91	0.2
rGORu-24 ML	230	8	12	8	0.64	2	1422	3	18	0.5	0.85	0.2
rGORu-48 ML	327	21	13	32	0.66	8	1230	10	31	4	0.81	4
rGO-4 ML	199	3	0.9	16	0.95	2	232	18	0.9	2	0.90	0.3
rGO-48 ML	206	21	8.8	10	0.77	12	365	2	11	2	0.85	0.6

The fitting was performed with Powell method to find local minimum as implemented in EIS spectrum analyzer. [247]

SOURCE: Author.

Additionally, as can be observed in Table 8-2 values higher than 0.81 were obtained for the exponent n_D of the constant phase element representing the low frequency capacitance. A value close to 1.0 is expected for ideal capacitors and 0.5 is expected for semi-infinite diffusion processes, so the low frequency processes are highly capacitive. Besides, Q_D values were higher for rGORu electrodes and thicker electrodes (see Table 8-2). Despite of Q_D value is not exactly the capacitance value, it is expected that the trend found be maintained for the capacitance values since the n_D values did not vary so much.

The real ($C'(\omega)$) and imaginary ($C''(\omega)$) part of the complex capacitance of rGORu was calculated using equation 3.15 and are shown in b and c respectively. $C'(\omega)$ at low frequencies gives the capacitance value of the whole system, we observed that the capacitance value increases as the number of layers increases reaching values relatively close to those found with discharge measurements, since the relative difference between them is below 8% for most of the films. Likewise, the values of $C'(\omega)$ at 0.02 Hz of rGORu were higher than those found for rGO as can be noted when Figure 8-8b and e are compared. Besides, $C''(\omega)$ is related with energy dissipation. [248,249] Also, the maximum in the $C''(\omega)$ is located at critical frequency at which the system transits from a behavior mostly resistive at high frequencies to

one mostly capacitive at low frequencies. A characteristic time constant τ is calculated with the critical frequency $f \tau = 1/f$.

Interestingly the characteristic time constant of rGORu electrodes are higher than those found for rGO as can be seen in Figure 8-8c and f, for example the τ values of 48 **ML** electrodes are 290 ms for rGORu and 37 ms for rGO. It is due to their higher charge transfer resistance and capacitance associated with the presence of triruthenium cluster. Additionally, the time constant increases as the thickness increases which is in accordance with the higher capacitance and charge transport resistance expected for thicker electrodes.

8.3 ENERGY STORAGE DEVICES BASED ON HYBRID HETEROSTRUCTURED LANGMUIR-BLODGETT ELECTRODES

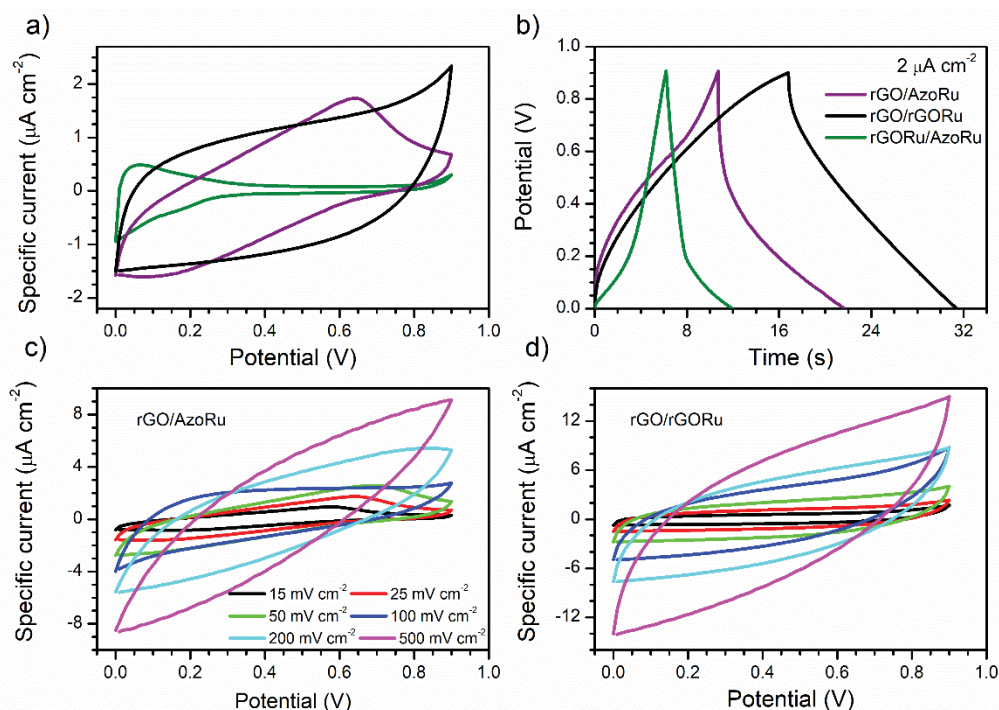
The thin films developed on this work were explored in portable and flexible energy storage devices, we constructed solid-state asymmetric supercapacitors based on rGO, rGORu and AzoRu LB electrodes and “boric acid crosslinked” (B-PVA-KCl) gel electrolyte. The B-PVA-KCl gel film works as solid electrolyte and separator between two electrodes. B-PVA-KCl hydrogel was used as electrolyte since hydrogel exhibits higher flexibility, thin film formation ability and ionic conductivity higher than dry electrolytes. [242,325] Moreover the chemical crosslinking may improve the mechanical properties of PVA-KCl film, [242,326,327] boric acid interacts with hydroxyl groups on PVA chains promoting a dehydration reaction, so the boron forms bonds with oxygen linking different chains of PVA. [242,328] Particularly, the boron can form dynamic diol-borate ester bonds, so the electrolyte could exhibit healing properties. [328]

The CV curves at 25 mV s⁻¹ of the three asymmetric devices are compared in Figure 8-9a. The asymmetric devices consist in a B-PVA-KCl electrolyte sandwiched between two different active materials deposited on ITO coated PET. For example, PET/ITO/rGO/B-PVA-KCl/rGORu/ITO/PET which we named by simplicity (rGO/rGORu). Likewise, the rGO/AzoRu and rGORu/AzoRu devices were constructed and tested. A rectangular CV shape and rapid current response upon the voltage reversal is observed for the rGO/rGORu device. Besides, the rGO/AzoRu device exhibited two peaks with a separation of 0.55 V, which corresponds to AzoRu redox reaction. The rGORu/AzoRu device exhibited an increased current at low potentials and a rectangular shaped voltammogram at high potentials, but the current notably smaller than the other devices at higher than 0.2 volts, so it indicates that the storage due to capacitive part of the device is significantly lower, maybe by an unbalance in the charge storage of the electrodes.

The galvanostatic charge-discharge profiles at relative high rate are shown in Figure 8-9b. rGO/rGORu exhibited a roughly triangular shape typical of capacitive behavior. However,

some asymmetries were observed, at the onset of charging process the potential increases rapidly from 0 to ~ 0.12 V, likewise at the onset of discharging process the potential decreases rapidly from 0.9 to ~ 0.78 V indicating an important internal resistance in the device, so a considerably high “IR drop”. rGO/AzoRu exhibited an IR-drop apparently higher, additionally it exhibited a curved and asymmetrical profile. It was observed the lowest slope from 0.4 V to 0.6 V during the charging process and from 0.2 to 0 V during discharging process, since it may occur the redox process in AzoRu in those regions, in fact redox peaks are observed in the voltammogram at these potentials. rGORu/AzoRu profile is almost symmetrical but two regions with different slope are identified, from 0 to 0.15 V the small slope is consistent with the increased current observed in the voltammogram at low potentials.

FIGURE 8-9- ELECTROCHEMICAL CHARACTERIZATION OF ASYMMETRICAL DEVICES.



a) Cyclic voltammogram at 25 mV s⁻¹ and b) charge discharge profiles at 2 μA cm⁻² of the asymmetrical supercapacitors. Cyclic voltammogram at different scan rates of c) rGO-AzoRu and d) rGORu device.

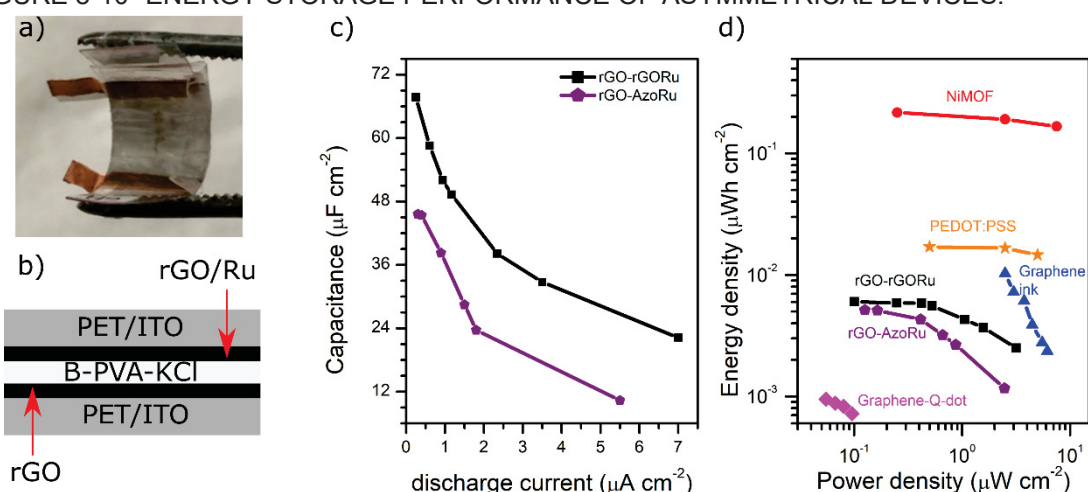
SOURCE: Author

The results suggest that the rGO/rGORu device, which have more content of graphene have the better capacitive performance, but with an important equivalent series resistance as suggested by the voltage drop at the beginning of the discharge curve and by the rounded features in the limiting potentials of the voltammograms. It is better visualized in Figure 8-9d, at higher scan rates the voltammogram was bent, so the capacity was considerably diminished. On the other hand, rGO/AzoRu device also present an important internal resistance which limits the storage by AzoRu redox reaction at scan rates higher or equal than 100 mV s⁻¹. The voltammogram bent and the redox peaks are no longer observed as can be seen in Figure

8-9c. rGORu/AzoRu device exhibited a straight voltammogram at high scan rates, but the lower currents obtained at high potentials decreased its capacity respect to other devices.

The devices initially manufactured were small with a working area (A_e) of $\sim 0.64 \text{ cm}^2$ in each electrode. They have been bent (curved) repeatedly without mechanical damage of the cell as observed in Figure 8-10a. The capacitance per unit of area of the rGO/rGORu and rGO/AzoRu devices were calculated from the CD measurements using the total geometric area of the two electrodes ($2A_e = 1.28 \text{ cm}^2$). As can be observed in Figure 8-10b the rGO/rGORu device exhibited higher capacitances than rGO/AzoRu, likewise the capacitance retention at high discharge rates of rGO/rGORu device (34%) was higher than that of rGO/AzoRu device (23%). It can be attributed to the presence of graphene in both electrodes which lead to better charge transport in the device. The maximum capacitance value of rGO/rGORu device was $68 \mu\text{F cm}^{-2}$ at $0.25 \mu\text{A cm}^{-2}$ which is lower than the maximum of $105 \mu\text{F cm}^{-2}$ expected for the cell considering the results of individual electrodes with a capacitance ranging from 320 and $420 \mu\text{F cm}^{-2}$ approximately.

FIGURE 8-10- ENERGY STORAGE PERFORMANCE OF ASYMMETRICAL DEVICES.



a) Digital photography of the flexible device and b) scheme of the device illustrating electrical contacts. c) Areal capacitance at different discharge currents of rGO-rGORu and rGO-AzoRu device. d) Ragone plot of device fabricated and its comparison with other supercapacitors.

SOURCE: Author.

The performance of the device here fabricated is not among the best, the capacitance of other micro-supercapacitors developed in other works using pseudocapacitive electrodes was superior. A high capacitance of $1560 \mu\text{F cm}^{-2}$ at $0.5 \mu\text{A cm}^{-2}$ was achieved with a Ni-MOF, [205] whereas the capacitance of symmetric capacitor using as electrodes poly(3,4-ethylenedioxythiophene):poly(styrene-4-sulfonate) (PEDOT:PSS) was $\sim 120 \mu\text{F cm}^{-2}$ at $1 \mu\text{A cm}^{-2}$. [329] Besides the capacitance of symmetric capacitors using graphene quantum dots was $9.9 \mu\text{F cm}^{-2}$ at $0.1 \mu\text{A cm}^{-2}$, [330] and $74 \mu\text{F cm}^{-2}$ at $5 \mu\text{A cm}^{-2}$ for capacitors with graphene printed electrodes. [331] So, the performance of the rGO/rGORu is similar to that of graphene ink and is far from the Ni-MOF capacitors as can be seen in the Ragone plot (Figure 8-10c).

Also, it was noted an important energy density decreasing at high power in accordance with the low capacitance retention at high discharge rates.

However, the performance of the device as proof of concept is promising since it demonstrates the application of Langmuir Blodgett films and hybrid materials to microcapacitors. The hybrid thin films fabricated by LB method exhibited a capacitive behavior and the contribution of redox reaction in ruthenium cluster, and the thin film structure achieved with the LB method have better performance, particularly at high discharge rates, than the drop casted electrode. Probably the LB films contain more interconnected structures and are less compacted than drop-casted films. The use of GO which disperses in water better than rGO-NHRu may lead to less aggregated structures, and graphene can be transferred to the substrate as thin sheets upon spread them on water. Whereas the compression of the graphene sheets can induce wrinkling and partial overlapping of the sheets in the 3D space, which improves electrical connection between material pieces and creates spaces which could serve for ion diffusion within the film. So, this work demonstrated that the design of nanoarchitectures can improve the performance of the materials as energy storage electrodes. The electrodes could be further improved exploring the structure control achieved with pressure deposition variation in the LB technique when a more uniform graphene oxide dispersion including sheets with large lateral dimensions are used.[235,236] Also, the co-deposition of graphene or functionalization with amphiphilic molecules/complexes could be explored to obtain other organization in graphene sheets.

The device fabricated could be further improved with variations in the materials and the fabrication process. For example, higher energy density would be achieved using electrodes with more mass loading, since the device would attain higher capacitance. Likewise, using other solid electrolytes allowing higher potential window, such as ionic liquid or organic gel polymers. On the other hand, the power density could be increased by the improving the integration between electrodes and electrolyte, which is a key challenge for high-performance flexible supercapacitors. [242,328] Since the charge transport in the device could be enhanced in this way, so the capacitance should be retained at high discharge rates. A feasible strategy to get better integration is the fabrication of the B-PVA-KCl film directly on the electrodes. As consequence, whereas the electrolyte is dried it works as a binder ensuring better electrical contacts between electrodes. It should be ideal to develop an “all-in-one” supercapacitor, with the electrodes and the electrolyte in a unique piece. [242,328,332,333]

9 FINAL REMARKS

The development of novel electrodes for supercapacitors based on triruthenium clusters ($\text{Ru}_3\text{O}(\text{CH}_3\text{CO}_2)_6\text{L}_3$) was described in this thesis. This work was envisioned as initial step to harness the interesting properties of triruthenium cluster and self-organized films in energy storage materials, which is an important and actual research area. So, this work takes advantage of the experience of Laboratório de Nanomateriais Inorgânicos in ruthenium complexes synthesis and characterization, and films fabrication using the Langmuir-Blodgett method to apply it in a technological development line new for the group. Different strategies were explored aiming to improve the capacity of the electrodes at high discharge rates. Such as, their hybridization with graphene, the fabrication of self-organized films and the generation of layered 2D heterostructures. The development of that electrodes involved the synthesis of three different triruthenium clusters ($\text{Ru}_3\text{O}(\text{CH}_3\text{CO}_2)_6\text{Py}_2\text{L}$ ($\text{L}=\text{AzoPy}$, NH_2Py , SHPy)), but the triruthenium cluster with mercaptopyridine (SHPy) was not successfully purified and probably other triruthenium cluster with 4,4'-dipyridyl disulfide was formed as byproduct. The electrochemical characterization of the complexes showed that all of them have several electrochemically reversible redox processes typical of the triruthenium clusters, which can be harnessed in electrodes for electrochemical energy storage devices.

So, a novel nanocomposite based on graphene and triruthenium cluster was synthesized (rGO-NHRu), probably the triruthenium cluster was coordinated to graphene functionalized with aminopyridine (NH_2Py) through the pyridinic site as suggested by Raman, XPS and EDS spectra. The electrochemical characterization revealed the contribution of both mechanisms, redox and capacitive, to the energy storage in the nanocomposite. The combination of the redox and capacitive material is promising, however, limitations in the redox mechanism at high scan rates or discharge currents were found, which can be attributed to charge transport limitations due to electrode structure. Enhancing the electrode porosity and structure to increase the surface area exposed probably led to electrodes with better performance.

LB technique was explored as promising technique to fabricate thin film electrodes with organized structure, the using of triruthenium cluster with amphiphilic ligand AzoPy allowed the self-organization of the clusters at water-air interface. The compression of the Langmuir film led to high packing and close interactions between molecules, that film was successfully transferred to substrate maintaining its organization as suggested by UV-vis and PM-IRRAS. Cyclic voltammetry of these films exhibited broadened redox peaks and an apparent shifting of $E_{1/2}$, these characteristics were explained by a mathematical model as result of lateral interactions and the existence of nonequivalent sites since the layer adjacent to substrate is stabilized in a different way that the layers far of the substrate. The LB film with 18 monolayers

exhibited a specific capacitance of 204 Fg^{-1} (1.02 mFcm^{-2}) at 50 mV s^{-1} . However, some limitations in the electrodes capacity were observed at higher scan rates, particularly in thicker electrodes. According to the model the kinetic and diffusion parameters describes these limitations, so improving the electron transfer and ion diffusion within the film through modifications in the materials used or the LB film fabrication are required to overcome these limitations.

Finally, the mathematical model study led us to investigate new graphene-ruthenium LB films with higher effective quantity of material used, probably because of the higher site exposition promoted by this method and the possibility of obtaining ultrathin films. The advantages of this technique were exploited in the fabrication of hybrid electrodes with alternated layers of graphene and triruthenium cluster, the electrode presented wrinkled graphene sheets, layered structure and the presence of triruthenium cluster as suggested by SEM images, IR, Raman and EDS. The hybrid rGORu LB electrodes exhibited performance superior to rGO-NHRu drop-casted electrodes at high discharge rates. The rGORu of 8 **ML** exhibited a capacitance per unit of area similar to rGO-NHRu, the former retained the 64% of the capacitance at high discharge rates whereas the rGO-NHRu only retained the 41% of its capacitance. It was attributed to higher accessible area and improved charge transport in LB electrodes.

The specific capacitance of 8 **ML** rGORu was 0.710 mF cm^{-2} (44.38 F g^{-1}) is comparable to other graphene metal oxide hybrid electrodes, but it was lower than other hybrid electrodes including metal complexes. Probably the electrode structure could be improved to achieve interconnected 3D structures with higher accessible surface area and improved ion diffusion in the whole electrode, particularly in thicker electrodes. It was observed that despite the capacitance per unit of area increased with the electrode thickness increasing, the proportion of material effectively used decreased and the electrode performance at high discharge rates was deteriorated. For these reasons, we considered that electrodes with 8 to 12 **ML** offered a good performance at high discharge rates and specific capacitances (per unit of mass and unit of area). So, rGORu electrodes with 12 **ML** were used to fabricate asymmetrical flexible devices combining it with AzoRu and rGO LB electrodes and B-PVA-KCl electrodes. The devices demonstrated that Langmuir Blodgett films can be applied to microcapacitors, an important technology for the energy storage management in electronic circuits, autonomous remote sensors among other applications. The device performance is not among the best, but considering it as a proof of concept, the new device is promising for energy storage.

9.1 FUTURE WORK

During the development of this work some problems or interesting observations which suggest several possible future works. Some of them are mentioned in the following paragraphs, following the order presented in the thesis. Some triruthenium clusters with N-heterocyclic ligands were synthesized and characterized in this work, they exhibit interesting electronic and electrochemical properties tunable through the choosing of ligand, so the reassessment of these properties with electronic structure calculations through DFT would be interesting to expand the actual knowledge explaining the relationship between electronic structure and the properties exhibited. Also, the synthesis condition of SHRu was not completely successful, so it could be replanned modifying the synthesis conditions, particularly the pH, to avoid the formation of thiolate ion and subsequent formation of dipyriddy disulfide or adding a reducing agent which breaks the disulfide bonds.

The hybrid nanomaterial rGO-NHRu exhibited a poor performance at high scan rates, probably due to the structure of the electrode. Probably, the difficulties for dispersing rGO-NHRu in water contribute to the aggregated and compact structure of this material. Modification of the synthesis method to obtain a highly porous material like the previously reported 3D graphene networks, such as self-assembled graphene hydrogels or aerogels, could lead to structures with higher surface area and redox sites exposed. [173,334,335] The method to be used may allow the simultaneous formation of the hydrogel and formation of the hybrid material. In an analogy with reported methods for the hydrogel synthesis, [173,334,335] one possible strategy should be the heating of the homogeneous mixture of graphene oxide functionalized with aminopyridine and triruthenium cluster precursor at 180 °C in autoclave, that could be a suitable way to synthesize the hybrid material in form of 3D graphene.

Likewise, as was herein demonstrated, the fabrication of graphene LB films is a suitable strategy to obtain structures that lead to improve the electrode performance. However, the LB films here obtained could be further improved exploring the structure control achieved with deposition at different pressures of large graphene oxide sheets, [236] and their co-deposition with amphiphilic ruthenium complexes which can interact with oxygenated groups in graphene. Despite the good performance of LB electrodes, some limitations are found for thicker electrodes at high discharge rates, for example AzoRu showed limitations at scan rates higher than 100 mV s⁻¹ which was attributed to slow charge transfer within the film and from the film to the substrate. It could be overcome including organic molecules with better self-assembly properties that force the organization of the multilayer films and improve the electron transfer within the film, for example constructing heterostructured films with layers of AzoRu and the organic molecules could lead to different film organization and behavior. [206]

Also, various designed complexes with different redox potential could be included in the same film to get a greater potential window, substrates different from ITO with higher conductivity could be used and other hybrid materials based on triruthenium cluster could be synthesized such as the combination of gold nanoparticles with ruthenium complexes planned in the project proposal, but not developed due to several drawbacks, still being an interesting alternative. The LB electrodes performance was demonstrated in a single cell device, which could be enhanced using electrodes with more mass loading to attain higher capacitance and with additional studies to adjust the charge balance between the two electrodes. Additionally, the exploring of other electrolytes such as ionic liquid or organic electrolytes is recommendable since they offer higher potential window, so higher energy density. The electrodes/electrolyte integration is key to achieve high-performance in flexible supercapacitors, [242,328] since in this way the internal resistance of the device could be decreased. A feasible strategy to get better integration is the using of wet B-PVA-KCl, so whereas the electrolyte is dried it can work as binder ensuring better electrical contacts between electrodes and acts as device sealer. Even better, it would be ideal to develop an “all-in-one” supercapacitor, thinking in strategies for electrode printing on the electrolytes to obtain a unique piece. [242,328,332,333]

Finally, we should remark that the model developed can be expanded including explicitly the capacitive process an ion transport within the film, also kinetic parameters could be calculated from DFT and integrated with the model in a parametric multiscale approach. The model code could be modified to calculate the electrochemical response when the input to the system is other signal different to the electrode potential. An interesting exercise is the restatement of the kinetic model considering other models for electron transfer such as the Marcus-Hush model and consider the electron transfer between molecules explicitly. As can be seen this work is just a small step, there are many possibilities for additional studies either continuing the work done or opening other lines based on the results found and I hope that this thesis will serve well other scientists who want to explore the areas of energy storage, or hybrid nanomaterials, or ruthenium complexes, as well self-organized thin films.

REFERENCES

- [1] W. Commission, Report of the World Commission on Environment and Development: Our Common Future, 1987.
- [2] R.W. Kates, T.M. Parris, A.A. Leiserowitz, What Is Sustainable Development?, *Environment*. 47 (2005) 8–21.
- [3] IEA, CO₂ Emissions from Fuel Combustion 2016, IEA, 2016. https://doi.org/10.1787/co2_fuel-2016-en.
- [4] K. Alanne, A. Saari, Distributed energy generation and sustainable development, *Renew. Sustain. Energy Rev.* 10 (2006) 539–558. <https://doi.org/10.1016/j.rser.2004.11.004>.
- [5] Organización de las Naciones Unidas (ONU), La Agenda de Desarrollo Sostenible, (n.d.). <http://www.un.org/sustainabledevelopment/es/la-agenda-de-desarrollo-sostenible/>.
- [6] C. Karakosta, C. Pappas, V. Marinakis, J. Psarras, Renewable energy and nuclear power towards sustainable development: Characteristics and prospects, *Renew. Sustain. Energy Rev.* 22 (2013) 187–197. <https://doi.org/10.1016/j.rser.2013.01.035>.
- [7] N. Girouard, E. Konialis, C. Tam, Peter, Taylor, Energy, OECD Publishing, 2012. <https://doi.org/10.1787/9789264115118-en>.
- [8] M. Beaudin, H. Zareipour, A. Schellenberglabe, W. Rosehart, Energy storage for mitigating the variability of renewable electricity sources: An updated review, *Energy Sustain. Dev.* 14 (2010) 302–314. <https://doi.org/10.1016/j.esd.2010.09.007>.
- [9] M.M. Mirzaeian, Q. Abbas, A. Ogwu, P. Hall, M. Goldin, M.M. Mirzaeian, H.F. Jirandehi, Electrode and electrolyte materials for electrochemical capacitors, *Int. J. Hydrogen Energy*. 42 (2017) 25565–25587. <https://doi.org/10.1016/j.ijhydene.2017.04.241>.
- [10] F. Wang, X. Wu, X. Yuan, Z. Liu, Y. Zhang, L. Fu, Y. Zhu, Q. Zhou, Y. Wu, W. Huang, Latest advances in supercapacitors: from new electrode materials to novel device designs, *Chem. Soc. Rev.* 46 (2017) 6816–6854. <https://doi.org/10.1039/C7CS00205J>.
- [11] B.E. Conway, Similarities and Differences between Supercapacitors and Batteries for Storing Electrical Energy, in: *Electrochem. Supercapacitors*, Springer US, Boston, MA, 1999: pp. 11–31. https://doi.org/10.1007/978-1-4757-3058-6_2.
- [12] P.T. Anastas, J.B. Zimmerman, The Molecular Basis of Sustainability, *Chem.* 1 (2016) 10–12. <https://doi.org/10.1016/j.chempr.2016.06.016>.
- [13] J. Yan, Q. Wang, T. Wei, Z. Fan, Recent advances in design and fabrication of electrochemical supercapacitors with high energy densities, *Adv. Energy Mater.* 4 (2014). <https://doi.org/10.1002/aenm.201300816>.
- [14] J. Liu, J. Wang, C. Xu, H. Jiang, C. Li, L. Zhang, J. Lin, Z.X. Shen, Advanced Energy Storage Devices: Basic Principles, Analytical Methods, and Rational Materials Design, *Adv. Sci.* 5 (2018) 1700322. <https://doi.org/10.1002/adv.201700322>.
- [15] S. Fleischmann, J.B. Mitchell, R. Wang, C. Zhan, D.E. Jiang, V. Presser, V. Augustyn, Pseudocapacitance: From Fundamental Understanding to High Power Energy Storage Materials, *Chem. Rev.* 120 (2020) 6738–6782. <https://doi.org/10.1021/acs.chemrev.0c00170>.

- [16] A.D.P. Alexiou, S. Dovidauskas, H.E. Toma, Propriedades e Aplicações de Clusters Trinucleares de Carboxilatos de Rutênio, 23 (2000) 785–793.
- [17] R.C. Rocha, H.E. Toma, Transferência de elétrons em sistemas inorgânicos de valência mista, *Quim. Nova.* 25 (2002) 624–638. <https://doi.org/10.1590/S0100-40422002000400018>.
- [18] F.A. Cotton, J.G. Norman, Structural characterization of a basic trinuclear ruthenium acetate, *Inorganica Chim. Acta.* 6 (1972) 411–419. [https://doi.org/10.1016/S0020-1693\(00\)91829-2](https://doi.org/10.1016/S0020-1693(00)91829-2).
- [19] H.E. Toma, K. Araki, A.D.P. Alexiou, S. Nikolaou, S. Dovidauskas, Monomeric and extended oxo-centered triruthenium clusters, *Coord. Chem. Rev.* 219–221 (2001) 187–234. [https://doi.org/10.1016/S0010-8545\(01\)00326-5](https://doi.org/10.1016/S0010-8545(01)00326-5).
- [20] A. Spencer, G. Wilkinson, μ -Oxo-triruthenium carboxylate complexes, *J. Chem. Soc., Dalton Trans.* (1972) 1570–1577. <https://doi.org/10.1039/DT9720001570>.
- [21] H.E. Toma, C.J. Cunha, C. Cipriano, Redox Potentials of Trinuclear μ -Oxo Ruthenium Acetate Clusters with Ligands, *Inorganica Chim. Acta.* 154 (1988) 63–66.
- [22] M. Abe, Y. Sasaki, Y. Yamada, K. Tsukahara, S. Yano, T. Ito, Reversible Multistep and Multielectron Redox Behavior of an Oxo-Centered Trinuclear Diruthenium- Rhodium Derivatives, *Inorg. Chem.* 34 (1995) 4490–4498.
- [23] J.A. Baumann, D.J. Salmon, S.T. Wilson, T.J. Meyer, W.E. Hatfield, Electronic Structure and Redox Properties of the Clusters $[\text{Ru}_3\text{O}(\text{CH}_3\text{CO}_2)_6\text{L}_3]^{n+}$, *Inorg. Chem.* 17 (1978) 3342–3350. <https://doi.org/10.1021/ic50190a007>.
- [24] International Energy Agency, Data and Statistics, (n.d.). <https://www.iea.org/data-and-statistics/data-browser>.
- [25] International Energy Agency, Global Energy Review 2021, *Glob. Energy Rev.* 2020. (2021) 1–36. <https://iea.blob.core.windows.net/assets/d0031107-401d-4a2f-a48b-9eed19457335/GlobalEnergyReview2021.pdf>.
- [26] N. Chouhan, R.-S. Liu, Electrochemical Technologies for Energy Storage and Conversion, in: *Electrochem. Technol. Energy Storage Convers.*, Wiley-VCH Verlag GmbH & Co. KGaA, Weinheim, Germany, 2012: pp. 1–43. <https://doi.org/10.1002/9783527639496.ch1>.
- [27] S.P.S. Badwal, S.S. Giddey, C. Munnings, A.I. Bhatt, A.F. Hollenkamp, Emerging electrochemical energy conversion and storage technologies, *Front. Chem.* 2 (2014). <https://doi.org/10.3389/fchem.2014.00079>.
- [28] T. Kousksou, P. Bruel, A. Jamil, T. El Rhafiki, Y. Zeraoui, Energy storage: Applications and challenges, *Sol. Energy Mater. Sol. Cells.* 120 (2014) 59–80. <https://doi.org/10.1016/j.solmat.2013.08.015>.
- [29] A.K. Hussein, Applications of nanotechnology in renewable energies—A comprehensive overview and understanding, *Renew. Sustain. Energy Rev.* 42 (2015) 460–476. <https://doi.org/10.1016/j.rser.2014.10.027>.
- [30] G. Huff, A.B. Currier, B.C. Kaun, D.M. Rastler, S.B. Chen, D.T. Bradshaw, W.D. Gauntlett, *Electricity Storage Handbook*, 2013.
- [31] European Commission-Directorate General for Energy, *The future role and challenges of Energy Storage*, 2013.

- [32] U.S. Department of Energy (DOE), Energy Storage Systems Program, (2018). <https://www.sandia.gov/ess-ssl/>.
- [33] European Commission, Energy Storage - The role of electricity, 2017.
- [34] R. Adib REN, M. Folkecenter, A. Development Bank, M. Eckhart Mohamed El-Ashry David Hales Kirsty Hamilton Peter Rae, F. Bariloche, Renewables 2018 · Global Status Report, 2018. www.ren21.net.
- [35] S.M. Schoenung, W. Hassenzahl, Characteristics and Technologies for Long-vs. Short-Term Energy Storage A Study by the DOE Energy Storage Systems Program SAND2001-0765, Sandia Natl. Lab. U.S. Dept. Energy. (2001) 46 pp.
- [36] R. Edwards, C. Gould, Review on micro-energy harvesting technologies, Proc. - 2016 51st Int. Univ. Power Eng. Conf. UPEC 2016. 2017-Janua (2017) 1–5. <https://doi.org/10.1109/UPEC.2016.8114023>.
- [37] C. Tudor, E. Sprung, J. Meyer, R. Tatro, Low power-energy storage system for energy harvesting applications, Proc. 2013 IEEE 14th Int. Conf. Inf. Reuse Integr. IEEE IRI 2013. (2013) 648–660. <https://doi.org/10.1109/IRI.2013.6642530>.
- [38] S. Kim, P.H. Chou, Energy Harvesting with Supercapacitor-Based Energy Storage, in: Smart Sensors Syst., Springer International Publishing, Cham, 2015: pp. 215–241. https://doi.org/10.1007/978-3-319-14711-6_10.
- [39] Y. Liang, C. Zhao, H. Yuan, Y. Chen, W. Zhang, J. Huang, D. Yu, Y. Liu, M. Titirici, Y. Chueh, H. Yu, Q. Zhang, A review of rechargeable batteries for portable electronic devices, InfoMat. 1 (2019) 6–32. <https://doi.org/10.1002/inf2.12000>.
- [40] G. Pistoia, APPLICATIONS – PORTABLE | Portable Devices: Batteries, in: Encycl. Electrochem. Power Sources, Elsevier, 2009: pp. 29–38. <https://doi.org/10.1016/B978-044452745-5.00358-0>.
- [41] S.F. Tie, C.W. Tan, A review of energy sources and energy management system in electric vehicles, Renew. Sustain. Energy Rev. 20 (2013) 82–102. <https://doi.org/10.1016/j.rser.2012.11.077>.
- [42] J. Ruan, P.D. Walker, N. Zhang, J. Wu, An investigation of hybrid energy storage system in multi-speed electric vehicle, Energy. 140 (2017) 291–306. <https://doi.org/10.1016/j.energy.2017.08.119>.
- [43] A. Burke, Z. Liu, H. Zhao, Present and future applications of supercapacitors in electric and hybrid vehicles, 2014 IEEE Int. Electr. Veh. Conf. (2014) 1–8. <https://doi.org/10.1109/IEVC.2014.7056094>.
- [44] A. González, E. Goikolea, J.A. Barrena, R. Mysyk, Review on supercapacitors: Technologies and materials, Renew. Sustain. Energy Rev. 58 (2016) 1189–1206. <https://doi.org/10.1016/j.rser.2015.12.249>.
- [45] L. Kouchachvili, W. Ya'ici, E. Entchev, Hybrid battery/supercapacitor energy storage system for the electric vehicles, J. Power Sources. 374 (2018) 237–248. <https://doi.org/10.1016/j.jpowsour.2017.11.040>.
- [46] D. Cericola, R. Kötz, Hybridization of rechargeable batteries and electrochemical capacitors: Principles and limits, Electrochim. Acta. 72 (2012) 1–17.

- <https://doi.org/10.1016/j.electacta.2012.03.151>.
- [47] a. Cooper, J. Furakawa, L. Lam, M. Kellaway, The UltraBattery—A new battery design for a new beginning in hybrid electric vehicle energy storage, *J. Power Sources*. 188 (2009) 642–649. <https://doi.org/10.1016/j.jpowsour.2008.11.119>.
- [48] O.M. Magnussen, A. Groß, Toward an Atomic-Scale Understanding of Electrochemical Interface Structure and Dynamics, *J. Am. Chem. Soc.* 141 (2019) 4777–4790. <https://doi.org/10.1021/jacs.8b13188>.
- [49] V. Augustyn, M.T. McDowell, A. Vojvodic, Toward an Atomistic Understanding of Solid-State Electrochemical Interfaces for Energy Storage, *Joule*. 2 (2018) 2189–2193. <https://doi.org/10.1016/j.joule.2018.10.014>.
- [50] A. Groß, Theory of Solid/Electrolyte Interfaces, *Surf. Interface Sci.* (2020) 471–515. <https://doi.org/10.1002/9783527680603.ch56>.
- [51] D. Noel Buckley, C. O'Dwyer, N. Quill, R.P. Lynch, *Electrochemical Energy Storage*, 2019. <https://doi.org/10.1039/9781788015530-00115>.
- [52] P. Simon, Y. Gogotsi, B. Dunn, Where Do Batteries End and Supercapacitors Begin?, *Science* (80-.). 343 (2014) 1210–1211. <https://doi.org/10.1126/science.1249625>.
- [53] P.E. Lokhande, U.S. Chavan, A. Pandey, *Materials and Fabrication Methods for Electrochemical Supercapacitors: Overview*, Springer Singapore, 2020. <https://doi.org/10.1007/s41918-019-00057-z>.
- [54] C. Zong, C.J. Chen, M. Zhang, D.Y. Wu, B. Ren, Transient Electrochemical Surface-Enhanced Raman Spectroscopy: A Millisecond Time-Resolved Study of an Electrochemical Redox Process, *J. Am. Chem. Soc.* 137 (2015) 11768–11774. <https://doi.org/10.1021/jacs.5b07197>.
- [55] T.S. Mathis, N. Kurra, X. Wang, D. Pinto, P. Simon, Y. Gogotsi, Energy Storage Data Reporting in Perspective—Guidelines for Interpreting the Performance of Electrochemical Energy Storage Systems, *Adv. Energy Mater.* 9 (2019) 1–13. <https://doi.org/10.1002/aenm.201902007>.
- [56] B.E. Conway, B.E. Conway, Electrochemical Capacitors Based on Pseudocapacitance, *Electrochem. Supercapacitors*. (1999) 221–257. https://doi.org/10.1007/978-1-4757-3058-6_10.
- [57] B.E. Conway, Transition from “Supercapacitor” to “Battery” Behavior in Electrochemical Energy Storage, *J. Electrochem. Soc.* 138 (1991) 1539–1548. <https://doi.org/10.1149/1.2085829>.
- [58] T. Brousse, D. Bélanger, J.W. Long, To be or not to be pseudocapacitive?, *J. Electrochem. Soc.* 162 (2015) A5185–A5189. <https://doi.org/10.1149/2.0201505jes>.
- [59] D.P. Dubal, O. Ayyad, V. Ruiz, P. Gómez-Romero, Hybrid energy storage: the merging of battery and supercapacitor chemistries, *Chem. Soc. Rev.* 44 (2015) 1777–1790. <https://doi.org/10.1039/C4CS00266K>.
- [60] Z.W. Seh, J. Kibsgaard, C.F. Dickens, I. Chorkendorff, J.K. Nørskov, T.F. Jaramillo, Combining theory and experiment in electrocatalysis: Insights into materials design, *Science* (80-.). 355 (2017) eaad4998. <https://doi.org/10.1126/science.aad4998>.
- [61] A. Jain, Y. Shin, K.A. Persson, Computational predictions of energy materials using density functional theory, *Nat. Rev. Mater.* 1 (2016) 1–13. <https://doi.org/10.1038/natrevmats.2015.4>.
- [62] J. Yan, S. Li, B. Lan, Y. Wu, P.S. Lee, Rational Design of Nanostructured Electrode Materials

- toward Multifunctional Supercapacitors, *Adv. Funct. Mater.* 30 (2020) 1–35. <https://doi.org/10.1002/adfm.201902564>.
- [63] Z. Liu, X. Yuan, S. Zhang, J. Wang, Q. Huang, N. Yu, Y. Zhu, L. Fu, F. Wang, Y. Chen, Y. Wu, Three-dimensional ordered porous electrode materials for electrochemical energy storage, *NPG Asia Mater.* 11 (2019). <https://doi.org/10.1038/s41427-019-0112-3>.
- [64] R. Liu, J. Duay, S.B. Lee, Heterogeneous nanostructured electrode materials for electrochemical energy storage, *Chem. Commun.* 47 (2011) 1384–1404. <https://doi.org/10.1039/c0cc03158e>.
- [65] S. Kajiyama, L. Szabova, K. Sodeyama, H. Iinuma, R. Morita, K. Gotoh, Y. Tateyama, M. Okubo, A. Yamada, Sodium-Ion Intercalation Mechanism in MXene Nanosheets, *ACS Nano.* 10 (2016) 3334–3341. <https://doi.org/10.1021/acsnano.5b06958>.
- [66] P. Simon, Y. Gogotsi, Materials for electrochemical capacitors, *Nat. Mater.* 7 (2008) 845–854. <https://doi.org/10.1038/nmat2297>.
- [67] Poonam, K. Sharma, A. Arora, S.K. Tripathi, Review of supercapacitors: Materials and devices, *J. Energy Storage.* 21 (2019) 801–825. <https://doi.org/10.1016/j.est.2019.01.010>.
- [68] H. Sun, J. Zhu, D. Baumann, L. Peng, Y. Xu, I. Shakir, Y. Huang, X. Duan, Hierarchical 3D electrodes for electrochemical energy storage, *Nat. Rev. Mater.* 4 (2019) 45–60. <https://doi.org/10.1038/s41578-018-0069-9>.
- [69] Lakes R. S., Materials with structural hierarchy, *Nature.* 361 (1993) 511–515.
- [70] R. Hou, G.S. Gund, K. Qi, P. Nakhnivej, H. Liu, F. Li, B.Y. Xia, H.S. Park, Hybridization design of materials and devices for flexible electrochemical energy storage, *Energy Storage Mater.* 19 (2019) 212–241. <https://doi.org/10.1016/j.ensm.2019.03.002>.
- [71] X. Peng, L. Peng, C. Wu, Y. Xie, Two dimensional nanomaterials for flexible supercapacitors, *Chem. Soc. Rev.* 43 (2014) 3303–3323. <https://doi.org/10.1039/c3cs60407a>.
- [72] M. Yu, X. Feng, Thin-Film Electrode-Based Supercapacitors, *Joule.* 3 (2019) 338–360. <https://doi.org/10.1016/j.joule.2018.12.012>.
- [73] Y. Guo, Y. Wei, H. Li, T. Zhai, Layer Structured Materials for Advanced Energy Storage and Conversion, *Small.* 13 (2017) 1–22. <https://doi.org/10.1002/sml.201701649>.
- [74] A.K. Geim, I. V. Grigorieva, Van der Waals heterostructures, *Nature.* 499 (2013) 419–425. <https://doi.org/10.1038/nature12385>.
- [75] J. Yan, C.E. Ren, K. Maleski, C.B. Hatter, B. Anasori, P. Urbankowski, A. Sarycheva, Y. Gogotsi, Flexible MXene/Graphene Films for Ultrafast Supercapacitors with Outstanding Volumetric Capacitance, *Adv. Funct. Mater.* 27 (2017) 1–10. <https://doi.org/10.1002/adfm.201701264>.
- [76] I. Shakir, High Energy Density based Flexible Electrochemical Supercapacitors from Layer-by-Layer Assembled Multiwall Carbon Nanotubes and Graphene, *Electrochim. Acta.* 129 (2014) 396–400. <https://doi.org/10.1016/j.electacta.2014.02.124>.
- [77] J. Zhu, Y. Shan, T. Wang, H. Sun, Z. Zhao, L. Mei, Z. Fan, Z. Xu, I. Shakir, Y. Huang, B. Lu, X. Duan, A hyperaccumulation pathway to three-dimensional hierarchical porous nanocomposites for highly robust high-power electrodes, *Nat. Commun.* 7 (2016) 1–10. <https://doi.org/10.1038/ncomms13432>.
- [78] K. Ariga, M. Nishikawa, T. Mori, J. Takeya, L.K. Shrestha, J.P. Hill, Self-assembly as a key player

- for materials nanoarchitectonics, *Sci. Technol. Adv. Mater.* 20 (2019) 51–95. <https://doi.org/10.1080/14686996.2018.1553108>.
- [79] K. Ariga, Don't Forget Langmuir-Blodgett Films 2020: Interfacial Nanoarchitectonics with Molecules, Materials, and Living Objects, *Langmuir*. 36 (2020) 7158–7180. <https://doi.org/10.1021/acs.langmuir.0c01044>.
- [80] H.E. Toma, Supramolecular nanotechnology: from molecules to devices, *Curr. Sci.* 95 (2008) 1202–1225. <http://www.jstor.org/stable/24103233>.
- [81] Q. An, T. Huang, F. Shi, Covalent layer-by-layer films: Chemistry, design, and multidisciplinary applications, *Chem. Soc. Rev.* 47 (2018) 5061–5098. <https://doi.org/10.1039/c7cs00406k>.
- [82] A. Schneemann, R. Dong, F. Schwotzer, H. Zhong, I. Senkovska, X. Feng, S. Kaskel, 2D framework materials for energy applications, *Chem. Sci.* 12 (2021) 1600–1619. <https://doi.org/10.1039/d0sc05889k>.
- [83] T.A. Matias, G.C. Azzellini, L. Angnes, K. Araki, Supramolecular Hybrid Organic/Inorganic Nanomaterials Based on Metalloporphyrins and Phthalocyanines, in: J.H. Zagal, F. Bedioui (Eds.), *Electrochem. N4 Macrocycl. Met. Complexes*, Springer International Publishing, Cham, 2016: pp. 1–82. https://doi.org/10.1007/978-3-319-31332-0_1.
- [84] H.E. Toma, Molecular materials and devices: developing new functional systems based on the coordination chemistry approach, *J. Braz. Chem. Soc.* 14 (2003) 845–869. <https://doi.org/10.1590/S0103-50532003000600002>.
- [85] T. Michi, M. Abe, S. Takakusagi, M. Kato, K. Uosaki, Y. Sasaki, Spontaneous rapid growth of triruthenium cluster multilayers on gold surface. Cyclic voltammetric in situ monitoring and AFM characterization, *Chem. Lett.* 37 (2008) 576–577. <https://doi.org/10.1246/cl.2008.576>.
- [86] V. Augustyn, P. Simon, B. Dunn, Pseudocapacitive oxide materials for high-rate electrochemical energy storage, *Energy Environ. Sci.* 7 (2014) 1597. <https://doi.org/10.1039/c3ee44164d>.
- [87] T. Brousse, D. Bélanger, K. Chiba, M. Egashira, F. Favier, J. Long, J.R. Miller, M. Morita, K. Naoi, P. Simon, W. Sugimoto, Materials for Electrochemical Capacitors, in: *Springer Handb. Electrochem. Energy*, Springer Berlin Heidelberg, Berlin, Heidelberg, 2017: pp. 495–561. https://doi.org/10.1007/978-3-662-46657-5_16.
- [88] G.A. Snook, P. Kao, A.S. Best, Conducting-polymer-based supercapacitor devices and electrodes, *J. Power Sources*. 196 (2011) 1–12. <https://doi.org/10.1016/j.jpowsour.2010.06.084>.
- [89] J. Kim, J.H. Kim, K. Ariga, Redox-Active Polymers for Energy Storage Nanoarchitectonics, *Joule*. 1 (2017) 739–768. <https://doi.org/10.1016/j.joule.2017.08.018>.
- [90] Q. Meng, K. Cai, Y. Chen, L. Chen, Research progress on conducting polymer based supercapacitor electrode materials, *Nano Energy*. 36 (2017) 268–285. <https://doi.org/10.1016/j.nanoen.2017.04.040>.
- [91] H. Gu, C. Liu, J. Zhu, J. Gu, E.K. Wujcik, L. Shao, N. Wang, H. Wei, R. Scaffaro, J. Zhang, Z. Guo, Introducing advanced composites and hybrid materials, *Adv. Compos. Hybrid Mater.* 1 (2018) 1–5. <https://doi.org/10.1007/s42114-017-0017-y>.
- [92] F. a. Cotton, J.G. Norman, a. Spencer, G. Wilkinson, Oxotruthenium cluster complexes, *J. Chem. Soc. D Chem. Commun.* (1971) 967. <https://doi.org/10.1039/c29710000967>.

- [93] B.E. Conway, E. Gileadi, Kinetic theory of pseudo-capacitance and electrode reactions at appreciable surface coverage, *Trans. Faraday Soc.* 58 (1962) 2493. <https://doi.org/10.1039/tf9625802493>.
- [94] S. Ardizzone, G. Fregonara, S. Trasatti, "Inner" and "outer" active surface of RuO₂ electrodes, *Electrochim. Acta.* 35 (1990) 263–267. [https://doi.org/10.1016/0013-4686\(90\)85068-X](https://doi.org/10.1016/0013-4686(90)85068-X).
- [95] T.-C. Liu, W.G. Pell, B.E. Conway, S.L. Roberson, Behavior of Molybdenum Nitrides as Materials for Electrochemical Capacitors: Comparison with Ruthenium Oxide, *J. Electrochem. Soc.* 145 (1998) 1882–1888. <https://doi.org/10.1149/1.1838571>.
- [96] J. Wang, J. Polleux, J. Lim, B. Dunn, Pseudocapacitive Contributions to Electrochemical Energy Storage in TiO₂ (Anatase) Nanoparticles, *J. Phys. Chem. C.* 111 (2007) 14925–14931. <https://doi.org/10.1021/jp074464w>.
- [97] H. Lindström, S. Södergren, A. Solbrand, H. Rensmo, J. Hjelm, A. Hagfeldt, S. Lindquist, Li⁺ Ion Insertion in TiO₂ (Anatase). 2. Voltammetry on Nanoporous Films, *J. Phys. Chem. B.* 101 (1997) 7717–7722. <https://doi.org/10.1021/jp970490q>.
- [98] K. Aoki, K. Tokuda, H. Matsuda, Theory of linear sweep voltammetry with finite diffusion space, *J. Electroanal. Chem. Interfacial Electrochem.* 160 (1984) 33–45. [https://doi.org/10.1016/S0022-0728\(84\)80113-8](https://doi.org/10.1016/S0022-0728(84)80113-8).
- [99] J.S. Ko, M.B. Sassin, D.R. Rolison, J.W. Long, Deconvolving double-layer, pseudocapacitance, and battery-like charge-storage mechanisms in nanoscale LiMn₂O₄ at 3D carbon architectures, *Electrochim. Acta.* 275 (2018) 225–235. <https://doi.org/10.1016/j.electacta.2018.04.149>.
- [100] B.E. Conway, H. Angerstein-Kozłowska, Electrochemical Study of Multiple-State Adsorption in Monolayers, *Acc. Chem. Res.* 14 (1981) 49–56. <https://doi.org/10.1021/ar00062a004>.
- [101] M. Okubo, E. Hosono, J. Kim, M. Enomoto, N. Kojima, T. Kudo, H. Zhou, I. Honma, Nanosize effect on high-rate Li-ion intercalation in LiCoO₂ electrode, *J. Am. Chem. Soc.* 129 (2007) 7444–7452. <https://doi.org/10.1021/ja0681927>.
- [102] W. Dmowski, T. Egami, K.E. Swider-Lyons, C.T. Love, D.R. Rolison, Local atomic structure and conduction mechanism of nanocrystalline hydrous RuO₂ from X-ray scattering, *J. Phys. Chem. B.* 106 (2002) 12677–12683. <https://doi.org/10.1021/jp026228l>.
- [103] J.P. Zheng, P.J. Cygan, T.R. Jow, Hydrous Ruthenium Oxide as an Electrode Material for Electrochemical Capacitors, *J. Electrochem. Soc.* 142 (1995) 2699–2703. <https://doi.org/10.1149/1.2050077>.
- [104] N. Yoshida, Y. Yamada, S.I. Nishimura, Y. Oba, M. Ohnuma, A. Yamada, Unveiling the origin of unusual pseudocapacitance of RuO₂·nH₂O from its hierarchical nanostructure by small-angle x-ray scattering, *J. Phys. Chem. C.* 117 (2013) 12003–12009. <https://doi.org/10.1021/jp403402k>.
- [105] I.C. Stefan, Y. Mo, M.R. Antonio, D.A. Scherson, In situ Ru LII and LIII edge x-ray absorption near edge structure of electrodeposited ruthenium dioxide films, *J. Phys. Chem. B.* 106 (2002) 12373–12375. <https://doi.org/10.1021/jp026300f>.
- [106] R.N. Reddy, R.G. Reddy, Porous structured vanadium oxide electrode material for electrochemical capacitors, *J. Power Sources.* 156 (2006) 700–704. <https://doi.org/10.1016/j.jpowsour.2005.05.071>.

- [107] Z. Lin, X. Yan, J. Lang, R. Wang, L. Bin Kong, Adjusting electrode initial potential to obtain high-performance asymmetric supercapacitor based on porous vanadium pentoxide nanotubes and activated carbon nanorods, *J. Power Sources*. 279 (2015) 358–364. <https://doi.org/10.1016/j.jpowsour.2015.01.034>.
- [108] J. Zhu, L. Cao, Y. Wu, Y. Gong, Z. Liu, H.E. Hoster, Y. Zhang, S. Zhang, S. Yang, Q. Yan, P.M. Ajayan, R. Vajtai, Building 3D structures of vanadium pentoxide nanosheets and application as electrodes in supercapacitors, *Nano Lett.* 13 (2013) 5408–5413. <https://doi.org/10.1021/nl402969r>.
- [109] B.T. Liu, X.M. Shi, X.Y. Lang, L. Gu, Z. Wen, M. Zhao, Q. Jiang, Extraordinary pseudocapacitive energy storage triggered by phase transformation in hierarchical vanadium oxides, *Nat. Commun.* 9 (2018) 1–9. <https://doi.org/10.1038/s41467-018-03700-3>.
- [110] Y.Q. Li, H. Shi, S.B. Wang, Y.T. Zhou, Z. Wen, X.Y. Lang, Q. Jiang, Dual-phase nanostructuring of layered metal oxides for high-performance aqueous rechargeable potassium ion microbatteries, *Nat. Commun.* 10 (2019) 1–9. <https://doi.org/10.1038/s41467-019-12274-7>.
- [111] N. Zhao, H. Fan, M. Zhang, J. Ma, C. Wang, A.K. Yadav, H. Li, X. Jiang, X. Cao, Beyond intercalation-based supercapacitors: The electrochemical oxidation from Mn₃O₄ to Li₄Mn₅O₁₂ in Li₂SO₄ electrolyte, *Nano Energy*. 71 (2020) 104626. <https://doi.org/10.1016/j.nanoen.2020.104626>.
- [112] M.P. Yeager, W. Du, Q. Wang, N.A. Deskins, M. Sullivan, B. Bishop, D. Su, W. Xu, S.D. Senanayake, R. Si, J. Hanson, X. Teng, Pseudocapacitive hausmannite nanoparticles with (101) facets: Synthesis, characterization, and charge-transfer mechanism, *ChemSusChem*. 6 (2013) 1983–1992. <https://doi.org/10.1002/cssc.201300027>.
- [113] D. Xuan, W. Chengyang, C. Mingming, J. Yang, W. Jin, Electrochemical performances of nanoparticle Fe₃O₄/activated carbon supercapacitor using KOH electrolyte solution, *J. Phys. Chem. C*. 113 (2009) 2643–2646. <https://doi.org/10.1021/jp8088269>.
- [114] R. Kumar, R.K. Singh, A.R. Vaz, R. Savu, S.A. Moshkalev, Self-Assembled and One-Step Synthesis of Interconnected 3D Network of Fe₃O₄/Reduced Graphene Oxide Nanosheets Hybrid for High-Performance Supercapacitor Electrode, *ACS Appl. Mater. Interfaces*. 9 (2017) 8880–8890. <https://doi.org/10.1021/acsami.6b14704>.
- [115] T.C. Liu, W.G. Pell, B.E. Conway, Stages in the development of thick cobalt oxide films exhibiting reversible redox behavior and pseudocapacitance, *Electrochim. Acta*. 44 (1999) 2829–2842. [https://doi.org/10.1016/S0013-4686\(99\)00002-X](https://doi.org/10.1016/S0013-4686(99)00002-X).
- [116] C. He, Y. Liang, P. Gao, L. Cheng, D. Shi, X. Xie, R. Kowk-Yiu Li, Y. Yang, Bioinspired Co₃O₄/graphene layered composite films as self-supported electrodes for supercapacitors, *Compos. Part B Eng.* 121 (2017) 68–74. <https://doi.org/10.1016/j.compositesb.2017.03.025>.
- [117] S.A. Pawar, D.S. Patil, J.C. Shin, Hexagonal sheets of Co₃O₄ and Co₃O₄-Ag for high-performance electrochemical supercapacitors, *J. Ind. Eng. Chem.* 54 (2017) 162–173. <https://doi.org/10.1016/j.jiec.2017.05.030>.
- [118] A.K. Yedluri, H.J. Kim, Enhanced electrochemical performance of nanoplate nickel cobaltite (NiCo₂O₄) supercapacitor applications, *RSC Adv.* 9 (2019) 1115–1122.

- <https://doi.org/10.1039/c8ra09081e>.
- [119] C. Yuan, J. Li, L. Hou, J. Lin, G. Pang, L. Zhang, L. Lian, X. Zhang, Template-engaged synthesis of uniform mesoporous hollow NiCo₂O₄ sub-microspheres towards high-performance electrochemical capacitors, *RSC Adv.* 3 (2013) 18573–18578. <https://doi.org/10.1039/c3ra42828a>.
- [120] I. Shown, A. Ganguly, L.C. Chen, K.H. Chen, Conducting polymer-based flexible supercapacitor, *Energy Sci. Eng.* 3 (2015) 1–25. <https://doi.org/10.1002/ese3.50>.
- [121] X. Wu, S. Jin, Z. Zhang, L. Jiang, L. Mu, Y. Hu, H. Li, X. Chen, M. Armand, L. Chen, X. Huang, Unraveling the storage mechanism in organic carbonyl electrodes for sodium-ion batteries, *Sci. Adv.* 1 (2015) e1500330. <https://doi.org/10.1126/sciadv.1500330>.
- [122] L. Li, Y. Wen, H. Ming, H. Zhang, W. Bian, H. Lin, Y. Yang, Insight into the Li- and Zn-Ion Synergistic Effect for Benzoquinone-Based Anodes in Aqueous Batteries, *ACS Appl. Energy Mater.* 3 (2020) 8309–8316. <https://doi.org/10.1021/acsaem.0c00830>.
- [123] Y. Chen, H. Li, M. Tang, S. Zhuo, Y. Wu, E. Wang, S. Wang, C. Wang, W. Hu, Capacitive conjugated ladder polymers for fast-charge and -discharge sodium-ion batteries and hybrid supercapacitors, *J. Mater. Chem. A.* 7 (2019) 20891–20898. <https://doi.org/10.1039/C9TA07546A>.
- [124] Y. Zhou, B. Wang, C. Liu, N. Han, X. Xu, F. Zhao, J. Fan, Y. Li, Polyanthraquinone-based nanostructured electrode material capable of high-performance pseudocapacitive energy storage in aprotic electrolyte, *Nano Energy.* 15 (2015) 654–661. <https://doi.org/10.1016/j.nanoen.2015.05.029>.
- [125] A.M. Navarro-Suárez, J. Carretero-González, T. Rojo, M. Armand, Poly(quinone-amine)/nanocarbon composite electrodes with enhanced proton storage capacity, *J. Mater. Chem. A.* 5 (2017) 23292–23298. <https://doi.org/10.1039/C7TA08489G>.
- [126] Z. Song, H. Zhan, Y. Zhou, Polyimides: Promising Energy-Storage Materials, *Angew. Chemie Int. Ed.* 49 (2010) 8444–8448. <https://doi.org/10.1002/anie.201002439>.
- [127] Y. Zhang, P. Nie, C. Xu, G. Xu, B. Ding, H. Dou, X. Zhang, High energy aqueous sodium-ion capacitor enabled by polyimide electrode and high-concentrated electrolyte, *Electrochim. Acta.* 268 (2018) 512–519. <https://doi.org/10.1016/j.electacta.2018.02.125>.
- [128] C. Wang, R. Chu, Z. Guan, Z. Ullah, H. Song, Y. Zhang, C. Yu, L. Zhao, Q. Li, L. Liu, Tailored polyimide as positive electrode and polyimide-derived carbon as negative electrode for sodium ion full batteries, *Nanoscale.* 12 (2020) 4729–4735. <https://doi.org/10.1039/C9NR09237D>.
- [129] S. Lei, X. Cui, X. Liu, X. Zhang, X. Han, Y. Yang, Hydrothermally self-templated synthesis of rectangular polyimide submicrotubes and promising potentials in electrochemical energy storage, *Chem. Commun.* 56 (2020) 1429–1432. <https://doi.org/10.1039/C9CC09526H>.
- [130] Q. Miao, F. Rouhani, H. Moghanni-Bavil-Olyaei, K.G. Liu, X.M. Gao, J.Z. Li, X. De Hu, Z.M. Jin, M.L. Hu, A. Morsali, Comparative Study of the Supercapacitive Performance of Three Ferrocene-Based Structures: Targeted Design of a Conductive Ferrocene-Functionalized Coordination Polymer as a Supercapacitor Electrode, *Chem. - A Eur. J.* 26 (2020) 9518–9526. <https://doi.org/10.1002/chem.202001109>.

- [131] M. Khrizanforov, R. Shekurov, V. Miluykov, L. Gilmanova, O. Kataeva, Z. Yamaleeva, T. Gerasimova, V. Ermolaev, A. Gubaidullin, A. Laskin, Y. Budnikova, Excellent supercapacitor and sensor performance of robust cobalt phosphinate ferrocenyl organic framework materials achieved by intrinsic redox and structure properties, *Dalt. Trans.* 48 (2019) 16986–16992. <https://doi.org/10.1039/c9dt03592c>.
- [132] S. Zheng, H. Xue, H. Pang, Supercapacitors based on metal coordination materials, *Coord. Chem. Rev.* 373 (2018) 2–21. <https://doi.org/10.1016/j.ccr.2017.07.002>.
- [133] J. Wu, J. Song, K. Dai, Z. Zhuo, L.A. Wray, G. Liu, Z.X. Shen, R. Zeng, Y. Lu, W. Yang, Modification of Transition-Metal Redox by Interstitial Water in Hexacyanometalate Electrodes for Sodium-Ion Batteries, *J. Am. Chem. Soc.* 139 (2017) 18358–18364. <https://doi.org/10.1021/jacs.7b10460>.
- [134] C.D. Wessells, R.A. Huggins, Y. Cui, Copper hexacyanoferrate battery electrodes with long cycle life and high power, *Nat. Commun.* 2 (2011) 2–6. <https://doi.org/10.1038/ncomms1563>.
- [135] V. Kaliginedi, H. Ozawa, A. Kuzume, S. Maharajan, I. V. Pobelov, N.H. Kwon, M. Mohos, P. Broekmann, K.M. Fromm, M.A. Haga, T. Wandlowski, Layer-by-layer grown scalable redox-active ruthenium-based molecular multilayer thin films for electrochemical applications and beyond, *Nanoscale.* 7 (2015) 17685–17692. <https://doi.org/10.1039/c5nr04087f>.
- [136] G. Cai, J. Chen, J. Xiong, A. Lee-Sie Eh, J. Wang, M. Higuchi, P.S. Lee, Molecular Level Assembly for High-Performance Flexible Electrochromic Energy-Storage Devices, *ACS Energy Lett.* 5 (2020) 1159–1166. <https://doi.org/10.1021/acseenergylett.0c00245>.
- [137] H. Wang, F. Qiu, C. Lu, J. Zhu, C. Ke, S. Han, X. Zhuang, On-Chip Micro-Supercapacitor with AC Line-Filtering Performance, (2021).
- [138] K. Wang, S. Wang, J. Liu, Y. Guo, F. Mao, H. Wu, Q. Zhang, Fe-Based Coordination Polymers as Battery-Type Electrodes in Semi-Solid-State Battery–Supercapacitor Hybrid Devices, *ACS Appl. Mater. Interfaces.* 13 (2021) 15315–15323. <https://doi.org/10.1021/acsaami.1c01339>.
- [139] A.T. Chidembo, K.I. Ozoemena, B.O. Agboola, V. Gupta, G.G. Wildgoose, R.G. Compton, Nickel(ii) tetra-aminophthalocyanine modified MWCNTs as potential nanocomposite materials for the development of supercapacitors, *Energy Environ. Sci.* 3 (2010) 228–236. <https://doi.org/10.1039/b915920g>.
- [140] W. Li, H. Yao, G. Zhang, Y. Yang, A Ni/Zn bi-metallic coordination supramolecular network applied for high performance energy storage material, *Electrochim. Acta.* 228 (2017) 233–240. <https://doi.org/10.1016/j.electacta.2017.01.066>.
- [141] C. Yang, K.S. Schellhammer, F. Ortmann, S. Sun, R. Dong, M. Karakus, Z. Mics, M. Löffler, F. Zhang, X. Zhuang, E. Cánovas, G. Cuniberti, M. Bonn, X. Feng, Coordination Polymer Framework Based On-Chip Micro-Supercapacitors with AC Line-Filtering Performance, *Angew. Chemie.* 129 (2017) 3978–3982. <https://doi.org/10.1002/ange.201700679>.
- [142] L. Wang, D. Shao, J. Guo, S. Zhang, Y. Lu, Superstable porous Co-coordination polymer as the electrode material for supercapacitor, *J. Solid State Chem.* 277 (2019) 630–635. <https://doi.org/10.1016/j.jssc.2019.06.039>.
- [143] A.E. Baumann, D.A. Burns, B. Liu, V.S. Thoi, Metal-organic framework functionalization and

- design strategies for advanced electrochemical energy storage devices, *Commun. Chem.* 2 (2019) 1–14. <https://doi.org/10.1038/s42004-019-0184-6>.
- [144] S. Sundriyal, H. Kaur, S.K. Bhardwaj, S. Mishra, K.H. Kim, A. Deep, Metal-organic frameworks and their composites as efficient electrodes for supercapacitor applications, *Coord. Chem. Rev.* 369 (2018) 15–38. <https://doi.org/10.1016/j.ccr.2018.04.018>.
- [145] J. Park, M. Lee, D. Feng, Z. Huang, A.C. Hinckley, A. Yakovenko, X. Zou, Y. Cui, Z. Bao, Stabilization of Hexaaminobenzene in a 2D Conductive Metal-Organic Framework for High Power Sodium Storage, *J. Am. Chem. Soc.* 140 (2018) 10315–10323. <https://doi.org/10.1021/jacs.8b06020>.
- [146] Y. Zhai, Y. Dou, D. Zhao, P.F. Fulvio, R.T. Mayes, S. Dai, Carbon materials for chemical capacitive energy storage, *Adv. Mater.* 23 (2011) 4828–4850. <https://doi.org/10.1002/adma.201100984>.
- [147] R. Warren, F. Sammoura, F. Tounsi, M. Sanghadasa, L. Lin, Highly active ruthenium oxide coating via ALD and electrochemical activation in supercapacitor applications, *J. Mater. Chem. A* 3 (2015) 15568–15575. <https://doi.org/10.1039/C5TA03742E>.
- [148] N. Lin, J. Tian, Z. Shan, K. Chen, W. Liao, Hydrothermal synthesis of hydrous ruthenium oxide/graphene sheets for high-performance supercapacitors, *Electrochim. Acta.* 99 (2013) 219–224. <https://doi.org/10.1016/j.electacta.2013.03.115>.
- [149] Z.S. Wu, D.W. Wang, W. Ren, J. Zhao, G. Zhou, F. Li, H.M. Cheng, Anchoring hydrous RuO₂ on graphene sheets for high-performance electrochemical capacitors, *Adv. Funct. Mater.* 20 (2010) 3595–3602. <https://doi.org/10.1002/adfm.201001054>.
- [150] A.K. Mishra, S. Ramaprabhu, Functionalized graphene-based nanocomposites for supercapacitor application, *J. Phys. Chem. C* 115 (2011) 14006–14013. <https://doi.org/10.1021/jp201673e>.
- [151] J. Yan, Z. Fan, T. Wei, W. Qian, M. Zhang, F. Wei, Fast and reversible surface redox reaction of graphene-MnO₂ composites as supercapacitor electrodes, *Carbon N. Y.* 48 (2010) 3825–3833. <https://doi.org/10.1016/j.carbon.2010.06.047>.
- [152] X. Dong, X. Wang, J. Wang, H. Song, X. Li, L. Wang, M.B. Chan-Park, C.M. Li, P. Chen, Synthesis of a MnO₂-graphene foam hybrid with controlled MnO₂ particle shape and its use as a supercapacitor electrode, *Carbon N. Y.* 50 (2012) 4865–4870. <https://doi.org/10.1016/j.carbon.2012.06.014>.
- [153] B. Wei, L. Wang, Q. Miao, Y. Yuan, P. Dong, R. Vajtai, W. Fei, Fabrication of manganese oxide/three-dimensional reduced graphene oxide composites as the supercapacitors by a reverse microemulsion method, *Carbon N. Y.* 85 (2015) 249–260. <https://doi.org/10.1016/j.carbon.2014.12.063>.
- [154] B. Pandit, D.P. Dubal, P. Gómez-Romero, B.B. Kale, B.R. Sankapal, V₂O₅ encapsulated MWCNTs in 2D surface architecture: Complete solid-state bendable highly stabilized energy efficient supercapacitor device, *Sci. Rep.* 7 (2017) 1–12. <https://doi.org/10.1038/srep43430>.
- [155] S. Gao, P. Zang, L. Dang, H. Xu, F. Shi, Z. Liu, Z. Lei, Extraordinarily high-rate capability of polyaniline nanorod arrays on graphene nanomesh, *J. Power Sources.* 304 (2016) 111–118.

- <https://doi.org/10.1016/j.jpowsour.2015.11.028>.
- [156] V.H.R. De Souza, M.M. Oliveira, A.J.G. Zarbin, Thin and flexible all-solid supercapacitor prepared from novel single wall carbon nanotubes/polyaniline thin films obtained in liquid-liquid interfaces, *J. Power Sources*. 260 (2014) 34–42. <https://doi.org/10.1016/j.jpowsour.2014.02.070>.
- [157] T. Wang, A. Kiebele, J. Ma, S. Mhaisalkar, G. Gruner, Charge transfer between polyaniline and carbon nanotubes supercapacitors: Improving both energy and power densities, *J. Electrochem. Soc.* 158 (2011) 3–7. <https://doi.org/10.1149/1.3505994>.
- [158] T. Abdiryim, A. Ubul, R. Jamal, A. Rahman, Solid-state synthesis of polyaniline/single-walled carbon nanotubes: A comparative study with polyaniline/multi-walled carbon nanotubes, *Materials (Basel)*. 5 (2012) 1219–1231. <https://doi.org/10.3390/ma5071219>.
- [159] Y. Ko, M. Kwon, W.K. Bae, B. Lee, S.W. Lee, J. Cho, Flexible supercapacitor electrodes based on real metal-like cellulose papers, *Nat. Commun.* 8 (2017) 536. <https://doi.org/10.1038/s41467-017-00550-3>.
- [160] E.G.C. Neiva, M.M. Oliveira, M.F. Bergamini, L.H. Marcolino, A.J.G. Zarbin, One material, multiple functions: Graphene/Ni(OH)₂ thin films applied in batteries, electrochromism and sensors, *Sci. Rep.* 6 (2016) 1–14. <https://doi.org/10.1038/srep33806>.
- [161] J. Yan, Z. Fan, W. Sun, G. Ning, T. Wei, Q. Zhang, R. Zhang, L. Zhi, F. Wei, Advanced asymmetric supercapacitors based on Ni(OH)₂/graphene and porous graphene electrodes with high energy density, *Adv. Funct. Mater.* 22 (2012) 2632–2641. <https://doi.org/10.1002/adfm.201102839>.
- [162] S. Chen, J. Duan, Y. Tang, S. Zhangqiao, Hybrid hydrogels of porous graphene and nickel hydroxide as advanced supercapacitor materials, *Chem. - A Eur. J.* 19 (2013) 7118–7124. <https://doi.org/10.1002/chem.201300157>.
- [163] J.M. Gonçalves, K.M. Alves, M.F. Gonzalez-Huila, A. Duarte, P.R. Martins, K. Araki, Unexpected stabilization of α -Ni(OH)₂ nanoparticles in GO nanocomposites, *J. Nanomater.* 2018 (2018). <https://doi.org/10.1155/2018/5735609>.
- [164] J.M. Gonçalves, R.R. Guimarães, C. V. Nunes, A. Duarte, B.B.N.S. Brandão, H.E. Toma, K. Araki, Electrode materials based on α -NiCo(OH)₂ and rGO for high performance energy storage devices, *RSC Adv.* 6 (2016) 102504–102512. <https://doi.org/10.1039/c6ra20317e>.
- [165] H. Ma, J. He, D.B. Xiong, J. Wu, Q. Li, V. Dravid, Y. Zhao, Nickel Cobalt Hydroxide @Reduced Graphene Oxide Hybrid Nanolayers for High Performance Asymmetric Supercapacitors with Remarkable Cycling Stability, *ACS Appl. Mater. Interfaces.* 8 (2016) 1992–2000. <https://doi.org/10.1021/acsami.5b10280>.
- [166] L. Mao, C. Guan, X. Huang, Q. Ke, Y. Zhang, J. Wang, 3D Graphene-Nickel Hydroxide Hydrogel Electrode for High-Performance Supercapacitor, *Electrochim. Acta.* 196 (2016) 653–660. <https://doi.org/10.1016/j.electacta.2016.02.084>.
- [167] S. Husmann, A.J.G. Zarbin, Cation effect on the structure and properties of hexacyanometallates-based nanocomposites: Improving cathode performance in aqueous metal-ions batteries, *Electrochim. Acta.* 283 (2018) 1339–1350. <https://doi.org/10.1016/j.electacta.2018.07.055>.

- [168] E. Nossol, V.H.R. Souza, A.J.G. Zarbin, Carbon nanotube/Prussian blue thin films as cathodes for flexible, transparent and ITO-free potassium secondary battery, *J. Colloid Interface Sci.* 478 (2016) 107–116. <https://doi.org/10.1016/j.jcis.2016.05.056>.
- [169] P.A. Shinde, Y. Seo, S. Lee, H. Kim, Q.N. Pham, Y. Won, S. Chan Jun, Layered manganese metal-organic framework with high specific and areal capacitance for hybrid supercapacitors, *Chem. Eng. J.* 387 (2020) 122982. <https://doi.org/10.1016/j.cej.2019.122982>.
- [170] M. Saraf, R. Rajak, S.M. Mobin, A fascinating multitasking Cu-MOF/rGO hybrid for high performance supercapacitors and highly sensitive and selective electrochemical nitrite sensors, *J. Mater. Chem. A* 4 (2016) 16432–16445. <https://doi.org/10.1039/c6ta06470a>.
- [171] P.C. Banerjee, D.E. Lobo, R. Middag, W.K. Ng, M.E. Shaibani, M. Majumder, Electrochemical capacitance of Ni-doped metal organic framework and reduced graphene oxide composites: More than the sum of its parts, *ACS Appl. Mater. Interfaces*. 7 (2015) 3655–3664. <https://doi.org/10.1021/am508119c>.
- [172] Y. Jiao, C. Qu, B. Zhao, Z. Liang, H. Chang, S. Kumar, R. Zou, M. Liu, K.S. Walton, High-Performance Electrodes for a Hybrid Supercapacitor Derived from a Metal–Organic Framework/Graphene Composite, *ACS Appl. Energy Mater.* 2 (2019) 5029–5038. <https://doi.org/10.1021/acsaem.9b00700>.
- [173] L. Yang, K. Zhuo, X. Xu, Z. Zhang, Q. Du, Y. Chen, D. Sun, J. Wang, Redox-active phthalocyanine-decorated graphene aerogels for high-performance supercapacitors based on ionic liquid electrolyte, *J. Mater. Chem. A*. 8 (2020) 21789–21796. <https://doi.org/10.1039/D0TA08054C>.
- [174] Y. Tan, Y. Zhang, L. Kong, L. Kang, F. Ran, Nano-Au@PANI core-shell nanoparticles via in-situ polymerization as electrode for supercapacitor, *J. Alloys Compd.* 722 (2017) 1–7. <https://doi.org/10.1016/j.jallcom.2017.06.068>.
- [175] K.N. Chaudhari, S. Chaudhari, J.S. Yu, Synthesis and supercapacitor performance of Au-nanoparticle decorated MWCNT, *J. Electroanal. Chem.* 761 (2016) 98–105. <https://doi.org/10.1016/j.jelechem.2015.12.020>.
- [176] X. Li, F. Wei, Y. Sui, J. Qi, Y. He, Q. Meng, Au&Co core-shell nanoparticles capped with porous carbon: High performance materials for supercapacitor applications, *Mater. Lett.* 183 (2016) 408–412. <https://doi.org/10.1016/j.matlet.2016.07.145>.
- [177] I. Tanahashi, Capacitance Enhancement of Activated Carbon Fiber Cloth Electrodes in Electrochemical Capacitors with a Mixed Aqueous Solution of H₂SO₄ and AgNO₃, *Electrochem. Solid-State Lett.* 8 (2005) A627. <https://doi.org/10.1149/1.2087187>.
- [178] X. Lang, A. Hirata, T. Fujita, M. Chen, Nanoporous metal/oxide hybrid electrodes for electrochemical supercapacitors, *Nat. Nanotechnol.* 6 (2011) 232–236. <https://doi.org/10.1038/nnano.2011.13>.
- [179] L. Khandare, S. Terdale, Gold nanoparticles decorated MnO₂ nanowires for high performance supercapacitor, *Appl. Surf. Sci.* 418 (2017) 22–29. <https://doi.org/10.1016/j.apsusc.2016.12.036>.
- [180] W. Yan, J.Y. Kim, W. Xing, K.C. Donovan, T. Ayvazian, R.M. Penner, Lithographically patterned gold/manganese dioxide core/shell nanowires for high capacity, high rate, and high cyclability

- hybrid electrical energy storage, *Chem. Mater.* 24 (2012) 2382–2390. <https://doi.org/10.1021/cm3011474>.
- [181] M. Choudhary, S. Siwal, D. Nandi, K. Mallick, Charge storage ability of the gold nanoparticles: Towards the performance of a supercapacitor, *Appl. Surf. Sci.* 424 (2017) 151–156. <https://doi.org/10.1016/j.apsusc.2017.01.258>.
- [182] P.C. Chen, G. Shen, S. Sukcharoenchoke, C. Zhou, Flexible and transparent supercapacitor based on In_2O_3 nanowire/carbon nanotube heterogeneous films, *Appl. Phys. Lett.* 94 (2009) 3–6. <https://doi.org/10.1063/1.3069277>.
- [183] S.L. Chou, J.Z. Wang, S.Y. Chew, H.K. Liu, S.X. Dou, Electrodeposition of MnO_2 nanowires on carbon nanotube paper as free-standing, flexible electrode for supercapacitors, *Electrochem. Commun.* 10 (2008) 1724–1727. <https://doi.org/10.1016/j.elecom.2008.08.051>.
- [184] T. Wanchaem, S. Rattanamai, P. Dulyaseree, P. Khanchaitit, W. Wongwiriyan, Facile synthesis of hybrid manganese oxide and multiwalled carbon nanotube by two-step electrodeposition for supercapacitor electrode, *Mater. Today Proc.* 4 (2017) 6620–6625. <https://doi.org/10.1016/j.matpr.2017.06.176>.
- [185] Q. Wu, Y. Xu, Z. Yao, A. Liu, G. Shi, Supercapacitors based on flexible graphene/polyaniline nanofiber composite films, *ACS Nano*. 4 (2010) 1963–1970. <https://doi.org/10.1021/nn1000035>.
- [186] M. Ghidui, M.R. Lukatskaya, M.Q. Zhao, Y. Gogotsi, M.W. Barsoum, Conductive two-dimensional titanium carbide “clay” with high volumetric capacitance, *Nature*. 516 (2015) 78–81. <https://doi.org/10.1038/nature13970>.
- [187] M.R. Lukatskaya, S. Kota, Z. Lin, M.Q. Zhao, N. Shpigel, M.D. Levi, J. Halim, P.L. Taberna, M.W. Barsoum, P. Simon, Y. Gogotsi, Ultra-high-rate pseudocapacitive energy storage in two-dimensional transition metal carbides, *Nat. Energy*. 6 (2017) 1–6. <https://doi.org/10.1038/nenergy.2017.105>.
- [188] M.R. Lukatskaya, O. Mashtalir, C.E. Ren, Y. Dall’Agnese, P. Rozier, P.L. Taberna, M. Naguib, P. Simon, M.W. Barsoum, Y. Gogotsi, Cation intercalation and high volumetric capacitance of two-dimensional titanium carbide, *Science* (80-.). 341 (2013) 1502–1505. <https://doi.org/10.1126/science.1241488>.
- [189] M.D. Levi, M.R. Lukatskaya, S. Sigalov, M. Beidaghi, N. Shpigel, L. Daikhin, D. Aurbach, M.W. Barsoum, Y. Gogotsi, Solving the capacitive paradox of 2D MXene using electrochemical quartz-crystal admittance and in situ electronic conductance measurements, *Adv. Energy Mater.* 5 (2015) 1–11. <https://doi.org/10.1002/aenm.201400815>.
- [190] N. Joseph, P.M. Shafi, A.C. Bose, Recent Advances in 2D-MoS₂ and its Composite Nanostructures for Supercapacitor Electrode Application, *Energy and Fuels*. 34 (2020) 6558–6597. <https://doi.org/10.1021/acs.energyfuels.0c00430>.
- [191] S. Gutić, A.S. Dobrota, N. Gavrilov, M. Baljovović, I.A. Pašti, Surface Charge Storage Properties of Selected Graphene Samples in pH-neutral Aqueous Solutions of Alkali Metal Chlorides - Particularities and Universalities, 11 (2016) 8662–8682. <https://doi.org/10.20964/2016.10.47>.
- [192] M.R. Lukatskaya, S.M. Bak, X. Yu, X.Q. Yang, M.W. Barsoum, Y. Gogotsi, Probing the Mechanism of High Capacitance in 2D Titanium Carbide Using in Situ X-Ray Absorption

- Spectroscopy, *Adv. Energy Mater.* 5 (2015) 2–5. <https://doi.org/10.1002/aenm.201500589>.
- [193] X. Mu, D. Wang, F. Du, G. Chen, C. Wang, Y. Wei, Y. Gogotsi, Y. Gao, Y. Dall'Agnese, Revealing the Pseudo-Intercalation Charge Storage Mechanism of MXenes in Acidic Electrolyte, *Adv. Funct. Mater.* 29 (2019) 1902953. <https://doi.org/10.1002/adfm.201902953>.
- [194] C. Zhan, M. Naguib, M. Lukatskaya, P.R.C. Kent, Y. Gogotsi, D.E. Jiang, Understanding the MXene Pseudocapacitance, *J. Phys. Chem. Lett.* 9 (2018) 1223–1228. <https://doi.org/10.1021/acs.jpcllett.8b00200>.
- [195] Y. Xia, T.S. Mathis, M. Zhao, B. Anasori, A. Dang, Z. Zhou, H. Cho, Y. Gogotsi, S. Yang, Thickness-independent capacitance of vertically aligned liquid-crystalline MXenes, *Nature*. 557 (2018) 409–412. <https://doi.org/10.1038/s41586-018-0109-z>.
- [196] X.Y. Lang, B.T. Liu, X.M. Shi, Y.Q. Li, Z. Wen, Q. Jiang, Ultrahigh-power pseudocapacitors based on ordered porous heterostructures of electron-correlated oxides, *Adv. Sci.* 3 (2015) 1–9. <https://doi.org/10.1002/advs.201500319>.
- [197] K.B. Blodgett, Films Built by Depositing Successive Monomolecular Layers on a Solid Surface, *J. Am. Chem. Soc.* 57 (1935) 1007–1022. <https://doi.org/10.1021/ja01309a011>.
- [198] S.A. Hussain, B. Dey, D. Bhattacharjee, N. Mehta, Unique supramolecular assembly through Langmuir – Blodgett (LB) technique, *Heliyon*. 4 (2018) e01038. <https://doi.org/10.1016/j.heliyon.2018.e01038>.
- [199] G. Roberts, ed., *Langmuir-Blodgett Films*, Springer US, Boston, MA, 1990. <https://doi.org/10.1007/978-1-4899-3716-2>.
- [200] J. Zasadzinski, R. Viswanathan, L. Madsen, J. Garnaes, D. Schwartz, Langmuir-Blodgett films, *Science* (80-.). 263 (1994) 1726–1733. <https://doi.org/10.1126/science.8134836>.
- [201] S.-A. HUSSAIN, D. BHATTACHARJEE, LANGMUIR–BLODGETT FILMS AND MOLECULAR ELECTRONICS, *Mod. Phys. Lett. B.* 23 (2009) 3437–3451. <https://doi.org/10.1142/S0217984909021508>.
- [202] R.H.A. Ras, Y. Umemura, C.T. Johnston, A. Yamagishi, R.A. Schoonheydt, Ultrathin hybrid films of clay minerals, *Phys. Chem. Chem. Phys.* 9 (2007) 918–932. <https://doi.org/10.1039/B610698F>.
- [203] C.M. Parnell, B.P. Chhetri, T.B. Mitchell, F. Watanabe, G. Kannarpady, A.B. RanguMagar, H. Zhou, K.M. Alghazali, A.S. Biris, A. Ghosh, Simultaneous Electrochemical Deposition of Cobalt Complex and Poly(pyrrole) Thin Films for Supercapacitor Electrodes, *Sci. Rep.* 9 (2019) 5650. <https://doi.org/10.1038/s41598-019-41969-6>.
- [204] K. Qi, R. Hou, S. Zaman, Y. Qiu, B.Y. Xia, H. Duan, Construction of Metal-Organic Framework/Conductive Polymer Hybrid for All-Solid-State Fabric Supercapacitor, *ACS Appl. Mater. Interfaces.* 10 (2018) 18021–18028. <https://doi.org/10.1021/acsami.8b05802>.
- [205] W. Zhao, T. Chen, W. Wang, B. Jin, J. Peng, S. Bi, M. Jiang, S. Liu, Q. Zhao, W. Huang, Conductive Ni₃(HITP)₂ MOFs thin films for flexible transparent supercapacitors with high rate capability, *Sci. Bull.* 65 (2020) 1803–1811. <https://doi.org/10.1016/j.scib.2020.06.027>.
- [206] H. Winnischofer, E. Cesca, A. Mendoza, I. Araújo, E. Westphal, D. Mezalira, D. Balogh, O. Oliveira Jr., Heterostructured Langmuir-Blodgett Films of Ruthenium Bipyridine with 1,3,4-

- Naphthooxadiazole-Derived Amphiphile Complex as a Charge Storage Electrode, *J. Braz. Chem. Soc.* 31 (2020) 2371–2384. <https://doi.org/10.21577/0103-5053.20200137>.
- [207] H. Li, C. Zhao, X. Wang, J. Meng, Y. Zou, S. Noreen, L. Zhao, Z. Liu, H. Ouyang, P. Tan, M. Yu, Y. Fan, Z.L. Wang, Z. Li, Fully Bioabsorbable Capacitor as an Energy Storage Unit for Implantable Medical Electronics, *Adv. Sci.* 6 (2019) 1801625. <https://doi.org/10.1002/advs.201801625>.
- [208] X.Y. Liu, Y.Q. Gao, G.W. Yang, A flexible, transparent and super-long-life supercapacitor based on ultrafine Co₃O₄ nanocrystal electrodes, *Nanoscale.* 8 (2016) 4227–4235. <https://doi.org/10.1039/c5nr09145d>.
- [209] J.L. Chen, X.D. Zhang, L.Y. Zhang, L.X. Shi, Z.N. Chen, Syntheses and characterization of oxo-centered triruthenium compounds with orthometalated bipyridine, *Inorg. Chem.* 44 (2005) 1037–1043. <https://doi.org/10.1021/ic048681c>.
- [210] A. Spencer, G. Wilkinson, Reactions of μ_3 -oxo-triruthenium carboxylates with π -acid ligands, *J. Chem. Soc., Dalt. Trans.* 23 (1974) 786–792. <https://doi.org/10.1039/DT9740000786>.
- [211] Z.-N. Chen, F.-R. Dai, Oxo-Centered Triruthenium-Acetate Cluster Complexes Derived from Axial or Bridging Ligand Substitution, in: 2009: pp. 93–120. https://doi.org/10.1007/430_2008_12.
- [212] Y. Sasaki, K. Umakoshi, T. Imamura, A. Kikuchi, A. Kishimoto, Reactivity of di- and tri-nuclear complexes of heavy mid-transition elements: A case of oxo-carboxylatobridged complexes, *Pure Appl. Chem.* 69 (1997) 205–210. <https://doi.org/10.1351/pac199769010205>.
- [213] A.D.P. Alexiou, H.E. Toma, Electrochemical parametrization of ruthenium cluster redox potentials, *J. Chem. Res. Synopses.* 11 (1993) 464–465.
- [214] A.B.P. Lever, Electrochemical Parametrization of Metal Complex Redox Potentials, Using the Ruthenium(III)/Ruthenium(II) Couple To Generate a Ligand Electrochemical Series, *Inorg. Chem.* 29 (1990) 1271–1285.
- [215] K.P. Naidek, Filmes finos baseados em complexos trinucleares de rutênio: Preparação, caracterização e confecção de dispositivos., Universidade Federal do Paraná, 2015.
- [216] Y. Tomiyasu, M. Abe, Y. Morihara, H. Ohgi, T. Otake, Y. Hisaeda, Organic Films Containing Trinuclear Ruthenium Clusters that Exhibit Redox-state-dependent Heat-shielding Characteristics, *Chem. Lett.* 38 (2009) 492–493. <https://doi.org/10.1246/cl.2009.492>.
- [217] B.J. Lear, C.P. Kubiak, Charge gating and electronic delocalization over a denderimeric assembly of trinuclear ruthenium clusters, *Inorg. Chem.* 45 (2006) 7041–7043. <https://doi.org/10.1021/ic060766l>.
- [218] L.F.O. Furtado, A.D.P. Alexiou, L. Gonçalves, H.E. Toma, K. Araki, TiO₂-Based Light-Driven XOR/INH Logic Gates, *Angew. Chemie.* 118 (2006) 3215–3218. <https://doi.org/10.1002/ange.200600076>.
- [219] K.P. Naidek, D.M. Hoffmeister, J. Pazinato, E. Westphal, H. Gallardo, M. Nakamura, K. Araki, H.E. Toma, H. Winnischofer, Ruthenium Acetate Cluster Amphiphiles and Their Langmuir-Blodgett Films for Electrochromic Switching Devices, *Eur. J. Inorg. Chem.* (2014) 1150–1157. <https://doi.org/10.1002/ejic.201301442>.

- [220] S.H. Toma, H.E. Toma, Versatile electrochromic displays based on TiO₂ nanoporous films modified with triruthenium clusters, *Electrochem. Commun.* 8 (2006) 1628–1632. <https://doi.org/10.1016/j.elecom.2006.07.043>.
- [221] C. Bilgrien, S. Davis, R.S. Drago, The selective oxidation of primary alcohols to aldehydes by oxygen employing a trinuclear ruthenium carboxylate catalyst, *J. Am. Chem. Soc.* 109 (1987) 3786–3787. <https://doi.org/10.1021/ja00246a049>.
- [222] M. Hitrik, A. Dandapat, Y. Sasson, A new mechanism for allylic alcohol isomerization involving ruthenium nanoparticles as a “true catalyst” generated through the self-assembly of supramolecular triruthenium clusters, *RSC Adv.* 6 (2016) 68041–68048. <https://doi.org/10.1039/c6ra14658a>.
- [223] S. Davis, R. Drago, Alkane Oxidations by a Novel p³-Oxo Trinuclear Ruthenium Carboxylate Complex, *J. Chem. Soc., Chem. Commun.* 30 (1990) 5–6. <https://doi.org/10.1039/c39900000250>.
- [224] S.A. Fouda, G.L. Rempel, μ -Oxo-triruthenium acetate cluster complexes as catalysts for olefin hydrogenation, *Inorg. Chem.* 18 (1979) 1–8. <https://doi.org/10.1021/ic50191a001>.
- [225] A. Dikhtiarenko, S. Khainakov, J.R. García, J. Gimeno, Mixed-valence μ ³-oxo-centered triruthenium cluster [Ru₃(II,III,III)(μ ³-O)(μ -CH₃CO₂)₆(H₂O)₃] \cdot 2H₂O: Synthesis, structural characterization, valence-state delocalization and catalytic behavior, *Inorganica Chim. Acta.* 454 (2017) 107–116. <https://doi.org/10.1016/j.ica.2016.05.046>.
- [226] G.S. Nunes, A.D.P. Alexiou, H.E. Toma, Catalytic oxidation of hydrocarbons by trinuclear μ -oxo-bridged ruthenium-acetate clusters: Radical versus non-radical mechanisms, *J. Catal.* 260 (2008) 188–192. <https://doi.org/10.1016/j.jcat.2008.10.002>.
- [227] N. Cacita, B. Possato, C.F.N. Da Silva, M. Paulo, A.L.B. Formiga, L.M. Bendhack, S. Nikolaou, Investigation of a novel trinuclear μ -oxo ruthenium complex as a potential nitric oxide releaser for biological purposes, *Inorganica Chim. Acta.* 429 (2015) 114–121. <https://doi.org/10.1016/j.ica.2015.01.038>.
- [228] G. Canzi, C.P. Kubiak, Ultrafast electron transfer across a gold nanoparticle: A study of ancillary ligand and solvent influences, *J. Phys. Chem. C.* 116 (2012) 6560–6566. <https://doi.org/10.1021/jp2119058>.
- [229] N. Naidek, A.J.G. Zarbin, E.S. Orth, Covalently linked nanocomposites of polypyrrole with graphene: Strategic design toward optimized properties, *J. Polym. Sci. Part A Polym. Chem.* 56 (2018) 579–588. <https://doi.org/10.1002/pola.28944>.
- [230] E.S. Orth, J.E.S. Fonsaca, S.H. Domingues, H. Mehl, M.M. Oliveira, A.J.G. Zarbin, Targeted thiolation of graphene oxide and its utilization as precursor for graphene/silver nanoparticles composites, *Carbon N. Y.* 61 (2013) 543–550. <https://doi.org/10.1016/j.carbon.2013.05.032>.
- [231] S.H. Domingues, R. V. Salvatierra, M.M. Oliveira, A.J.G. Zarbin, Transparent and conductive thin films of graphene/polyaniline nanocomposites prepared through interfacial polymerization, *Chem. Commun.* 47 (2011) 2592–2594. <https://doi.org/10.1039/c0cc04304d>.
- [232] W.S. Hummers, R.E. Offeman, Preparation of Graphitic Oxide, *J. Am. Chem. Soc.* 80 (1958) 1339. <https://doi.org/10.1021/ja01539a017>.

- [233] M.D. Hanwell, D.E. Curtis, D.C. Lonie, T. Vandermeersch, E. Zurek, G.R. Hutchison, Avogadro: an advanced semantic chemical editor, visualization, and analysis platform, *J. Cheminform.* 4 (2012) 17. <https://doi.org/10.1186/1758-2946-4-17>.
- [234] L.J. Cote, F. Kim, J. Huang, Langmuir-blodgett assembly of graphite oxide single layers, *J. Am. Chem. Soc.* 131 (2009) 1043–1049. <https://doi.org/10.1021/ja806262m>.
- [235] Q. Zheng, W.H. Ip, X. Lin, N. Yousefi, K.K. Yeung, Z. Li, J.K. Kim, Transparent conductive films consisting of ultralarge graphene sheets produced by Langmuir-Blodgett assembly, *ACS Nano.* 5 (2011) 6039–6051. <https://doi.org/10.1021/nn2018683>.
- [236] M.M. Jaafar, G.P.M.K. Ciniciato, S.A. Ibrahim, S.M. Phang, K. Yunus, A.C. Fisher, M. Iwamoto, P. Vengadesh, Preparation of a Three-Dimensional Reduced Graphene Oxide Film by Using the Langmuir-Blodgett Method, *Langmuir.* 31 (2015) 10426–10434. <https://doi.org/10.1021/acs.langmuir.5b02708>.
- [237] M.J. Fernández-Merino, L. Guardia, J.I. Paredes, S. Villar-Rodil, P. Solís-Fernández, A. Martínez-Alonso, J.M.D. Tascón, Vitamin C is an ideal substitute for hydrazine in the reduction of graphene oxide suspensions, *J. Phys. Chem. C.* 114 (2010) 6426–6432. <https://doi.org/10.1021/jp100603h>.
- [238] C. Xu, X. Shi, A. Ji, L. Shi, C. Zhou, Y. Cui, Fabrication and characteristics of reduced graphene oxide produced with different green reductants, *PLoS One.* 10 (2015). <https://doi.org/10.1371/journal.pone.0144842>.
- [239] Y. Wang, X. Wang, X. Li, X. Li, Y. Liu, Y. Bai, H. Xiao, G. Yuan, A High-Performance, Tailorable, Wearable, and Foldable Solid-State Supercapacitor Enabled by Arranging Pseudocapacitive Groups and MXene Flakes on Textile Electrode Surface, *Adv. Funct. Mater.* 31 (2021) 1–12. <https://doi.org/10.1002/adfm.202008185>.
- [240] J. Feng, N.A. Chernova, F. Omenya, L. Tong, A.C. Rastogi, M. Stanley Whittingham, Effect of electrode charge balance on the energy storage performance of hybrid supercapacitor cells based on LiFePO₄ as Li-ion battery electrode and activated carbon, *J. Solid State Electrochem.* 22 (2018) 1063–1078. <https://doi.org/10.1007/s10008-017-3847-1>.
- [241] Y. Pavani, M. Ravi, S. Bhavani, A.K. Sharma, V.V.R.N. Rao, Characterization of Poly (vinyl alcohol)/ Potassium Chloride Polymer Electrolytes for Electrochemical Cell Applications, (2012). <https://doi.org/10.1002/pen>.
- [242] K. Sun, E. Feng, G. Zhao, H. Peng, G. Wei, Y. Lv, G. Ma, A Single Robust Hydrogel Film Based Integrated Flexible Supercapacitor, *ACS Sustain. Chem. Eng.* 7 (2019) 165–173. <https://doi.org/10.1021/acssuschemeng.8b02728>.
- [243] A. Qian, K. Zhuo, P. Karthick Kannan, C. Chung, Neutral pH Gel Electrolytes for V₂O₅·0.5H₂O-Based Energy Storage Devices, *ACS Appl. Mater. Interfaces.* 8 (2016) 34455–34463. <https://doi.org/10.1021/acsami.6b12672>.
- [244] G. Gritzner, Standard electrode potentials of M⁺|M couples in non-aqueous solvents (molecular liquids), *J. Mol. Liq.* 156 (2010) 103–108. <https://doi.org/10.1016/j.molliq.2010.03.010>.
- [245] P. Taberna, P. Simon, *Electrochemical Techniques*, in: *Supercapacitors*, Wiley-VCH Verlag GmbH & Co. KGaA, Weinheim, Germany, 2013: pp. 111–130.

- <https://doi.org/10.1002/9783527646661.ch3>.
- [246] J. Shao, X. Zhou, Q. Liu, R. Zou, W. Li, J. Yang, J. Hu, Mechanism analysis of the capacitance contributions and ultralong cycling-stability of the isomorphous MnO₂@MnO₂ core/shell nanostructures for supercapacitors, *J. Mater. Chem. A* 3 (2015) 6168–6176. <https://doi.org/10.1039/c4ta06793b>.
- [247] A.S. Bondarenko, G.A. Ragoisha, Inverse Problem In Potentiodynamic Electrochemical Impedance, in: A.L. Pomerantsev (Ed.), *Prog. Chemom. Res.*, Nova Science Publishers, New York, 2005: pp. 89–102. <http://www.abc.chemistry.bsu.by/vi/analyser/>.
- [248] P.L. Taberna, P. Simon, J.F. Fauvarque, Electrochemical Characteristics and Impedance Spectroscopy Studies of Carbon-Carbon Supercapacitors, *J. Electrochem. Soc.* 150 (2003) A292–A300. <https://doi.org/10.1149/1.1543948>.
- [249] P. Navalpotro, M. Anderson, R. Marcilla, J. Palma, Insights into the energy storage mechanism of hybrid supercapacitors with redox electrolytes by Electrochemical Impedance Spectroscopy, *Electrochim. Acta* 263 (2018) 110–117. <https://doi.org/10.1016/j.electacta.2017.12.167>.
- [250] F. Neese, Software update: the ORCA program system, version 4.0, *Wiley Interdiscip. Rev. Comput. Mol. Sci.* 8 (2018) 1–6. <https://doi.org/10.1002/wcms.1327>.
- [251] F. Weigend, R. Ahlrichs, Balanced basis sets of split valence, triple zeta valence and quadruple zeta valence quality for H to Rn: Design and assessment of accuracy, *Phys. Chem. Chem. Phys.* 7 (2005) 3297–3305. <https://doi.org/10.1039/b508541a>.
- [252] D. Andrae, U. Häußermann, M. Dolg, H. Stoll, H. Preuß, Energy-adjusted ab initio pseudopotentials for the second and third row transition elements: Molecular test for M₂ (M=Ag, Au) and MH (M=Ru, Os), *Theor. Chim. Acta* 78 (1991) 247–266. <https://doi.org/10.1007/BF01112848>.
- [253] F. Weigend, Accurate Coulomb-fitting basis sets for H to Rn, *Phys. Chem. Chem. Phys.* 8 (2006) 1057–1065. <https://doi.org/10.1039/b515623h>.
- [254] S. Grimme, J. Antony, S. Ehrlich, H. Krieg, A consistent and accurate ab initio parametrization of density functional dispersion correction (DFT-D) for the 94 elements H-Pu, *J. Chem. Phys.* 132 (2010) 154104. <https://doi.org/10.1063/1.3382344>.
- [255] C. Adamo, V. Barone, Toward reliable density functional methods without adjustable parameters: The PBE0 model, *J. Chem. Phys.* 110 (1999) 6158–6170. <https://doi.org/10.1063/1.478522>.
- [256] T. Petrenko, F. Neese, Analysis and prediction of absorption band shapes, fluorescence band shapes, resonance Raman intensities, and excitation profiles using the time-dependent theory of electronic spectroscopy, *J. Chem. Phys.* 127 (2007). <https://doi.org/10.1063/1.2770706>.
- [257] ChemicalBook, 4,4'-DIPYRIDYL DISULFIDE(2645-22-9) 1H NMR, (n.d.). https://www.chemicalbook.com/SpectrumEN_2645-22-9_1HNMR.htm.
- [258] R.M. Silverstein, F.X. Webster, D.J.C.N.-Q.S.S. 2005 Kiemle, *Spectrometric identification of organic compounds*, 7th ed, John Wiley & Sons, Hoboken, NJ, 2005.
- [259] L. Peng, Y. Zhu, H. Li, G. Yu, Chemically Integrated Inorganic-Graphene Two-Dimensional Hybrid Materials for Flexible Energy Storage Devices, *Small* 12 (2016) 6183–6199. <https://doi.org/10.1002/sml.201602109>.

- [260] G. Canzi, C.P. Kubiak, Mixed-valence nanoclusters: Fast electron transfer in mixed-valence systems with a gold nanoparticle as the bridge, *Small*. 7 (2011) 1967–1971. <https://doi.org/10.1002/sml.201100483>.
- [261] A. Gevaerd, S.F. Blaskiewicz, A.J.G. Zarbin, E.S. Orth, M.F. Bergamini, L.H. Marcolino-Junior, Nonenzymatic electrochemical sensor based on imidazole-functionalized graphene oxide for progesterone detection, *Biosens. Bioelectron.* 112 (2018) 108–113. <https://doi.org/10.1016/j.bios.2018.04.044>.
- [262] J.E.S. Fonsaca, L. Hostert, E.S. Orth, A.J.G. Zarbin, Tailoring multifunctional graphene-based thin films: from nanocatalysts to SERS substrates, *J. Mater. Chem. A*. 5 (2017) 9591–9603. <https://doi.org/10.1039/C7TA01967J>.
- [263] A.E. Pérez Mendoza, N. Naidek, E.C. Cesca, J.C. Sagás, E.S. Orth, A.J.G. Zarbin, H. Winnischofer, Graphene Modified with Triruthenium Acetate Clusters as an Electrode for the Hybrid Energy Storage System, *ACS Appl. Nano Mater.* 3 (2020) 6757–6765. <https://doi.org/10.1021/acsanm.0c01170>.
- [264] H.E. Toma, P.S. Santos, C. Cipriano, Electronic and resonance raman spectra of the hexanuclear cluster $[\text{Ru}_3\text{O}(\text{O}_2\text{Cch}_3)_6\{\text{pyrazine}\text{Ru}(\text{Nh}_3)_5\}_3]^{6+}$, *Spectrosc. Lett.* 21 (1988) 909–918. <https://doi.org/10.1080/00387018808082353>.
- [265] A.C. Ferrari, Raman spectroscopy of graphene and graphite: Disorder, electron-phonon coupling, doping and nonadiabatic effects, *Solid State Commun.* 143 (2007) 47–57. <https://doi.org/10.1016/j.ssc.2007.03.052>.
- [266] A. Bagri, C. Mattevi, M. Acik, Y.J. Chabal, M. Chhowalla, V.B. Shenoy, Structural evolution during the reduction of chemically derived graphene oxide, *Nat. Chem.* 2 (2010) 581–587. <https://doi.org/10.1038/nchem.686>.
- [267] M.A. Pimenta, G. Dresselhaus, M.S. Dresselhaus, L.G. Cançado, A. Jorio, R. Saito, Studying disorder in graphite-based systems by Raman spectroscopy, *Phys. Chem. Chem. Phys.* 9 (2007) 1276–1291. <https://doi.org/10.1039/b613962k>.
- [268] K.N. Kudin, B. Ozbas, H.C. Schniepp, R.K. Prud'homme, I.A. Aksay, R. Car, Raman spectra of graphite oxide and functionalized graphene sheets, *Nano Lett.* 8 (2008) 36–41. <https://doi.org/10.1021/nl071822y>.
- [269] R.J.J. Jansen, H. van Bekkum, XPS of nitrogen-containing functional groups on activated carbon, *Carbon N. Y.* 33 (1995) 1021–1027. [https://doi.org/10.1016/0008-6223\(95\)00030-H](https://doi.org/10.1016/0008-6223(95)00030-H).
- [270] S. Kabir, K. Artyushkova, A. Serov, B. Kiefer, P. Atanassov, Binding energy shifts for nitrogen-containing graphene-based electrocatalysts - Experiments and DFT calculations, *Surf. Interface Anal.* 48 (2016) 293–300. <https://doi.org/10.1002/sia.5935>.
- [271] M. Camalli, F. Caruso, G. Mattogno, E. Rivarola, Adducts of tin(IV) and organotin(IV) derivatives with 2,2'-azopyridine II. Crystal and molecular structure of $\text{SnMe}_2\text{Br}_2\text{AZP}$ and further mössbauer and photoelectronic spectroscopic studies, *Inorganica Chim. Acta.* 170 (1990) 225–231. [https://doi.org/10.1016/S0020-1693\(00\)80479-X](https://doi.org/10.1016/S0020-1693(00)80479-X).
- [272] H. Shinohara, A. Nakahara, F. Kitagawa, Y. Takahashi, K. Otsuka, S. Shoji, O. Ohara, J. Mizuno, XPS and NEXAFS studies of VUV/O₃-treated aromatic polyurea and its application to microchip

- electrophoresis, *IET Nanobiotechnology*. 5 (2011) 136–142. <https://doi.org/10.1049/iet-nbt.2011.0006>.
- [273] J.E.S. Fonsaca, A.L. Elías, S.H. Domingues, M.M. Oliveira, M. Endo, E.S. Orth, M. Terrones, A.J.G. Zarbin, Graphene nanoribbons inducing cube-shaped Ag nanoparticle assemblies, *Carbon N. Y.* 93 (2015) 800–811. <https://doi.org/10.1016/j.carbon.2015.05.098>.
- [274] N. Naidek, *Desenvolvimento De Nanocompósitos Entre Derivados De Grafeno/Nanotubos De Carbono E Polímeros Condutores: Funcionalização Direcionada Desenvolvimento De Nanocompósitos Entre Derivados De Grafeno / Nanotubos*, Universidade Federal do Paraná, 2018.
- [275] J. Senthilnathan, M. Yoshimura, Low energy liquid plasma for direct reduction and formation of rGO-aminopyridine hybrid for electrical and environmental applications, *J. Hazard. Mater.* 340 (2017) 26–35. <https://doi.org/10.1016/j.jhazmat.2017.06.061>.
- [276] X. Zhang, D. Wang, M. Yang, X. Xia, H. Chen, Y. Chen, H. Liu, Pyridine-enriched graphene sheets for high volumetric performance supercapacitors, *J. Solid State Electrochem.* 22 (2018) 1921–1931. <https://doi.org/10.1007/s10008-017-3879-1>.
- [277] C.T. Hsieh, H. Teng, Influence of oxygen treatment on electric double-layer capacitance of activated carbon fabrics, *Carbon N. Y.* 40 (2002) 667–674. [https://doi.org/10.1016/S0008-6223\(01\)00182-8](https://doi.org/10.1016/S0008-6223(01)00182-8).
- [278] B. Xu, S. Yue, Z. Sui, X. Zhang, S. Hou, G. Cao, Y. Yang, What is the choice for supercapacitors: Graphene or graphene oxide?, *Energy Environ. Sci.* 4 (2011) 2826–2830. <https://doi.org/10.1039/c1ee01198g>.
- [279] Q. Abbas, B. Gollas, V. Presser, Reduced Faradaic Contributions and Fast Charging of Nanoporous Carbon Electrodes in a Concentrated Sodium Nitrate Aqueous Electrolyte for Supercapacitors, *Energy Technol.* 7 (2019) 1–9. <https://doi.org/10.1002/ente.201900430>.
- [280] F. Béguin, M. Friebe, K. Jurewicz, C. Vix-Guterl, J. Dentzer, E. Frackowiak, State of hydrogen electrochemically stored using nanoporous carbons as negative electrode materials in an aqueous medium, *Carbon N. Y.* 44 (2006) 2392–2398. <https://doi.org/10.1016/j.carbon.2006.05.025>.
- [281] Y.J. Lee, H.W. Park, S. Park, I.K. Song, Electrochemical properties of Mn-doped activated carbon aerogel as electrode material for supercapacitor, *Curr. Appl. Phys.* 12 (2012) 233–237. <https://doi.org/10.1016/j.cap.2011.06.010>.
- [282] A. Bakandritsos, P. Jakubec, M. Pykal, M. Otyepka, Covalently functionalized graphene as a supercapacitor electrode material, *FlatChem.* 13 (2019) 25–33. <https://doi.org/10.1016/j.flatc.2018.12.004>.
- [283] W. Ma, M. Li, X. Zhou, J. Li, Y. Dong, M. Zhu, Three-Dimensional Porous Carbon Nanotubes/Reduced Graphene Oxide Fiber from Rapid Phase Separation for a High-Rate All-Solid-State Supercapacitor, *ACS Appl. Mater. Interfaces.* 11 (2019) 9283–9290. <https://doi.org/10.1021/acsami.8b19359>.
- [284] M.D. Levi, D. Aurbach, Simultaneous measurements and modeling of the electrochemical impedance and the cyclic voltammetric characteristics of graphite electrodes doped with lithium,

- J. Phys. Chem. B. 101 (1997) 4630–4640. <https://doi.org/10.1021/jp9701909>.
- [285] B.A. Mei, O. Munteshari, J. Lau, B. Dunn, L. Pilon, Physical Interpretations of Nyquist Plots for EDLC Electrodes and Devices, *J. Phys. Chem. C.* 122 (2018) 194–206. <https://doi.org/10.1021/acs.jpcc.7b10582>.
- [286] T.Q. Nguyen, C. Breitkopf, Determination of Diffusion Coefficients Using Impedance Spectroscopy Data, *J. Electrochem. Soc.* 165 (2018) E826–E831. <https://doi.org/10.1149/2.1151814jes>.
- [287] V.F. Lvovich, *Impedance Spectroscopy*, John Wiley & Sons, Inc., Hoboken, NJ, USA, 2012. <https://doi.org/10.1002/9781118164075>.
- [288] Y. Wang, W. Zhang, X. Guo, K. Jin, Z. Chen, Y. Liu, L. Yin, L. Li, K. Yin, L. Sun, Y. Zhao, Ni-Co Selenide Nanosheet/3D Graphene/Nickel Foam Binder-Free Electrode for High-Performance Supercapacitor, *ACS Appl. Mater. Interfaces.* 11 (2019) 7946–7953. <https://doi.org/10.1021/acsami.8b19386>.
- [289] C. Zhan, C. Lian, Y. Zhang, M.W. Thompson, Y. Xie, J. Wu, P.R.C. Kent, P.T. Cummings, D. Jiang, D.J. Wesolowski, Computational Insights into Materials and Interfaces for Capacitive Energy Storage, *Adv. Sci.* 4 (2017) 1700059. <https://doi.org/10.1002/adv.201700059>.
- [290] V.R. Stamenkovic, D. Strmcnik, P.P. Lopes, N.M. Markovic, Energy and fuels from electrochemical interfaces, *Nat. Mater.* 16 (2016) 57–69. <https://doi.org/10.1038/nmat4738>.
- [291] H.E. Toma, K. Araki, Exploring the Supramolecular Coordination Chemistry-Based Approach for Nanotechnology, *Prog. Inorg. Chem.* 56 (2009) 380–485. <https://doi.org/10.1002/9780470440124.ch5>.
- [292] D.H. McCullough, III, S.L. Regen, Don't forget Langmuir–Blodgett films, *Chem. Commun.* (2004) 2787–2791. <https://doi.org/10.1039/B410027C>.
- [293] M.C. Petty, *Langmuir-Blodgett films: An introduction*, Cambridge University Press, 1996.
- [294] V.P. Tolstoy, I. V. Chernyshova, V.A. Skryshevsky, *Handbook of Infrared Spectroscopy of Ultrathin Films*, John Wiley & Sons, Inc., Hoboken, NJ, USA, 2003. <https://doi.org/10.1002/047123432X>.
- [295] Y. Tang, Y. Zhuang, S. Zhang, Z.J. Smith, Y. Li, X. Mu, M. Li, C. He, X. Zheng, F. Pan, T. Gao, L. Zhang, Azo-Enhanced Raman Scattering for Enhancing the Sensitivity and Tuning the Frequency of Molecular Vibrations, *ACS Cent. Sci.* 7 (2021) 768–780. <https://doi.org/10.1021/acscentsci.1c00117>.
- [296] W. Rhodes, Hypochromism and Other Spectral Properties of Helical Polynucleotides, *J. Am. Chem. Soc.* 83 (1961) 3609–3617. <https://doi.org/10.1021/ja01478a017>.
- [297] I. Tinoco, Hypochromism in Polynucleotides 1, *J. Am. Chem. Soc.* 82 (1960) 4785–4790. <https://doi.org/10.1021/ja01503a007>.
- [298] M. Kasha, Energy Transfer Mechanisms and the Molecular Exciton Model for Molecular Aggregates, *Radiat. Res.* 178 (2012) AV27–AV34. <https://doi.org/10.1667/RRAV03.1>.
- [299] M. Kasha, H.R. Rawls, M. Ashraf El-Bayoumi, The exciton model in molecular spectroscopy, *Pure Appl. Chem.* 11 (1965) 371–392. <https://doi.org/10.1351/pac196511030371>.
- [300] M. Kasha, Energy Transfer Mechanisms and the Molecular Exciton Model for Molecular

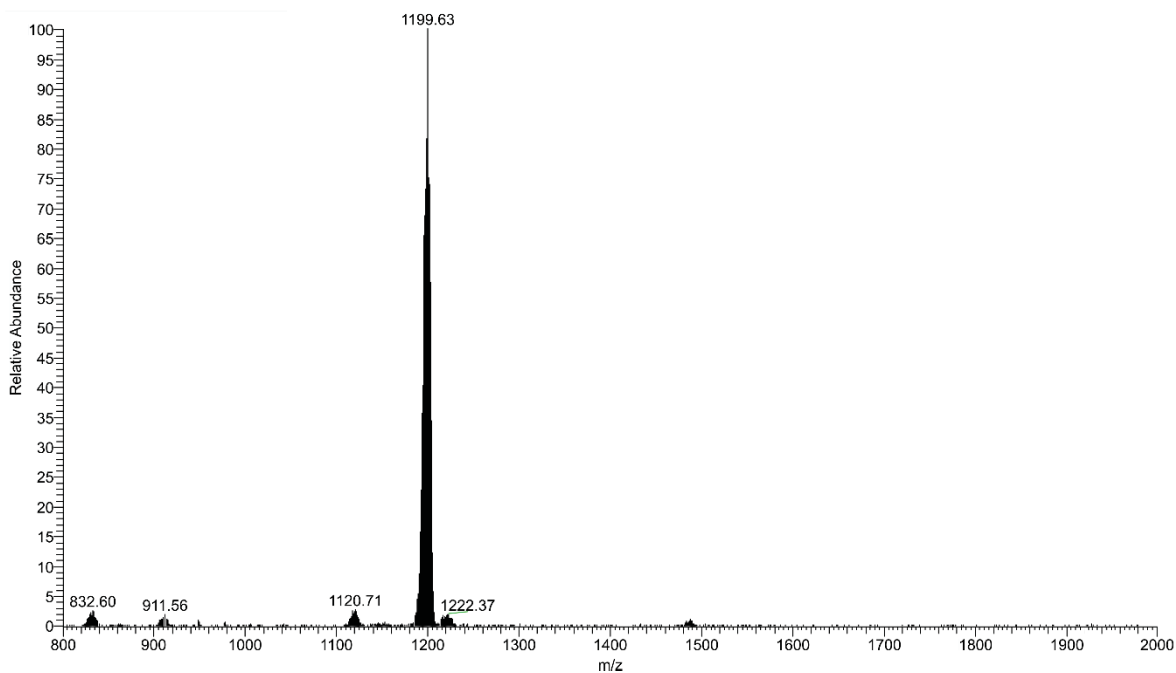
- Aggregates 1, 2, *Radiat. Res.* 20 (1963) 55–71.
- [301] A.E. Pérez Mendoza, H. Winnischofer, Understanding the Electrochemistry of Ruthenium Complex Thin Films to Guide the Design of Improved Energy Storage Electrodes, *J. Phys. Chem. C.* 125 (2021) 8965–8979. <https://doi.org/10.1021/acs.jpcc.1c01544>.
- [302] R. Parsons, The rate of electrolytic hydrogen evolution and the heat of adsorption of hydrogen, *Trans. Faraday Soc.* 54 (1958) 1053–1063. <https://doi.org/10.1039/tf9585401053>.
- [303] P.J. Pearce, A.J. Bard, Polymer films on electrodes, *J. Electroanal. Chem. Interfacial Electrochem.* 114 (1980) 89–115. [https://doi.org/10.1016/S0022-0728\(80\)80438-4](https://doi.org/10.1016/S0022-0728(80)80438-4).
- [304] E. Laviron, The use of linear potential sweep voltammetry and of a.c. voltammetry for the study of the surface electrochemical reaction of strongly adsorbed systems and of redox modified electrodes, *J. Electroanal. Chem. Interfacial Electrochem.* 100 (1979) 263–270. [https://doi.org/10.1016/S0022-0728\(79\)80167-9](https://doi.org/10.1016/S0022-0728(79)80167-9).
- [305] Y.Q. Li, J.C. Li, X.Y. Lang, Z. Wen, W.T. Zheng, Q. Jiang, Lithium Ion Breathable Electrodes with 3D Hierarchical Architecture for Ultrastable and High-Capacity Lithium Storage, *Adv. Funct. Mater.* 27 (2017) 1–8. <https://doi.org/10.1002/adfm.201700447>.
- [306] M. Abe, T. Michi, A. Sato, T. Kondo, W. Zhou, S. Ye, K. Uosaki, Y. Sasaki, Electrochemically controlled layer-by-layer deposition of metal-cluster molecular multilayers on gold, *Angew. Chemie - Int. Ed.* 42 (2003) 2912–2915. <https://doi.org/10.1002/anie.200351334>.
- [307] J. Pazinato, D.M. Hoffmeister, K.P. Naidek, E. Westphal, H. Gallardo, H. Winnischofer, Amphiphilic ruthenium bipyridine complex containing long-chain azopyridine group and the mechanism of electron transfer in Langmuir-Blodgett films, *Electrochim. Acta.* 153 (2015) 574–582. <https://doi.org/10.1016/j.electacta.2014.11.136>.
- [308] L. Maggini, R.R. Ferreira, 2D material hybrid heterostructures: Achievements and challenges towards high throughput fabrication, *J. Mater. Chem. C.* 9 (2021) 15721–15734. <https://doi.org/10.1039/d1tc04253j>.
- [309] J. Sun, Y. Choi, Y.J. Choi, S. Kim, J.H. Park, S. Lee, J.H. Cho, 2D–Organic Hybrid Heterostructures for Optoelectronic Applications, *Adv. Mater.* 1803831 (2019) 1–30. <https://doi.org/10.1002/adma.201803831>.
- [310] F. Ishiwari, Y. Shoji, T. Fukushima, Supramolecular scaffolds enabling the controlled assembly of functional molecular units, *Chem. Sci.* 9 (2018) 2028–2041. <https://doi.org/10.1039/c7sc04340f>.
- [311] C. Ybert, W. Lu, G. Möller, C.M. Knobler, Collapse of a monolayer by three mechanisms, *J. Phys. Chem. B.* 106 (2002) 2004–2008. <https://doi.org/10.1021/jp013173z>.
- [312] Q. Zheng, L. Shi, P.-C. Ma, Q. Xue, J. Li, Z. Tang, J. Yang, Structure control of ultra-large graphene oxide sheets by the Langmuir–Blodgett method, *RSC Adv.* 3 (2013) 4680. <https://doi.org/10.1039/c3ra22367a>.
- [313] W. Wan, Z. Zhao, H. Hu, Y. Gogotsi, J. Qiu, Highly controllable and green reduction of graphene oxide to flexible graphene film with high strength, *Mater. Res. Bull.* 48 (2013) 4797–4803. <https://doi.org/10.1016/j.materresbull.2013.08.031>.
- [314] P. V. Kumar, N.M. Bardhan, S. Tongay, J. Wu, A.M. Belcher, J.C. Grossman, Scalable

- enhancement of graphene oxide properties by thermally driven phase transformation, *Nat. Chem.* 6 (2014) 151–158. <https://doi.org/10.1038/nchem.1820>.
- [315] M.K. Rabchinskii, V. V. Shnitov, A.T. Dideikin, A.E. Aleksenskii, S.P. Vul, M. V. Baidakova, I.I. Pronin, D.A. Kirilenko, P.N. Brunkov, J. Weise, S.L. Molodtsov, Nanoscale perforation of graphene oxide during photoreduction process in the argon atmosphere, *J. Phys. Chem. C* 120 (2016) 28261–28269. <https://doi.org/10.1021/acs.jpcc.6b08758>.
- [316] I. Assunção, S. Sério, Q. Ferreira, N. Jones, S. Hoffmann, P. Ribeiro, M. Raposo, Graphene Oxide Layer-by-Layer Films for Sensors and Devices, *Nanomaterials*. 11 (2021) 1556. <https://doi.org/10.3390/nano11061556>.
- [317] J. Ning, L. Hao, M. Jin, X. Qiu, Y. Shen, J. Liang, X. Zhang, B. Wang, X. Li, L. Zhi, A Facile Reduction Method for Roll-to-Roll Production of High Performance Graphene-Based Transparent Conductive Films, (2017) 1–8. <https://doi.org/10.1002/adma.201605028>.
- [318] B.D. Ossoinon, D. Bélanger, functionalized reduced graphene oxide sheets, (2017) 27224–27234. <https://doi.org/10.1039/c6ra28311j>.
- [319] A. Jorio, E.H.M. Ferreira, F. Stavale, C.A. Achete, R.B. Capaz, M.V.O. Moutinho, A. Lombardo, T.S. Kulmala, A.C. Ferrari, Quantifying Defects in Graphene via Raman Spectroscopy at Different Excitation Energies, (2011) 3190–3196.
- [320] R. Arat, G. Jia, J. Plentz, *Diamond & Related Materials* Low temperature chemical treatment of graphene films made by double self-assembly process to improve sheet resistance, *Diam. Relat. Mater.* 111 (2021) 108218. <https://doi.org/10.1016/j.diamond.2020.108218>.
- [321] M. Ates, M. Yildirim, O. Kuzgun, H. Ozkan, The synthesis of rGO, rGO/RuO₂ and rGO/RuO₂/PVK nanocomposites, and their supercapacitors, *J. Alloys Compd.* 787 (2019) 851–864. <https://doi.org/10.1016/j.jallcom.2019.02.126>.
- [322] J.-G. Wang, L. Ren, Z. Hou, M. Shao, Flexible reduced graphene oxide/prussian blue films for hybrid supercapacitors, *Chem. Eng. J.* 397 (2020) 125521. <https://doi.org/10.1016/j.cej.2020.125521>.
- [323] B. Jia, L. Zou, Langmuir–Blodgett assembly of sulphonated graphene nanosheets into single- and multi-layered thin films, *Chem. Phys. Lett.* 568–569 (2013) 101–105. <https://doi.org/10.1016/j.cplett.2013.02.073>.
- [324] A. Yu, I. Roes, A. Davies, Z. Chen, Ultrathin, transparent, and flexible graphene films for supercapacitor application, *Appl. Phys. Lett.* 96 (2010) 253105. <https://doi.org/10.1063/1.3455879>.
- [325] S. Alipoori, S. Mazinani, S.H. Aboutalebi, F. Sharif, Review of PVA-based gel polymer electrolytes in flexible solid-state supercapacitors: Opportunities and challenges, *J. Energy Storage*. 27 (2020) 101072. <https://doi.org/10.1016/j.est.2019.101072>.
- [326] K. Wang, X. Zhang, C. Li, X. Sun, Q. Meng, Y. Ma, Z. Wei, Chemically Crosslinked Hydrogel Film Leads to Integrated Flexible Supercapacitors with Superior Performance, *Adv. Mater.* 27 (2015) 7451–7457. <https://doi.org/10.1002/adma.201503543>.
- [327] Z. Liu, J. Zhang, J. Liu, Y. Long, L. Fang, Q. Wang, T. Liu, Highly compressible and superior low temperature tolerant supercapacitors based on dual chemically crosslinked PVA hydrogel

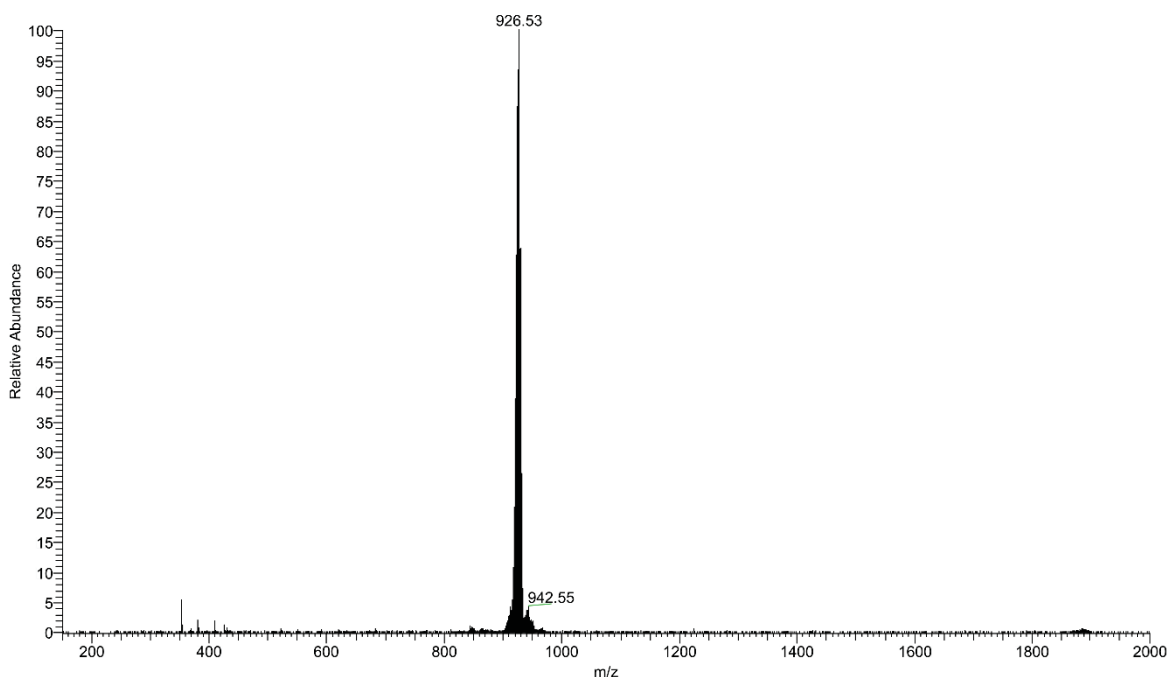
- electrolytes, *J. Mater. Chem. A*. 8 (2020) 6219–6228. <https://doi.org/10.1039/c9ta12424a>.
- [328] Z. Wang, Q. Pan, An Omni-Healable Supercapacitor Integrated in Dynamically Cross-Linked Polymer Networks, *Adv. Funct. Mater.* 27 (2017) 1–8. <https://doi.org/10.1002/adfm.201700690>.
- [329] C. (John) Zhang, T.M. Higgins, S.H. Park, S.E. O'Brien, D. Long, J.N. Coleman, V. Nicolosi, Highly flexible and transparent solid-state supercapacitors based on RuO₂/PEDOT:PSS conductive ultrathin films, *Nano Energy*. 28 (2016) 495–505. <https://doi.org/10.1016/j.nanoen.2016.08.052>.
- [330] K. Lee, H. Lee, Y. Shin, Y. Yoon, D. Kim, H. Lee, Highly transparent and flexible supercapacitors using graphene-graphene quantum dots chelate, *Nano Energy*. 26 (2016) 746–754. <https://doi.org/10.1016/j.nanoen.2016.06.030>.
- [331] A.P.S. Gaur, W. Xiang, A. Nepal, J.P. Wright, P. Chen, T. Nagaraja, S. Sigdel, B. Lacroix, C.M. Sorensen, S.R. Das, Graphene Aerosol Gel Ink for Printing Micro-Supercapacitors, *ACS Appl. Energy Mater.* 4 (2021) 7632–7641. <https://doi.org/10.1021/acsaem.1c00919>.
- [332] Y. Wang, S. Su, L. Cai, B. Qiu, N. Wang, J. Xiong, C. Yang, X. Tao, Y. Chai, Monolithic Integration of All-in-One Supercapacitor for 3D Electronics, *Adv. Energy Mater.* 9 (2019) 19–21. <https://doi.org/10.1002/aenm.201900037>.
- [333] Y.W. Na, J.Y. Cheon, J.H. Kim, Y. Jung, K. Lee, J.S. Park, J.Y. Park, K.S. Song, S.B. Lee, T. Kim, S.J. Yang, All-in-one flexible supercapacitor with ultrastable performance under extreme load, *Sci. Adv.* 8 (2022) 1–11. <https://doi.org/10.1126/sciadv.abl8631>.
- [334] Y. Xu, X. Huang, Z. Lin, X. Zhong, Y. Huang, X. Duan, One-step strategy to graphene/Ni(OH)₂ composite hydrogels as advanced three-dimensional supercapacitor electrode materials, *Nano Res.* 6 (2013) 65–76. <https://doi.org/10.1007/s12274-012-0284-4>.
- [335] Y. Xu, Z. Lin, X. Zhong, X. Huang, N.O. Weiss, Y. Huang, X. Duan, Holey graphene frameworks for highly efficient capacitive energy storage, *Nat. Commun.* 5 (2014). <https://doi.org/10.1038/ncomms5554>.

APPENDIX A SUPPLEMENTARY INFORMATION

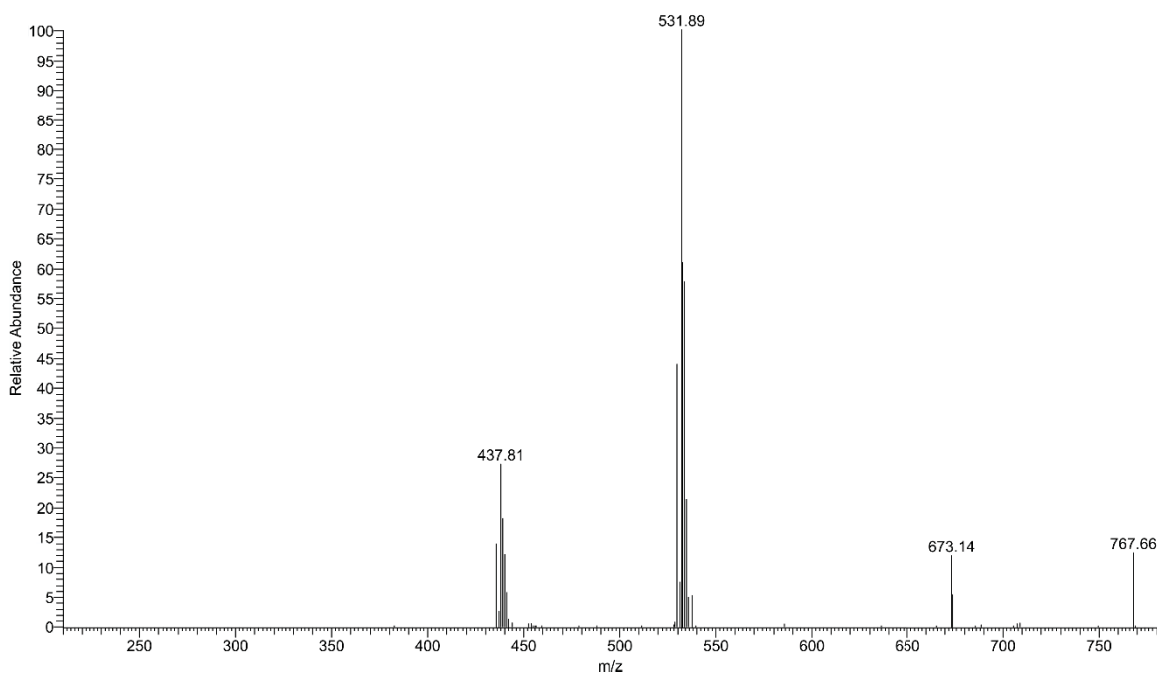
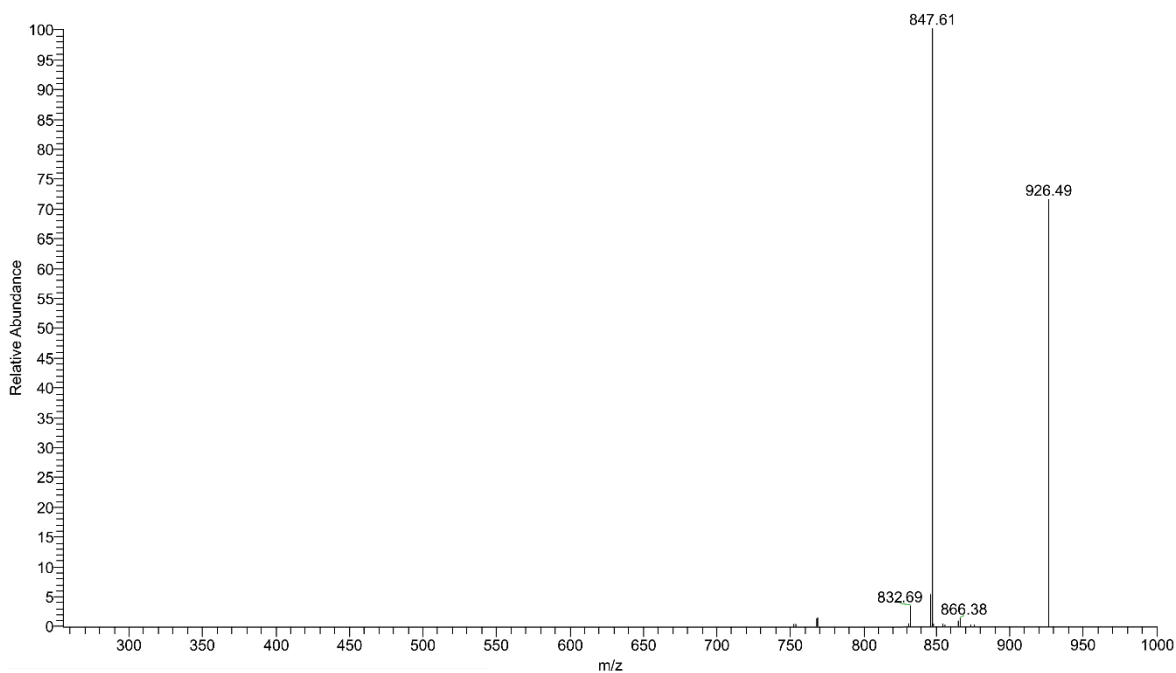
Structure of Triruthenium Clusters

FIGURE A-1- MASS SPECTRUM OF $[\text{RU}_3\text{O}(\text{CH}_3\text{CO}_2)_6\text{PY}_2\text{AZOPY}]^+$ 

SOURCE: Author

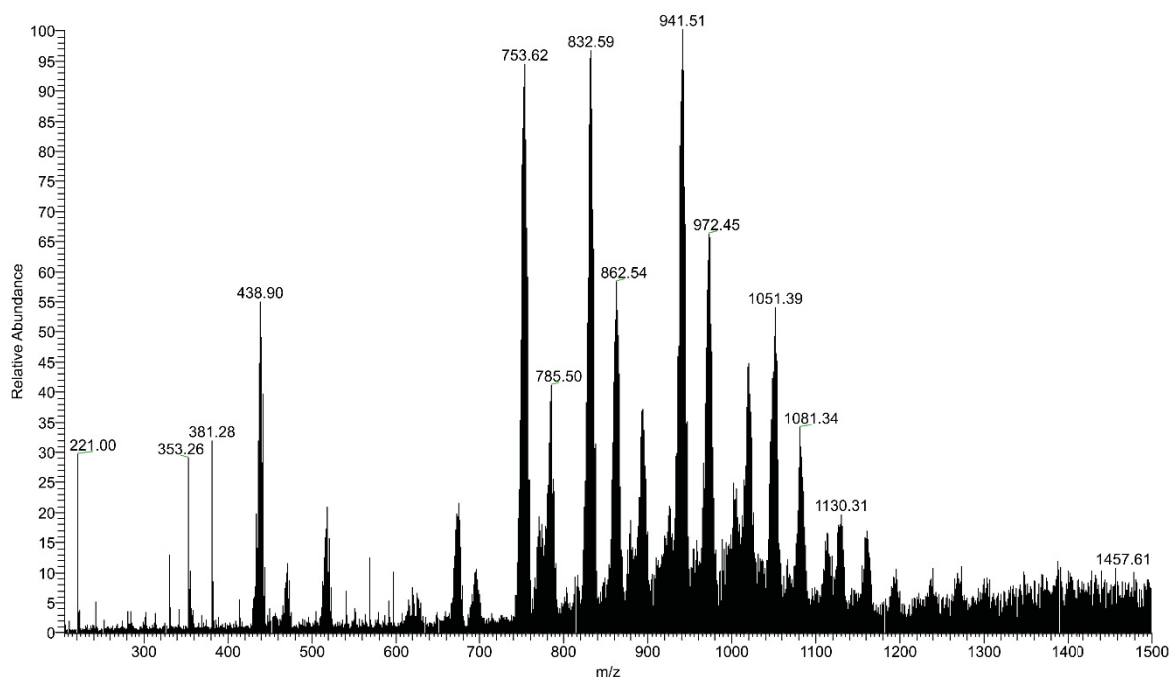
FIGURE A-2 - MASS SPECTRUM OF $[\text{RU}_3\text{O}(\text{CH}_3\text{CO}_2)_6\text{PY}_2\text{NH}_2\text{PY}]^+$ 

SOURCE: Author

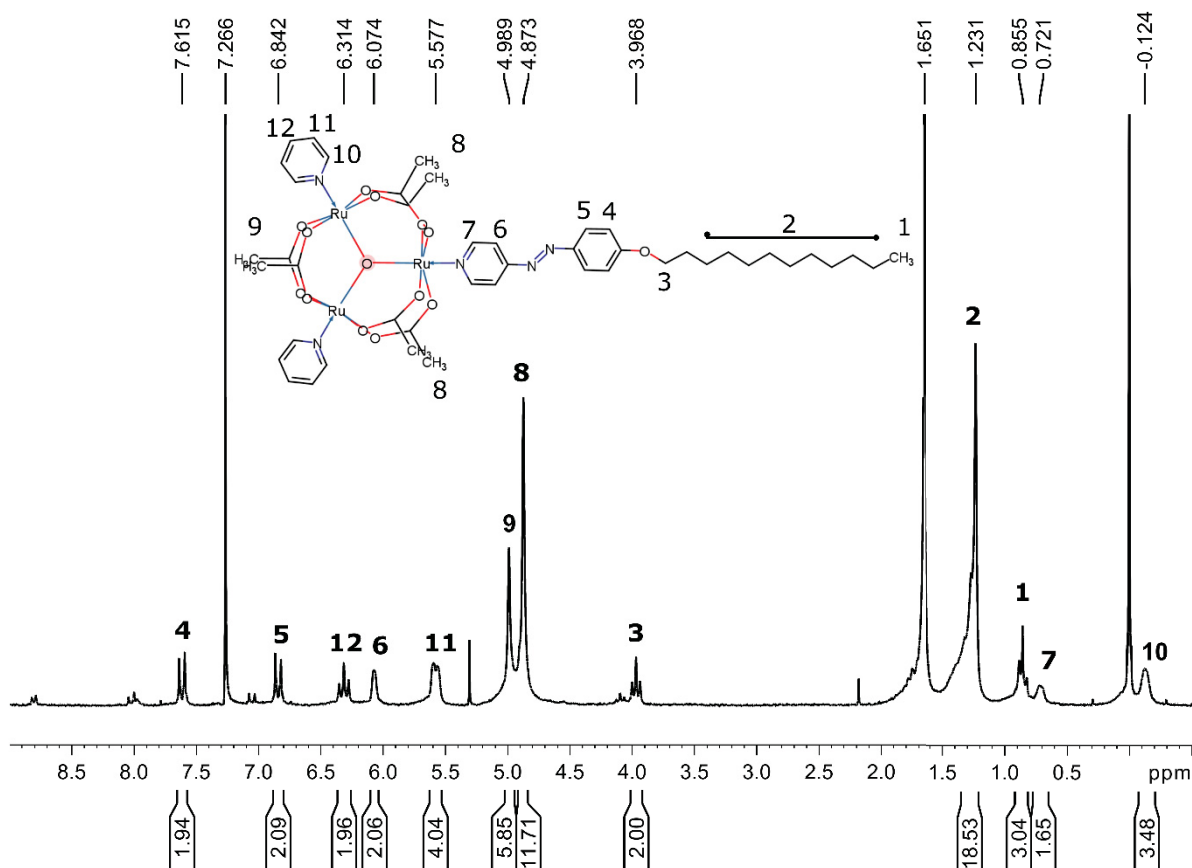
FIGURE A-3 - MASS SPECTRUM OF FRAGMENTS DERIVED FROM $[\text{Ru}_3\text{O}(\text{CH}_3\text{CO}_2)_6\text{Py}_2\text{NH}_2\text{Py}]^+$ 

Upper image show the fragment derived from the cation $\text{Ru}_3\text{O}(\text{CH}_3\text{CO}_2)_6\text{Py}_2\text{NH}_2\text{Py}]^+$ m/z = 926.49. The bottom image show the fragment derived from the cation $\text{Ru}_3\text{O}(\text{CH}_3\text{CO}_2)_6\text{Py}_2\text{NH}_2\text{Py}]^+$ m/z = 767.66.

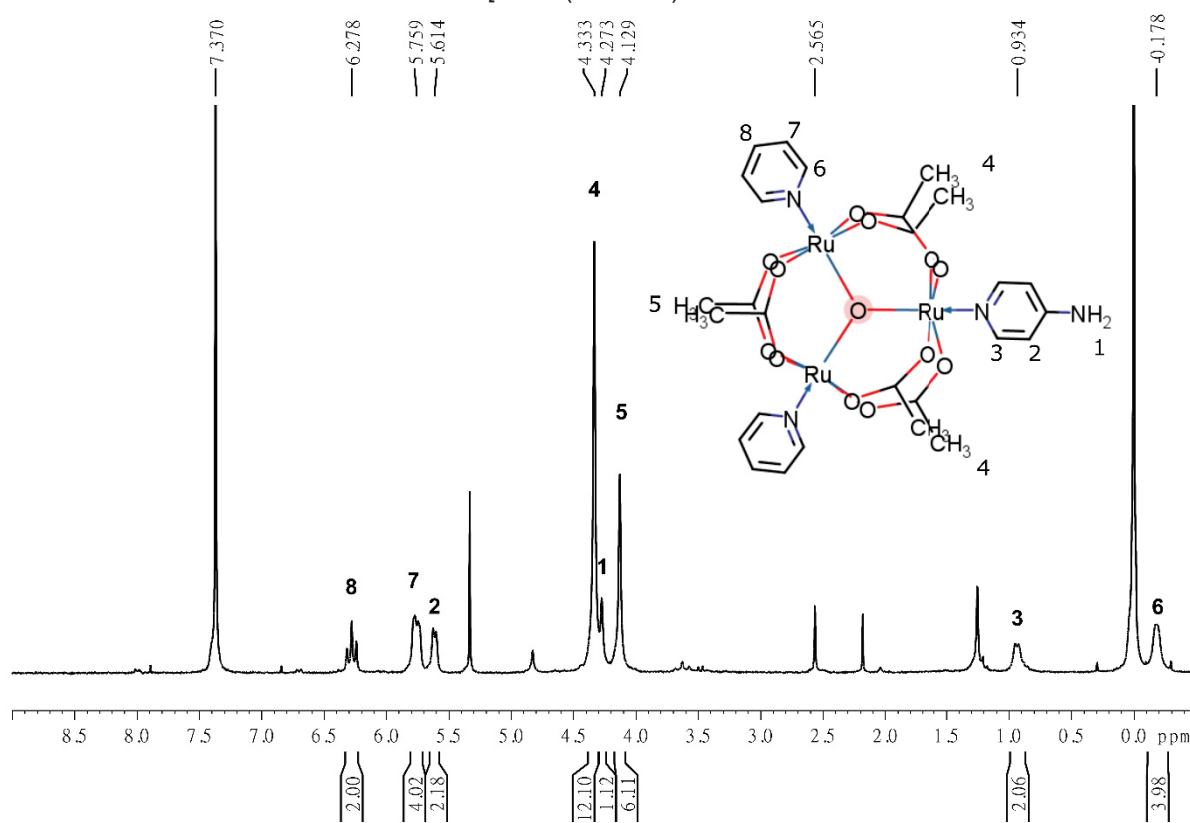
SOURCE: Author

FIGURE A-4- MASS SPECTRUM OF $[\text{Ru}_3\text{O}(\text{CH}_3\text{CO}_2)_6\text{PY}_2\text{SHPY}]^+$ 

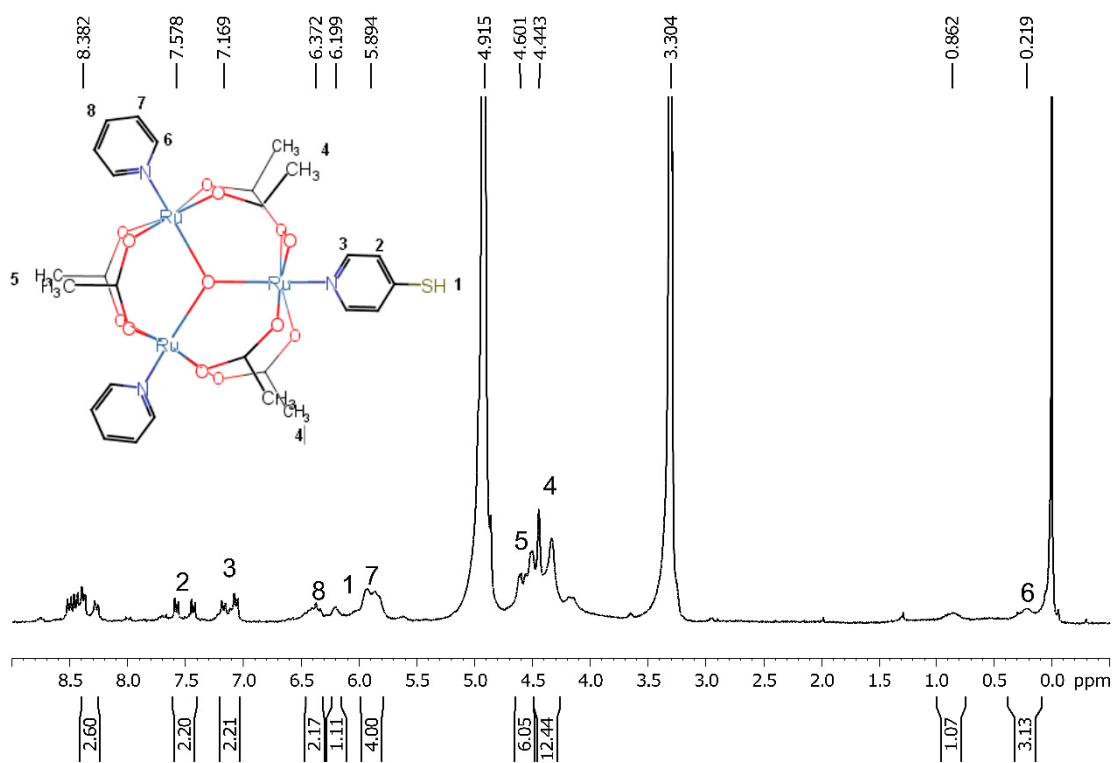
SOURCE: Author

FIGURE A-5 – $^1\text{H-NMR}$ SPECTRUM OF $[\text{Ru}_3\text{O}(\text{CH}_3\text{CO}_2)_6\text{PY}_2\text{AZOPY}]^+$ 

SOURCE: Author

FIGURE A-6 – $^1\text{H-NMR}$ SPECTRUM OF $[\text{Ru}_3\text{O}(\text{CH}_3\text{CO}_2)_6\text{PY}_2\text{NH}_2\text{PY}]$ 

SOURCE: Author

FIGURE A-7 – $^1\text{H-NMR}$ SPECTRUM OF $[\text{Ru}_3\text{O}(\text{CH}_3\text{CO}_2)_6\text{PY}_2\text{SHPY}]$ 

Theoretical Assignment of FTIR spectra

<http://d4mzdebau954.cloudfront.net/>

Simulation Details

Dimensionless concentration, length and time variables θ_R , z , t' were defined to implement the computational simulation, since a better numerical behavior could be obtained.

$x = Lz$ with L : the film thickness.

$\Gamma_R = \Gamma_S \theta_R$ with Γ_S : the total surface concentration in one monolayer.

$t = t' t_f$ with t_f : time of duration of electrochemical experiment (s1)

So, the equations -7.4 in their dimensionless form are:

$$\begin{aligned} \frac{\partial \theta_R(x,t)}{\partial t'} &= \frac{D_e t_f}{L^2} \frac{\partial^2 \theta_R(x,t)}{\partial z^2} \\ \frac{\partial \theta_R(0,t)}{\partial t} &= \frac{D_e t_f}{L^2 \Delta z} \frac{\partial \theta_R(0,t)}{\partial z} + r'_R, \quad r'_R = (k_f \theta_O(0,t) - k_b \theta_R(0,t)) t_f = (k_f - k_f \theta_R(0,t) - k_b \theta_R(0,t)) t_f \\ \frac{\partial \theta_R(0,t)}{\partial t'} &= -\frac{D_e t_f}{L^2 \Delta z} \frac{\partial \theta_R(L,t)}{\partial z} \quad (\text{s2}) \end{aligned}$$

The kinetic parameters were calculated as indicated in equations 7.12 of the main text. Note that r'_R is redefined including the total mass balance $\Gamma_O(t) = \Gamma^S - \Gamma_R(t)$ or $\theta_O(t) = 1 - \theta_R(t)$, also they have the same units as k^0 (s^{-1}), so r'_R in the above equation is defined as a dimensionless quantity. Furthermore, the equivalent exponential factor $\frac{\gamma \Gamma_S}{RT} \theta$ is obtained when expressed in terms of the dimensionless concentration θ as is shown in (s3).

$$\begin{aligned} k_f &= k^0 e^{-\frac{\Delta G_{film,O}}{RT}} e^{-\frac{F\eta}{RT}} \quad \text{with} \quad \Delta G_{film,O} = \gamma \Gamma^S \theta_O - \Delta G_O^{ads} \\ k_b &= k^0 e^{-\frac{\Delta G_{film,R}}{RT}} e^{(1-\alpha)\frac{F\eta}{RT}} \quad \text{with} \quad \Delta G_{film,R} = \gamma \Gamma^S \theta_R - \Delta G_R^{ads} \quad (\text{s3}) \end{aligned}$$

For the simulation of films with several layers the ΔG_i^{ads} was calculated as the mean value of the m layers in the film, if the adsorption energy in the first layer (adjacent to substrate) is different to the adsorption in the other layers, in this way the experimental variation of $E_{1/2}$ is captured:

$$\Delta G_i^{ads} = \frac{\Delta G_i^{ads}(1) + \Delta G_i^{ads}(k) \times (m-1)}{m} \quad (\text{s4})$$

According to experimental results O adsorption in the first layer should be more favorable than R adsorption, whereas O adsorption in the other layers should be significantly lower than R adsorption. Finally, the right-hand part of the equations (s2) was discretized using central finite differences, leading to a set of ordinary differential equations with t' as the only independent variable:

$$\frac{\partial \theta_R(i,t)}{\partial t'} = \frac{D_e t_f}{\Delta z^2 L^2} \theta_R(i+1,t) - 2\theta_R(i,t) + \theta_R(i-1,t) \text{ with } i = 2, \dots, m-1 \text{ } m: \text{ number of layers}$$

$$\frac{\partial \theta_R(1,t)}{\partial t'} = \frac{D_e t_f}{L^2 \Delta z^2} [\theta_R(2) - \theta_R(1)] + (k_f - k_f \theta_R(1,t) - k_b \theta_R(1,t)) t_f$$

$$\frac{\partial \theta_R(m,t)}{\partial t'} = \frac{D_e t_f}{L^2 \Delta z^2} [\theta_R(m-1) - \theta_R(m)] \quad (\text{s5})$$

A code using the command `ode15s` of MATLAB was implemented to solve the set equations s5 with the constitutive equation s3. For the model implementation was required, in addition to constants and model parameters defined in Table 1, the definition of the t' interval simulated (from 0 to 1), the η values in each time and the initial condition set ($\theta_R(i,t)$). The lasts were initially chosen arbitrarily as 3/5, so a constant η value in each time was defined as $\eta = E_1 - E^0$ with E_1 the lower potential value defined for cyclic voltammetry experiment. Then the obtained $\theta_R(i,t)$ values which were close to equilibrium value were used as initial condition for cyclic voltammetry simulation, for which the potential E used was the typical triangular signal depending on time and the scan rate v .

It worth to point out that the values of L , Γ_s , and t_f were estimated based on experimental and theoretical results. The one monolayer thickness Δx was estimated from the optimized geometry obtained with DFT assuming that cluster is oriented with ligand AzoPy normal to the surface, so the film thickness L is obtained multiplying Δx by the number of layers. Γ_s was estimated from monolayer isotherms on the water air interface, and t_f of cyclic voltammetry is estimated multiplying the potential window tested by two and dividing by the scan rate.

MATLAB Codes used to simulate the model and to fit cyclic voltammetry data

<https://github.com/aleperezme/Rufilmmodel>

APPENDIX B ACADEMIC INFORMATION

Subject	Code	Credits	Grade
NANOQUÍMICA E NANOMATERIAIS	QUIM-7023	4	A
ESPECTROSCOPIA VIBRACIONAL E ELETRÔNICA	QUIM-7007	4	A
REAÇÕES DE TRANSFERÊNCIA ELETRÔNICA	QUIM-7034	4	A
QUÍMICA INORGÂNICA AVANÇADA	QUIM-7031	4	A
SEMINÁRIOS D1	QUIM-7038	1	A
SEMINÁRIOS D2	QUIM-7039	1	A
PRÁTICA DE DOCÊNCIA EM QUÍMICA	QUIM-7024	1	
MATERIAIS LAMELARES – SÍNTESE, CARACTERIZAÇÃO E APLICAÇÕES	QUIM-7045	2	A
ELECTROCHEMISTRY: FUNDAMENTAL AND APPLICATIONS	QUIM-7048	1	A
ELECTRONIC PROPERTIES IN ISOLATED AND EXTENDED STRUCTURES: COMPUTATIONAL STUDIES	QUIM-7045	2	A
PRÁTICA DE DOCÊNCIA EM QUÍMICA-2	QUIM-7024	1	A

APPENDIX C PUBLICATIONS AND EVENTS

Peer-reviewed research papers

(1) Pérez Mendoza, A. E.; Naidek, N.; Cesca, E. C.; Sagás, J. C.; Orth, E. S.; Zarkin, A. J. G.; Winnischofer, H. Graphene Modified with Triruthenium Acetate Clusters as an Electrode for the Hybrid Energy Storage System. *ACS Appl. Nano Mater.* 2020, 3 (7), 6757–6765. <https://doi.org/10.1021/acsnm.0c01170>

(2) Winnischofer, H.; Cesca, E.; Mendoza, A.; Araújo, I.; Westphal, E.; Mezalira, D.; Balogh, D.; Oliveira Jr., O. Heterostructured Langmuir-Blodgett Films of Ruthenium Bipyridine with 1,3,4-Naphthooxadiazole-Derived Amphiphile Complex as a Charge Storage Electrode. *J. Braz. Chem. Soc.* 2020, 31 (11), 2371–2384. <https://doi.org/10.21577/0103-5053.20200137>.

(3) Pérez Mendoza, A. E.; Winnischofer, H. Understanding the Electrochemistry of Ruthenium Complex Thin Films to Guide the Design of Improved Energy Storage Electrodes. *J. Phys. Chem. C* 2021, 125 (17), 8965–8979. <https://doi.org/10.1021/acs.jpcc.1c01544>.

Events

8° Congresso Brasileiro de Carbono, 2019. Oral Presentation: Triruthenium cluster modified graphene electrodes for increment pseudocapacitor efficiency. São João del-Rei.

XIX Brazil MRS Meeting & International Union of Materials Research Societies-International Conference on Electronic Materials (I), 2021. Oral Presentation: High Performance Energy Storage Devices Based on Triruthenium Acetate Complex Based Thin Films. Online.

1st PhD Student Symposium on “Materials for Energy, Environment and Health”, 2021. Oral Presentation: Electrochemical Energy Storage Devices Based on Ruthenium Complexes Nanomaterials. Online.